



Turbulence

Lecture Notes for the M2 Soft Matter-Bio

Preliminay Version

Please report any typo or bug

Bérénègre Dubrulle

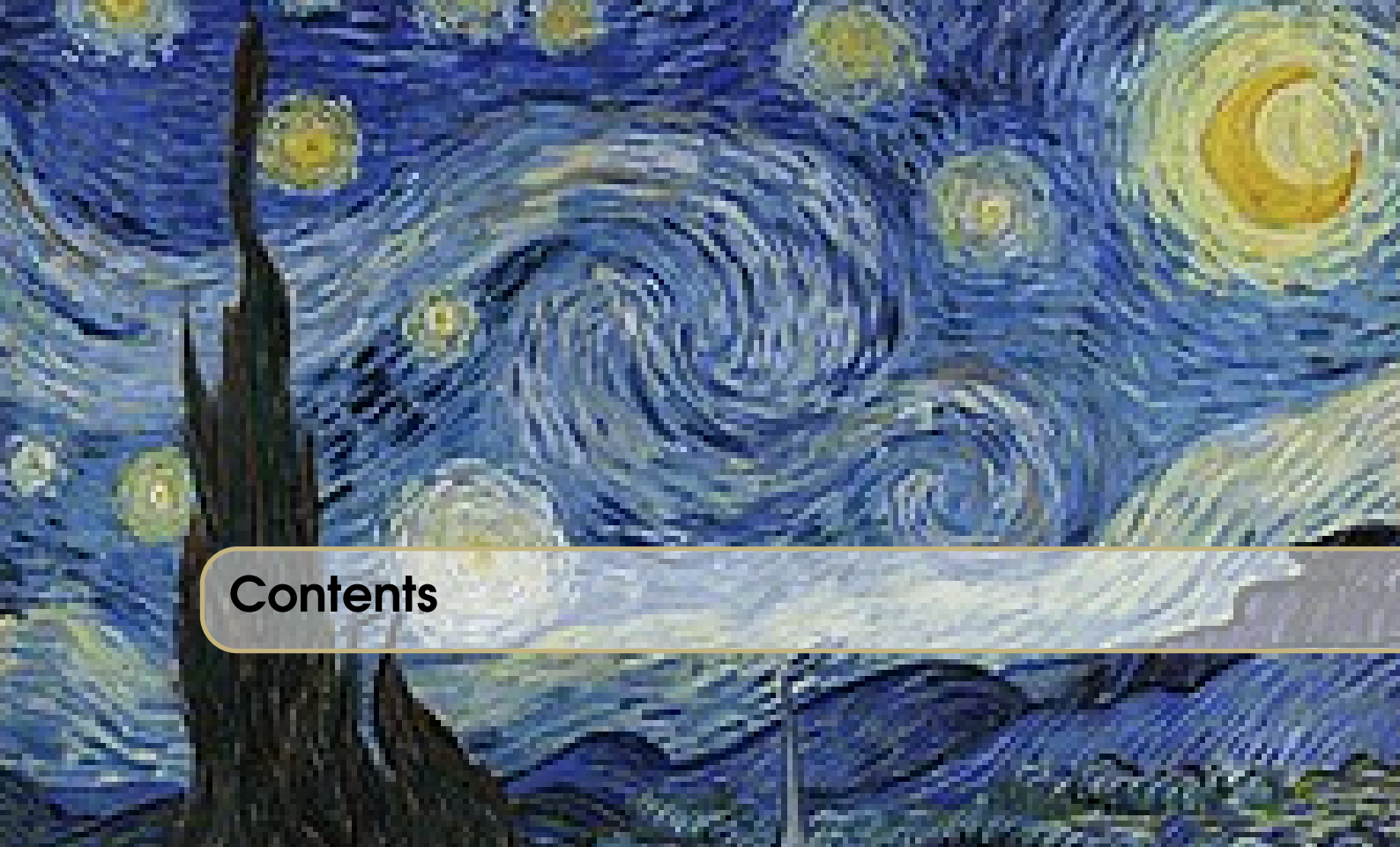
Copyright © 2019 BD

PUBLISHED BY PUBLISHER

BOOK-WEBSITE.COM

Licensed under the Creative Commons Attribution-NonCommercial 3.0 Unported License (the "License"). You may not use this file except in compliance with the License. You may obtain a copy of the License at <http://creativecommons.org/licenses/by-nc/3.0>. Unless required by applicable law or agreed to in writing, software distributed under the License is distributed on an "AS IS" BASIS, WITHOUT WARRANTIES OR CONDITIONS OF ANY KIND, either express or implied. See the License for the specific language governing permissions and limitations under the License.

First printing, March 2019

A reproduction of Vincent van Gogh's painting "The Starry Night". It depicts a dark blue night sky filled with swirling, yellow and white stars and a crescent moon. In the foreground, a dark, silhouetted cypress tree stands on the left, and rolling hills with green fields and small town houses are visible in the middle ground.

Contents

I

Introduction

1	Turbulence	13
1.1	Generalities	13
1.2	What is turbulence?	14
1.2.1	A tentative definition	14
1.2.2	The equations of fluid dynamics	15
1.3	What is the problem with turbulence?	16
1.4	What will we do in that course?	17
1.5	Description of data sets	18

II

Mathematical singularities

2	Singularities, blow-up and poles	23
2.1	Generalities	23
2.1.1	Regularity and dimension	23
2.1.2	Regularity and symmetry?	23
2.2	Blow-up scenarios	24
2.2.1	Self-similar blow-up solutions in non-linear systems	24
2.2.2	Singularity in the Complex Plane	24
2.3	Blow-up diagnostics	24
2.3.1	Euler case: Inviscid case	24
2.3.2	Navier-Stokes: Viscous case	25
2.3.3	Poles: Singularity Strip	25

2.4	Some useful analytical results	25
2.4.1	Probability of occurrence of singularities	25
2.4.2	Bounds for flows on torus	26
3	Illustration: blow-up in log-lattices	27
3.1	Log-lattice framework	27
3.1.1	Definitions and notations	27
3.1.2	Global quantities	28
3.1.3	Regularity	28
3.1.4	Singularity strip method for log-lattices	28
3.2	1D case: Burgers	28
3.2.1	Inviscid case	29
3.2.2	Viscous case	29
3.3	3D case: Euler and Navier-Stokes	32
3.3.1	Inviscid case: Euler	32
3.3.2	Viscous case: Navier-Stokes	32
3.4	Discussion	32
4	Singularities in fluids	37
4.1	Self-similar blow-up solutions	37
4.1.1	1D: Burgers	37
4.1.2	3D: Euler and navier-Stokes	37
4.2	Possible mechanisms for singularity	38
4.2.1	Gradient blow-up in 1D Burgers	38
4.2.2	Pressure Mediated Singularity in 3D Euler	38
4.2.3	Singularity of Vortex Filaments in 3D Navier-Stokes	39
4.2.4	Singularity in the Complex Plane	39
5	Useful tools for studying irregular motions	41
5.1	Multi-fractals	41
5.1.1	Hölder continuity	41
5.1.2	Measurements using wavelet transforms	41
5.1.3	Examples of rough fields	42
5.1.4	The multifractal phenomenology	42
5.2	Illustration: Burgers solution	42
5.3	Weak Formalism	43
5.3.1	How to implement a weak formulation?	43
5.3.2	Small scale limit	43

III

Physics of incompressible turbulence

6	Energetics of turbulence and the first law	47
6.1	Global energy budget	47
6.2	Velocity correlations and energy spectrum	47
6.3	Universality of the spectrum	49

7	The K41 theory and its consequences	51
7.1	Derivation of the Kármán-Howarth-Monin equation	51
7.2	Preliminaries	51
7.2.1	Useful identities	51
7.3	Summary of K41 theory	52
7.4	K41 as a phenomenology of cascade and energy balance in scale space 53	
7.5	Universality of the energy budget in scale	55
7.6	Statistical properties of the energy cascade in scale space	55
8	K41 theory and symmetries: successes and limitations	57
8.1	Some basic symmetries of Navier-Stokes	57
8.2	Rescaling symmetry breaking and generalized skewness	57
8.3	Energy cascade and inhomogeneity	58
8.4	Vortex stretching and $1/3$ rescaling	58
8.5	Global scale symmetry breaking and intermittency	60
8.6	Time reversal breaking and enstrophy blow up	61
9	The Kolmogorov-Obukhov refined similarity hypothesis	67
9.1	Summary of the theory K62	67
9.2	Test of refined similarity hypothesis	68
9.3	Problems and issues set by K62	69
10	Weak formulation of Karman-Howarth-Monin equation	73
10.1	Derivation of the weak Karman-Howarth-Monin equation	73
10.1.1	Why a weak formulation?	73
10.1.2	Summary of Duchon-Robert derivation	74
10.2	Properties of WKHM	75
10.2.1	Robustness with respect to noise	75
10.2.2	Interpretation of WKHM as local KHM	75
10.2.3	Small scale limit	76
10.2.4	Inertial dissipation and Onsager's conjecture	77
10.2.5	Illustration: inertial dissipation by a shock	77
10.2.6	Effects of viscosity and resolution	77
10.3	WKHM and intermittency	79
10.3.1	Spatial distribution of energy transfers and dissipation	79
10.3.2	Statistical properties of local energy transfers and dissipation	81
10.3.3	Scaling of energy transfers and dissipation	83
10.3.4	Intermittency and energy transfers	83

IV

Application of Multifractals to Turbulence

11	Beyond Kolmogorov using multi-fractals	87
11.1	The multifractal model for turbulence	87

11.2	The multifractal and Onsager's dissipative solutions	87
11.3	Illustration: Burgers solution	88
11.4	Interpretation of extreme events of local energy transfers	88
11.5	Scaling range	89
11.6	Scaling exponents and signs of \mathcal{D}_ℓ^I and \mathcal{D}_ℓ^V	89
12	Constraints on the multifractal spectrum	93
12.1	Theoretical constraints	93
12.1.1	For general boundary conditions	93
12.1.2	Flows on a torus	93
12.1.3	Illustration: the log-normal model	96
12.2	Observational Constraints on the MFR spectrum	96
13	Additional properties of Multifractals	99
13.1	WKHM-Multifractal refined similarities	99
13.2	Thermodynamical analogy	100
13.2.1	The large deviation formulation and thermodynamics	100
13.2.2	Recovering universality	100
13.3	Local multi-fractal analysis	102
13.3.1	Active regions and the nested (concentration) volume interpretation	102
13.3.2	Connection with multi-fractal formalism and construction of local exponents	102

V

Modelling turbulence

14	Generalities on Turbulent transport	107
14.1	Introduction	107
14.1.1	Transport turbulent?	107
14.1.2	Propriétés générales du transport turbulent	107
14.1.3	Comment modéliser le transport turbulent?	111
14.2	Approche Lagrangienne	113
14.2.1	Particules neutres	113
14.2.2	Diffusion anormale	114
14.2.3	Particules lourdes/légères	118
14.3	Approche Eulérienne	120
14.3.1	La méthode multi-échelle	120
14.3.2	Quelques compléments	124
14.4	En guise de conclusion	127
15	Closures and Computation of turbulent transport coefficients	129
15.1	Basic equations and definitions	130
15.1.1	Filters	130
15.1.2	Equations	130
15.2	RANS	130
15.2.1	Equations	131

15.3 Large eddy simulations	131
15.3.1 Filter properties	131
15.3.2 Physical constraints on the closure	132
15.3.3 Eddy viscosity models	132
15.3.4 Homogenization	132
15.4 Rapid Distortion Theory	137
15.4.1 Filtering	137
15.4.2 Gabor transform	138
15.4.3 Derivation of the dynamical equation	139
15.4.4 Interest of RDT model	140
15.5 Beyond eddy-viscosity models	140
15.5.1 Viscosity-entropy method	141
15.5.2 REWA models	142
15.5.3 Log-lattices	143

VI

Beyond incompressible turbulence

16 Rayleigh-Benard Convection	147
16.1 Phenomenology	147
16.1.1 Description	147
16.1.2 Observations	147
16.2 Equations	148
16.3 Physics of Convection	149
16.3.1 Energy budget	149
16.3.2 Example: the Earth climate as a thermal engine	149
16.4 Convection onset	150
16.4.1 Non-rotating case	150
16.4.2 Rotating case	151
16.5 Scaling laws in convection	151
16.5.1 Convection onset and Transitional regime	152
16.5.2 Turbulent regime	152
Bibliography	155
Articles	155
Books	159
Index	161



Introduction

1	Turbulence	13
1.1	Generalities	
1.2	What is turbulence?	
1.3	What is the problem with turbulence?	
1.4	What will we do in that course?	
1.5	Description of data sets	



1. Turbulence

1.1 Generalities

Fluids and condensed gases represent a major fraction of our surroundings: our sun was born within the spiral arms of the Galaxy, an enormous mass of gas; our planet was born within an accretion disks, made with the remaining parts of the forming Sun; our body is made of 75 % of water; the oceans fill 70 % of the Earth surface; above it, the atmosphere governs the water cycle and is the location of winds, re-circulations, typhoons and storms; below the Earth surface, the melting rocks and metals move so as to generate plate tectonics, volcano eruptions and magnetic fields. Fluids and condensed gases are also heavily used in our every day life and in our industries, to mix, stir, shape, dilute, burn or construct various species or objects.

Like matter and solid, fluids and condensed gas are characterized by different states, depending on external and internal conditions. In this book, we shall focus on a state of fluid that is characterized by swirling motions, a state referred to as *Turbulence*. There is however no official definition of turbulence, and sometimes, wording may provide a wrong feeling of what turbulence really is. For example, a *turbulent* child has a tendency to jump and run everywhere, never stay still and requires constant attention. Any passenger on a transatlantic flights fears the occurrence of *turbulences* during the journey, that causes the plane to abruptly rock around. Stock markets are shaken by *turbulences* from time to time, following the alea of wars, politics or crisis. In summary, the word *turbulence* awake in our imaginations visions of shaky, disorganized or chaotic situations. Yet, if you look at turbulent flows that are part of our daily life, you see organized, coherent structures, that are called vortices. Such structures are so beautiful, so ubiquitous and so remarkable that they have attracted the attention of painters of all nationality, from the japanese Hiroshige, to the italien Leonardo Da Vinci and the dutsch Vincent Van Gogh (Figure 1.1). The structures represented by these painters are mesoscopic, in the sense that their dimension are commensurable to human dimension: they range fro a few centimeters, for the vortices in a river, to a few 10 or hundred of meters for the Naruto vortex or vortices in the clouds. In later time, when technology progress allowed the exploration of smaller scales (through microscope) or planetary or galactic time scales (through satellites or telescopes), we discovered that vortices are apparently an essential component of turbulent natural flows, with scales ranging from an angstrom (in Bose-Einstein condensates), to



Figure 1.1: Vortices in art: Leonardo; river: vortices; Van Gogh: atmosphere; Hiroshige: Narito vortex, the wave (one sees very small scale)

parsecs (xx) in Galaxies (see Figure 1.2). Refined observations of the universe, and well controlled laboratory experiments or numerical simulations of turbulent flows revealed actually the presence of other types of structures, like filaments , that arise at either the very largest scales of the Universe, or at the smaller scale of a turbulent flow. This shows that the turbulence is not simply "made of vortices", and calls for a deeper comprehension of how and why such structures are created, how they disappear, and how they are important for the flow dynamics. The answer to this questions is not simple, and many famous scientists have tried without success to build a complete et useful theory of turbulence. There is a legend according to which Sir Lamb would have said something like: *"there are two problems for which I would dream to find a solution when I reach paradise: reunification of all the forces, and turbulence. For the former, I am rather optimistic."*

1.2 What is turbulence?

1.2.1 A tentative definition

The first lesson I learned as a graduate student is that there is no official definition of turbulence. According to consensual observations, turbulence is a state of the fluids characterized by swirling motions. Such motions are observed in a variety of phenomena, covering a wide range of scales, from angstrom in Bose-instein condensate, centimeter for tap water vortex to 10^2 km size hurricanes or 10^4 light years galaxies. The building of a comprehensive theory of turbulence, allowing understanding and prediction of these phenomena is therefore a long-standing issue. The situation of turbulence with respect to other outstanding problems in physics, such as unification of gravity and quantum mechanics, is paradoxical. Contrary to the other problems, the constitutive equations governing the dynamics of turbulent flows are well-known.

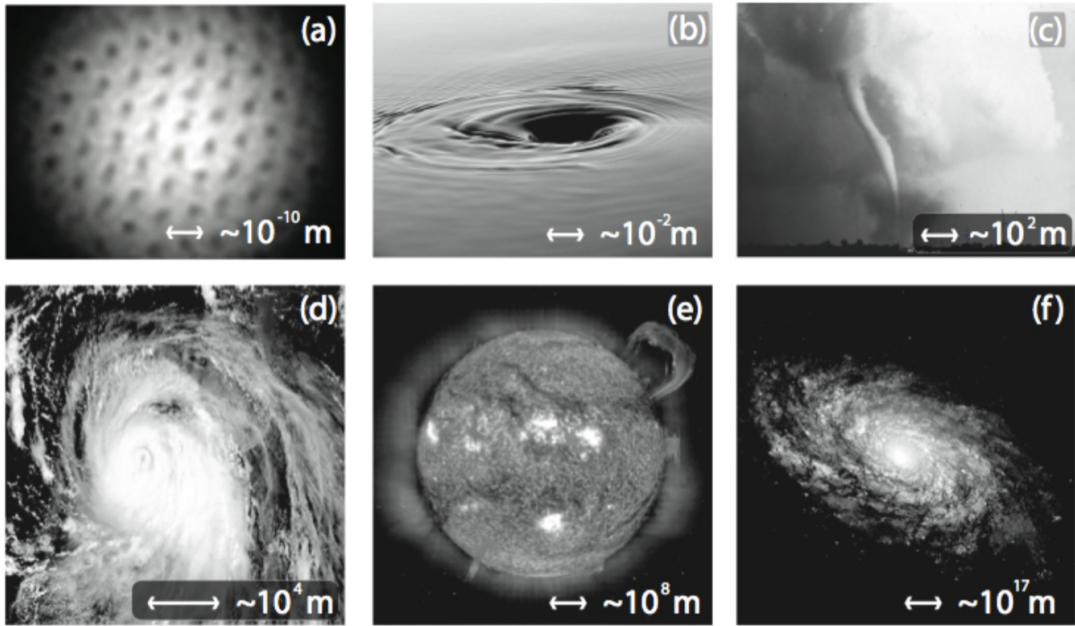


Figure 1.2: Vortices in universe: (a) quantum vortices; (b) bathtub vortex; (c) tornado; (d) hurricane; (e) sunspot vortices; (f) spiral galaxy. Figure extracted from R. Fuchs PhD Thesis.

1.2.2 The equations of fluid dynamics

At mesoscales, the equations are the **incompressible Navier-Stokes equations** (INSE) for unstratified fluids:

$$\partial_t u_i + u_j \partial_j u_i = -\frac{1}{\rho} \partial_i p + \nu \partial_j \partial_j u_i + f_i, \quad (1.1)$$

$$\partial_j u_j = 0, \quad (1.2)$$

where u_i is the d-dimensional velocity field, p the kinematic pressure, ρ the (constant) density, f_i is the forcing and ν the molecular viscosity. Since Reynolds' pioneering work, we know that after a proper rescaling of the equations by L and U , some characteristic length and velocity, the INSE only depend on one parameter, the Reynolds number $Re = LU/\nu$.

At very small scales, Bose-Einstein vortices are associated to a famous transition occurring in He4 at temperature below $T = 2.17K$, namely the superfluid transition. In this state, the fluid viscosity cancels, and the fluid behaves as a compressible quantum fluid described by the Gross-Pitaevskii (GP) equations:

$$i \partial_t \psi = \frac{c}{\sqrt{2}\xi} (-\xi^2 \Delta \psi + (-1 + |\psi|^2) \psi), \quad (1.3)$$

where ψ is the wave-function of the system, c is the sound velocity and ξ a correlation length. Such equation can actually be mapped to a more familiar PDE using the Madelung transformation:

$$\psi = \sqrt{\rho} \exp\left(\frac{i\phi}{\sqrt{2}\xi}\right). \quad (1.4)$$

Defining then the density ρ and the velocity:

$$u = \nabla \phi, \quad (1.5)$$

and separating real and imaginary part of the equation, we get the equation:

$$\begin{aligned}\partial_t u_i + u_j \partial_j u_i &= -\partial_i p, \\ \partial_t p + \partial_j \rho u_j &= 0,\end{aligned}\tag{1.6}$$

where $p = c^2(\rho - 1) - c^2\xi^2 - \Delta\sqrt{\rho}/\sqrt{\rho}$ is a pressure. These are compressible **Euler equations**. Note that the velocity equations resemble those of the Navier-Stokes equation, with setting $\nu = 0$. This is natural, as the fluid is "superfluid".

At very large scale, the Universe is described by Newton equations in a flat, expanding geometry. The equations are:

$$\begin{aligned}\partial_t u_i + \frac{\dot{a}}{a} u_i + \frac{1}{a} u_j \partial_j u_i &= -\frac{1}{a} \partial_i \Phi, \\ \partial_t \rho + 3\frac{\dot{a}}{a} \rho + \frac{1}{a} \partial_j \rho u_j &= 0, \\ \Delta \Phi &= 4\pi G a^2 (\rho - \rho_b),\end{aligned}\tag{1.7}$$

where $a(t)$ is the expansion factor. Using Zeldovich transformation:

$$\begin{aligned}V &= \frac{u}{ab} = -\nabla \tilde{\Psi}, \\ \left(\partial_t + 2\frac{\dot{a}}{a} \right) \partial_t b &= 4\pi G \rho_b(t) b \\ \tilde{\Phi} &= \frac{\Phi}{4\pi \rho_b a^2 b}, \\ \tilde{\Psi} &= \Psi,\end{aligned}\tag{1.8}$$

we get the equation:

$$\begin{aligned}\partial_t V_i + V_j \partial_j V_i &= 0, \\ V &= -\nabla \tilde{\Psi},\end{aligned}\tag{1.9}$$

which is the (inviscid) **Burger equation**. One can add a viscous term to stabilize solutions, see later. Note that this equation can be seen as a Navier-Stokes equation with no pressure, or equivalently, with no vorticity.

Those three equations (Navier-Stokes, Euler and Burgers) are the core PDE of fluid mechanics, and we will meet them throughout the course.

1.3 What is the problem with turbulence?

Equipped with a set of equations depending only of one parameter, we should be in the most favorable situation to build a theory of turbulence- at least, that is often what my colleagues in quantum mechanics seem to think. When confronted with this question, I always give the same answer, which is probably the second lesson I learned from my turbulence classes: the INSE are nonlinear partial differential equations, and they have been resisting mathematical and analytical treatments for almost two centuries: i) it is still not known whether their solutions with finite energy remain regular for all time- this is the subject of the Clay prize-; ii) very few analytical solutions exist. Until the first half of the XXth century, before the advent of the computers, any theory of turbulence could therefore only be based on hypotheses derived from observations or experimental data, as noted by Kolmogorov. Using a minimal set of such hypotheses, he was able in 1941 to construct a simple theory of turbulence based on the concept of energy cascade. Most of the present models or theories of turbulence are based on the Kolmogorov picture. It appears to describe

successfully the large-scales structure of many turbulent flows encountered in practical situations such as aeronautics, industry, meteorology or astrophysics, but becomes increasingly inaccurate when going down the scales. This is problematic for the modeling of all processes that depend on small scales of turbulence, such as combustion instabilities, droplet atomization in industrial burners or cloud formation.

We now have powerful computers, insist my quantum physicist colleagues. Why not abandon any modeling and turn to direct numerical simulation (DNS) of turbulent flows using the INSE? My reply to this is of course that DNS implies discretizing the equations in space and time, i.e. choosing an appropriate time and space resolution. For this, we still need a good model of turbulence. As we will see, if we use Kolmogorov theory, we find that to simulate a flow of scale L and velocity U at a given Reynolds number Re , the resolution in space and time should be $\Delta x \sim L Re^{-3/4}$ and $\Delta t \sim (L/U) Re^{-1/2}$. The number of nodes N to simulate then scales like $Re^{9/4}$ and the number of time steps to reach a time $T = L/U$ is $Re^{1/2}$, making the computational burden $O(Re^{11/4})$ to simulate the flow over such a period. For any aeronautical, geophysical or astrophysical application, this exceeds by far the capabilities of the most powerful computers. It seems that, for the time being, we still are in need of a theory of turbulence, that goes beyond the Kolmogorov picture so as to be able to handle better the small scales of turbulence and provide us with as sharp as possible bounds on the time and space discretization of DNS.

Even if we were able to simulate the flows using the INSE, we would still run into trouble if they are not well-posed: indeed, if a singularity develops, there can be a breaking of unicity of solution, for a given initial data. This is annoying, because then you are never sure that the simulation you just ran corresponds to the physical solution of the system you are considering: imagine that you want to build a brand new plane, using only numerical simulations of INSE to optimize its wings shape. Imagine also that this problem includes a singularity, resulting in two solutions: one in which the wings induce correct lift, and the plane can fly, and one with a stalling solution, in which the plane fall. What if, when running your simulation, you obtain the "flying" solution, and, as an engineer, validate the wing design... and later, when the plane is in operation, from time to time, it is the other solution that is realized????

To avoid that, either one has to find a way to pave completely the phase space of the solutions and select only those physically admissible solutions, or, we have to come back to quantum mechanics to compute the problem! This possibility could be catastrophic, in the sense that it could require to go back to Schrödinger's equations to simulate an airplane wing (which we would like to avoid, because of insufficient numerical resources!).

In the physics community, the "singularity hypothesis" is generally discarded, following the reasonable principle that "singularities are a mathematical curiosity, in nature they do not exist". In these lectures, I will show that this attitude is not so reasonable, and that taking into account possible mathematical singularities allows to understand fundamental mechanisms of turbulence. To quote Batterman (Emergence, Singularities, and Symmetry Breaking, Foundations of Physics, 2011) "*Many physicists and philosophers apparently believe that singularities appearing in our theories are indications of modeling failures [...]. Singularities are, on this view, information sinks [...] On the contrary, I am suggesting that an important lesson from the renormalization group successes is that we rethink the use of models in physics. If we include mathematical features as essential parts of physical modeling then we will see that blowups or singularities are often sources of information.*".

1.4 What will we do in that course?

For sake of clarity, I kept the calculations in the present lectures note to a minimal complexity level. I refer the reader to the lecture notes of [26], where many details about Onsager's conjecture,

multifractal theory and weak solutions can be found. I also will leave it to my mathematician colleagues to give rigorous proofs of theorems.

I will first review some of the available tools to investigate statistical and deterministic regularity of turbulent flows, some of which are directly inspired from regularity tools developed by mathematicians for NSE. I will then discuss how to deal with the existence of singularities using the multifractal formalism, showing how it allows to deal with situations where the velocity field is Hölder continuous with some exponent $h < 1$ (i.e. not necessarily differentiable) at small scales. I will explore what are the constraints that are imposed on the multifractal spectrum, both from mathematical properties of the NSE and from empirical laws of turbulence. I will then review computation of this spectrum from turbulent data, either numerical simulations of NSE or to state-of-the art experimental measurements.

Finally, I will discuss a local generalization of multifractal theory that allows to the local regularity properties of a velocity field. I will show how the application of such method allows to define a *typical irregular structure*, which is found to be similar to a Burgers vortex, with non-axisymmetric corrections. A possible explanation of such asymmetry is provided by a detailed time-resolved analysis of birth and death of the irregular structures, which shows that they are connected to vortex interactions, possibly vortex reconnection.

1.5 Description of data sets

To illustrate my lectures, I will use many different data. Indeed, thanks to progress in imaging and computers, we have access to a much more detailed set of observations and data. The numerical data will be based on DNS of INSE at moderate space resolution, so as to be able to accumulate time statistics. They are described in [15]. The experimental data sets are based on torques and velocity fields measured in the von Karman flow, using torque-meters and stereoscopic particle image velocimetry at different resolutions and Reynolds numbers. These data are described in [59, 60]. The main characteristics of these data are summarized in Table 1.1. The geometry of the von Karman flow is depicted in figure 1.3. The numerical data are by construction noise-free and representative of homogeneous isotropic turbulence, but are limited in Reynolds numbers, and space and time statistics. The experimental data are subject to unavoidable noise and include anisotropy and inhomogeneities, but cover a wide range of scale and Reynolds numbers, with good statistics. In these lectures I will mainly use the experimental data, but resort to numerical data to remove any doubt regarding the universality or validity of a given result.

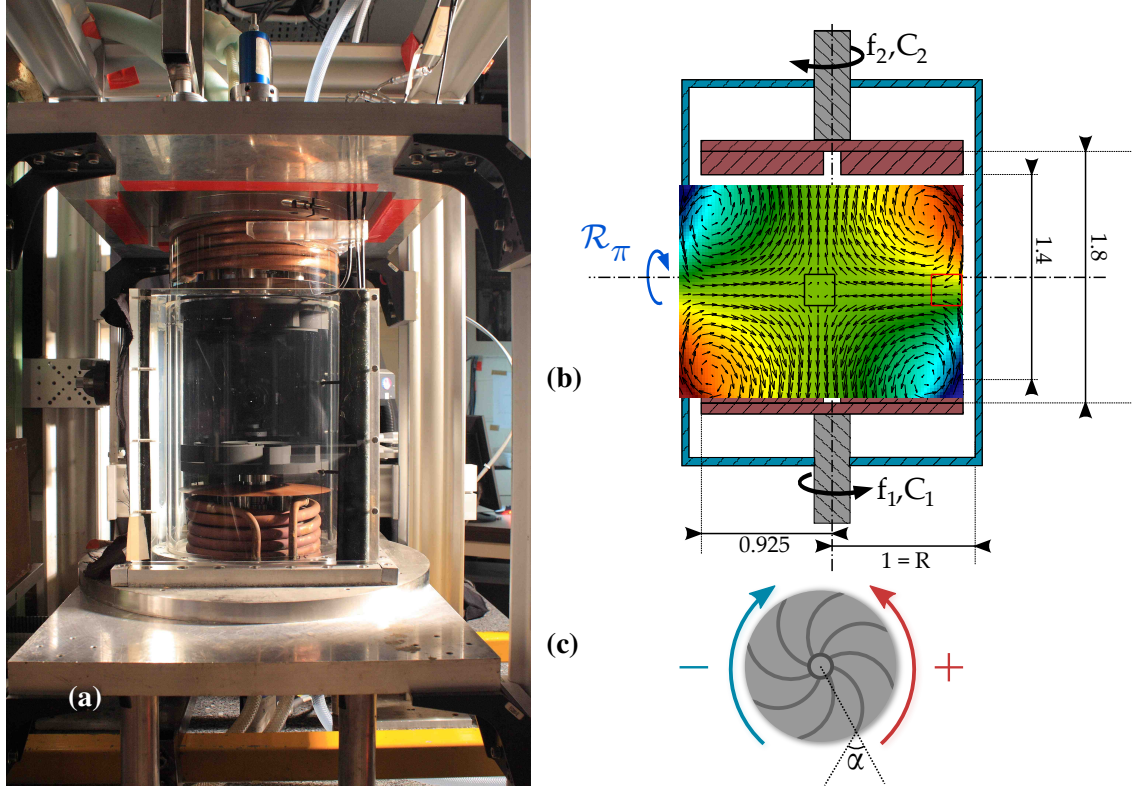


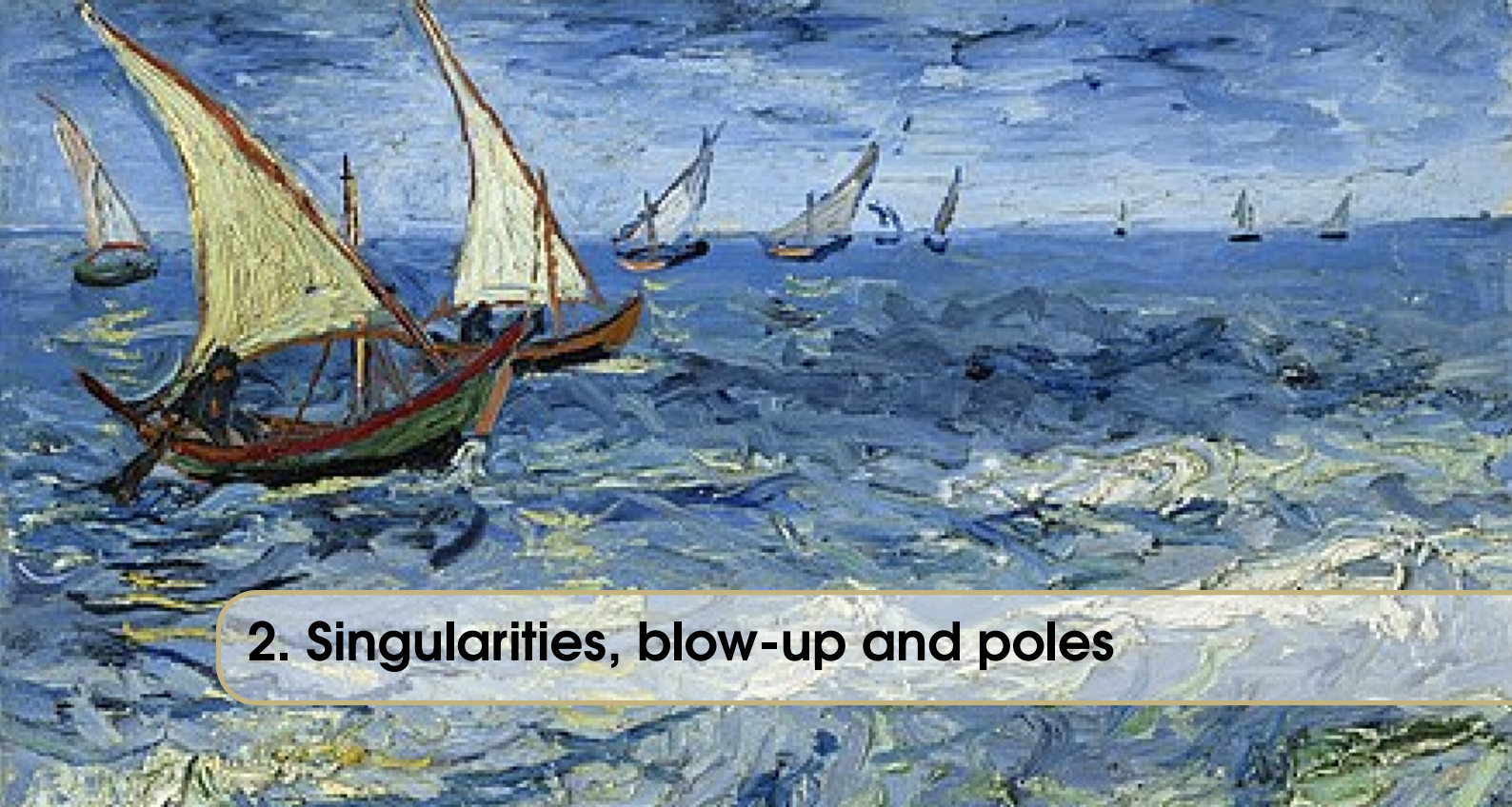
Figure 1.3: Von Karman flow geometry. a) General view of the experiment in Saclay. The von Karman flow is generated in a plexiglass cylinder of Radius R , filled with fluid at a controlled temperature. The flow is driven by two counter-rotating curve-bladed impellers at frequencies $f_1 = f_2$, rotating with their blades concave face pushing forward, corresponding to the - sign in figure c) (hereafter referred to as ANTI). For a given $F = (f_1 + f_2)/2$, this forcing produces the most intense turbulence, with strongest fluctuations. b) Schematic design of the experiment. The torque and frequency of each impeller is measured using torque-meter. Unless explicitly specified, all experimental quantities presented in the present paper are made dimensionless using R as a unit of length, and $1/(2\pi F)$ as a unit of time. The mean velocity field measured through stereoscopic particle image velocimetry (SPIV) is shown as an inset. The arrows traces the in-plane velocity. The color traces the out-of-plane velocity. Three types of measurement were done. Either over the whole plane in between the impeller, corresponding to the area covered by the inset (referred to as G like global); or inside the black square (referred as C like center); or inside the red square (referred to as W like wall). Most of the measurements used in the present essay are done with impellers rotating in - direction and performed in C where the turbulence is the most isotropic and homogeneous. In some cases, we have also added measurements with + direction (called CON), and in W area, to explore effects of inhomogeneity, anisotropy or forcing. Adapted from [14].

Case	F (Hz)	Glycerol content	Re	R_λ	$\varepsilon(adim)$	η (mm)	Δx (mm)	Symbol
ANTIG	5	0%	3×10^5	1870	0.045	0.02	2.4	○
ANTIC-1	5	0%	3×10^5	2750	0.0450	0.02	0.48	□
ANTIC-2	5	0%	3×10^5	2510	0.045	0.02	0.24	◇
ANTIC -3	1	0%	4×10^4	917	0.045	0.08	0.48	△
ANTIC-4	1.2	59%	6×10^3	214	0.045	0.37	0.24	★
CONC-3D	0.1	0%	6×10^3	—	0.019	0.37	0.96	—
DNS A		512^3	—	138	0.02	0.009	$k_{max}\eta = 1.6$	—
DNS B		728^3	—	54	0.11	0.032	$k_{max}\eta = 4.2$	—
DNS C		728^3	—	146	0.08	0.009	$k_{max}\eta = 1.1$	—

Table 1.1: Parameters describing the main datasets used in this paper. ANTI (resp. CON) means impeller rotation in the scooping (resp. unscooping) direction, while G or C refers to the location of the measurement (G for global, C for center, see figure 1.3; F is the rotation frequency of the impellers in Hz; Re is the Reynolds number based on the radius of the tank; Re_λ is the Taylor-microscale Reynolds number; ε is the global dimensionless energy dissipation, η is the Kolmogorov dissipation length scale; and Δx represents the spatial resolution in the measurements and the DNS. The last column shows the symbols used to represent the experimental datasets. The experiment CONC-3D corresponds to a case where the velocity is measured by TPIV, providing access to the 3 components of velocity.

Mathematical singularities

2	Singularities, blow-up and poles	23
2.1	Generalities	
2.2	Blow-up scenarios	
2.3	Blow-up diagnostics	
2.4	Some useful analytical results	
3	Illustration: blow-up in log-lattices	27
3.1	Log-lattice framework	
3.2	1D case: Burgers	
3.3	3D case: Euler and Navier-Stokes	
3.4	Discussion	
4	Singularities in fluids	37
4.1	Self-similar blow-up solutions	
4.2	Possible mechanisms for singularity	
5	Useful tools for studying irregular motions	
	41	
5.1	Multi-fractals	
5.2	Illustration: Burgers solution	
5.3	Weak Formalism	



2. Singularities, blow-up and poles

2.1 Generalities

2.1.1 Regularity and dimension

Regularity properties of NSE equations may depend on dimension. In $d = 1$, NSE become the Burgers equations, which are known to blow-up at finite time in the inviscid limit. In $d = 2$, the existence and smoothness theorems for NSE solutions have been obtained a long time ago [L69]. In $d = 3$, it is however still unclear whether the NSE are a well-posed problem, i.e. whether their solutions remain regular over sufficient large time or develop singularities. This motivated the inclusion of regularity properties of the Navier-Stokes equations in the AMS Clay Millennium Prize list [F00,T07]. Other speakers of this school will present detailed results about regularity properties and recent breakthrough, using e.g. convex integration. In this lecture, I will concentrate only on simple concepts, that will be helpful for devising theories about physics of turbulence.

2.1.2 Regularity and symmetry?

Very often, we have a symmetry in the system. For example, the von Karman flow [C97,A00], resulting from stirring by two coaxial, counter-rotating impellers in a cylinder filled with a viscous fluid (Fig. 1b of B1). The resulting flow is statistically axisymmetric, with a time-averaged velocity including a swirl component, whose intensity is controlled by the impellers geometry [R08]. The von Karman flow is an example of a system with rotation symmetry along a vertical axis. In this case, two important theorems are available: i) NSE are regular if the swirl component of the flow is zero [L68] ; ii) When the swirl is non-zero, the regularity can also be proven for finite time, in a domain excluding the symmetry axis [H08], showing that any singularity is necessarily located along the symmetry axis. This suggests monitoring the regularity either via the flow symmetry (axi-symmetric or not), or via the swirl intensity.

2.2 Blow-up scenarios

2.2.1 Self-similar blow-up solutions in non-linear systems

There is now evidence of existence of self-similar solutions (SSs) for several nonlinear systems, with same symmetries and conserved quantities as Navier-Stokes. These solutions are invariant under the scaling symmetry $(t, \mathbf{x}, \mathbf{u}) \rightarrow (\lambda^{1-h}t, \lambda\mathbf{x}, \lambda^h\mathbf{u})$ and satisfy

$$\begin{aligned}\mathbf{u}(\mathbf{x}, t) &= (t_* - t)^{h/(1-h)} F(\mathbf{x}/(t_* - t)^{1/(1-h)}), \quad \text{backward solution,} \\ \mathbf{u}(\mathbf{x}, t) &= (t - t_*)^{h/(1-h)} F(\mathbf{x}/(t - t_*)^{1/(1-h)}), \quad \text{forward solution,}\end{aligned}\tag{2.1}$$

where t_* is the blow up-time and $h < 1$ has the meaning of a Hölder exponent. The backward solutions may describe a singularity formation, while the forward solutions may be associated with non-uniqueness of associated weak solutions. An example of backward SS is the Khokhlov saw-tooth solution with $L \rightarrow 0$, a solution with $h = 0$ and $t_* = 0$ (see [25] for more examples). In inviscid shell-models of turbulence, the backward SSs were studied by [16, 46, 47]. The velocity $U(k_n, t)$ in the shell of wavenumber k_n then takes the form (2.1) with $h = 0.281$ and x being replaced by $1/k_n$. In the presence of viscosity, these solutions disappear, but the system "keeps the memory" of their existence via extreme events of velocity or velocity derivatives, correlated over space and time, sometimes named "instantons" [47].

2.2.2 Singularity in the Complex Plane

Another possibility was initially proposed by Frisch and Morf [FM81]. It corresponds to a situation where the analytical continuation of the velocity field has complex branching points or poles that cross the real axis. When this happens, a singularity occurs at the location of the real part of the pole or of the branching point. This possibility is hard to investigate theoretically, because it is hard to establish the dynamics of those potential poles from the NSE. This has only be done for simpler 1D partial differential equations such as Burgers or KdV, using a technique invented by Calogero [Ca78]. For example, Senouf et al. [SRE96] found that the poles of Burgers equation with imaginary viscosity $I\nu$ follow a Calogero dynamics, with logarithmic potential. The distance of the closest poles to the real axis is $O(\nu^{3/4})$, while distance between poles on the imaginary axis is $O(\nu)$.

2.3 Blow-up diagnostics

2.3.1 Euler case: Inviscid case

The most useful criterion for blow-up of solutions of Euler equation is provided by the Beale, Kato and Majda (BKM) criterion [BKM1984]. This criterion provides a necessary condition for a solution to lose its regularity. Namely, if a solution becomes singular at some time T_* , then

$$\int_0^{T_*} \|\omega\|_\infty dt = \infty,\tag{2.2}$$

so that

$$\lim_{t \rightarrow T_*} |\omega| = \infty.\tag{2.3}$$

It immediately follows that if there exists a time T_* such that the norm of the vorticity remains finite on any interval $[0, T]$ where $T \leq T_*$, then the solution is regular on $[0, T_*]$.

2.3.2 Navier-Stokes: Viscous case

In the case of Navier-Stokes, blow-up conditions are stronger than for Euler and involve the velocity. For example, a solution of the incompressible Navier-Stokes blows-up provided its spatial \mathbb{L}^3 -norm is unbounded

$$\left(\int_{\Omega} (|\mathbf{u}|_3 d^3x) \right)^{1/3} = \infty, \quad (2.4)$$

(for a review of various regularity criteria, see [Gibbon16]). From that, one can show that the velocity necessarily blows-up at the location of a singularity [Gallagher16].

2.3.3 Poles: Singularity Strip

In the case of singularity occurring via a complex pole crossing the real axis, one can try to follow numerically the fate of the poles that lay closest to the real axis, using the “singularity strip” method. This method is based on the observation that if the velocity field follows $u(z) \sim 1/(z - z_*)^\gamma$, with $z_* = a + ib$, then its Fourier transform satisfies:

$$FT(u)(k) \sim k^{-d-\gamma} \sin(ka) e^{-bt}. \quad (2.5)$$

The exponential decay of $FT(u)$ results in a similar exponential decay for the energy spectrum, over a typical distance $\delta = 2b$. Monitoring the decay of the velocity spectrum therefore enables to measure the distance to the axis of the closest pole.

Such a method is simple to implement in theory, but difficult in practice because one needs to have a very good resolution to resolve the dissipative range and be able to have a reliable fit of the potential exponential decay.

2.4 Some useful analytical results

Given the millennium prize framework, regularity of Navier-Stokes and Euler equations attracted a lot of attention and many theorems were derived. Here, I collect only a selection of a few ones, that bear interesting information for a physicist.

2.4.1 Probability of occurrence of singularities

Many useful results were derived regarding the spacetime distribution of possible singularities. Considering the whole space \mathbb{R}^3 , Leray ?? derived his "structure theorem" which states that the *time* set for which global weak solutions lose their regularities has zero Lebesgue measure. Later, in a series of papers [Scheffer1976a, Scheffer1976b, Scheffer1977, Scheffer1980], Scheffer was able to improve this result. In [Scheffer1976a], it was shown that Leray's structure theorem yields that the set of singular *times* has zero half-dimensional Hausdorff measure¹. This result was shown to hold for a bounded domain in [Foias1979]. In [Scheffer1976b], Scheffer showed that if the velocity field loses its regularity at a certain time T_* , then the *space* set of singularities at T_* has a finite one-dimensional Hausdorff measure. In [Scheffer1977], the *spacetime* set of singularities was proved to have finite two-dimensional Hausdorff measure. This result was refined in [Scheffer1980] where it was shown that for a bounded domain, the *spacetime* set of singularities has finite one-dimensional Hausdorff measure. Finally, this study culminated with the famous Caffarelli-Kohn-Nirenberg (CKN) theorem [CKN1982] which states that for "suitable" (in a sense that we will precise in section ??) weak solutions the *spacetime* set of singularities has zero one-dimensional Hausdorff measure. This is an important theorem since it says that singularities cannot curve in spacetime. As a consequence, these events do not persist in time, they must be extremely rare events.

¹blabla sur la mesure de Hausdorff

2.4.2 Bounds for flows on torus

One can derive general bounds for triply periodic flows based on a bounded, weighted, double hierarchy of their time averages proved in [JDG2018]: We define a doubly-labelled set of norms in dimensionless form

$$F_{n,m}(t) = \nu^{-1} L^{1/\alpha_{n,m}} \|\nabla^n \mathbf{u}\|_{2m}, \quad (2.6)$$

for $1 \leq n < \infty$ and $1 \leq m \leq \infty$, where

$$\|\nabla^n \mathbf{u}\|_{2m} = \left(\int_V |\nabla^n \mathbf{u}|^{2m} dV \right)^{1/2m}. \quad (2.7)$$

The $\alpha_{n,m}$ in the exponents of $L^{1/\alpha_{n,m}}$ in (??) are defined by

$$\alpha_{n,m} = \frac{2m}{2m(n+1)-3}. \quad (2.8)$$

Theorem 2.4.1 For $n \geq 1$ and $1 \leq m \leq \infty$, on periodic boundary conditions, weak solutions of the three-dimensional Navier-Stokes equations obey

$$\left\langle F_{n,m}^{\alpha_{n,m}} \right\rangle_T \leq c_{n,m} Re^3 + O(T^{-1}), \quad (2.9)$$

where the $c_{n,m}$ are a set of constants.

Note that for $n = m = 1$, the theorem states that non-dimensional energy dissipation rate is bounded for the standard three-dimensional Navier-Stokes equations.

Indeed, we have:

$$\begin{aligned} \alpha_{1,1} &= 2, \\ \left\langle F_{1,1}^{\alpha_{1,1}} \right\rangle_T &= \nu^{-2} L \left\langle \int_V |\nabla \mathbf{u}|^2 dV \right\rangle_T, \\ &= \nu^{-3} L^4 \varepsilon, \end{aligned} \quad (2.10)$$

where ε is the (mean) viscous energy dissipation rate per unit volume, that has dimensions U^3/L . From Eq. (??), we then get:

$$\frac{\varepsilon}{U^3/L} \leq c_{1,1} + O(T^{-1}). \quad (2.11)$$

This equation will be very useful in the sequel, when discussing Onsager conjecture, singularities and properties of the multi-fractal spectrum of turbulence.



3. Illustration: blow-up in log-lattices

3.1 Log-lattice framework

3.1.1 Definitions and notations

We consider d -dimensional complex vectors $u = (u_1, \dots, u_d)$ depending on time and on a real vectorial parameter k , each component of which follow a geometric progression $k = k^0(\lambda^{m_1}, \dots, \lambda^{m_d})$. The dependence of u on k is henceforth implicit and specified only when ambiguity prevails. Fluid dynamics on log-lattice (hereafter FDLL) is defined [CM21] as sets of u solutions of the equation :

$$\begin{aligned} ik_\beta u_\beta &= 0 \\ \partial_t u_\alpha + ik_\beta (u_\alpha * u_\beta) &= -ik_\alpha p - \nu k^{2\gamma} u_\alpha + f_\alpha, \\ (u_\alpha * u_\beta)(k) &= \sum_{p+q=k} u_\alpha(p) u_\beta(q), \end{aligned} \tag{3.1}$$

where p is a complex, k -dependent field that enforces incompressibility, and f is a vectorial forcing. The parameter γ measures the "strength" of the dissipation: it is hypo-dissipative if $\gamma < 1$, hyper-dissipative if $\gamma > 1$ and normal if $\gamma = 1$. The convolution of Eq. (3.1-c) defines triadic interaction onto a logarithmic grid that are possible only if the equation $\lambda^m = \lambda^p + \lambda^q$ has integers solutions. As shown in [CM21], this is possible only for special values of λ , that determine the number of possible interactions on the grid. In this paper, we consider 3 cases: $\lambda = 2$, $\lambda = \phi \approx 1.618$ (the golden number) and $\lambda = \sigma \approx 1.325$ (the plastic number). As $\lambda \rightarrow 1$, the number of possible interactions per direction increases: it is 3 for $\lambda = 2$, 6 for $\lambda = \phi$ and 12 for $\lambda = \sigma$. As a consequence, the computational burden to integrate such equations increases significantly as λ is decreased. In the sequel, the equations (3.1) are integrated using an implicit 4th order Runge-Kutta with adaptative time-step. Technical details can be found in [BD22].

3.1.2 Global quantities

By analogy with classical Fourier representation, we can derive interesting global quantities representing total energy E , or helicity H as:

$$\begin{aligned} E &= \sum_k |u|^2, \\ H &= \sum_k \varepsilon_{\alpha\beta\gamma} k^\beta \operatorname{Im}(u_\gamma * u_\alpha). \end{aligned} \quad (3.2)$$

These quantities are exactly conserved in the inviscid limit in $d = 3$ [CM21].

It is likewise possible to define an "energy spectrum $E(k)$ in FDLL, that measures the energy of the mode at k as:

$$E(k) = k^{-1} \langle |u|^2 \rangle_{S_k}, \quad (3.3)$$

where the average is taken over wave numbers in the shell S_k delimited by spheres with radii k and Λk . Specifically:

$$\langle |u|^2 \rangle_{S_k} = \frac{1}{N_k} \sum_{k \leq |p| \leq \Lambda k} \sum_{\alpha=1}^d |u_\alpha(p)|^2, \quad (3.4)$$

where d is the space dimension and $N_k \sim (\log(k))^{d-1}$ is the number of wave-numbers in the shell S_k .

3.1.3 Regularity

Unlike NSE, we have many results regarding regularity properties of FDLL. In $d = 1$, Constantin et al [CLT07] proved global regularity and existence of a finite dimensional attractor and inertial manifold for $\lambda = \phi$ (Sabra shell model), while the global regularity for $\lambda = 2$ was proved in [Ch08]. In the later case, finite-time blow-up is observed for hypo-diffusive cases with $\gamma \leq 1/3$. In $d = 3$, no theorems have been proved so far, but a finite-time blow-up in the inviscid limit was observed for $\lambda = 2$ and $\lambda = \phi$ by [CM18]. In both cases, the blow-up follow a self-similar scenario, and took place on a chaotic attractor in wave-number space [CM18].

3.1.4 Singularity strip method for log-lattices

Extension of the singularity strip method notion to log-lattice relies on the observation that if a fluid on log-lattice satisfies $u(k) \sim k^{-d-\xi} e^{-bk}$, then its inverse Fourier transform obeys $FT^{-1}(u)(x) \sim (x-b)^\xi G(x/b)$, where G is a scaling function, so that it has a pole or a turning point on the imaginary axis, at a distance b from the real axis. Therefore, it is natural to generalize the singularity strip method to log-lattices, where the computation of δ can also be done by fitting the compensated spectrum $\log(k^{-\gamma} \langle |u(k)|^2 \rangle_{S_k})$ as a function of k . The slope of this fit gives 2δ .

3.2 1D case: Burgers

To calibrate our results, we thus start with the case $d = 1$, where many analytical results are available. In that case, we ignore the first equation of Eqs. (3.1) and set $p = 0$. The resulting equation then boils-down to a Burgers equation on a log-lattice [CM21]. Moreover, for $\lambda = 2$, the model is equivalent to the dyadic model, while for $\lambda = \phi$, the model is equivalent to the Sabra shell model.

Table 3.1: Exponent of the inviscid and viscous scaling of various quantities measured for different values of the grid spacing λ and dimension d . The scalings are with respect to $\tau = 1 - t/t_b$ in the inviscid case, where t_b is the blow up time, or $\tau = v$ in the viscous case, where v is the viscosity. By definition, the energy spectrum scales like $E(k) \sim k^{-1-2\alpha}$, the maximal value of the vorticity scales like $\omega_{max} \sim \tau^{-\beta}$ and the width of the singularity strip scales like $\delta \sim \tau^\mu$. The ⁽⁰⁾ indicates simulation made with no forcing. The * indicates simulations made with another initial condition.

dim.	λ	t_b	Inviscid $v = 0$			Viscous $\gamma = 1$		
			α	β	μ	α	β	μ
2	0.3898	0.37	1	1.55		1/3	1/2	0.71
$d = 1$	ϕ	0.5193	0.37	1	1.55	—	—	—
	σ	0.4300	0.37	1	1.55	—	—	—
	$2^{(0)}$	0.1460	0.37	1	1.55	—	—	—
	$\phi^{(0)}$	0.2687	0.37	1	1.55	—	—	—
$d = 3$	2	0.8481	0.67	1	2.81	0.40	0.39	0.65
	ϕ	5.8005	0.67	1	2.83	—	—	—
	ϕ^*	0.1542	0.67	1	2.82	—	—	—
	σ^*	0.8430	0.67	1	2.67	—	—	—

r

3.2.1 Inviscid case

Starting we the inviscid case $v = 0$, we observe a finite-time self-similar blow up for the 3 values of λ , evidenced in Fig. 3.1, both without and with a (power-constant) forcing. The blow-up time is smaller in the absence of a forcing. The energy spectrum gradually widens towards larger and larger values of k , developing a power law spectrum $k^{-2\alpha-1}$ with $1 + 2\alpha = 1.733$, corresponding to a scaling law for $u(k) \sim k^{-\alpha}$ with $\alpha = 0.367$, in agreement with exact result from the renormalization group applied to the Sabra shell model[FTBC22]. The maximal gradient $\omega_{max}(t) = \max_k(|ku(k)|^2$ blows-up in finite time, following a self-similar law

$$t_b \omega_{max} = \frac{1}{1 - t/t_b}, \quad (3.5)$$

displayed in Fig. 3.1-b, where t_b is the blow-up time. While the blow-up time depends on the forcing and on the value of λ (see Table 3.1), the self-similar law is independent of these quantities. We also check that the blow-up evolution for $E(k)$ is universal, in the sense that it only depends on $\tau = 1 - t/t_b$, as illustrated in Figure 3.1-a, where spectra at different λ but similar τ are shown to overlap.

We then compute the strip width δ for each time before blow-up, using formula (??), with $\xi + 1 = 1.733$. The result is shown in Figure 3.1-c. We see that δ decays to 0 in finite time, following a power law $\delta(t) \sim (1 - t/t_b)^\mu$, with $\mu = 1.546$. This decay is universal and does not depend on the value of λ . The width of the analyticity strip is closely associated to k_{max} , representing the wavenumber at which ω attains its maximum. Indeed, we see in 3.1-d that $k_{max}\delta$ is approximately constant with time. This is in agreement with the picture convienied by Eq. (??), which implies that ω_{max} is achieved at $k_{max} \sim 1/\delta$.

3.2.2 Viscous case

We now introduce a normal viscosity ($\gamma = 1$), with various amplitude and focus on the case $\lambda = 2$, where computations are faster. To reach a stationary situation, we introduce a forcing at large scale (at $k = xx$), the amplitude of which is adjusted at each time so that the total power-input is constant in time. In this viscous case, there is no more a blow-up, and the solution reaches a stationary

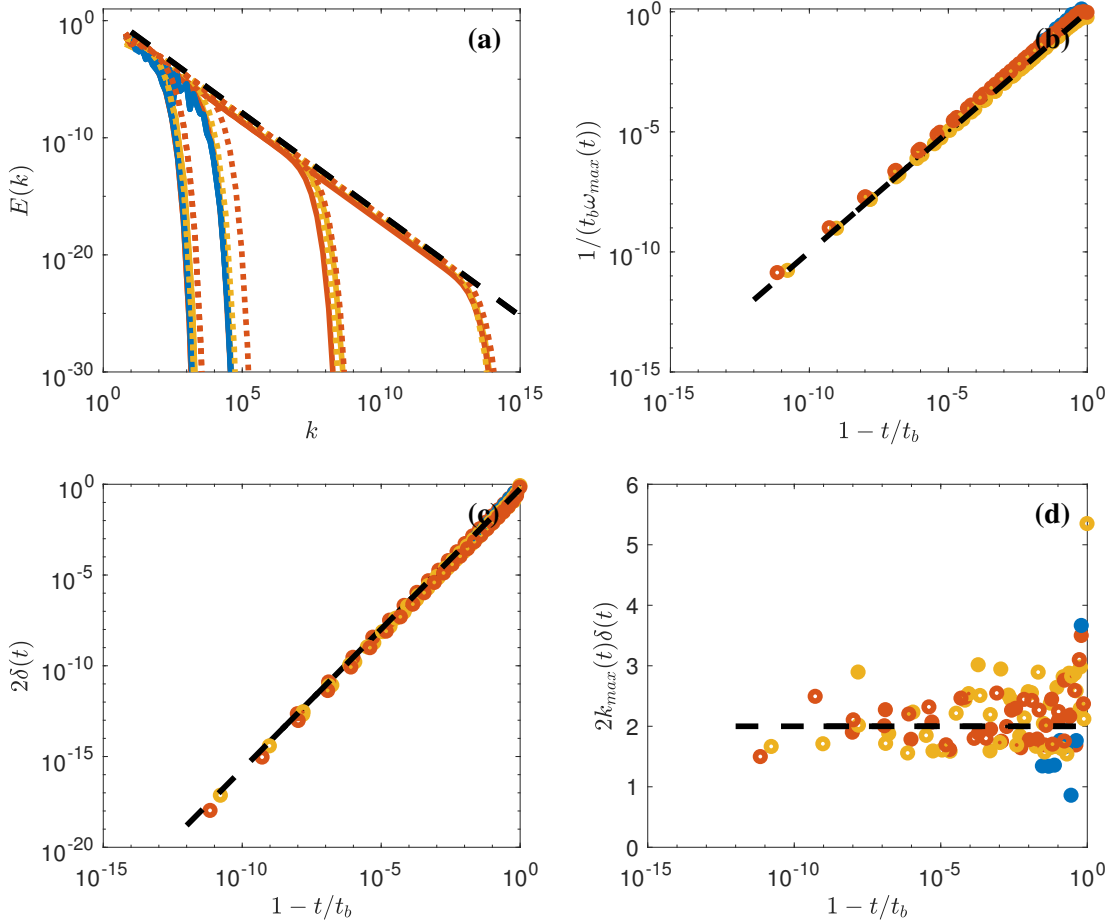


Figure 3.1: Inviscid blow-up for Burgers (1D) case for $\lambda = 2$ (yellow), $\lambda = \phi$ (red) and $\lambda = \sigma$ (blue).. (a) Spectre at different renormalized relative time $\tau = 1 - t/t_b$. The continuous line are for simulation with constant power forcing, while the dotted lines denote simulation with no forcing; The black dotted line has slope -1.733 . (b) Maximal value of derivative $1/t_b \omega_{max}$ as a function of τ ; The black dotted line is the theoretical value Eq.(4.4). (c) Width of analyticity strip δ as a function of τ . The black dotted line has slope given in Table 3.1. (d) Renormalized width $k_{max}\delta$ as a function of τ . The black dotted line has slope 0. The filled symbols are for simulation with constant power forcing, while the open symbols denote simulation with no forcing.

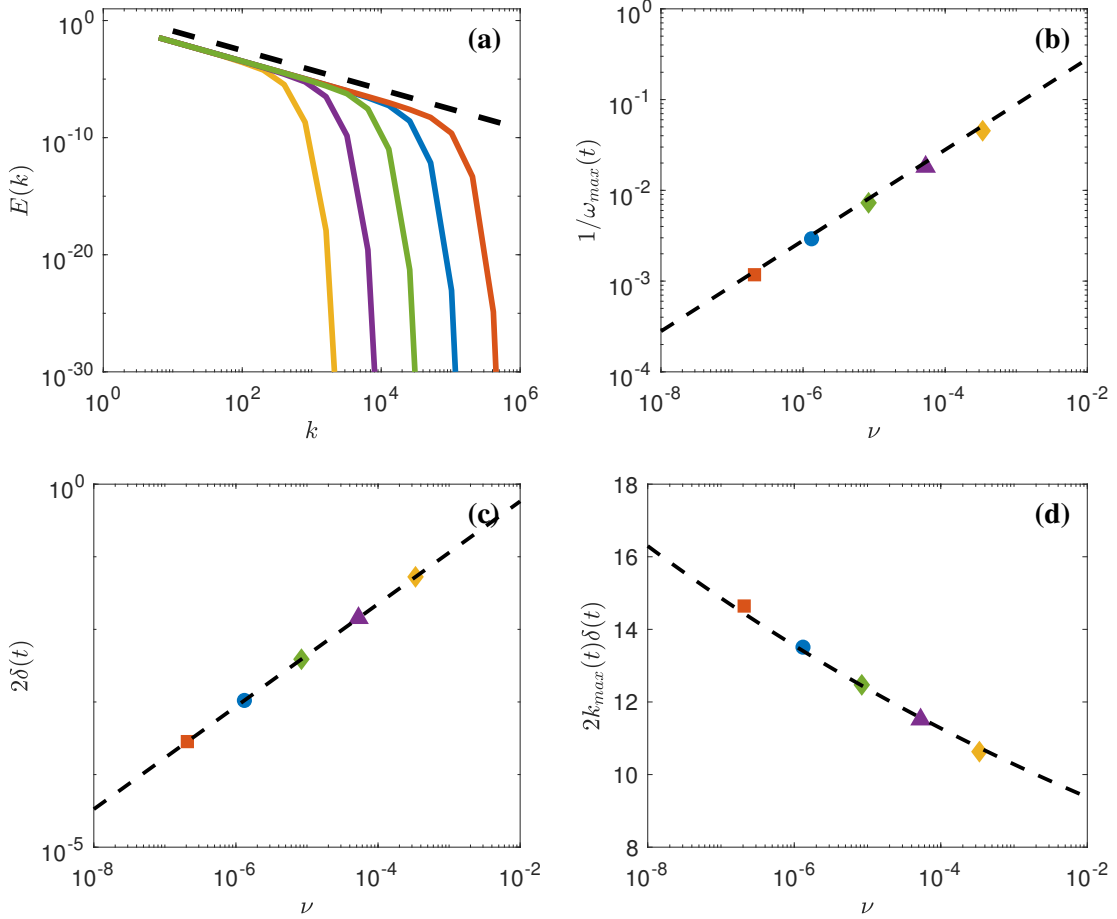


Figure 3.2: Stationary dynamics for viscous Burgers (1D) case for $\lambda = 2$ (a) Spectre at different viscosity. The color codes different viscosity (same color code than in figures (b) to (d)) (b) The black dotted line has slope $-5/3$; (b) Maximal value of derivative $1/t_b \omega_{max}$ as a function of viscosity. The black dotted line has slope $1/2$ (c) Width of singularity strip δ as a function of viscosity. The black dotted line has slope -0.7067 . (d) Renormalized width $k_{max}\delta$ as a function of viscosity. The black dotted line is a power-law with slope -0.04 .

state, with self-similar spectrum shown in Figure ??, with a power-law "inertial range" followed by an exponential decay at large k . The slope of the spectrum in the inertial range is a power-law is very close to $-5/3$ corresponding to $u(k) \sim k^{-1/3}$. The maximal value of the derivative ω_{max} depends on the value of the viscosity, see Figure ??-b. It increases with decreasing viscosity as a power-law ν , $\omega_{max} \sim \nu^{-\beta}$, with $\beta = 0.5$. This scaling law is similar to the scaling derived when assuming an "anomalous dissipation", $\nu\omega^2 = \varepsilon$ (where ε is independent of viscosity), resulting in $1/\omega \sim \sqrt{\nu/\varepsilon}$.

In that viscous case, the width of the strip does not decline to zero, but stabilizes at a finite value which depends on the viscosity, see Fig. ??-c. It follows a power-law with ν , with exponent $\xi = 0.7067$. This is smaller than what would be expected from dimensional argument "a la Kolmogorov", that would instead predict $\delta = \nu^{3/4}$. The strip width follows the approximate scaling $\delta \sim 1/k_{max}$, as shown in Fig. ??-c, even though it is less clean than in the inviscid case.

3.3 3D case: Euler and Navier-Stokes

3.3.1 Inviscid case: Euler

We now turn to the case $d = 3$, for $\lambda = 2$, ϕ and σ . To test universality, we have ran the case $\lambda = \phi$ with two different initial conditions. (QUENTIN ET AMAURY: Precuser). In all cases, we observe a finite-time blow up, already documented in [CM21]. Here, we observe that while the blow-up time depends on initial conditions, the dynamics becomes universal when plotted in suitable non-dimensional variables, as illustrated in Fig. 3.3. The spectrum develops a power-law as a function of time, that only depends on the non-dimensional time $1 - t/t_b$ and not on the value of λ , as evidenced in Fig. 3.3-a. The slope of the power law is much steeper than in the 1D case, with a value very close to $-7/3$. This is the slope expected for an helicity cascade. This slope is a little but smaller than those observed in simulation of Euler equation on a regular grid (corresponding to $\lambda = 1$), where k^{-3} spectra are observed [OPC12, BB12], but comparable to slopes measured in more recent simulations [FKMW22].

The maximal value of the vorticity ω_{max} diverges during the blow-up, as shown in Fig. 3.3-b. Like in the 1D case, its time variation is similar in both cases, with a blow-up scaling like $1/(1 - t/t_b)$. However, contrarily to the 1D case, the scaling constant in front of the power-law varies as a function of λ , and is not simply given by $1/t_b$. This is not too surprising given the 3D nature of the flow, that prevent application of the simple blow-up argument used in the 1D case. Note however that as λ is decreased towards $\lambda = 1$, the non-dimensional curve becomes closer to the 1D case.

During the blow-up, the width of the analyticity strip decays to 0 as a power-law with exponent $\mu \approx 2.81 \pm 0.02$, see Fig. 3.3-c. This is larger than in the 1D case. This decay is also universal, as it does not depend on λ . However, it does not show a simple dependence with k_{max} as seen in Fig. 3.3-d. This might be due to the chaotic nature of the attractor of the blow-up [CM21].

3.3.2 Viscous case: Navier-Stokes

Turning on the viscosity, and forcing at constant power, to reach stationary situations, we observe a similar situation as in the 1D case, with slight differences, see Fig. ??-. The energy spectra display a power-law shape until the viscous range turns on, with an inertial range widening as ν is decreased. The slope of the energy spectrum is slightly steeper than $-5/3$, with an intermittency correction of the order of 0.13. As a result, the exponent for u is slightly larger than $1/3$, $\alpha = 0.40$. The maximal vorticity ω_{max} increases with decreasing viscosity like a power-law, with an exponent significantly lower than the Kolmogorov value: $\beta = 0.39$.

The width of the analyticity strip decays less strongly with viscosity, with an exponent $\mu = 0.65$. However, in contrast with the 1D viscous case, it appears to scale simply like $1/k_{max}$ as can be seen on Fig. ??-d. Therefore the intermittency corrections strongly influence the maximal value of ω and its corresponding wavenumber.

3.4 Discussion

Predictions for the scaling laws are actually possible using simple dimensional arguments if we impose $\delta \sim 1/k_{max}$, as empirically observed. Indeed, from $u \sim k^{-\alpha}$ and $\omega \sim ku$, we get $\omega_{max} \sim k_{max}^{1-\alpha} \sim \delta^{\alpha-1}$ so that we get:

$$\beta = \mu(1 - \alpha). \quad (3.6)$$

This fixes a link between the 3 exponents, that is actually well satisfied, see Fig. ??-b. On the other hand, one can connect μ and α by extending the argument fixing the Kolmogorov scale to hypo and

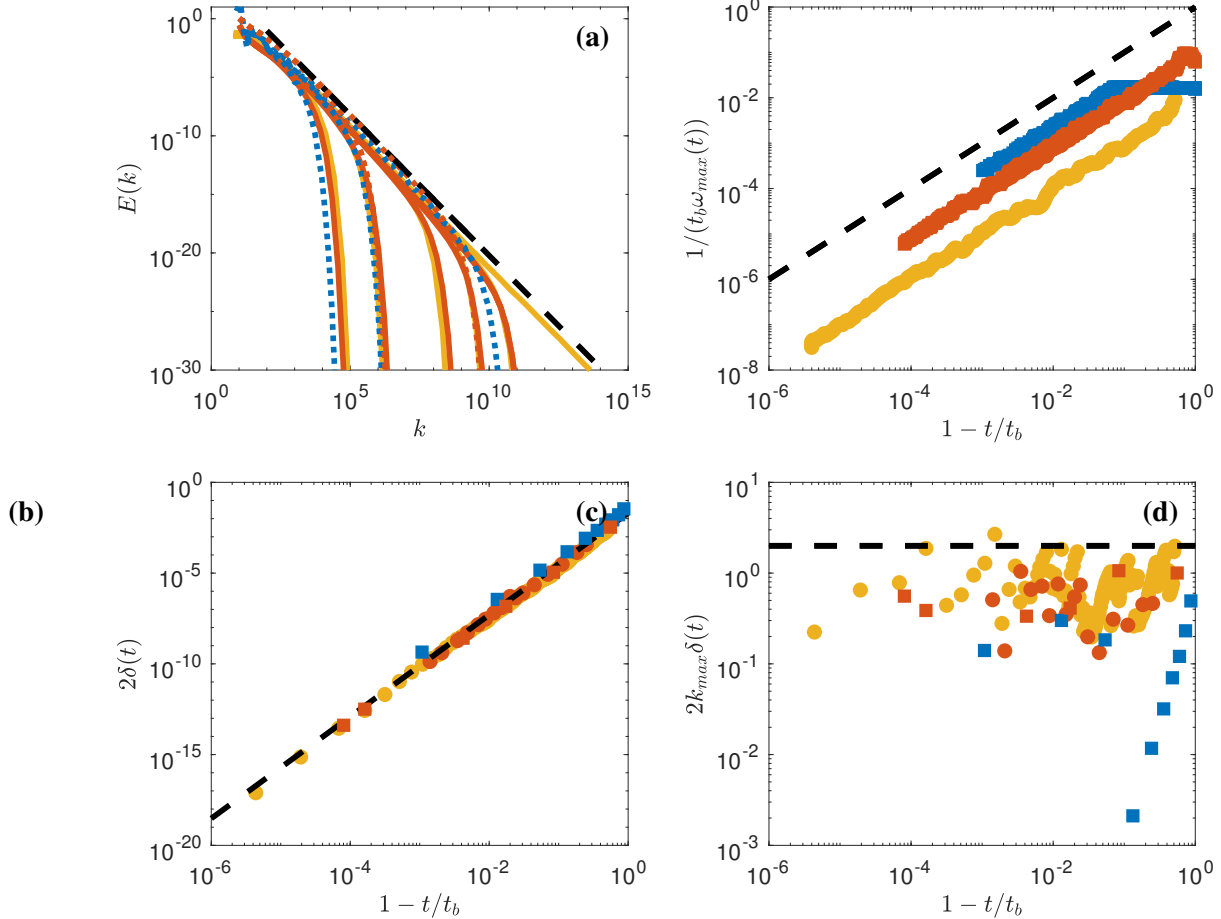


Figure 3.3: Inviscid blow-up for Euler (3D) case for $\lambda = 2$ (yellow), $\lambda = \phi$ (red) and $\lambda = \sigma$ (blue). (a) Spectre at different renormalized relative time $\tau = 1 - t/t_b$, from 0.2542 to 0.00001 from left to right. Spectra with continuous line and dotted line correspond to different initial conditions. The black dotted line has slope $-7/3$; (b) Maximal value of derivative $1/t_b \omega_{max}$ as a function of τ . The black dotted line has slope 1; (c) Width of analyticity strip δ as a function of τ ; The black dotted line has slope 2.805. (d) Renormalized width $k_{max}\delta$ as a function of τ . In panel b), c) and d), we used different symbols for different initial conditions: circles, and squares.

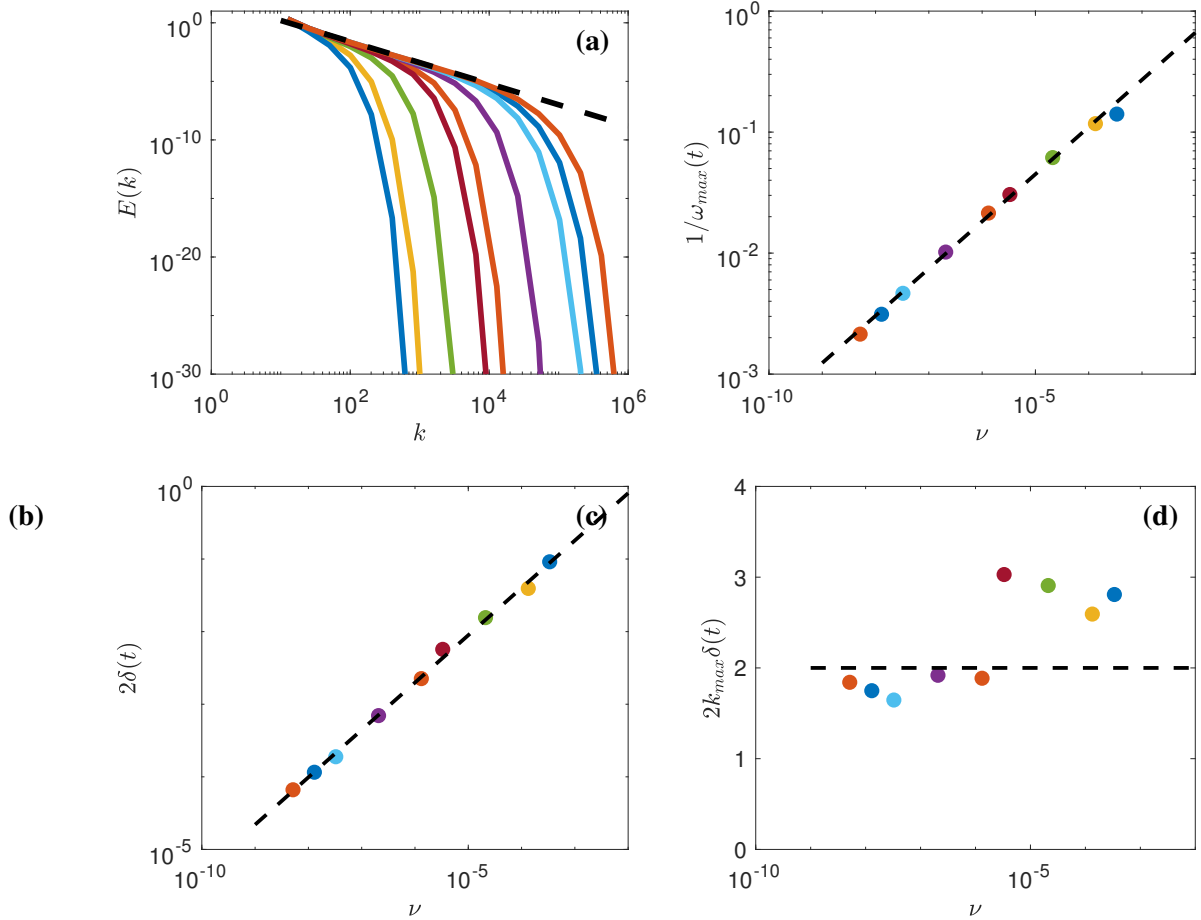
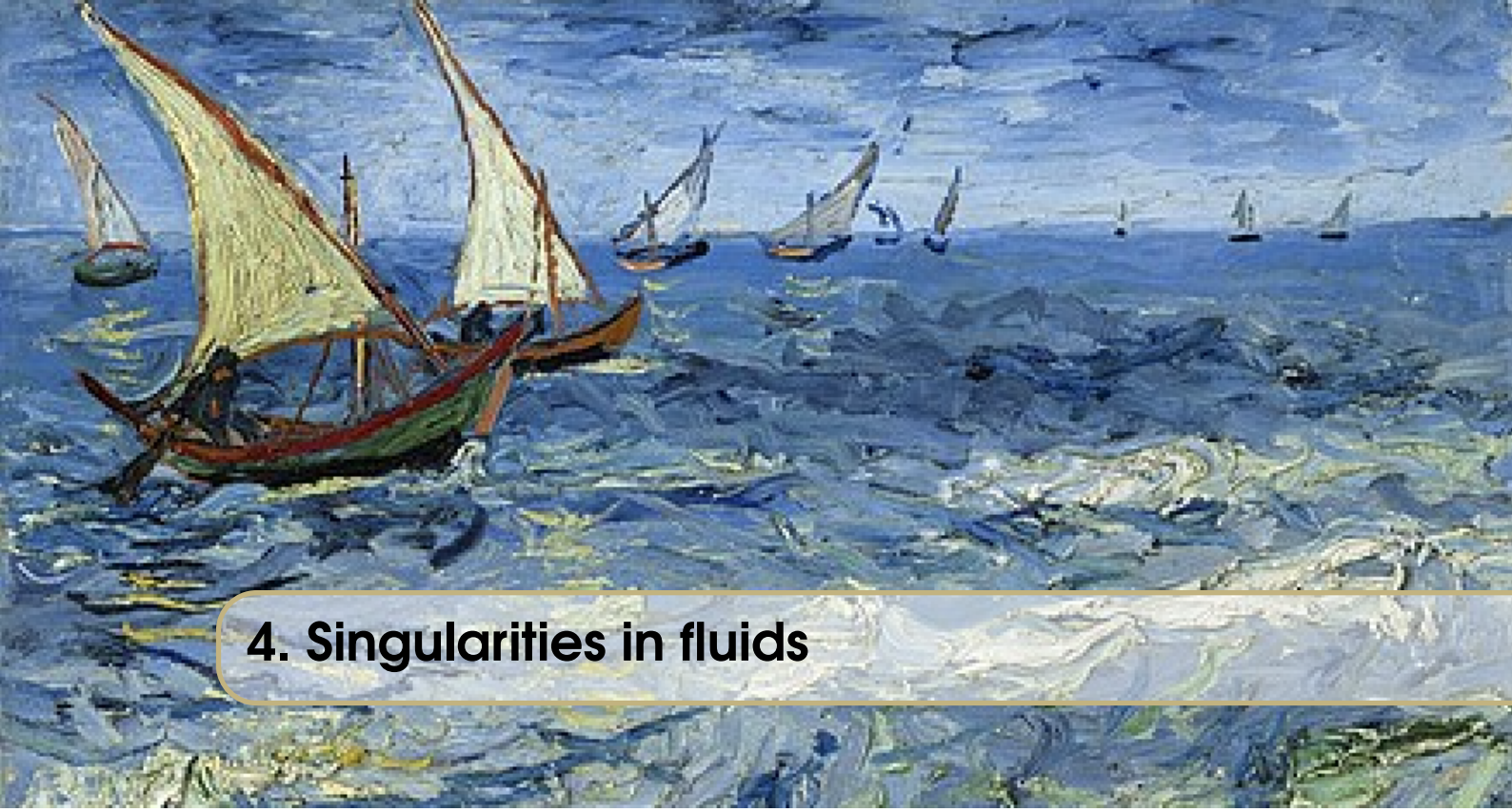


Figure 3.4: Stationary dynamics for Navier-Stokes (3D, viscous) case for $\lambda = 2$ (a) Spectre at different viscosity. The black dotted line has slope -1.8 . The color codes different viscosity (same color code than in figures (b) to (d) ; (b) Maximal value of derivative $1/t_b \omega_{\max}$ as a function of viscosity. The black dotted line has slope 0.39 ; (c) Width of singularity strip δ as a function of viscosity/ The black dotted line has slope 0.6523 : (d) Renormalized width $k_{\max}\delta$ as a function of viscosity.

hyper-viscous cases: we impose that k_{max} is fixed by the condition that the viscous term balances the non-linear term $\nu k_{max}^{2\gamma} u_{max} \sim k_{max} u_{max}^2$. Using $u_{max} \sim k_{max}^{-\alpha}$ and $\delta \sim 1/k_{max}$ we then get:

$$\mu = -\frac{1}{1-\alpha-2\gamma}, \quad (3.7)$$

This prediction is tested in Fig. ??-c and is also well satisfied. The only free parameter is then $\alpha(\gamma)$ (say). In the limit $\gamma \rightarrow 1/3$, we can fix it by imposing that $\beta = 1$, which is the scaling corresponding to conservation of the circulation [Po18]. From Eqs. (3.7) and (3.6), we then get $\alpha = 1 - \gamma = 2/3$, corresponding to helicity cascade. In all other cases, we have no clear theories to predict the variations of α with γ . Notably, when $\gamma \rightarrow \infty$, it seems that we recover $\alpha = 1/3$ corresponding to the energy cascade.



4. Singularities in fluids

4.1 Self-similar blow-up solutions

4.1.1 1D: Burgers

Simple self-similar solutions can be found in the 1D case. One famous example is defined in the interval $[-L, L]$ and is given by

$$u_s(x, t) = \lim_{v \rightarrow 0} u^v(x, t) = \lim_{v \rightarrow 0} (x - Lt \tanh(Lx/2vt))/t. \quad (4.1)$$

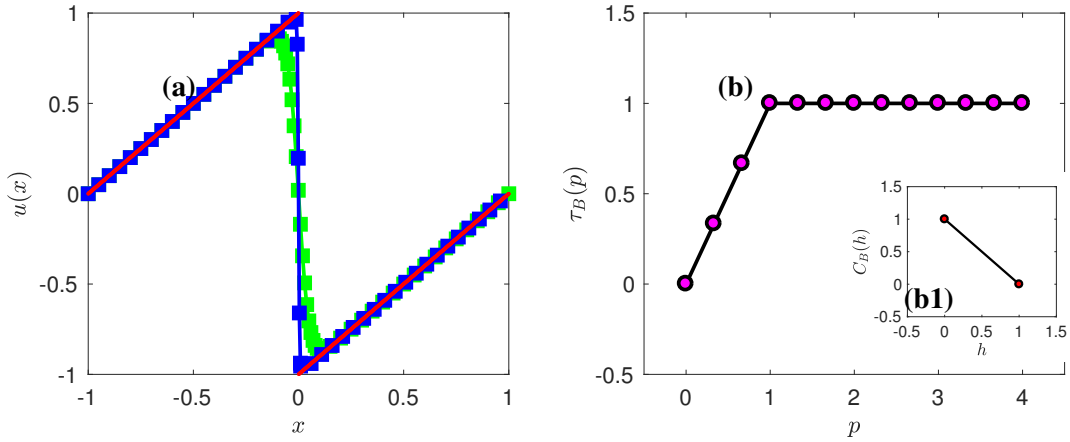
In the inviscid limit $v \rightarrow 0$, this solution is called the "Khokhlov saw-tooth solution" and reads:

$$u_s(x, t) = \begin{cases} (x + L)/t & -L \leq x < 0, \\ (x - L)/t & 0 < x \leq L. \end{cases} \quad (4.2)$$

The velocity field is singular at $x = 0$, where it exhibits a jump (a shock) of size $\Delta u = 2L/t$ (see figure 4.1-a).

4.1.2 3D: Euler and navier-Stokes

The existence of SSs for Euler or Navier-Stokes is still controversial. In the Euler case, Chae proved that there is no backward SS [11], but self-similar blow-up behaviours with $h = -1$ were found on logarithmically spaced lattice [10], or during reconnection of tent vortices [34]. In the Navier-Stokes case (see [7] for a recent review), the SS necessarily has an $h = -1$ exponent (in agreement with the $h = -1$ rescaling symmetry, see Section 8.1) and blows up in finite time. The backward case was first investigated by [43] and was excluded by [53] for a large class of initial conditions. It has however recently been claimed to be observed in high speed wind tunnel experiments [42]. In the forward case, existence of SS solutions is known under certain regularity conditions. Nevertheless, both backward and forward SS have been observed for energy spectra in the Leith model of turbulence [52]. The backward solution corresponds to an initial explosive propagation of the spectral front from the smallest to the largest wavenumbers reaching arbitrarily large wavenumbers in a finite time, and is described by a self-similar solution of the second kind. The forward solution manifests itself as a reflection wave in the wavenumber space propagating



130

Figure 4.1: Self-similar solutions to Burgers equations. a) Velocity fields $u^V(x, t)$ at $t = 1$ for solution of Burgers equation for different viscosity in a domain of size $2L = 2$, with shock amplitude $\Delta u = 2$: blue symbols: $\nu = 1/100$; green symbols $\nu = 1/10$. The red line is the Khokhlov saw tooth solution, corresponding formally to $\nu = 0$. b) Scaling exponents τ_B as a function of order p . Insert (b1): multifractal spectrum $C_B(h)$ obtain by taking inverse Legendre transform of $\tau_B(p)$.

from the largest toward the smallest wavenumbers, and is described by a self-similar solution of a new (third) kind.

4.2 Possible mechanisms for singularity

4.2.1 Gradient blow-up in 1D Burgers

Consider Burgers equation (1.9) in $d = 1$, and differentiate it with respect to x . We then get that the space derivative $\omega = \partial_x u$ obeys $d\omega/dt = -\omega^2$, where $d/dt = \partial_t + u\partial_x$. The solution of this equation can be simply found as a self-similar law

$$t_b \omega = \frac{1}{1 - t/t_b}, \quad (4.4)$$

with $t_b = 1/\omega(t=0)$. We then see that if $t_b > 0$ (i.e. the gradient at $t = 0$ is positive), then we have a self-similar blow-up of the velocity gradient in finite time. Note that this mechanism does not extend to Navier-Stokes or Euler in higher dimensions, due to the presence of strain.

4.2.2 Pressure Mediated Singularity in 3D Euler

In 2014, Luo and Hou [LH14] provided a detailed numerical evidence of the existence of a finite-time blow up in an inviscid axisymmetric fluid with swirl. The flow is initially put into a kind of “differential rotation”, with the upper part of the tank rotating in one direction, and the lower part rotating in the other direction. The blow-up is characterized by a very strong increase of the amplitude of the vorticity, and occurs at the radial boundary and at the altitude of the shear layer. This blow-up was interpreted by Barkley [Ba20] in terms of a “tea-cup like” singularity driven by the pressure field. This singularity mechanism is interesting because of the similarity of the geometry with a von Karman experiment, where the differential rotation is imparted by counter-rotating impellers [[D19]]. It may then provide a suitable mechanism for building of singularities or quasi-singularities.

4.2.3 Singularity of Vortex Filaments in 3D Navier-Stokes

Another type of singularity can occur during vortex dynamics or interaction. Investigating such possibility with DNS or experiments is hard, and there is only limited evidence so far, for vortices starting perpendicular to each others [OMBR+21, KerrPrivate]. Several simplified models however hints at a potential singularity.

Curvature Gradient Blow-Up

The first one is DLA: vortex filaments are modeled by one-dimensional lines with a given vorticity density. The line is allowed to move under the action of its own velocity field, computed using a Biot–Savart law, truncated at a given order. This provides the evolution of the curvature κ and the torsion τ of the vorticity line, as a function of time. Using the Hasimoto’s transformation [Ha72] $\psi = \kappa \exp(i \int \tau)$, one can map the corresponding equations to focusing non-linear Schrödinger equations for ψ . The equation corresponding to the lowest order truncation was studied by Konopelchenko and Ortenzi [KO11]. They proved the existence of a finite-time blow-up, during which the gradient of the curvature and torsion becomes infinite, and the vorticity filaments undergo wild fluttering.

Reconnection Blow-Up

The previous “gradient catastrophe” scenario is interesting because large gradients curvature are typically observed during vortex reconnection, where “vorticity kinks” are built at early stages. Evidence of a singularity was actually observed in a simplified model of reconnection by Moffatt and Kimura [MK19a, MK19b, MK20]. In this model, vorticity filaments are also modeled by lines with constant vorticity density. Two filaments are initially placed at the ridges of a tetrahedra, and then allowed to interact via their mutual velocity field computed using the Biot–Savart law. The vortices interaction results in a self-similar evolution, with vorticity diverging as $1/(t_* - t)$ as the distance between the two filaments decreases as $\sqrt{t_* - t}$. There laws are exactly the laws that one would expect from scale symmetry argument of the viscous Navier–Stokes equation, that corresponds to a typical pseudo Holder exponent $h = -1$. It is not yet clear whether this blow-up scenario via reconnection is indeed present in Navier–Stokes, where interactions are more complex and self-regularizing mechanisms are present [BPB20]. On the one hand, this blow-up scenario may explain why most irregular places are found near vortex interaction (see previous section). On the other hand, the value $h = -1$ is forbidden by the properties of NSE (see Section ??), and no value of h lower than $h = -0.2$ has ever been observed.

4.2.4 Singularity in the Complex Plane

We can try and look for possible singularities in fluid by using the singularity strip method. As previously discussed, this is challenging because one needs to have a very good resolution to resolve the dissipative range and be able to have a reliable fit of the potential exponential decay. This difficulty is illustrated in Figure 4.2a for results of numerical simulations of Navier-Stokes at different Reynolds numbers. One sees that one needs a very good resolution to be able to distinguish clear exponential decay, that shows up only when $k\eta \geq 4$. For $k\eta$ near unity, it may well be that the decay is in fact a stretched exponential [BS20], with exponent that may be close to the prediction by the renormalization group [CRWB17, DKSD+18, BS20]. Given these caveats, one may try to infer the behaviour of the width of the singularity strip as a function of R_λ . This is shown in Figure 4.2b. One observes that the singularity strip width decays faster than the Kolmogorov length. Specifically, δ/η displays a power-law decay with exponent -0.29 . Taking into account that $R_\lambda \sim v^{-1/2}$ and that $\eta \sim v^{-3/4}$, we thus get a variation of δ with viscosity like $\delta v^{-0.89}$. This is a bit larger than what we obtained for logLattices see Table ??.

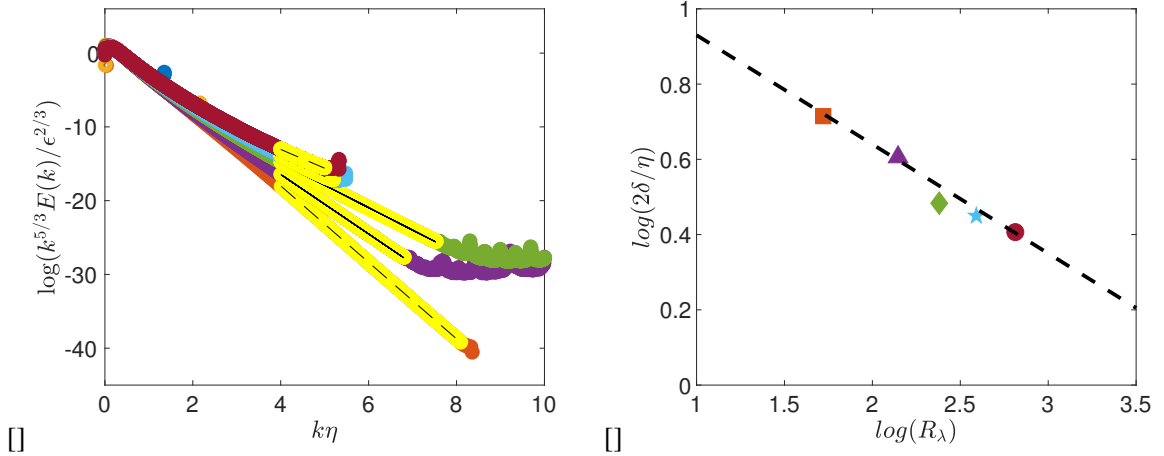


Figure 4.2: (a) Compensated energy spectrum $k^{5/3}E(k)/\epsilon^{2/3}$ vs. $k\eta$ in the dissipative range for DNS at $R_\lambda = 52$ to 650 , where the color codes the Reynolds number, and with color code provided in panel (b). The plot is in log-lin so that a straight line corresponds to an exponential decay. The area where this is satisfied is delimited on each case via yellow symbols. The fit is materialized by a black line. (b) Non-dimensional width of the singularity strip $2\delta/\eta$ as a function of R_λ . The black dotted line corresponds to a power-law $R_\lambda^{-0.29}$.

Regarding Euler equation, there have been recent high resolution numerical simulation in the axi-symmetric by [KSP22] that explored the scaling of the singularity strip in the blowing situation proposed by [LH14]. They found an exponent $\mu = 2.6 \pm 0.5$, which is compatible with the value 2.8 ± 0.1 that we get for LogLattices see Table ??.



5. Useful tools for studying irregular motions

In the rest of the class, we will try to do physics using singularities, or quasi-singularities. This sets a number of practical problems, and we will have to devise suitable tools to handle this.

5.1 Multi-fractals

5.1.1 Hölder continuity

A velocity field is said to be h -Hölder continuous with some exponent $h < 1$ if there exists C such that for ℓ small enough:

$$\|\mathbf{u}(\mathbf{x} + \ell) - \mathbf{u}(\mathbf{x})\| < C\ell^h. \quad (5.1)$$

where $\mathbf{u}(x)$ is the velocity field and ℓ is a vector of length ℓ .

This regularity condition is intermediate between simple continuity and differentiability and is based on the velocity increment $\delta\mathbf{u}(\mathbf{x}, \ell) = \mathbf{u}(\mathbf{x} + \ell) - \mathbf{u}(\mathbf{x})$.

Velocity fields with exponent $h < 1$ are locally non-differentiable, but since velocity gradients can blow up like ℓ^{h-1} in the limit $\ell \rightarrow 0$. We call such fields "rough", by opposition to "smooth" fields, characterized by a Hölder continuous exponent $h = 1$ everywhere.

5.1.2 Measurements using wavelet transforms

A wavelet transform is a kind of "local Fourier transform". As such, it is more suitable for application onto non-homogeneous fields and will naturally deal with the observed breaking of the space translation symmetry (section 8.3). A wavelet transform is also by construction "locally self-similar". It is therefore the relevant tool to measure local Hölder exponents, as proved by Arneodo and his group[51]. Specifically, it can be shown that if a field is locally Hölder continuous with exponent h around \mathbf{x}_0 , then, its wavelet transform will scale locally like $|u_i^\ell(\mathbf{x}_0, t)| \sim \ell^{h1}$.

¹Rigorously, this is valid only when the wavelet has enough vanishing moments, namely more than the degree of a local polynomial corresponding to the regular part of the Taylor expansion of u near x_0

5.1.3 Examples of rough fields

We already met a rough velocity when dealing with the "Khokhlov saw-tooth solution" (4.3). Indeed, velocity increments $\delta_\ell u$ are proportional to ℓ/t whenever 0 is outside the range $[x, x+\ell]$ and of the order $\Delta u + O(\ell/t)$ whenever 0 is inside this range. Formally, the shock is therefore a singularity with Hölder exponent $h = 0$.

Other examples are also given by self-similar blowing up solutions we found on logLattices. Indeed, for fixed time, their Fourier coefficient scale like k^{-h} , meaning that they are characterized by Hölder exponent h . Specifically, we see that inviscid blow-up in Euler is characterized by $h = 2/3$, which means that the field is non-differentiable. More generally, it was shown by [8] that it is possible to construct explicit solutions of the Euler equations solutions with Hölder exponent $h < 1/3$.

5.1.4 The multifractal phenomenology

Self-similar blow ups are characterized by one single Hölder exponent h . The multifractal model [30] generalizes this notion to more general fields $\mathbf{W}(\mathbf{x}, t, \mathbf{r})$ representing a whole family of locally self-similar solutions, labelled by a scalar field $h(\mathbf{x}, t, \mathbf{r})$, such that

$$h(\mathbf{x}, t, \mathbf{r}) = \frac{\ln |\delta_r \mathbf{W}(\mathbf{x}, t, \mathbf{r})|}{\ln(\ell/L)}, \quad \ell = |\mathbf{r}|. \quad (5.2)$$

Most fields we will encounter are fluctuating, so does the local scaling exponent h . Therefore h can be seen as a stochastic process labelled continuously by $\ln(\ell/L)$. By Kramer's theorem [67], one sees that as in the limit $\ell \rightarrow 0$, $\ln(L/\ell) \rightarrow \infty$ and we have

$$\text{Prob} [\ln(\delta W(\ell)) = h \ln(\ell/L)] \sim e^{\ln(\ell/L)C(h)} = \left(\frac{\ell}{L}\right)^{C(h)}, \quad (5.3)$$

where $C(h)$ is the rate function of h , also called multifractal spectrum. Formally, $C(h)$ can be interpreted as the co-dimension of the set where the local Hölder exponent at scale ℓ is equal to h . This observation allows us to single out the exponents where $C(h) > d$, the space dimension. Indeed, such exponents correspond to solutions that are so rare that the probability to observe them in a finite volume during a finite time interval is negligible.

Using Gärtner-Elis theorem [67], one can connect C and the moments of the multifractal field as

$$\langle \delta W^p \rangle = \langle e^{ph \ln(\ell/L)} \rangle \approx_{\ell \rightarrow 0} e^{\ln(\ell/L)\tau(p)}, \quad (5.4)$$

where $\tau(p)$ is the Legendre transform of the rate function, i.e. $\tau(p) = \min_h(ph + C(h))$. This means that we can compute the probability of finding a given exponent h by performing a Legendre transform on the scaling exponents of the moments $\lambda(p)$. Because $C(h)$ is a Legendre transform, it is necessarily convex. The set of points where it satisfies $C(h) \leq d$ (representing the set of admissible, or observable h) is therefore necessarily an interval, bounded by $-1 \leq h_{\min}$ and $h_{\max} \leq 1$. We will see later in the class how to apply this formalism to turbulence, and how to constrain $C(h)$.

5.2 Illustration: Burgers solution

The multifractal spectrum can be computed analytically in some simple cases, such as the Khokhlov solution of the inviscid Burgers equation (4.3). The structure function of order p is given by [26]

$$\langle |\delta u|^p \rangle = \left(1 - \frac{\ell}{2L}\right) \left(\frac{\ell}{t}\right)^p + \frac{\ell}{2L} \left(\frac{2L+\ell}{t}\right)^p. \quad (5.5)$$

When $p < 1$, the first term dominates and is equal to $(\Delta u)^p (\ell/2L)^p$ when $\ell \ll L$ so that $\tau(p) = p$. When $p \geq 1$, the second term dominates and is equal to $(\Delta u)^p (\ell/2L)$ when $\ell \ll L$, so that $\tau(p) = 1$, see Figure 4.1-b. Taking the inverse Legendre transform, for $p < 1$, we get $C(1) = 0$: the set points with Hölder exponent $h = 1$ (the regular points) indeed covers almost all the interval $[-L, L]$. Taking the inverse Legendre transform for $p > 1$, we get $C(0) = 1$: the location where $h = 0$ (the shock) corresponds to the point $x = 0$, which is a set of codimension 1. In this example $h_{min} = 0$ and $h_{max} = 1$. The solution is termed a "bi-fractal", even though, formally, its multifractal spectrum is a line because the convex envelop of two points is the segment that joins them.

5.3 Weak Formalism

Rough fields are delicate to deal with, especially in the context of partial differential equations such that Navier-Stokes equations, because derivatives are not necessarily well-behaved. A suitable tool to deal with them was invented by [43] and named "weak formulation". The main idea is to make a detour via the scale space, and work with smoothed version of the initial field (a "mollified" field), over a characteristic scale (resolution) ℓ . At any given resolution ℓ , the mollified field is sufficiently regular, so that all classical tools and manipulation of analysis of vector fields are valid. Limiting behaviors as resolution $\ell \rightarrow 0$ can then be used to infer results and properties for the rough field.

5.3.1 How to implement a weak formulation?

The implementation of weak formulation requires the introduction of a smoothing operator (or test function) $\phi(x)$, with suitable properties: it must be smooth (at least twice differentiable for Navier-Stokes) with compact support on \mathbb{R}^3 , even, non-negative, spatially localized and such that $\int d\mathbf{r} \phi(\mathbf{r}) = 1$. The smoothing at a resolution ℓ is then achieved through the function ϕ_ℓ , defined as $\phi_\ell(\mathbf{r}) = \ell^{-3} \phi(\mathbf{r}/\ell)$. For any given rough field $\mathbf{u}(\mathbf{x}, t)$, the *mollified field* is defined as:

$$u_i^\ell(\mathbf{x}, t) = \int d\mathbf{r} \phi_\ell(\mathbf{r}) u_i(\mathbf{x} + \mathbf{r}, t). \quad (5.6)$$

The properties of ϕ guarantee that when $\ell \rightarrow 0$, $u_i^\ell \rightarrow u_i$. Moreover, the velocity derivative of the rough field u_i can be written as:

$$\partial_j u_i^\ell(\mathbf{x}, t) = - \lim_{\ell \rightarrow 0} \int d\mathbf{r} \partial_j \phi_\ell(\mathbf{r}) u_i(\mathbf{x} + \mathbf{r}, t), \quad (5.7)$$

as well as any higher order derivative of u_i , as long as ϕ is sufficiently regular.

The weak formalism has some interesting connections with classical tools of turbulence. First, (5.6) shows that the mollifying process is a coarse-graining. As such, it averages out fine details about the fields while keeping informations about large scales. Formally, the mollified velocity can also be seen as a continuous wavelet transform of the velocity \mathbf{u} with respect to the wavelet ϕ . Note, however, that since we have chosen ϕ to be of unit integral, it is not admissible, meaning that the wavelet transform is not invertible.

5.3.2 Small scale limit

In the next part of the class, we will often have to take the limit $\ell \rightarrow 0$. This involves mathematical subtleties due to the possible roughness of the velocity field. Consider for example the limit of \mathbf{u}^ℓ . By construction, we have

$$\mathbf{u}^\ell(\mathbf{x}) = \int d\xi \phi^\ell(\xi) \mathbf{u}(\mathbf{x} + \xi) = \mathbf{u}(\mathbf{x}) + \int d\xi \phi^\ell(\xi) \delta_\xi \mathbf{u}. \quad (5.8)$$

At all points x where \mathbf{u} is regular, we have $\delta_\xi \mathbf{u} = \xi \cdot \partial \mathbf{u} + O((\xi)^2)$, so that for sufficiently small ℓ , $\mathbf{u}^\ell(x) = \mathbf{u}(x) + O(\ell)$. There is therefore no problem to take the small scale limit of \mathbf{u}^ℓ , and we have $\lim_{\ell \rightarrow 0} \mathbf{u}^\ell(x) = \mathbf{u}(x)$. When the velocity field is rough, the limit is less trivial. At such points, we define the Hölder exponent $h < 1$ (depending upon the considered point) such that the velocity field obeys the condition

$$\exists C \quad \forall \ell \leq \ell_0, \quad |\delta_\ell \mathbf{u}(x)| \leq C \ell^h. \quad (5.9)$$

Substituting this into (10.17), we now see that for sufficiently small ℓ , $\mathbf{u}^\ell(x) = \mathbf{u}(x) + O(\ell^h)$. So, as long as $h \geq 0$ -this includes the case $h = 1/3$ corresponding to K41-, the small scale limit of $\mathbf{u}^\ell(x)$ is still simple and equal to $\mathbf{u}(x)$. Things become more delicate for quantities involving derivatives, as they may now behave wildly in the small scale limit. We have indeed

$$\begin{aligned} \partial \mathbf{u}^\ell(x) &= \int d\xi \phi^\ell(\xi) \partial \mathbf{u}(x + \xi) = \int d\xi \phi^\ell(\xi) \nabla (\mathbf{u}(x + \xi) - \mathbf{u}(x)), \\ &= - \int d\xi \nabla \phi^\ell(\xi) \delta_\xi \mathbf{u}(x) = O(\ell^{h-1}). \end{aligned} \quad (5.10)$$

Therefore, for $h < 1$, the derivative $\partial \mathbf{u}^\ell(x)$ is unbounded and its limit (if it exists), noted $\partial \mathbf{u}(x)$ may be infinite.

Physics of incompressible turbulence

6	Energetics of turbulence and the first law	47
6.1	Global energy budget	
6.2	Velocity correlations and energy spectrum	
6.3	Universality of the spectrum	
7	The K41 theory and its consequences	51
7.1	Derivation of the Kármán-Howarth-Monin equation	
7.2	Preliminaries	
7.3	Summary of K41 theory	
7.4	K41 as a phenomenology of cascade and energy balance in scale space	
7.5	Universality of the energy budget in scale	
7.6	Statistical properties of the energy cascade in scale space	
8	K41 theory and symmetries: successes and limitations	57
8.1	Some basic symmetries of Navier-Stokes	
8.2	Rescaling symmetry breaking and generalized skewness	
8.3	Energy cascade and inhomogeneity	
8.4	Vortex stretching and 1/3 rescaling	
8.5	Global scale symmetry breaking and intermittency	
8.6	Time reversal breaking and enstrophy blow up	
9	The Kolmogorov-Obukhov refined similarity hypothesis	67
9.1	Summary of the theory K62	
9.2	Test of refined similarity hypothesis	
9.3	Problems and issues set by K62	
10	Weak formulation of Karman-Howarth-Monin equation	73
10.1	Derivation of the weak Karman-Howarth-Monin equation	
10.2	Properties of WKHM	
10.3	WKHM and intermittency	

6. Energetics of turbulence and the first law

6.1 Global energy budget

In 1845, James Prescott Joule published an account of his experiment showing that the application of a 772.24 foot pound force ($\approx 1050 \text{ J}$) on a paddle stirring a pound of water raises the temperature of the fluid by one degree Fahrenheit. This is an illustration of a global process occurring in most fluids, by which mechanical energy (work) is converted into thermal energy (heat), in agreement with the first law of thermodynamics governing the variation of the fluid total energy in a closed system $\Delta E^{\text{tot}} = Q + W$, as a function of the heat Q and work W added. The actual fluid energy balance of Joule's experiment is easily derived from the constitutive equation of the fluid. Taking the scalar product of equation (1.1) with \mathbf{u} and integrating over the whole volume, we then get the equation governing the time variation of the total kinetic energy $E = (1/2)\partial_t \int \rho \mathbf{u}^2 d\mathbf{x}$

$$\partial_t E = \int \rho \mathbf{u} \cdot \mathbf{f} d\mathbf{x} - v \int \rho (\nabla \mathbf{u})^2 d\mathbf{x}, \quad (6.1)$$

$$\equiv P_{inj} - P_{diss}, \quad (6.2)$$

where P_{inj} is the injected power through the mechanical work of the paddle, and P_{diss} is the dissipated energy through the action of the viscous forces. An example of such balance computed in the statistically stationary DNS A of Table 1 is shown in Figure 6.1. Besides checking the validity of equation (6.2), this figure illustrates a puzzling feature: the injected power and the dissipated power display similar oscillations around a common mean value $\bar{P}_{inj} = \bar{P}_{diss}$, albeit shifted by a constant time lag τ_c . This means that the conversion of work into heat is not instantaneous nor direct, and takes place within the flow via a process that connects different parts of the fluids. To unravel such a process, it is necessary to analyze velocity correlations inside the fluids.

6.2 Velocity correlations and energy spectrum

A classical statistical measure of spatial velocity correlations is the function $C(\mathbf{x}, \mathbf{r}, t) = \langle \mathbf{u}(\mathbf{x}, t) \mathbf{u}(\mathbf{x} + \mathbf{r}, t) \rangle$, where $\langle \cdot \rangle$ means statistical average. For any practical application throughout this paper, we shall take advantage, whenever appropriate, of statistical homogeneity, stationarity or isotropy to estimate

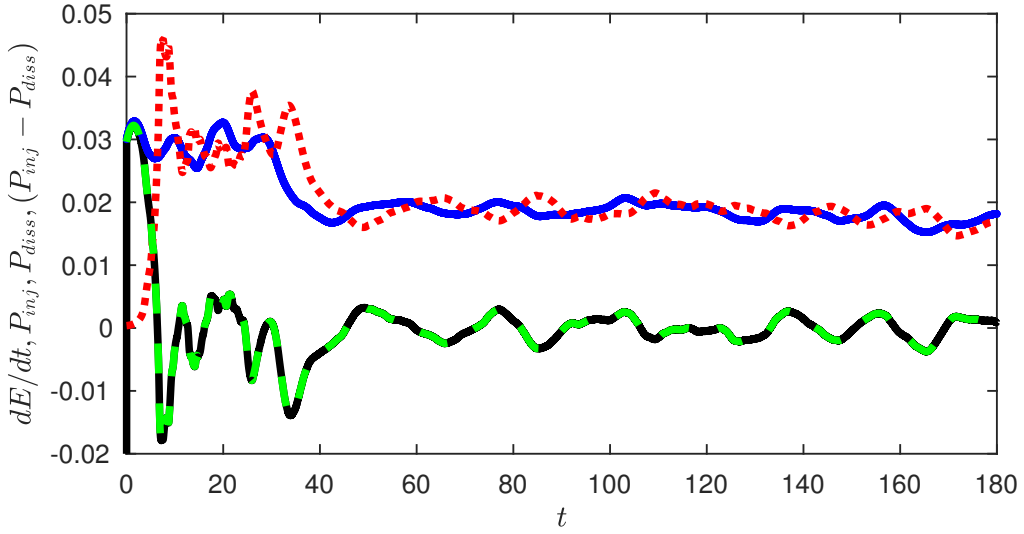


Figure 6.1: Global energy budget for the DNS A. The different terms of equation (6.2) are plotted as a function of (non-dimensional) time: P_{inj} : blue continuous line; P_{diss} : red dotted line; $\partial_t E$: black dotted line. The green dotted line is $P_{inj} - P_{diss}$, which should coincide with $\partial_t E$ in a stationary state. This is indeed the case for this DNS where both curves superpose exactly.

it through spatial average ($\langle A \rangle_x \equiv \langle A \rangle$), time average ($\langle A \rangle_t \equiv \bar{A}$) or an angle average over the scale direction ($\langle A \rangle_\phi$).

If the turbulence is statistically homogeneous and stationary, $C(\mathbf{x}, \mathbf{r}, t)$ depends neither on space \mathbf{x} nor on time t , and can be studied through its Fourier transform, $\mathcal{C}(\mathbf{k}) = \int e^{i\mathbf{k} \cdot \mathbf{r}} C(\mathbf{x}, \mathbf{r}, t) d\mathbf{r}$. If the turbulence is homogeneous, the average involved in the correlation function can be transformed into a space average. We then get :

$$\begin{aligned} \mathcal{C}(\mathbf{k}) &= \int \int e^{i\mathbf{k} \cdot \mathbf{r}} \mathbf{u}(\mathbf{x}, t) \mathbf{u}(\mathbf{x} + \mathbf{r}, t) d\mathbf{r} d\mathbf{x}, \\ &= \hat{\mathbf{u}}(\mathbf{k}, t) \hat{\mathbf{u}}(-\mathbf{k}, t), \end{aligned} \quad (6.3)$$

where $\hat{\mathbf{u}}$ is the Fourier transform of \mathbf{u} . If, further, the turbulence is isotropic, $\mathcal{C}(\mathbf{k})$ only depends on $k = \|\mathbf{k}\|$ and by Parseval equality, we have :

$$\int \mathcal{C}(\mathbf{k}) d\mathbf{k} = \int k^{d-1} |\hat{\mathbf{u}}(k, t)|^2 dk = \int \mathbf{u}(\mathbf{x}, t) \mathbf{u}(\mathbf{x}, t) d\mathbf{x} \equiv \langle \mathbf{u}(\mathbf{x}, t) \mathbf{u}(\mathbf{x}, t) \rangle. \quad (6.4)$$

This defines the energy spectrum $E(k) = Ak^{d-1} \mathcal{C}(\mathbf{k})$, where A is a normalization factor so that $\int E(k) dk = 0.5 \langle \mathbf{u}(\mathbf{x}, t) \mathbf{u}(\mathbf{x}, t) \rangle$.

The energy spectrum corresponding to the DNS A is shown in figure 6.2-a. It is self-similar at small wave numbers (large scales), with power law approximately equal to $k^{-5/3}$ and exponentially decay at large wave numbers (small scales). The spectrum peaks at a wavenumber $k_f = 1/L_f$ corresponding to the forcing scale L_f . The exponential decay starts around $\eta = (\nu^3/\varepsilon)^{1/4}$. This is actually the only characteristic scale one can build using the fluid viscosity ν and the mean injected power per unit mass $\varepsilon = \overline{P_{inj}}/\rho \mathcal{V}$ where \mathcal{V} is the volume enclosing the fluid. If we assume that the shape of the spectrum only depends on two variables, ε and ν , we can further build an energy by unit wavenumber $\varepsilon^{2/3} \eta^{5/3}$, so that the energy spectrum is characterized by the function $E(k)/\varepsilon^{2/3} \eta^{5/3}$ as a function of $k\eta$, which are the "universal coordinates" considered in figure 6.2-a. Is this indeed a "universal representation", i.e. does it change when we vary the parameters of the flow?

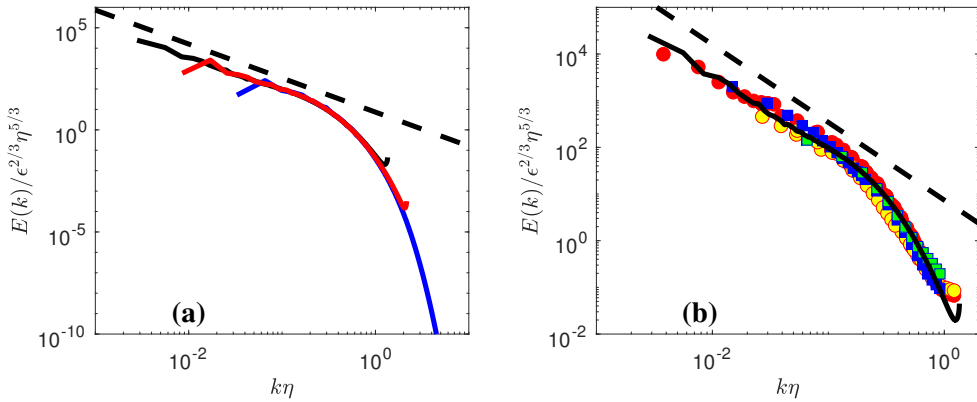


Figure 6.2: Spatial kinetic energy spectra at various R_λ , and for different forcing or anisotropy conditions. The black dotted line is $k^{-5/3}$. a): in numerical simulations: DNS B: blue line; DNS C: red line; the black continuous line is from the JHU Turbulent data base (<http://turbulence.pha.jhu.edu>), at $R_\lambda = 433$ [44]. Picture courtesy F. Nguyen and J-Ph. Laval. b): in experiments: CON C: red circle, CON W: yellow circle; ANTI C: blue square; ANTI W: green square. Adapted from [14].

6.3 Universality of the spectrum

The first thing we can change is the Reynolds number. In figure 6.2-a), we add the energy spectrum of two additional DNS, one at lower and one at higher Reynolds number. We observe that the range over which the self-similar range is observed is decreased when the Reynolds is decreased, but apart from that, no noticeable change is observed, and the three spectra collapse in universal coordinates. Increasing further the Reynolds number is difficult through numerical simulations. We can turn to experiment to reach larger Reynolds numbers, but then the isotropy and homogeneity conditions will not be met anymore, at least not as cleanly as in numerical simulations. This is a good test of robustness of the universality spectrum anyway.

To illustrate this, we plot in figure 6.2-b) the spatial energy spectrum, computed for a series of experimental data fields measured by SPIV in a turbulent von Karman flow, at different spatial locations, using a variety of forcing and flows parameters. The von Karman flow being globally non-homogeneous, we cannot expect the statistics of the turbulence to be identical everywhere in the tank [15]. We have selected two special locations in that respect (see figure 1.3): i) an area centered around the center of the experimental set -up, where the mean velocity is zero, and where large velocity fluctuations exist, due to the presence of a strong mixing shear layer; ii) an area centered around the mid-plane, but located near one of the edge of the tank. At such location, turbulence is highly anisotropic, and dominated by boundary layer effects. Measurements corresponding to these different locations have been associated with different colors in figure 6.2-b). We see no systematic differences with respect to the numerical energy spectrum.

The flow forcing conditions and the flows properties have also been changed by changing the rotation direction of the impellers (labelled by different symbols in figure 6.2-b)), as well as the flow viscosity. This results in different values of ϵ (measured independently by torquemeters), R_λ (computed using the r.m.s of the velocity and the viscosity) and η (computed from the value of the viscosity and ϵ) for different data sets. Again, we observe that all spectra collapse on the same universal curve as the DNS. This means that properties of the function $E(k\eta)/\epsilon^{2/3}\eta^{5/3}$ are very robust, an indication that it is built in the properties of the equations of motions. It was indeed Kolmogorov's remarkable achievement to derive a simple explanation of the shape of $E(k)$ from simple manipulations of the INSE, resulting in what is commonly called the "Kolmogorov 1941 theory of turbulence" (hereafter K41, [37]).

7. The K41 theory and its consequences

7.1 Derivation of the Kármán-Howarth-Monin equation

7.2 Preliminaries

The explanation of Kolmogorov is based on the Kármán-Howarth-Monin equation (hereafter KHM). This equation has been derived in several textbooks, but I present here a simple derivation for consistency. KHM equation can be derived for solutions \mathbf{u} of the Navier-Stokes equations Eq. (1.1) and involve the velocity increments:

$$\delta\mathbf{u} = \mathbf{u}(x+r,t) - \mathbf{u}(x,t). \quad (7.1)$$

These increments depend both on x and r , so can can be independently differentiated with respect to x -we denote it by ∂ - or by r , we denote it by ∇ . We now take the Eq. (1.1) for $\mathbf{u}(x,t)$, multiply it by $\mathbf{u}(x+r,t)$, and sum it with Eq. (1.1) written for $\mathbf{u}(x+r,t)$ and multiplied by $\mathbf{u}(x,t)$. We then get:

$$\partial_t u_i u'_i + u'_i u_j \partial_j u_i + u_i u'_j \partial_j u'_i = -u'_i \partial_i p - u_i \partial_i p' + v (u'_i \partial^2 u_i + u_i \partial^2 u'_i) + f_i u'_i + f'_i u_i, \quad (7.2)$$

where we have used the short hand notation $u' \equiv \mathbf{u}(x+r,t)$ and $u' \equiv \mathbf{u}(x,t)$.

We are now going to take statistical averages of this equation, in the *homogeneous case*, i.e. when the velocity field is statistically invariant by translation. In this case, we will be able to set to zero any quantity looking like $\langle \partial(\bullet) \rangle$, where \bullet is any quantity that depend on x (and r). So in the manipulation that I will perform now, I will not explicit any term of the type $\partial(\bullet)$.

7.2.1 Useful identities

Here I derive useful identities that I will use later. In the sequel, I will use heavily the fact that $\nabla \cdot \mathbf{u} = 0$ (since \mathbf{u} does not depend on r), $\nabla u' = \partial u'$ and incompressibility.

First identity concerns the non-linear term. Indeed, we have:

$$\begin{aligned} \nabla_j (\delta u_j \delta u_i \delta u_i) &= \partial_j (u'_j u'_i u'_i) - 2u_i \partial_j (u'_j u'_i) - u_j \partial_j (u'_i u'_i) + 2u_j u_i \partial_j u'_i, \\ &= \partial_j (\bullet) - 2u_i u'_j \partial_j u'_i - 2u'_i u_j \partial_j u_i. \end{aligned} \quad (7.3)$$

From this, we get the first useful formula $\langle u'_i u_j \partial_j u_i + u_i u'_j \partial_j u'_i \rangle = -\nabla \cdot \langle \delta u (\delta u)^2 \rangle / 2$.

The second identity concerns the pressure term. Indeed, due to incompressibility, we have:

$$u'_i \partial_i p + u_i \partial_i p' = \partial_i(\bullet). \quad (7.4)$$

So that, by homogeneity, $\langle u'_i \partial_i p + u_i \partial_i p' \rangle = 0$.

The third identity concerns the viscous term. Indeed, we have:

$$\begin{aligned} \nabla^2 (\delta u_i \delta u_i) &= \nabla^2 (u'_i u'_i - 2u_i u'_i), \\ &= \partial^2 u'^2 - 2u_i \partial^2 u'_i. \end{aligned} \quad (7.5)$$

So, by taking average, we have that $\langle u_i \partial^2 u'_i \rangle = -\nabla^2 \langle (\delta u)^2 \rangle / 2$. On the other hand, by homogeneity, we have that $\langle \nabla^2 \delta u^2 \rangle = \langle \nabla^2 \delta' u^2 \rangle$, where $\delta' u = u(x, t) - u(x - r, t) \equiv u - u''$. By the same computation than in Eq. (7.5), we then find that $\langle \nabla^2 \delta' u^2 \rangle = -2 \langle u_i \partial^2 u''_i \rangle$. By homogeneity, we have $\langle u_i \partial^2 u''_i \rangle = \langle u'_i \partial^2 u_i \rangle$. Collecting all that, we find then that:

$$\nu \langle u'_i \partial^2 u_i + u_i \partial^2 u'_i \rangle = -\nu \nabla^2 \langle (\delta u)^2 \rangle. \quad (7.6)$$

Finally, by homogeneity, we have $\langle f_i u'_i \rangle = \langle u_i f''_i \rangle$. Taking average of Eq. (7.2), using all previous identities, and collecting all terms, we finally get the Karman-Howarth-Monin equation involving the correlation function $C(\mathbf{r}, t) = \langle u_i u'_i \rangle$ as:

$$\begin{aligned} \frac{1}{2} \partial_t C(\mathbf{r}, t) - \mathcal{P}_\ell &= \frac{1}{4} \nabla_{\mathbf{r}} \cdot \langle \delta \mathbf{u} (\delta \mathbf{u})^2 \rangle - \frac{\nu}{2} \nabla_{\mathbf{r}}^2 \langle (\delta \mathbf{u})^2 \rangle \equiv \nabla_{\mathbf{r}} \mathbf{J}_\ell, \\ &\equiv -\Pi_\ell^I - \Pi_\ell^V, \end{aligned} \quad (7.7)$$

where $\langle \rangle$ denotes the statistical average, $\nabla_{\mathbf{r}}$ is the divergence with respect to \mathbf{r} , $\ell = ||\mathbf{r}||$ denotes the scale, $\mathcal{P}_\ell = \langle \mathbf{u}(\mathbf{x}) \cdot (\mathbf{f}(\mathbf{x} + \mathbf{r}) + \mathbf{f}(\mathbf{x} - \mathbf{r})) \rangle / 2$ is a measure of the mean energy injection rate at scale ℓ , $\delta \mathbf{u} = \mathbf{u}(\mathbf{x} + \mathbf{r}) - \mathbf{u}(\mathbf{x})$ is the velocity increments over a displacement \mathbf{r} .

7.3 Summary of K41 theory

The explanation of Kolmogorov is based on the Kármán-Howarth-Monin equation and proceeds as follows. For very large value of ℓ , $\overline{\mathcal{P}_\ell} \rightarrow 0$ since the force and the velocity become uncorrelated. For $\ell \rightarrow 0$, $\overline{\mathcal{P}_\ell}$ tends to ε , the mean energy injection rate (which is also the mean energy dissipation rate). More precisely, for $\ell \ll L_f$, where L_f is the forcing scale, one can Taylor expand $\mathbf{f}(\mathbf{x} + \mathbf{r})$ and $\mathbf{f}(\mathbf{x} - \mathbf{r})$ to second order in ℓ to get $\overline{\mathcal{P}_\ell} = \varepsilon + O(\ell/L_f)^2$. Now, we note that the last term of the r.h.s. of equation (7.7) is proportional to the viscosity. Kolmogorov first assumes that there is a range of scales $L_{min} \ll \ell \ll L_f$ -the "inertial range", to be characterized consistently later by providing expression of L_{min} - where this term is negligible with respect to the first term of the r.h.s. Looking for a statistically stationary solution, he then takes time average to get $\nabla_{\mathbf{r}} \cdot \overline{\langle \delta \mathbf{u} (\delta \mathbf{u})^2 \rangle} = -4\varepsilon$, which can be readily integrated into

$$\overline{\langle (\delta \mathbf{u})^3 \rangle} = -4\varepsilon \mathbf{r} / 3. \quad (7.8)$$

This is called the "Kolmogorov 4/3 law" and is a basic law of turbulence. Kolmogorov further assumes that, over the range of scales where this holds, the function $\mathcal{S} = \overline{\langle (\delta \mathbf{u})^3 \rangle} / \overline{\langle (\delta \mathbf{u})^2 \rangle}^{3/2}$ is constant. We shall come back to this assumption later. It means anyway that $\overline{\langle (\delta \mathbf{u})^2 \rangle} \propto (\varepsilon \ell)^{2/3}$, with $\ell = ||\mathbf{r}||$, or, after twice differentiation $\nabla_{\mathbf{r}}^2 C(\mathbf{r}) \propto \varepsilon^{2/3} \ell^{-4/3}$, since $\overline{\langle (\delta \mathbf{u})^2 \rangle} = 2(\langle \mathbf{u}^2 \rangle - C(\mathbf{r}))$. By Fourier transform, we then get:

$$\begin{aligned} \mathcal{E}(\mathbf{k}) &= \int e^{i\mathbf{k} \cdot \mathbf{r}} C(\mathbf{x}, \mathbf{r}, t) d\mathbf{r}, \\ &\sim \int e^{i\mathbf{k} \cdot \mathbf{r}} (\varepsilon r)^{2/3} d\mathbf{r}, \\ &\sim \varepsilon^{2/3} k^{-3-2/3} \int e^{iy} y^{2/3} dy. \end{aligned} \quad (7.9)$$

Since $E(k) = k^2 \mathcal{E}(\mathbf{k})$, this leads to $E(k)/\varepsilon^{2/3} \eta^{5/3} \propto (k\eta)^{-5/3}$, which is the behavior we observe for small enough $k\eta$ in figure 6.2. Moreover, the scaling of $C(\mathbf{r})$ provides us with an estimate of the range of the inertial range. It is indeed characterized by scales $\ell \sim 1/k$ such that:

$$\nabla_{\mathbf{r}} \cdot \overline{\langle \delta \mathbf{u} (\delta \mathbf{u})^2 \rangle} \sim \varepsilon \gg v \nabla_{\mathbf{r}}^2 \overline{\langle (\delta \mathbf{u})^2 \rangle} \sim v \varepsilon^{2/3} \ell^{-4/3}, \quad (7.10)$$

which is valid as long as $\ell \gg (v^3/\varepsilon)^{1/4} = \eta$, i.e. $k\eta \gg 1$. This is indeed what is observed in figure 6.2.

7.4 K41 as a phenomenology of cascade and energy balance in scale space

The theory of Kolmogorov successfully explains, as we have seen, the shape of the energy spectrum in universal coordinates in the inertial range. From a broader point of view, it can in fact be seen as a theory of energy balance in the scale-time domain, that helps to build a phenomenology of the energy cascade from the injection scale to the dissipation scales. Indeed, comparing equation (7.7) with equation (6.2), we see that KHM describes a global energy balance for $C(\mathbf{r}, t)$ that can be seen as representative of the energy contained at scale $\ell = \|\mathbf{r}\|$. Its time variation is governed by two types of terms: the first one is the divergence, in the scale space, of a vector $\mathbf{J}_{\ell} = (1/4) \cdot \langle \delta \mathbf{u} (\delta \mathbf{u})^2 \rangle - v \nabla_{\mathbf{r}} \langle (\delta \mathbf{u})^2 \rangle / 2$. The second term is independent of scale and describes the energy injection/dissipation ε . The vector \mathbf{J}_{ℓ} can be split into two components, one "inertial" $\mathbf{J}_{\ell}^I = (1/4) \langle \delta \mathbf{u} (\delta \mathbf{u})^2 \rangle$, that does only depends on velocity, and a viscous component $\mathbf{J}_{\ell}^V = -v \nabla_{\mathbf{r}} \langle (\delta \mathbf{u})^2 \rangle / 2$. The vector \mathbf{J}_{ℓ} encodes an energy flux through the scale space (rate at which energy is transferred from scales to scales).

The theory of Kolmogorov already provides us with the scaling of the divergence of the time average of the two components in the inertial range

$$\begin{aligned} \overline{\Pi}_{\ell}^I &\equiv -\nabla_{\mathbf{r}} \cdot \overline{\mathbf{J}_{\ell}^I} \sim \varepsilon, \\ \overline{\Pi}_{\ell}^V &\equiv -\nabla_{\mathbf{r}} \cdot \overline{\mathbf{J}_{\ell}^V} \sim v \varepsilon^{2/3} \ell^{-4/3} \sim \varepsilon \left(\frac{\ell}{\eta} \right)^{-4/3}, \end{aligned} \quad (7.11)$$

which is valid as long as $\ell \geq \eta$. At $\ell \sim \eta$, the two terms coincide. The typical velocity at this scales is $u_{\eta} \sim (\eta \overline{\mathbf{J}_{\ell}^I})^{1/3} \sim (\varepsilon \eta)^{1/3}$, so that the Reynolds number at this scale is $Re(\eta) = (\varepsilon \eta^4)^{1/3} / v = 1$: viscosity becomes the preponderant process and the flow is laminar below η . It is then meaningful to perform a Taylor expansion on the velocity, to get the scaling of the velocity increment as $\delta u \sim \mathbf{r} \cdot \nabla \mathbf{u} = O(\ell \sqrt{\varepsilon/v})$, where we have used $\varepsilon \sim v(\nabla \mathbf{u})^2$. We thus infer the following scaling laws for scales below η as

$$\begin{aligned} \overline{\Pi}_{\ell}^I &\sim \left(\frac{\varepsilon}{v} \right)^{3/2} \ell^2 \sim \varepsilon \left(\frac{\ell}{\eta} \right)^2, \\ \overline{\Pi}_{\ell}^V &\sim v \frac{\varepsilon}{\eta} \sim \varepsilon. \end{aligned} \quad (7.12)$$

The viscous component then carries most of the flux, and the inertial component vanishes like ℓ^2 . The different scaling laws are summarized in figure 7.1-a). The overall picture associated with these scalings is that of an "energy cascade": the energy is injected at large scale at a rate ε . It is transferred down the scales at a constant rate ε by the inertial flux, until it reaches the scale η where the viscous flux takes over, and carries this flux down to $\ell \sim 0$ (actually the hydrodynamic scale) where it is transformed into heat. The time lag τ_c observed in figure 6.1 between the time of energy injection and energy dissipation corresponds then to a "cascade time", the time it takes for a parcel of energy to be transferred from scale L_f to η .

The validity of this picture can be tested against DNS of homogeneous, isotropic turbulence. This is done in figure 7.2-a). One sees that all the scalings laws of the K41 picture of turbulence are satisfied. Moreover, the "inertial" range indeed expands as L_f/η .

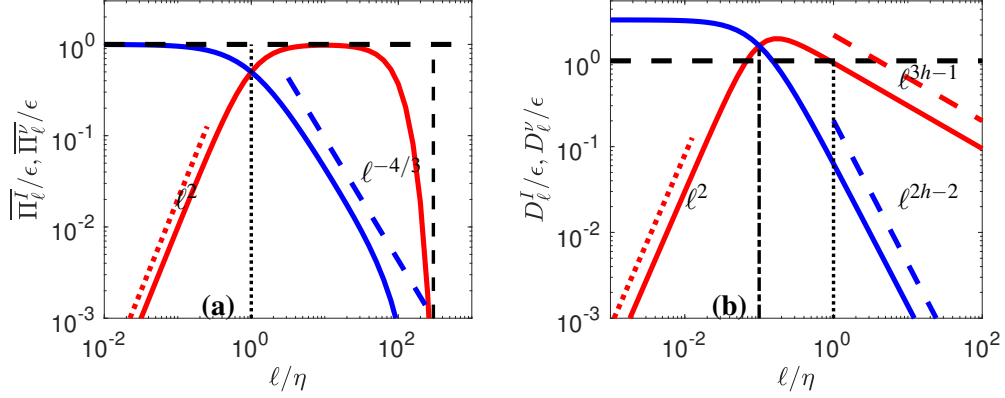


Figure 7.1: K41 vs multifractal picture of turbulence. a) K41 picture: the energy injected at scale L_f (vertical black dashed line) is transferred at a constant rate ϵ by the energy flux $\overline{\Pi}_\ell^I$ (red line) down the the scale where it becomes equal to the viscous flux $\overline{\Pi}_\ell^V$ (blue line). From downwards on, it it transported by the latter to the smallest hydrodynamic scale, where it is dissipated into heat. In the inertial range, the energy flux is constant, and the viscous flux increases like $\ell^{-4/3}$. In the dissipative range, the viscous flux is constant, while the energy flux decreases like ℓ^2 in the dissipative range. The energy flux and the viscous flux become equal at the Kolmogorov scale, indicated by a black dotted line. b) Multifractal picture: the energy is transferred at smaller scale by the energy flux (red line) up to the scale η_h (vertical dashed dotted line) where the energy flux and the viscous flux (blue line) balance. In the inertial range, the energy flux and viscous flux scale respectively like ℓ^{3h-1} and ℓ^{2h-2} , while they obey the same scaling than in the K41 picture in the dissipative range. When $h < 1/3$, the energy flux and the viscous flux become equal at a scale smaller than the Kolmogorov scale, indicated by a black dotted line.

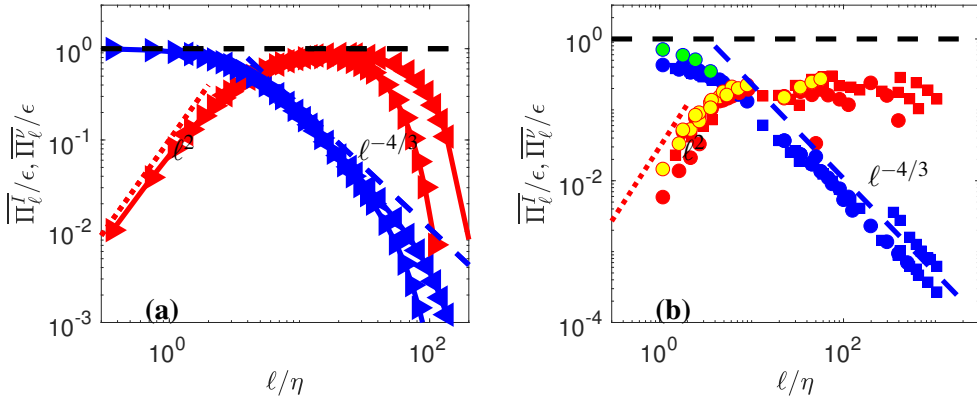


Figure 7.2: Test of K41 picture: a) in numerical simulations: left pointing triangles: DNS B; right pointing triangles: DNS A. Red symbols: mean energy flux $\overline{\Pi}_\ell^I/\epsilon$; blue symbol: mean viscous flux $\overline{\Pi}_\ell^V/\epsilon$. The red dotted line is $0.1(\ell/\eta)^2$ and the blue dashed line is $5(\ell/\eta)^{-4/3}$. b) In experiments using SPIV data. mean energy flux for CON C: red circle, CON W: yellow circle; ANTI C: red square , ANTI W: yellow square ; mean viscous flux for CON C: blue circle, CON W: green circle, ANTI C: blue square, ANTI W: green square. Adapted from [14].

7.5 Universality of the energy budget in scale

The energy budget in scale given by (7.7) and its associated picture of the energy cascade (figure 7.1-a) and figure 7.1-b)), derived for ideal, homogeneous turbulence, is actually very robust. Not surprisingly (remember the results for the spectra), the scaling properties of the divergence of the time average of the two components of the energy flux density \mathbf{J}_ℓ , reported in figure 7.2-b), display a remarkable agreement with the expected scaling laws, with no systematic effect due to different locations (coded by color), or forcing condition (coded by symbols). The main difference with the results of the DNS is the value of the plateau for $\overline{\Pi}_\ell^I$, which is around 0.3 rather than 1. This is because, due to the planar measurement, we can only have access to the in-plane component of this flux. If the flow were isotropic, we would thus get 2/3 of the total value. The von Karman flow is highly anisotropic at this location, so that the out-of-plane component actually carries a large fraction of the flux, which explains our result.

7.6 Statistical properties of the energy cascade in scale space

Experiments provide large data sets of independent realizations of the cascade so that we can use them to study the statistical properties of the energy cascade in scale space. In figures 7.3-a) and 7.3-b), we plot the probability distribution functions (PDFs) of Π_ℓ^I and Π_ℓ^V , obtained through velocity measurements at uncorrelated times at the center of the experiment, for a flow forced in the scooping direction (minus sign direction in figure 1.3-c), for scale ranging from $1 \leq \ell/\eta \leq 10^3$. We see that the two PDFs are very different and vary significantly with scale: the PDF of Π_ℓ^I is almost symmetrical around 0 with exponential tails widening as scale increases; the PDF of Π_ℓ^V are lognormal (parabolic in log-log plot, not shown) with tails narrowing as scale increase.

Both PDFs however carry the same universal features: when plotted using centered reduced variables $\Pi_\ell^{I*} = (\Pi_\ell^I - \overline{\Pi}_\ell^I)/\sigma^I$ and $\Pi_\ell^{V*} = (\Pi_\ell^V - \overline{\Pi}_\ell^V)/\sigma^V$, the PDFs collapse on two universal curves, see figure 7.3-a and 7.3-b. The PDF of Π_ℓ^{V*} is similar in shape to the PDF of energy dissipation (displayed in figures 7.3-b1)). Summarizing, we see that both the local energy transfer Π_ℓ^I and dissipation Π_ℓ^V have universal statistical properties, following

$$P(\Pi_\ell^I) = \mathcal{P}^I \left(\frac{\Pi_\ell^I - \overline{\Pi}_\ell^I}{\sigma^I(\ell)} \right), \quad (7.13)$$

$$P(\Pi_\ell^V) = \mathcal{P}^V \left(\frac{\Pi_\ell^V - \overline{\Pi}_\ell^V}{\sigma^V(\ell)} \right), \quad (7.14)$$

where all the scale dependance are encoded in the means $\overline{\Pi}_\ell^I, \overline{\Pi}_\ell^V$ and the standard deviations (std) $\sigma^I(\ell), \sigma^V(\ell)$ shown in figure 7.4.

Not surprisingly, the means of Π_ℓ^V and Π_ℓ^I obey the Kolmogorov scaling sketched in figure 7.1-a. The standard deviations however, display new behaviors that are not predicted by K41 theory: the std of Π_ℓ^V decreases with increasing scale with an exponent slightly smaller than $-4/3$, while the std of Π_ℓ^I increases slightly with scales (like $\ell^{0.25}$). To understand such behavior, one needs to leave empirical observation and dig deeper into theoretical consequences and meaning of K41.

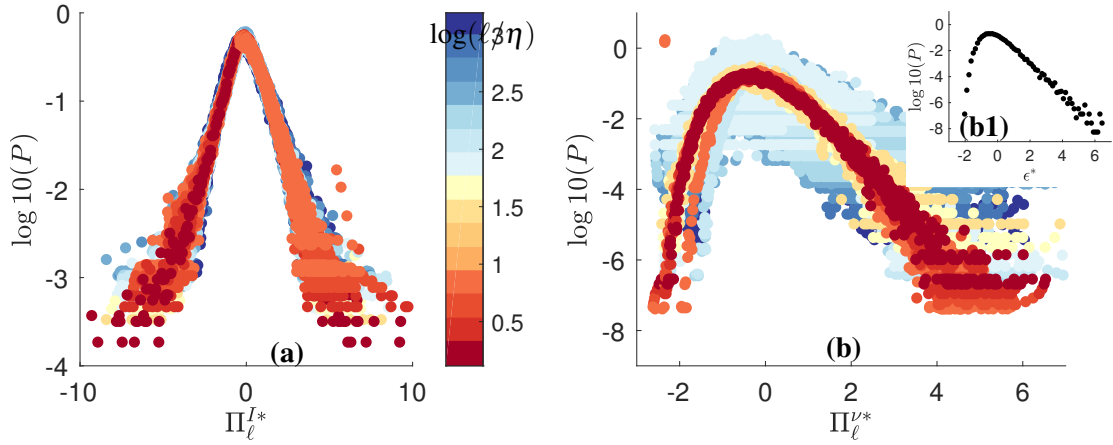


Figure 7.3: PDF's of flux terms, centered and reduced as explained in the text, for experiments ANTIG and ANTIC-1 to ANTIC-4 (see figure 7.4 for corresponding mean and standard deviation and Table 1 for symbols). a) Centered and reduced PDF of Π_ℓ^I at different scale, coded by color, following the colorbar. b) Centered and reduced PDF of Π_ℓ^V at different scale, coded by color. Inset b1): Centered and reduced PDF of dissipation.

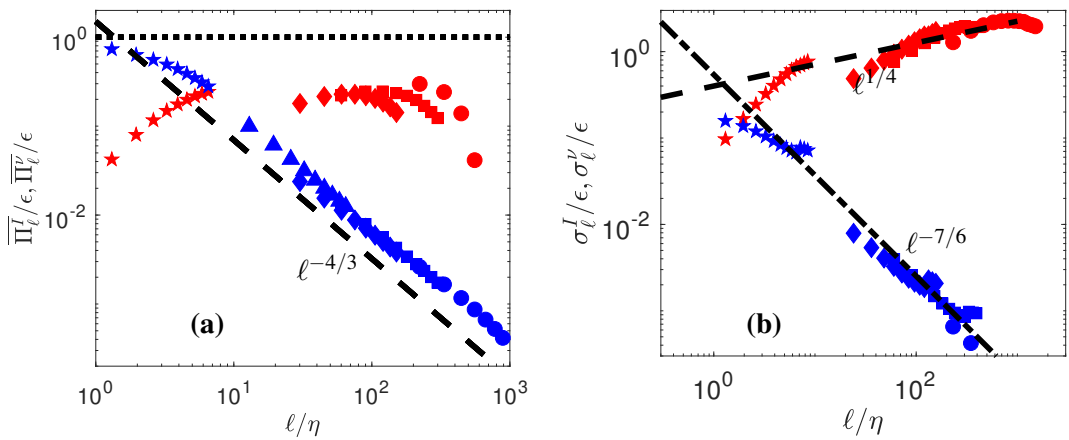


Figure 7.4: Scale variation of the mean and standard deviations of the flux terms for experiments ANTIG and ANTIC-1 to ANTIC-4 . a) Time average: $\overline{\Pi}_\ell^I$: red symbols; $\overline{\Pi}_\ell^V$: blue symbols . b) Standard deviation σ_ℓ^I : red symbols; σ_ℓ^V : blue symbols. The black dashed line is $\ell^{1/4}$. The dashed-dot line in figure b) is $\ell^{-4/3}\ell^{1/6}$ deduced from the ℓ^2 scaling of the std ratio shown in figure 8.1-a and the scaling of σ_ℓ^I .

8. K41 theory and symmetries: successes and limits

8.1 Some basic symmetries of Navier-Stokes

As pointed out by [29], K41 theory is deeply connected with basic symmetry properties of the Navier-Stokes equations (1.1), namely:

- i) space translation (homogeneity): $\mathbf{x} \rightarrow \mathbf{x} + \mathbf{r}$, for arbitrary \mathbf{r} ;
- ii) time translation (stationarity): $t \rightarrow t + \tau$, for arbitrary τ ;
- iii) rescaling: $(t, \mathbf{x}, \mathbf{u}) \rightarrow (\lambda^2 t, \lambda \mathbf{x}, \lambda^{-1} \mathbf{u})$, for arbitrary λ ;

and **in the inviscid limit**, $v \rightarrow 0$:

- iv) time reversal: $(t, \mathbf{u}) \rightarrow (-t, -\mathbf{u})$,
- v) h rescaling: $(t, \mathbf{x}, \mathbf{u}) \rightarrow (\lambda^{1-h} t, \lambda \mathbf{x}, \lambda^h \mathbf{u})$, for arbitrary λ and h . Note that the rescaling iii) is equivalent to a -1 rescaling (property v with $h = -1$).

Let us explore in more details such connections and their consequences.

8.2 Rescaling symmetry breaking and generalized skewness

A basic ingredient of K41 is that the skewness $\mathcal{S} = \overline{\langle (\delta \mathbf{u})^3 \rangle} / \overline{\langle (\delta \mathbf{u})^2 \rangle}^{3/2}$ is constant or equivalently, the generalized skewness $\mathcal{S}_1 \equiv \overline{\Pi_\ell^I} / \overline{(\Pi_\ell^V)}^{3/2}$ scales like $\mathcal{S}_1 \sim \ell^2$. This is very well satisfied by the experimental data up to at least the Kolmogorov scale, as shown in figure 8.1-a. Moreover, the scaling law is also satisfied by the standard deviations $\sigma_\ell^I / (\sigma_\ell^V)^{3/2} \sim \ell^2$. Because of the universal properties of the PDFs of Π_ℓ^V and Π_ℓ^I (equation (7.14)), this means that any generalized skewness $\mathcal{S}_q \equiv \overline{(\Pi_\ell^I)^q} / \overline{(\Pi_\ell^V)^q}^{3/2}$ scales like ℓ^{2q} .

On the other hand, if we apply the h rescaling symmetry iv) to Π_ℓ^I and Π_ℓ^V , we notice that they are respectively rescaled by a factor λ^{3h-1} and λ^{2h-2} , so that all the generalized skewness \mathcal{S}_q are rescaled by a factor λ^{2q} , in agreement with their observed scaling. The minimal hypothesis to explain the experimental behavior of the high order properties of the energy cascade is therefore that it is statistically invariant by h rescaling, with no special emphasis on a particular h so far.

Furthermore, if one compares the individual behavior of Π_ℓ^I and Π_ℓ^V under h rescaling symmetry iv) and compare then with the scaling behaviors of the K41 theory, we see that they are compatible

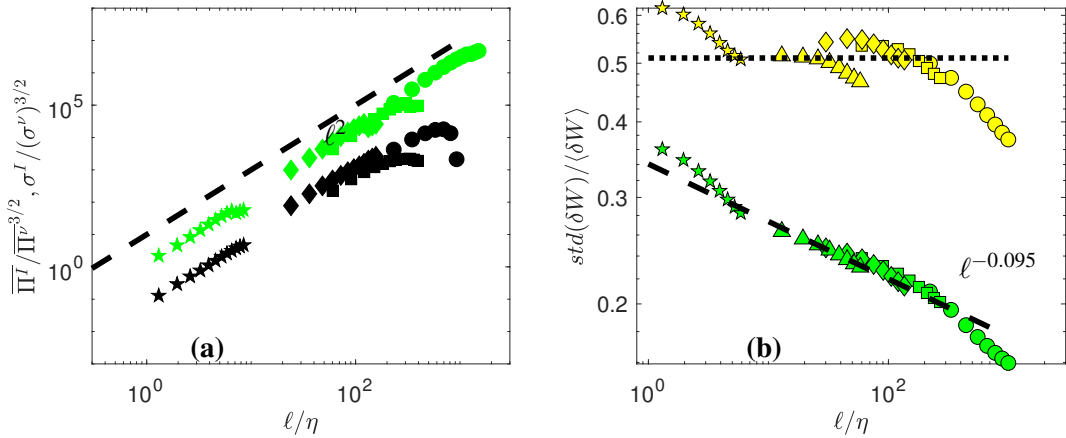


Figure 8.1: Test of rescaling symmetry for experiments ANTIG and ANTIC-1 to ANTIC-4 . a) For the flux Π_ℓ^I and Π_ℓ^v via the generalized skewness $\overline{\Pi_\ell^I}/\overline{\Pi_\ell^v}^{3/2}$ (black symbols) and std ratio $\sigma_\ell^I/(\sigma_\ell^v)^{3/2}$ (green symbols). The dashed line is ℓ^2 . b) For the wavelet velocity increments δW at different scale, using ratio of standard deviation to average for δW (green symbols) and δW^C (yellow symbols). For self-similar variables, the ratio should be constant (dotted line), which is true for δW^C but not for δW . The dashed line is $\ell^{-0.095}$.

with respectively $3h - 1 = 0$ and $2h - 2 = -4/3$, i.e. $h = 1/3$ for both. This mean that the rescaling symmetry iii) is broken, so that viscosity becomes irrelevant (in agreement with the "inertial range" assumption) and only h rescaling v) with $h = 1/3$ should be considered. There is however no understanding at this stage of how the special value $h = 1/3$ is selected with respect to other possible values. For this, we need to dive more deeply into the energy cascade and its properties.

8.3 Energy cascade and inhomogeneity

Taking into account the K41 scaling, we can take the limit $\ell \rightarrow 0$ of the KHM equation (7.7) to get

$$\frac{1}{2} \partial_t \langle u^2(x, t) \rangle - \langle \mathbf{f} \cdot \mathbf{u} \rangle = -\nu \langle (\nabla u)^2(x, t) \rangle, \quad (8.1)$$

which is nothing but the global energy budget equation (6.2). Small scale behavior of the energy cascade picture has, therefore, an immediate consequence on the enstrophy scaling. Indeed, in homogeneous turbulence, the enstrophy $\langle \omega^2(x, t) \rangle = \langle (\nabla u)^2(x, t) \rangle$, so we get from (8.1)

$$\Omega \equiv \overline{\langle \omega^2(x, t) \rangle} = \frac{\varepsilon}{\nu}. \quad (8.2)$$

For this equality to hold, it means that there is in the flow at least one point where the magnitude of the vorticity $\omega = \nabla \times \mathbf{u}$ exceeds the threshold: $|\omega| \geq \sqrt{\varepsilon/\nu} = \varepsilon^{1/3} \eta^{-2/3}$. There are in fact many points where this happens, as can be seen in figure 8.2-a), where peaks of vorticity, over regions of size 30η , exist. Overall, the vorticity field is very intermittent, meaning that if the homogeneity postulated by Kolmogorov holds, it is only valid in a statistical sense [29].

8.4 Vortex stretching and 1/3 rescaling

Another measure of the intermittency of the vorticity field is provided by the PDF of the magnitude of the vorticity, shown in figure 8.2-b). It is highly non Gaussian, with tails extending over values much larger than $\varepsilon^{1/3} \eta^{-2/3}$. Such behavior requires a mechanism of amplification of vorticity:

indeed, the forcing injects typical value of the velocity $(\varepsilon L)^{1/3}$, resulting in typical vorticity of $\varepsilon^{1/3} L^{-2/3}$, smaller than the threshold by a value $(\eta/L)^{2/3}$. The mechanism has been identified by [66]. It is based on the observation that in the inviscid limit, both vorticity ω_i and lines ℓ_i are dynamically stretched by the velocity field, according to

$$\partial_t A_i + u_j \partial_j A_i = A_j \partial_j u_i, \quad (8.3)$$

where $A_i = \omega_i$ or ℓ_i . In a first approximation, let us ignore viscosity and concentrate on the Lagrangian kinematic of vorticity in the frame where the tensor $\partial_j u_i$ is diagonal $\partial_j u_i = \text{Diag}(\lambda_1, \lambda_2, \lambda_3)$, with $|\lambda_1| \geq |\lambda_2| \geq |\lambda_3|$. Due to incompressibility, $\lambda_1 + \lambda_2 + \lambda_3 = 0$, so that either all the λ_i are real, and $\lambda_1 \lambda_3 \leq 0$ or one is real, equal say to λ_1 , and two complex conjugate, equal to $\lambda_2 = \lambda_3^*$, with $\lambda_1 \times \text{real}(\lambda_2) \leq 0$. In such frame, the kinematic behavior associated with (8.4) is simply

$$D_t A_i = \text{Diag}(\lambda_1 A_1, \lambda_2 A_2, \lambda_3 A_3). \quad (8.4)$$

A blob of initial vorticity $(\omega_1, \omega_2, \omega_3)$ with characteristic dimension $(\delta_1, \delta_2, \delta_3)$ will experience two processes: its magnitude along the direction corresponding to the eigenvalue with largest positive real part (say λ_1) will be exponentially amplified $\omega_1 = \exp(\lambda_1 t)$, while its dimension along the direction corresponding to the eigenvalue with largest negative real part (say λ_3) will be exponentially compressed $\delta_3 = \exp(-|\lambda_3|t)$. During such process, the maximum vorticity ω_{max} will then scale like

$$\omega_{max} = \delta_3^{h_\omega}, \quad (8.5)$$

with $h_\omega = -\lambda_1/|\lambda_3|$. Direct numerical simulations of this inviscid kinematic stage are difficult, since they require tracking of exponentially decreasing scales. A clear observation of this amplification process in a vorticity pancake was achieved recently, using combined high resolution direct numerical simulations[1], and vortex line dynamics [2]. They observe the scaling of equation (8.5), with $h_\omega = -\lambda_1/|\lambda_3| \approx -0.66$. This kinematic amplification cannot hold indefinitely, since there are at least two limiting processes: viscosity and self-stretching. They arise as soon as either the smallest scale reaches the Kolmogorov scale or when the vorticity produces a local self-stretching that can oppose the velocity field stretching. This produces for example a rotation of vorticity field that becomes aligned with the eigenvalue of intermediate magnitude [58], thereby saturating the vorticity amplification.

If we assume that the maximum vorticity is attained when the smallest scale reaches $\delta_3 \sim \eta$, the Kolmogorov scale, we observe that the the vorticity amplification mechanism discovered by [2] results in $\omega_{max} \sim \eta^{-2/3}$, i.e. precisely the scaling required by the Kolmogorov cascade picture and corresponding to a 1/3 rescaling symmetry for the velocity field. Such mechanism requires that the eigenvalues of the tensor $\partial_j u_i$ are in a ratio $[2 : 1 : -3]$. This ratio has indeed been reported to occur frequently in turbulent flows, but other frequent ratios, such as $[3 : 1 : -4]$ have also been reported [62], which would correspond to $h_\omega = -3/4$ (1/4 rescaling symmetry for the velocity field) if the same kind of mechanism holds. This would mean that $h = 1/3$ is not the only special exponent in a turbulent flow, and this would explain why we see other exponents appearing in the scaling behavior of the standard deviations of the cascade components Π_ℓ^I and Π_ℓ^V (figure 7.4-b).

Are there more indications of the existence of a multiplicity relevant scaling exponents h ? To answer this question, we need to explore local scaling properties of the velocity field.

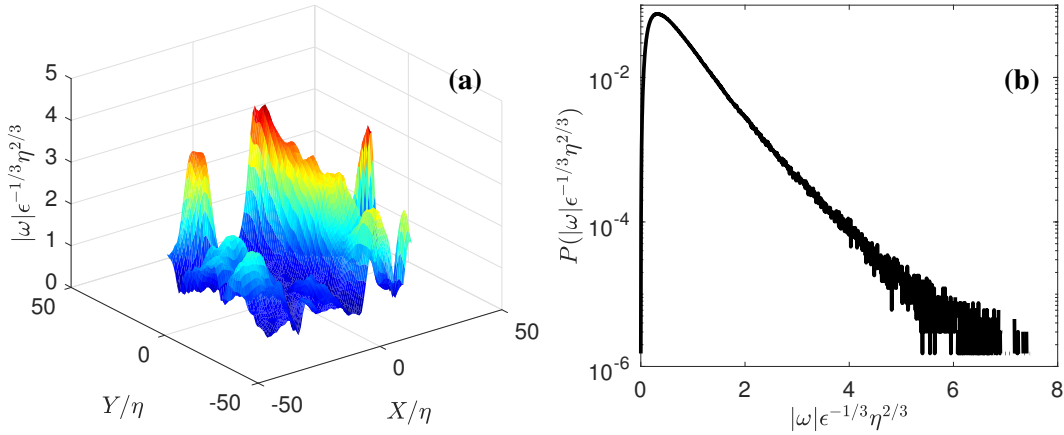


Figure 8.2: Non-dimensional vorticity magnitude (a) and PDF of non-dimensional vorticity magnitude (b) in the experiment CONC-3D. The figures are drawn using unpublished data collected by the EXPLOIT collaboration (F. Daviaud, B. Dubrulle, P. Debue, V. Valori, J-P. Laval, J-M. Foucaut, Ch. Cuvier, Y. Ostovan), with permission.

8.5 Global scale symmetry breaking and intermittency

As pointed out by [51], a natural tool to characterize local scaling properties of the velocity field is the wavelet transform of the tensor $\partial_j u_i$, defined as

$$G_{ij}(\mathbf{x}, \mathbf{r}) = \int d\mathbf{r} \nabla_{\mathbf{j}} \square_{\ell}(\mathbf{r}) \mathbf{u}_i(\mathbf{x} + \mathbf{r}), \quad (8.6)$$

where $\Phi_{\ell}(x) = \ell^{-3}\Phi(x/\ell)$ is a smooth function, nonnegative with unit integral. For all applications in the sequel, we choose a Gaussian function $\Psi(\vec{x}) = \exp(-x^2/2\ell^2)/N$ where N is the normalization constant such that $\int d\mathbf{x} \square(\mathbf{x}) = \mathbf{1}$. We then compute the wavelet velocity increments as

$$\delta W(\mathbf{u})(\mathbf{x}, \ell) = \ell \max_{ij} |\mathbf{G}_{ij}(\mathbf{x}, \mathbf{r})|, \quad \ell = |\mathbf{r}|. \quad (8.7)$$

As shown in [51], if the velocity field satisfies locally the h rescaling symmetry, then $\delta W(\mathbf{u})(\mathbf{x}, \ell) \sim \ell^h$. Due to the observed inhomogeneity of the velocity field derivatives (see Section 8.3), the direct validation of this property via local fit of $\delta W(\mathbf{u})(\mathbf{x}, \ell)$ is not possible in turbulent fields. Instead, one can look for statistical signatures of the h rescaling symmetry via scaling properties of the PDF of $\delta W(\mathbf{u})(\mathbf{x}, \ell)$. As shown in figure 8.3-a, this PDF is non Gaussian, with fat tails that vary with the scale ℓ . Both their mean and their standard deviation follow a $\ell^{1/3}$ scaling (figure 8.4-a) with tiny deviations. This is suggestive of a $1/3$ rescaling symmetry. A closer inspection of the ratio of the std to the mean (figure 8.1-b) shows that it is however not constant, suggesting a breaking of the $1/3$ rescaling symmetry. This is confirmed by a plot of centered and reduced PDFs of $\delta W(\mathbf{u})(\mathbf{x}, \ell)$, that do not collapse on a single curve, as evidenced in figure 8.3-a1: the tails become increasingly wider as scale decreases, showing that some small scale process is responsible for the breaking of the $1/3$ rescaling symmetry.

A quantitative measure of this effect is provided by the structure functions $\mathcal{S}_p = \langle (\delta W)^p \rangle$. If the $1/3$ rescaling symmetry holds exactly, one expects them to be power-law, $\mathcal{S}_p \sim \ell^{\zeta(p)}$, with $\zeta(p) = p/3$. These quantities are plotted on figure 8.5-a, for $p = 1$ to 6. One sees that they indeed follow a power-law with an exponent that is displayed in figure 8.6-a. It is increasing with p and deviates further from the straight line $p/3$ as p increases. Note that we find $\zeta(3) = 0.8$ and not $\zeta(3) = 1$ that would naively been expected from K41. Indeed, the prediction of K41 is only

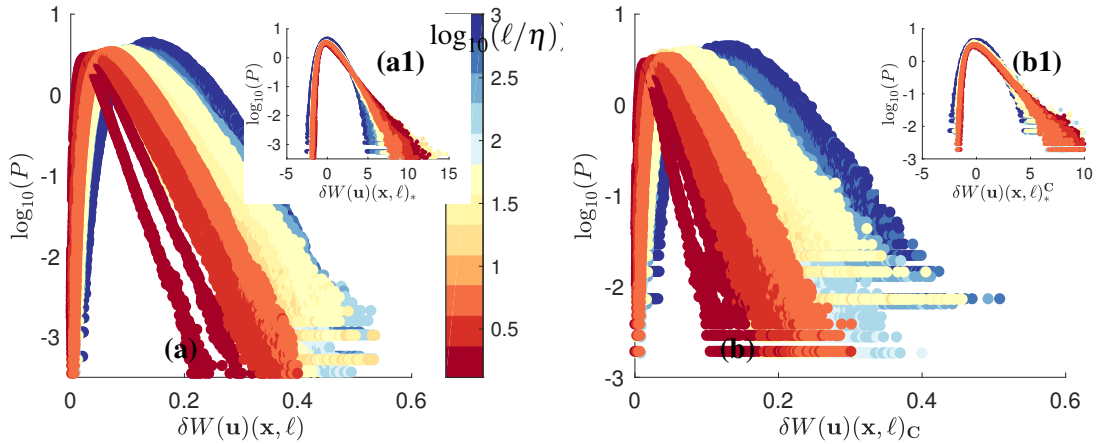


Figure 8.3: PDF's of wavelet velocity increments at different scale, coded by color, for experiments ANTIG and ANTIC-1 to ANTIC-4 (see figure 8.4 for corresponding mean and standard deviation and Table 1 for symbols). a) PDF of δW . Inset a1): Centered and reduced PDF of δW at different scale, i.e. PDF of $\delta W_* = (\delta W - \langle \delta W \rangle)/\text{std}(\delta W)$. b) PDF of δW^C corresponding to δW conditioned on locations of low of $|\mathcal{D}_{\Delta x}^1|$. Inset b1): Reduced and centered PDF of δW^C .

for the scaling of the velocity increment of order 3. Here, $\zeta(3)$ corresponds to the scaling of the absolute value of the wavelet increment. There is no prediction for this quantity in K41. However, we can note that if we consider a rescaled scaling exponent, $\zeta_r(p) = \zeta(p)/\zeta(3)$ ¹, we guarantee that $\zeta_r(3) = 1$, and we obtain something that appears to be more universal [3]. The deviation from the Kolmogorov law of the scaling exponent, $\xi^V = \zeta(p) - p/3$, is shown in figure 9.3-b. It is well fitted by a parabola.

Such a shape is puzzling, and implies strange pathologies for values of δW that deviates strongly from the mean, as noted in [29]. A way to study their behavior is through the function $U(p, \ell) = \langle (\delta W)^{p+1} \rangle / \langle (\delta W)^p \rangle$. Indeed, as p increases, this function samples values of δW that deviate increasingly from the mean. Taking into account the observed scaling properties of δW , we get the scaling $U(p, \ell) \sim \ell^{\Delta(p)}$ with $\Delta(p) = 1/3 + \xi^V(p+1) - \xi^V(p)$ which becomes negative as soon as $p > p_* \approx 9$. This means that if we take first the limit $v \rightarrow 0$ and then $\ell \rightarrow 0$, the corresponding values $U(p > p_*, \ell)$ can take arbitrary large values. This is another indication that the process that is responsible for the breaking of the global symmetry occurs at small scale, and involves very large values of the velocity gradients, in the limit $v \rightarrow 0$. Where does this phenomenon come from?

8.6 Time reversal breaking and enstrophy blow up

Let us come back to the enstrophy balance (8.2) - a by-product of the cascade picture- and explore its consequences as we let $v \rightarrow 0$. For this, we need to characterize the behavior of ε , the rate of injected power, as a function of the viscosity v . In the von Karman flow (figure 1b), where the fluid is forced by rotating paddles, this has been done recently using measurements in experiments with the same geometry, but different fluids and tank size [60]. It was found that ε depends on the fluid viscosity v and on the geometry, size L and rotation velocity Ω of the paddle. However, a remarkable universality appears in the limit of large Reynolds numbers, $Re = L^2\Omega/v$, where the flow becomes turbulent. In this limit, the energy injection rate becomes independent of viscosity,

¹This is the exponent we may get by looking at the scaling of S_p vs S_3 , a technique called extended self-similarity [5].

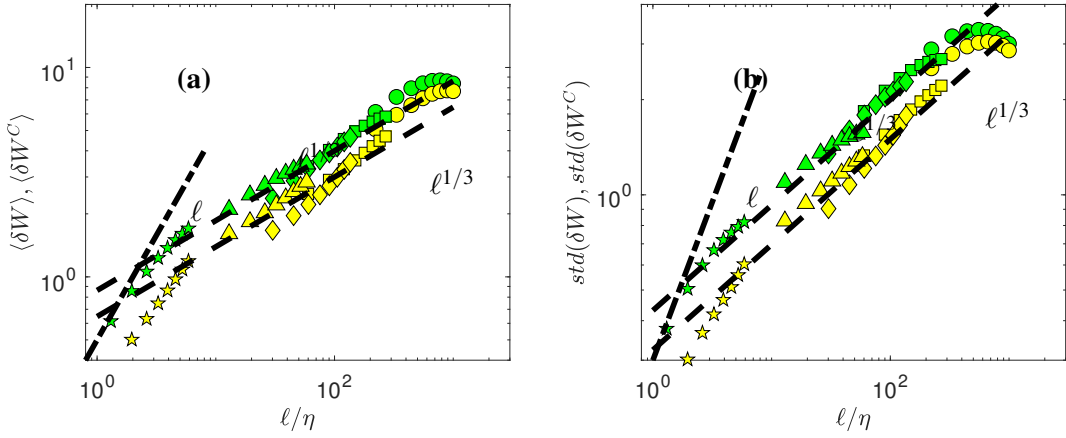


Figure 8.4: Scale variation of the mean and standard deviations of the PDFs of wavelet velocity increments for experiments ANTIG and ANTIC-1 to ANTIC-4 . a) Average: $\langle \delta W \rangle$: green symbols; $\langle \delta W^C \rangle$: yellow symbols . b) Standard deviation $std(\delta W)$: green symbols; $std(\delta W^C)$: yellow symbols.

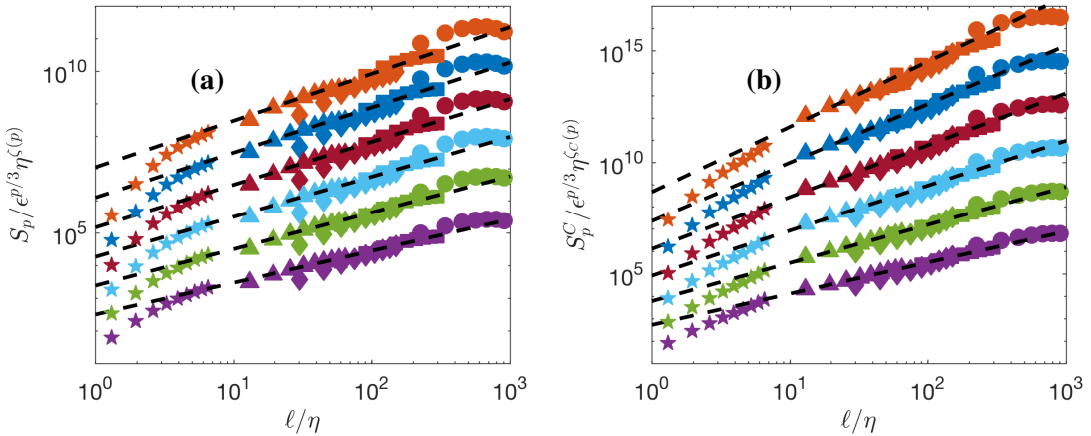


Figure 8.5: Scale variation of the non-dimensional wavelet structure function of order $p = 1$ to $p = 6$ for experiments ANTIG and ANTIC-1 to ANTIC-4 . The structure functions have been shifted by arbitrary factors for clarity and are coded by color: $p = 1$: magenta symbols; $p = 2$: green symbols; $p = 3$: light blue symbols; $p = 4$: red symbols; $p = 5$: blue symbols; $p = 6$: orange symbols. . a) Structure functions for δW . b) Structure functions for δW^C corresponding to δW conditioned on locations of low of local energy transfer at the resolution scale $|\mathcal{D}_{\Delta x}^I|$. The dashed lines are power laws with exponents shown in figure 8.6-a. Adapted from [15].

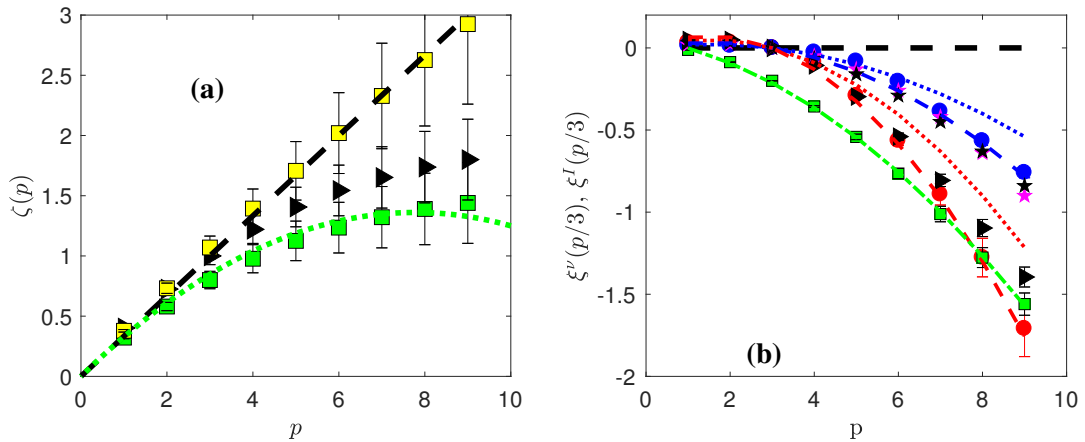


Figure 8.6: Scaling exponents as a function of order for experiments ANTIG and ANTIC-1 to ANTIC-4. a) Scaling exponents $\zeta(p)$ of the wavelet structure functions of δW (green symbols) and δW^C (yellow symbols). The exponents have been computed through a least square algorithm upon $\zeta(p)$, minimizing the scatter of the non-dimensional structure functions of different experiments with respect to the line $(\ell/\eta)^{\zeta(p)}$. The green dotted line is the function $\min_h(hp + C(h))$ with $C(h)$ given in figure 12.2-a. The black triangles are the rescaled scaling exponents $\zeta_r(p) = \zeta(p)/\zeta(3)$. b) Scaling exponents of the structure function of $|\mathcal{D}_1^I|$ and of $|\mathcal{D}_1^V|$: $\xi^I(p/3)$: red circle; $\xi^V(p/3)$: blue circle. The red dotted (resp. dashed) lines are log-normal fits $\xi^I(p) = 9bp(1-p)/2$ with $b = 0.045$ (resp. 0.065). The blue dotted (resp. dashed) lines are log-normal fits $\xi^V(p) = 2bp - 2bp^2$ with $b = 0.045$ (resp. 0.065). For comparison, we also reported other scaling exponents: $\xi^V = \zeta(p) - p/3$ (green squares); $\tau_{rsh} = \zeta(p) - \zeta(3)p/3$ (black triangles); $\tau_e(p/3)$ for DNS (black stars) and experiment ANTIC-4 (magenta stars), computed from figure 9.3. The green dot-dashed line is a parabolic fit : $\xi^V = -0.015p^2 - 0.046p + 0.06$. Adapted from [15].

and scales like

$$\lim_{Re \rightarrow \infty} \varepsilon = 2K_p L^2 \Omega^3, \quad (8.8)$$

where K_p is a parameter that only depends on the geometry of the paddles for a given the topology of the mean flow (figure 8.7). This universality carries on to the $Re = \infty$ limit as proved by recent experiments using super-fluid Helium 4 at low temperature [60]. The behavior described in (8.8) is well known in the turbulence community and is one of the most robust laws in turbulence. It is sometimes referred to as the *zeroth law of turbulence*. It is however a rather puzzling law: in the cascade picture, all injected energy is dissipated into heat, i.e. into entropy. Production of entropy is natural in a dissipative system, and is the signature of the breaking of the time reversal symmetry- in the langage of statistical physics, we would call it an order parameter of the time reversal symmetry. As we have seen in Section 8.1, this symmetry is explicitly broken by viscosity. Then, the zeroth law of turbulence means that in a turbulent fluid, at large Reynolds numbers, the order parameter becomes independent of the process that breaks the symmetry. In statistical physics, this behavior is referred to as a *spontaneous symmetry breaking*, while in modern field theory langage, it is called an *anomaly* [28], so that the constancy of $\varepsilon/L^2\Omega^3$ is called the *dissipation anomaly*.

This anomaly has important physical implication in the fluid. When plugged into the enstrophy balance (8.2), it leads to $\lim_{v \rightarrow 0} \Omega = \infty$ i.e. enstrophy blow-up. This means that there is at least one location in the flow where the vorticity becomes infinite, i.e. that there is a singularity in the flow in the inviscid limit. This conclusion may be disturbing for physicists, but not so much for mathematicians, who have been hunting singularities in Navier-Stokes and its inviscid limit, the Euler equation, for almost a century, starting from [43]. In any case, it is an indication that suitable mathematical tools should be used to understand in greater details the physics of turbulence. This will be the topic of Section 10.

Before that, we note that the enstrophy blow-up in the inviscid limit is a very strong argument against the universality of small-scale statistics K41 theory, as noted by Landau. Indeed, K41 assumes that everything only depends on the viscosity v and on ε , the mean energy dissipation rate. The enstrophy blow-up in the inviscid limit means that the energy dissipation is subject to large statistical fluctuations that are not necessarily universal, as can be directly observed from figure 7.3-b1 where the distribution of the energy dissipation displays wide tails. This means that the fluctuations of the energy dissipation cannot be ignored and may break the universality of K41. This remark led Obukhov and [38] to build a "refined" theory (hereafter named K62) that takes explicitly into account these fluctuations.

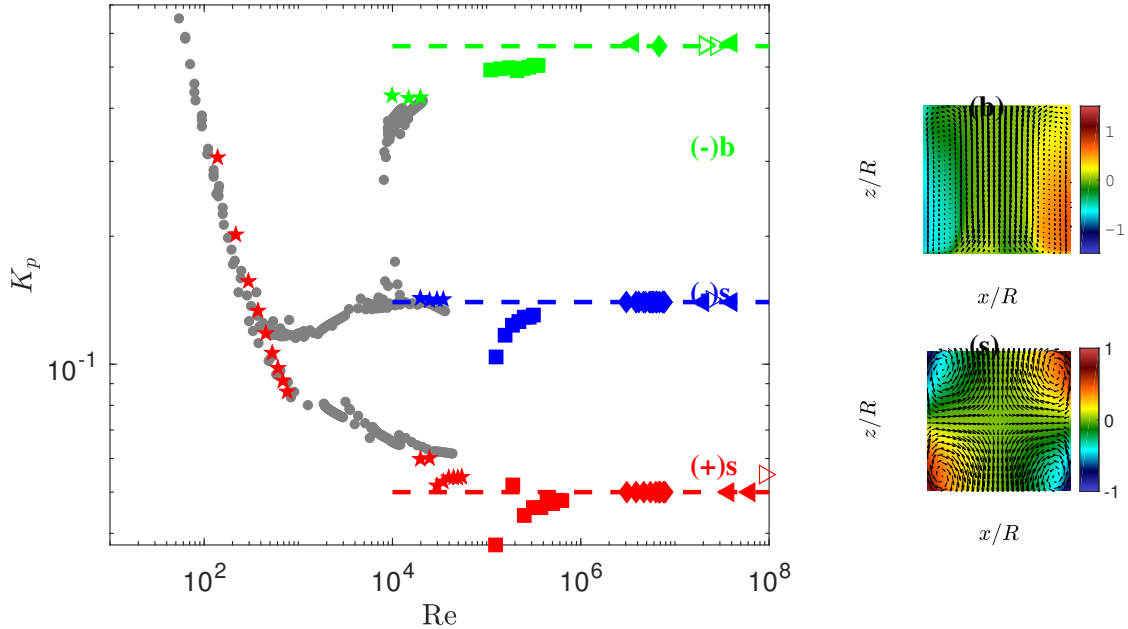


Figure 8.7: Non-dimensional energy injection rate $\varepsilon/2L^2\Omega^3$ as a function of Reynolds number Re in von Karman flow using different fluids and different forcing in different experiments. For $Re > 10^4$, the mean flow is bistable for the $(-)$ forcing, and displays two different topology: (i) a symmetric one, noted (s) , shown on the right-south of the main figure; (ii) a non symmetric one, noted (b) shown on the right-north of the main figure. For a given $(-)$ forcing, the energy injection rate is much higher if the flow is in (b) topology than in the (s) topology. The color codes the various forcing and flow topology: Red symbols: $(+)$ forcing according to figure 1.3-c, with symmetric mean flow topology; Blue and green symbols: $(-)$ forcing in respectively symmetric and bifurcated mean flow topology. The symbols code the fluid: pentagones: mixture of water and glycerol, at different concentration; square: water; diamonds: liquid sodium; left pointing arrows: Helium 4 at $T = 2.3K$. Right pointing arrows: Helium 4 at $T = 2K$, i.e. in its superfluid phase. The grey symbols are measurements performed in mixture of water and glycerol, with impellers similar to the one shown in figure 1.3-c, except that they are fitted with 16 blades, instead of 8. The diamonds are unpublished data from the VKS experiment. Courtesy VKS collaboration (M. Faure, N. Bonnefoy, S. Miralles, N. Plihon, J-F. Pinton, Ph. Odier, G. Verhille, M. Bourgoin, S. Fauve, F. Petrelis, M. Berhanu, N. Mordant, B. Gallet, S. Aumaitre, F. Daviaud, A. Chiffaudel, R. Monchaux, P. Gutierrez). The arrows are obtained from data from the SHREK experiment, with special help from B. Rousset. Adapted from Saint-Michel PhD thesis.

9. The Kolmogorov-Obukhov refined similarity hypothesis

9.1 Summary of the theory K62

Kolmogorov considers the quantity ε_ℓ , defined as the viscous dissipation ε_v averaged over a ball of size ℓ and assumes further that ε_ℓ has a log-normal distribution, with mean and variance of log given by

$$\overline{\varepsilon_\ell} = \varepsilon, \quad \forall \ell, \quad \eta \leq \ell \leq L, \quad (9.1)$$

$$\sigma^2(\ln(\varepsilon_\ell)) = -2A - 2\mu_{K62} \ln(\ell/L), \quad (9.2)$$

where A is a non-universal constant, that depends on the flow geometry, and μ_{K62} is a universal constant, that characterizes the fluctuations. Since the characteristic function of $\ln \varepsilon_\ell$ gives the moments of ε and is quadratic for a Gaussian, it is straightforward to show that the two hypothesis result in a universal scaling for all moments of ε_ℓ according to

$$\overline{\varepsilon_\ell^p} \sim \varepsilon^p e^{p(1-p)A} \left(\frac{\ell}{L}\right)^{\mu_{K62} p(1-p)}. \quad (9.3)$$

From this, we can deduce the scaling law of two other interesting quantities:

$$\sigma^2(\varepsilon_\ell) \equiv \overline{\varepsilon_\ell^2} - \overline{\varepsilon_\ell}^2 = \varepsilon^2 e^{-2A} \left[\left(\frac{\ell}{L}\right)^{-2\mu_{K62}} - 1 \right], \quad (9.4)$$

$$\overline{\ln(\varepsilon_\ell)} \equiv \partial_p \left(\overline{\varepsilon_\ell^p} \right) |_{p=0} = \ln(\varepsilon) + \mu_{K62} \ln(\ell/L) + A. \quad (9.5)$$

Kolmogorov then postulates local universality, so that locally, all quantities only depends on ℓ , v and ε_ℓ . From this, he can define local velocity scales as $U_\ell = \ell^{1/3} \varepsilon_\ell^{1/3}$, dissipative scale $\eta_\ell = v^{3/4} \varepsilon_\ell^{-1/4}$ and Reynolds number $Re_\ell = \ell U_\ell / v = (\ell / \eta_\ell)^{4/3}$. He then obtains

$$\begin{aligned} \overline{(\delta u_\ell)^p} &= \overline{(\ell \varepsilon_\ell)^{p/3}}, \\ &= C_p (\ell \varepsilon)^{p/3} \left(\frac{\ell}{L}\right)^{\mu_{K62}(1-p/3)p/3}. \end{aligned} \quad (9.6)$$

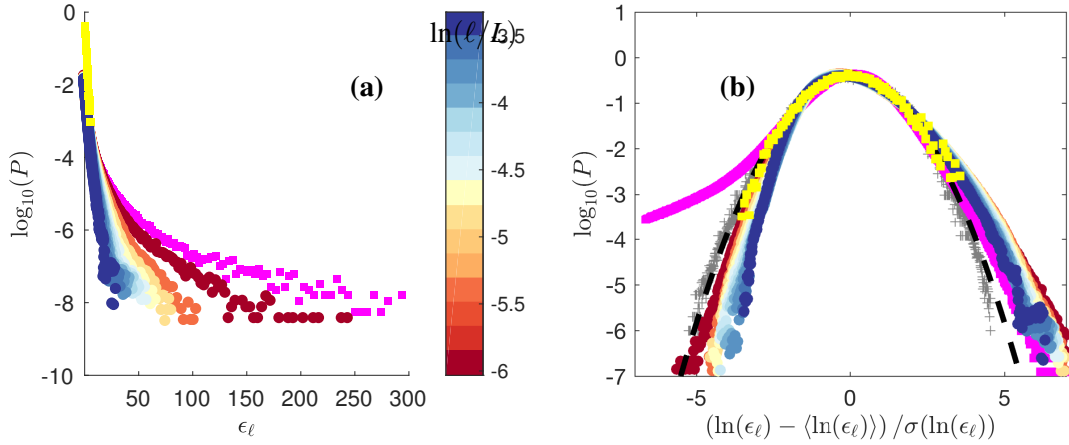


Figure 9.1: Probability distribution functions of the pseudo-energy dissipation averaged over a ball of size ℓ in experiment ANTIC-4 at various scale ℓ/L , coded by colors (see colorbar). The magenta squares are for the non-averaged pseudo-dissipation ϵ_v . The yellow symbols, for the time averaged pseudo-dissipation $P_{diss}/\rho L^3$. a) PDF of ϵ_ℓ . b) Centered reduced PDF of $\ln(\epsilon_\ell)$. The black dashed line is a log-normal with zero mean and unit variance. The grey crosses are centered and reduced distributions of ϵ_ℓ in DNS A, at scales corresponding to $\ell/L = 0$ and $\ell/L = n\eta/L$, with $n = 1, 3$ and 10.

The scaling of (9.6) means that the global self-similarity is broken, since the rescaled moments $\overline{(\delta u_\ell)^p} / \left(\overline{(\delta u_\ell)^3} \right)^{p/3}$ scale like $\ell^{\tau_{K62}(p)}$ with $\tau_{K62}(p) = \mu_{K62}(1 - p/3)p/3$. Moreover, it provides the origin of the symmetry breaking, as resulting from large fluctuations of the local energy dissipation rate over a ball of size ℓ . In such process, a new length scale (namely L) now appears to play a major role, contributing to scale symmetry breaking.

9.2 Test of refined similarity hypothesis

The refined similarity hypothesis can be tested easily on numerical data. The test with experimental data is more tricky, as it requires measurements of 3 components of velocities at a resolution at least equal to the Kolmogorov scale. Our SPIV data in glycerol are resolved down to the Kolmogorov scale, but they are not rigorously 3D, since they are measured only in a plane. They can however be used to compute a pseudo-energy dissipation as $\epsilon_v = -v(\partial_P u)^2$, where ∂_P means derivative taken only onto the plane of measurements. Given the local instantaneous energy dissipation $\epsilon_v(\mathbf{x}, t)$, an estimate of ϵ_ℓ is through a convolution through the smoothing function we used for wavelets

$$\epsilon_\ell(\mathbf{x}, t) = \int d\mathbf{r} \mathbf{\Pi}_\ell(\mathbf{r}) \epsilon_v(\mathbf{x} + \mathbf{r}, t), \quad (9.7)$$

$$\epsilon_v(\mathbf{x}, t) = v(\partial u)^2(x, t). \quad (9.8)$$

Observe that for $\ell \rightarrow 0$, $\epsilon_\ell \rightarrow \epsilon_v$ and that for $\ell \rightarrow L$ (L being the size of the volume containing the fluid, $\epsilon_\ell \rightarrow P_{diss}/\rho L^3$, the instantaneous energy dissipation rate).

The PDF of the resulting distributions, for various ℓ is provided in figure 9.1-a, along with the distribution of ϵ_v and $P_{diss}/\rho L^3$. One sees that they vary widely in shape, as ℓ is varied, with a variance decreasing as scale is increased. To test the hypothesis of K62, we compute the PDF of $\ln(\epsilon_\ell)$ for various ℓ/L , shown in figure 9.1-b. They are indeed close to parabolic, with deviations that could be due noise or projection effect. By comparison, the PDF of $\ln(\epsilon_\ell)$ for the numerical simulation DNS A is indeed perfectly parabolic, for all scales. To investigate the accuracy of K62

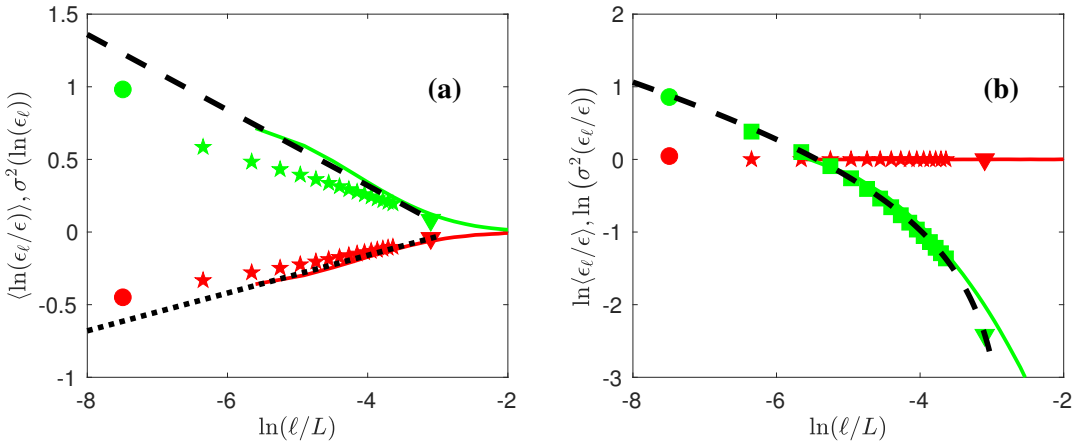


Figure 9.2: Mean (red symbols) and variances (green symbols) of PDF of a) ϵ_ℓ and b) $\ln(\epsilon_\ell)$ in experiment ANTIC-4 as a function of scale ℓ/L : circle: ϵ_V ; stars: ϵ_ℓ ; triangles: $P_{diss}/\rho L^3$. In a), the dashed line is a fit using the shape given by equation (9.4), with $\mu_{K62} = 0.13$ and $A = 0.36$. These two numbers are then used to compute the dotted (resp. the dashed line) in figure b), via (9.5) (resp. (9.2)). The colored full lines are obtained using the DNS A.

to describe the data, we compute the mean and variances of ϵ_ℓ and $\ln \epsilon_\ell$ and plot them as a function of ℓ/L in figures 9.2-a and 9.2-b, for both numerical and experimental data. The average of ϵ_ℓ is indeed constant (equation (9.1)), while its variance decreases and is well described by (9.4) using $\mu = 0.13$ and $A = 0.36$. With these two numbers, we can then fit the mean and variances of $\ln(\epsilon_\ell)$ using (9.5) and (9.2) without adjusting parameters. We see that the fit is fair for experiments, but rather good for the numerical data.

Consistency with K62, can be further checked by computing moments of higher order for ϵ_ℓ as a function of ℓ . They are reported in figure 9.3-a. In the inertial range $\ln(\ell/\eta) \geq 4$, they follow power-law $\langle (\epsilon_\ell)^{p/3} \rangle \sim \epsilon^{p/3} \ell^{\tau_\epsilon(p/3)}$, with $\tau_\epsilon(p/3)$ reported in figure 9.3-b for both experiments and DNS. They are parabolic, as suggested by K62, and well fitted by the exact log-normal shape $\tau_\epsilon(p/3) = \mu_{K62}(1 - p/3)p/3$, with $\mu_{K62} = 0.13$. The moments $\langle (\epsilon_\ell)^{p/3} \rangle$ can also be well fitted without adjustable parameter by (9.3), with μ_{K62} and A computed using variance of $\ln(\epsilon_\ell)$. From all this, we see that the log-normal hypothesis formulated by Kolmogorov is fairly well satisfied by numerical and experimental data.

However, when we compare $\tau_\epsilon(p/3)$ and $\xi^V = \zeta(p) - p/3$ computed from the wavelet analysis in section 8.5, we observe a rather large discrepancy, in contradiction with Kolmogorov refined similarity hypothesis (9.6). We can argue that the problem is due to the fact that $\zeta(3)$ is not equal to one (see section 8.5), meaning that $\xi^V(1)$ is not zero, as necessary in the refined scaling hypothesis. We may correct that by using $\tau_{rsh}(p/3) = \zeta(p) - \zeta(3)p/3$, which is indeed closer to $\tau_\epsilon(p/3)$, but there is still a discrepancy. Where does the problem come from?

9.3 Problems and issues set by K62

Let us come back to the mathematics behind K62. In the Kolmogorov cascade picture, the energy is transferred locally from a scale ℓ to a scale $\Gamma\ell$ ($\Gamma \leq 1$) in a self-similar way, so that the distribution of $\epsilon_\ell/\epsilon_{\Gamma\ell}$ only depend on the ratio of scales Γ . Writing $\epsilon_L/\epsilon_{\Gamma^N L} = (\epsilon_L/\epsilon_{\Gamma L}) \dots (\epsilon_{\Gamma^{N-1} L}/\epsilon_{\Gamma^N L})$, we see that for any $\ell = \Gamma^N L$, the quantity $\ln(\epsilon_\ell/\epsilon_L)$ is the sum of $N = \ln(L/\ell)/\ln(\Gamma)$ variables with identical distribution

$$\ln(\epsilon_\ell/\epsilon_L) = \sum_{n=1}^{\ln(L/\ell)/\ln(\Gamma)} \ln(\epsilon_{\Gamma^n L}/\epsilon_{\Gamma^{n-1} L}). \quad (9.9)$$

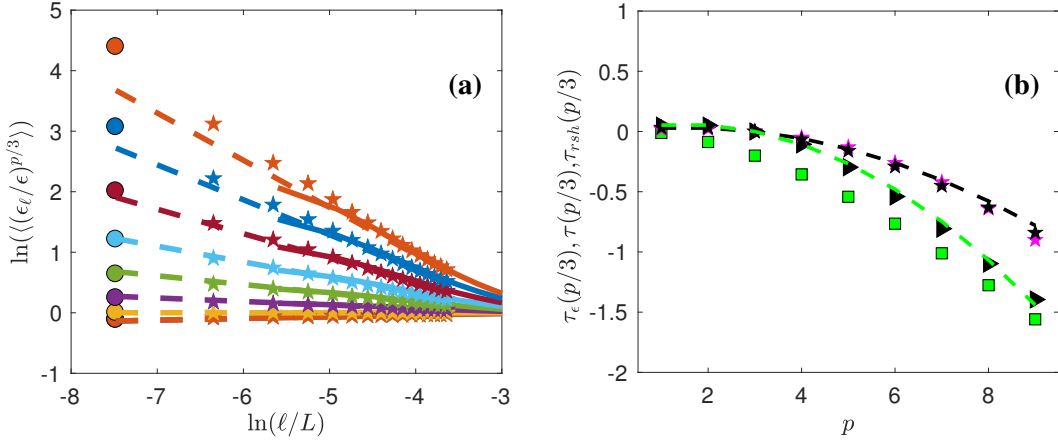


Figure 9.3: Test of refined similarity hypothesis. a) Structure functions of ε_ℓ as a function of ℓ/L in experiment ANTIC-4 (symbols): ℓ/L : circle; ε_v ; stars: ε_ℓ ; triangles: $P_{diss}/\rho L^3$, and in DNS A (continuous line). The structure functions are coded by color: $p = 1$: blue; $p = 2$: orange; $p = 3$: yellow; $p = 4$: magenta; $p = 5$: green; $p = 6$: light blue; $p = 7$: red; $p = 8$: blue; $p = 9$: orange. The colored dashed lines are (9.3), with μ_{K62} and A computed using variance of $\ln(\varepsilon_\ell)$. b) Scaling exponents of the structure functions: $\tau_\varepsilon(p/3)$ for experiment ANTIC-4 (magenta stars); for DNS A (black stars). The black dashed line is $\mu_{K62}(1 - p/3)p/3$, with $\mu_{K62} = 0.13$, obtained in figure 9.2. These values do not coincide with the quantity $\tau(p/3) = \zeta(p) - p/3$ (green squares), and $\tau_{rsh}(p/3) = \zeta(p) - \zeta(3)p/3$ (black triangles) inferred from figure 8.6-a using directly wavelet velocity increments, that are best fitted (green dotted line) by $\mu(1 - p/3)p/3$ with $\mu = 0.24 > \mu_{K62}$, in contradiction with K62.

When $N = \ln(L/\ell)/\ln(\Gamma) \rightarrow \infty$, and if the distributions are independent, we can then use large deviation theory (Kramer's theorem) [67] to write the probability of observing $\ln(\varepsilon_\ell/\varepsilon_L)$ as

$$P(\ln(\varepsilon_\ell/\varepsilon_L) = x) \sim e^{-NF(x/N)}, \quad (9.10)$$

where F is the large deviation function, that only depends on the distribution of $\varepsilon_\ell/\varepsilon_{\Gamma\ell}$. The highest probability (the most likely event) is obtained for the value x that is connected to the z^* , the location of the maximum value of F , via $x = Nz^*$. For values of x/N close to z^* , the function F is parabolic, so that $F(z) = F(z^*) + F''(z^*)(z - z^*)^2/2$ and

$$P(\ln(\varepsilon_\ell/\varepsilon_L) = x \approx z^* \ln(L/\ell)) \sim e^{-NF(z^*) - (F''(z^*)/N)(x - Nz^*)^2/2}, \quad (9.11)$$

corresponding to a log-normal distribution for $\varepsilon/\varepsilon_L$, with a variance $\ln(L/\ell)/F''(z^*)$. This is K62 theory, with $\mu_{K62} \propto 1/F''(z^*)$. However, for values far from the most probable value, the large deviation function F can differ from a parabola, and deviation from log-normal can be observed.

This argument is only valid provided the distribution of $\varepsilon_{\Gamma^{p-1}\ell}/\varepsilon_{\Gamma^p\ell}$ for different p are independent. If they are correlated, no general prediction about their sum can be given (see [12] for solvable examples), and one can obtain shapes different from log-normal. We thus see that the K62 theory is based on an idealized treatment of the fluctuations that does not necessarily reflect reality.

Another questionable assumption holds in the interpretation of equation (9.6), that allows us to connect the velocity structure function to the quantity ε_ℓ . Indeed, in the original K41 theory, ε_ℓ was inferred from KHM equation as the constant scale-to-scale energy transfer. This remark led [39] to suggest that if such a relation holds, ε_ℓ should represent some well-defined local energy flux Π_ℓ rather than a local energy dissipation averaged over a volume of linear dimension ℓ . Since K62 is not derived directly from the Navier-Stokes equations, it is not obvious how to define precisely

the expression and properties of Π_ℓ . To make further progress, we need to find a generalization of K41 that i) provides an expression of such local energy flux; ii) does not suffer from the main drawbacks of K41, namely that it does not assume homogeneity, nor stationarity, that allows for breaking of the time symmetry and iii) takes into account the fluctuations of energy dissipation and allows for the breaking of the self-similarity. This generalization was derived in 1990 by two French mathematicians, Duchon and Robert. The purpose of the next section is to summarize their derivation, and explore its outcomes.

10. Weak formulation of Karman-Howarth-Monin equation

10.1 Derivation of the weak Karman-Howarth-Monin equation

10.1.1 Why a weak formulation?

In previous sections, we have identified many clues about a pathological behavior of the velocity field in turbulent flows: development of large gradients, inhomogeneity and intermittency of the dissipation, spontaneous breaking of the time-reversal symmetry... Even the simple Kolmogorov picture involves lack of regularity for the velocity field. Indeed, we have

$$|\overline{\langle (\delta \mathbf{u})^3 \rangle}| \leq \overline{\langle |\delta \mathbf{u}|^3 \rangle}. \quad (10.1)$$

Let us further assume that there exist an h and a C , such that $\forall x$ and $\ell \leq \ell_0$

$$|\delta \mathbf{u}| \leq C\ell^h. \quad (10.2)$$

In mathematical langage, this means that the velocity field is uniform Hölder continuous with exponent h . Substituting in (10.1), we then see that

$$|\overline{\langle (\delta \mathbf{u})^3 \rangle}| \leq C^3 \ell^{3h}, \quad (10.3)$$

so that Kolmogorov scaling cannot be satisfied if $h > 1/3$, because $\overline{\langle (\delta \mathbf{u})^3 \rangle}$ will tend to zero always faster than ℓ . This means that there is at least one point in the flow where the inequality (10.2) with $h > 1/3$ is violated, possibly satisfied only with some $h \leq 1/3$. As we have seen previously, this means that the velocity field is not differentiable. We thus need to resort to weak formulation to treat this possibility, using the tools developed in Chapter xx.

In fact, the weak formulation, and its associated continuous wavelet transform, is the natural tool to generalize the KHM equation into a "local" version, that will help to go beyond K41 and K62. Let us now summarize the main steps of Duchon and Robert's derivation [24].

10.1.2 Summary of Duchon-Robert derivation

We first apply the wavelet transform to the Navier-Stokes equations (1.1), to get a classical coarse-grained equation

$$\partial_t u_i^\ell + u_j^\ell \partial_j u_i^\ell = -\partial_j \tau_{ij}^\ell - \frac{1}{\rho} \partial_i p^\ell + v \partial_{jj} u_i^\ell, \quad (10.4)$$

where $\tau_{ij}^\ell = (u_i u_j)^\ell - u_i^\ell u_j^\ell$ is the classical Reynolds stress tensor. We multiply equations (1.1) and (10.4) by u^ℓ and u , respectively, and add them together; after the rearrangement of terms we obtain the following balance equation:

$$\partial_t u_i u_i^\ell + \partial_i T_i = \mathcal{E}^\ell + v u_i \partial^2 u_i^\ell + v u_i^\ell \partial^2 u_i, \quad (10.5)$$

where

$$\begin{aligned} T_i &= u_j u_j^\ell u_i + (p^\ell u_i + p u_i^\ell) / \rho, \\ \mathcal{E}^\ell &= u_i u_j \partial_i u_j^\ell - u_j \partial_i (u_i u_j)^\ell. \end{aligned} \quad (10.6)$$

Developing terms and using properties of ϕ , it is simple to check that \mathcal{E}^ℓ can be split into

$$2\mathcal{E}^\ell = -\partial_i (u_i u_j u_j)^\ell + \partial_i (u_i (u_j u_j)^\ell) - \int d\xi \nabla \phi^\ell(\xi) \cdot \delta_\xi u (\delta_\xi u)^2, \quad (10.7)$$

where $\delta_\xi u$ is the velocity increment over a distance ξ and ∇ the gradient over ξ . We can also split

$$u_i^\ell \partial^2 u_i = \partial_j (u_i^\ell \partial_j u_i - u_i \partial_j u_i^\ell) + u_i \partial^2 u_i^\ell. \quad (10.8)$$

Finally, it is straightforward to check that

$$\frac{1}{2} \int d\xi \nabla^2 \phi^\ell(\xi) (\delta_\xi u)^2 = \frac{1}{2} \partial^2 (u_i u_i)^\ell - u_i \partial^2 u_i^\ell. \quad (10.9)$$

After the rearrangement of terms, we finally get a local balance equation for the quantity $E^\ell(x) \equiv u_i u_i^\ell / 2$ as:

$$\partial_t E^\ell(x) + \partial_j J_j = -\mathcal{D}_\ell^I - \mathcal{D}_\ell^V, \quad (10.10)$$

where

$$\begin{aligned} J_i &= u_i E^\ell + \frac{1}{2} (p^\ell u_i + p u_i^\ell) + \frac{1}{4} ([u_i u_j u_j]^\ell - u_i [u_j u_j]^\ell) \\ &\quad - v \partial_i (u_i^\ell \partial_j u_i - u_i \partial_j u_i^\ell), \end{aligned} \quad (10.11)$$

$$\mathcal{D}_\ell^I = \frac{1}{4} \int d\xi \nabla \phi^\ell(\xi) \cdot \delta_\xi u (\delta_\xi u)^2, \quad (10.12)$$

$$\mathcal{D}_\ell^V = \frac{v}{2} \int d\xi \nabla^2 \phi^\ell(\xi) (\delta_\xi u)^2. \quad (10.13)$$

We name such balance equation "weak KHM equation", denoted WKHM. Its physical interpretation is provided in section 10.2.2

10.2 Properties of WKHM

10.2.1 Robustness with respect to noise

WKHM is robust with respect to the addition of noise that is isotropic, Gaussian and not correlated to the velocity- this is often true for velocity measurements, in the absence of systematic errors. In such a case, the measured velocity increments can be simply written as $\delta \mathbf{u}_{meas} = \delta \mathbf{u} + \alpha$, where $\delta \mathbf{u}$ is the true velocity increment and α is the noise, such that for any (i, j, k) $\langle \alpha_i \rangle = \langle \alpha_i \alpha_j \alpha_k \rangle = 0$ and $\langle \alpha_i \alpha_j \rangle = \mathcal{N} \delta_{ij}$, where \mathcal{N} is the noise amplitude. Since we further have

$$\delta \mathbf{u}_{meas} | \delta \mathbf{u}_{meas} |^2 = \delta \mathbf{u} | \delta \mathbf{u} |^2 + \alpha | \delta \mathbf{u} |^2 + 2\delta \mathbf{u} (\alpha \cdot \delta \mathbf{u}) + 2\alpha (\alpha \cdot \delta \mathbf{u}) + \delta \mathbf{u} | \alpha |^2 + \delta \alpha | \delta \alpha |^2, \quad (10.14)$$

we get by statistical averaging

$$\langle \delta \mathbf{u}_{meas} | \delta \mathbf{u}_{meas} |^2 \rangle = \langle \delta \mathbf{u} | \delta \mathbf{u} |^2 \rangle + 3\mathcal{N} \langle \delta \mathbf{u} \rangle. \quad (10.15)$$

If the velocity field is statistically homogeneous at the considered location, then $\langle \delta \mathbf{u} \rangle = 0$, so that all the noise contribution has been averaged out and there is no noise amplification introduced by taking the divergence. In the same way, if the noise has no spatial correlation, the statistical average guarantees that the noise contribution is averaged out in $\langle (\delta \mathbf{u})^2 \rangle$, so that it can be differentiated twice without noise amplification.

In the weak formulation, the gradient is not applied directly to the velocity increments, but rather on the smooth test function, preceded by a local angle averaging. The latter plays a role similar to statistical averaging for isotropic noise. The convolution with the derivative of the smoothing function further guarantees that there is no noise amplification when computing \mathcal{D}_I^ℓ and \mathcal{D}_V^ℓ . This robustness with respect to noise makes the quantities \mathcal{D}_I^ℓ and \mathcal{D}_V^ℓ very interesting tools to characterize local energy transfers in laboratory flows using e.g. particle image velocimetry (PIV) measurements: it involves only velocity increments, which are easily computed from the velocity field data obtained by such technique. For numerical flows, the potential gain is not on noise, but rather on accuracy of description in regions where the velocity field presents sharp discontinuity or local strong variations, as illustrated in section 10.2.5.

10.2.2 Interpretation of WKHM as local KHM

Equation (10.10) describes the evolution of $E^\ell(\mathbf{x})$, the point-split kinetic energy at scale ℓ and at position \mathbf{x} , through three main ingredients: (1) a spatial flux term $\nabla \cdot \mathbf{J}$, which describes how the input energy is transported within the flow; (2) an inter-scale flux \mathcal{D}_ℓ^I , which describes how the energy cascades locally across the length scales; and (3) \mathcal{D}_ℓ^V , which describes energy space transfer and dissipation by viscosity. It is, in fact, a local non-random form of the classical KHM equation, as already recognized in [24]. To see that, we note that the quantity $E^\ell(\mathbf{x})$ can also be written as $E^\ell(\mathbf{x}) \equiv u_i u_i^\ell = (1/2) \int \phi^\ell(\xi) \mathbf{u}_i(\mathbf{x}) \mathbf{u}_i(\mathbf{x} + \xi) \mathbf{d}\xi$, which may be interpreted as a local average over a ball of size ℓ of the quantity $e(\mathbf{x}, \mathbf{r}) = u_i(\mathbf{x}) u_i(\mathbf{x} + \mathbf{r})$, i.e. the local equivalent of the correlation function of KHM equation, where the statistical average is replaced by a local average over scale. In the same way, the inter-scale flux term \mathcal{D}_ℓ^I can be written after integration by parts as

$$\mathcal{D}_\ell^I = -\frac{1}{4} \int d\xi \phi^\ell(\xi) \nabla_\xi \cdot \langle \delta_\xi \mathbf{u} (\delta_\xi \mathbf{u})^2 \rangle, \quad (10.16)$$

so that it is the local equivalent of Π_ℓ^I . Finally, we can perform two integrations by parts on the viscous term \mathcal{D}_ℓ^V to show that it is the local average over a ball of size ℓ of $v \nabla_r^2 e(\mathbf{x}, \mathbf{r})$ so that it

is the local equivalent of Π_ℓ^V . The spatial flux term $\nabla \cdot \mathbf{J}$ has no equivalent in KHM, because it describes purely local effect: it vanishes when integrated over space, if there are no input of energy at the flow boundary. However, if turbulence is forced by boundaries, like in a plane Couette flow, its space average will contribute to \mathcal{P}_ℓ , the mean energy injection rate at scale ℓ .

In the same way, we note that by space average, $\langle E^\ell(\mathbf{x}) \rangle_{\mathbf{x}} = \langle C(\mathbf{r}) \rangle_{\mathcal{B}_\ell}$, the average over a ball of size ℓ of the correlation function. In the same way, the space average of \mathcal{D}_ℓ^I and \mathcal{D}_ℓ^V are exactly the average over a ball of size ℓ of Π_ℓ^I and Π_ℓ^V . These are the quantities that are plotted in figure 7.2 for both numerical and experimental data, and that are shown to obey, on average over the space, the classical K41 scaling. Being local in space and time, \mathcal{D}_ℓ^I and \mathcal{D}_ℓ^V are however natural candidates to trace and understand dynamics of energy cascades and dissipation in turbulent flows, and their link with symmetry breaking and intermittency, as we see now.

10.2.3 Small scale limit

WKHM allows us to define energy transfers and dissipation for any given scale ℓ . Before investigating their properties at various scales, let us focus on their limit $\ell \rightarrow 0$, which involves mathematical subtleties due to the possible roughness of the velocity field. Consider for example the limit of \mathbf{u}^ℓ . By construction, we have

$$\mathbf{u}^\ell(\mathbf{x}) = \int d\xi \phi^\ell(\xi) \mathbf{u}(\mathbf{x} + \xi) = \mathbf{u}(\mathbf{x}) + \int d\xi \phi^\ell(\xi) \delta_\xi \mathbf{u}. \quad (10.17)$$

At all points \mathbf{x} where \mathbf{u} is regular, we have $\delta_\xi \mathbf{u} = \xi \cdot \partial \mathbf{u} + O((\xi)^2)$, so that for sufficiently small ℓ , $\mathbf{u}^\ell(\mathbf{x}) = \mathbf{u}(\mathbf{x}) + O(\ell)$. There is therefore no problem to take the small scale limit of \mathbf{u}^ℓ , and we have $\lim_{\ell \rightarrow 0} \mathbf{u}^\ell(\mathbf{x}) = \mathbf{u}(\mathbf{x})$. When the velocity field is rough, the limit is less trivial. At such points, we define the Hölder exponent $h < 1$ (depending upon the considered point) such that the velocity field obeys the condition

$$\exists C \quad \forall \ell \leq \ell_0, \quad |\delta_\ell \mathbf{u}(\mathbf{x})| \leq C \ell^h. \quad (10.18)$$

Substituting this into (10.17), we now see that for sufficiently small ℓ , $\mathbf{u}^\ell(\mathbf{x}) = \mathbf{u}(\mathbf{x}) + O(\ell^h)$. So, as long as $h \geq 0$ -this includes the case $h = 1/3$ corresponding to K41-, the small scale limit of $\mathbf{u}^\ell(\mathbf{x})$ is still simple and equal to $\mathbf{u}(\mathbf{x})$. Things become more delicate for quantities involving derivatives, as they may now behave wildly in the small scale limit. We have indeed

$$\begin{aligned} \partial \mathbf{u}^\ell(\mathbf{x}) &= \int d\xi \phi^\ell(\xi) \partial \mathbf{u}(\mathbf{x} + \xi) = \int d\xi \phi^\ell(\xi) \nabla (\mathbf{u}(\mathbf{x} + \xi) - \mathbf{u}(\mathbf{x})), \\ &= - \int d\xi \nabla \phi^\ell(\xi) \delta_\xi \mathbf{u}(\mathbf{x}) = O(\ell^{h-1}). \end{aligned} \quad (10.19)$$

Therefore, for $h < 1$, the derivative $\partial \mathbf{u}^\ell(\mathbf{x})$ is unbounded and its limit (if it exists), noted $\partial \mathbf{u}(\mathbf{x})$ may be infinite. Using equation (10.18), we then get

$$\mathcal{D}_\ell^V = O(v \ell^{2h-2}), \quad (10.20)$$

$$\mathcal{D}_\ell^I = O(\ell^{3h-1}). \quad (10.21)$$

The limit of the viscous term is

$$\lim_{\ell \rightarrow 0} \mathcal{D}_\ell^V = \varepsilon_v, \quad (10.22)$$

where $\varepsilon_v = v(\partial \mathbf{u})^2$ is the local viscous dissipation (potentially infinite if $\partial \mathbf{u}$ is infinite). We call $\mathcal{D}^I = \lim_{\ell \rightarrow 0} \mathcal{D}_\ell^I$. From equation (10.21), we see that $\mathcal{D}^I = 0$ whenever $h > 1/3$. For $h \leq 1/3$, it is possible that \mathcal{D}^I is non zero. What does it mean?

$130\mathcal{D}_\ell^I/\varepsilon$

Figure 10.1: b) Space/scale diagram of the non-dimensional local energy transfer $\mathcal{D}_\ell^I/\varepsilon$ for the Khokhlov saw tooth solution. The intensity of $\mathcal{D}_\ell^I/\varepsilon$ is coded in colour, following the colorbar.

10.2.4 Inertial dissipation and Onsager's conjecture

Consider WKHM and perform first the limit $v \rightarrow 0$, and then $\ell \rightarrow 0$. From previous estimates (10.17), (10.19) and (10.21), we then get

$$\frac{1}{2}\partial_t u^2 + \partial \left(\frac{1}{2}u^3 + pu \right) = -\mathcal{D}^I. \quad (10.23)$$

This local energy budget shows that even in the absence of viscosity, the energy is not conserved and can be changed by the term \mathcal{D}^I , emerging from the roughness of the velocity field. If $\mathcal{D}^I > 0$, we can rephrase this observation into Onsager's own words [55] as: *in three dimensions a mechanism for complete dissipation of all kinetic energy, even without the aid of viscosity, is available*. Lars Onsager was the first to make the connection between the regularity properties of the velocity field and kinetic energy conservation in the Euler equations. His finding remained unnoticed for a long time [27]. It was not until 2000 that Duchon and Robert brought the attention of the turbulent community on this mechanism and named it "inertial dissipation". They proved that in 2D, $\mathcal{D}^I = 0$. In 3D, the condition of existence of a suitable weak solution only implies that the spatial average $\langle \mathcal{D}^I \rangle \geq 0$. Note that, because of (10.21), $h = 1/3$, the Kolmogorov value, is the maximum regularity condition compatible with a nonzero inertial dissipation. This provides another indication of why this value is so special in turbulence.

10.2.5 Illustration: inertial dissipation by a shock

A simple illustration of the concept of inertial dissipation can be given using the "Khokhlov saw-tooth solution" (4.3). As we saw previously Formally, the shock is a singularity with Hölder exponent $h = 0$. Plugging this into (10.12), we see that $\mathcal{D}_\ell^I = O(\ell^2)$ for x outside the range $[-\ell, \ell]$ and $\mathcal{D}_\ell^I \propto (\Delta u)^3/L + O(\ell^2)$ for $x \in [-\ell, \ell]$, so that $\mathcal{D}^I \propto (\Delta u)^3/L > 0$: the shock dissipates energy. Exact calculations (see e.g. [26]) show that $\mathcal{D}^I = (\Delta u)^3/12L = \varepsilon$, where $\varepsilon = \lim_{v \rightarrow 0} v(\partial u^v)^2$, so that the discontinuity dissipates exactly the same energy as the viscous solution. Figure 10.1-b shows the space/scale diagram of the local energy transfer \mathcal{D}_ℓ^I for the shock solution. One sees that at a given scale, it is concentrated on the range $[-\ell, \ell]$ around the shock. As ℓ decreases, \mathcal{D}_ℓ^I concentrates more and more around the shock, "pointing" the singularity. If we now look at the behaviour of $\mathcal{D}_\ell^I(0)$ with ℓ - the amplitude of the local energy transfer at the singularity point- we see that it diverges like $1/\ell$, i.e. $\mathcal{D}_\ell^I(0) \sim \ell^{3h-1}$ with $h = 0$ (figure 10.2-a). Its space average converges towards ε like $\langle \mathcal{D}_\ell^I \rangle - \varepsilon \sim \ell$ (figure 10.2-b), which corresponds to the probability of hitting a point like singularity (codimension 1). By looking at the behaviour of \mathcal{D}_ℓ^I with decreasing scale, one sees that it is possible to infer where there is a singularity, what is its Hölder exponent and its probability.

10.2.6 Effects of viscosity and resolution

In the previous section, we discussed the properties of the energy transfer and inertial dissipation around an exact singularity. How is this picture changed for a quasi-singularity, i.e. a singularity that is smoothed (regularized) by the introduction of viscosity? To answer this question, we can again take the shock as an illustration. We consider the energy transfer for the finite viscosity solution $u^v(x, t)$ for two values of v , corresponding to a very smooth solution (large viscosity) and a nearly singular solution (small viscosity), for which the length of variation of the velocity near the jump has a size comparable to the resolution, see figure 10.1-a. The space/scale diagram for the

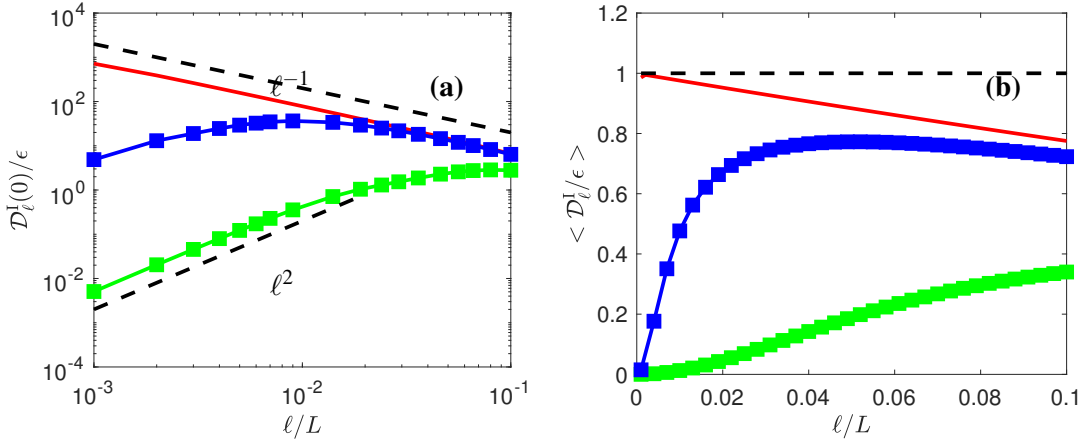


Figure 10.2: Properties of the local energy transfers for the Khokhlov (red) and viscous solutions (blue: $\nu = 1/100$; green: $\nu = 1/10$) of Burgers equation shown in figure 10.1-a. a) $\mathcal{D}_\ell^I(0)/\epsilon$ as a function of scale ℓ . Note that $\mathcal{D}_\ell^I(0)/\epsilon$ is the maximum of $\mathcal{D}_\ell^I(x)/\epsilon$ over the interval $[-L, L]$. b) Average of $\mathcal{D}_\ell^I(x)/\epsilon$ over the interval $[-L, L]$ as a function of scale ℓ .

local energy transfer \mathcal{D}_ℓ^I for these two solutions depends on the viscosity. For the nearly singular solution, it is very similar to the space/scale diagram of the singular solution (not shown). For larger viscosity, one starts observing differences, as illustrated in figure 10.3-a: the intensity of the signal is smaller, and decreases towards zero at sufficiently small scale. A quantification of this effect can be obtained by looking at the values of the inertial dissipation at the shock, represented by $\mathcal{D}_\ell^I(0)$ and the mean value of the inertial dissipation, represented by $\langle \mathcal{D}_\ell^I \rangle$. They are reported on figure 10.2 for the two cases. We see that in both cases, $\mathcal{D}_\ell^I(0)$ tends to 0 as $\ell \rightarrow 0$, meaning that the inertial dissipation is zero. This is natural, since both solutions are regular (see section 10.2.3). Also, looking at $\langle \mathcal{D}_\ell^I \rangle$, we see that it converges to zero like ℓ^2 for the more regular solution. The less regular solution does not satisfy this scaling, because one would need a resolution smaller than the size of the velocity variation to observe this. However, $\mathcal{D}_\ell^I(0)$ still follows the $1/\ell$ scaling for large enough scales, like the singular solution. There is therefore a "footprint" of the singularity at finite but small enough scales, as discussed in [61], which opens the pathway to "scan" quasi-singularities of the Navier-Stokes equations by tracking the energy transfers. Such observations motivate singularity or quasi-singularities detection in turbulent flows using \mathcal{D}_ℓ^I , as discussed in [41, 61].

The variations of \mathcal{D}_ℓ^I with scale seem to depend strongly on viscosity. However, there is a way to collapse all viscous solutions onto universal curves by introducing the typical length $\eta_s = \nu/\Delta u$, which is the only characteristic scale one can build using the shock amplitude and the viscosity. Expressing all scales in units of η_s , we then get figure 10.3-b for $\mathcal{D}_\ell^I(0)$. One sees that the curves corresponding to different viscosities now collapse, scaling like ℓ^{-1} for $\ell > \eta_s$ and ℓ^2 for $\ell < \eta_s$. The same universality also holds for the viscous term $\mathcal{D}_\ell^V(0)$ that now scales like ℓ^{-2} for $\ell > \eta_s$ and tends towards ϵ for $\ell < \eta_s$. The location where $\ell = \eta_s$ is precisely the location where the "inertial" term $\mathcal{D}_\ell^I(0)$ balances the viscous term $\mathcal{D}_\ell^V(0)$. These observations are one of the basic ingredients of the generalization of the Kolmogorov picture of turbulence, described in Section 11. The other ingredients result from the link between WKHM and intermittency in 3D turbulent flows.

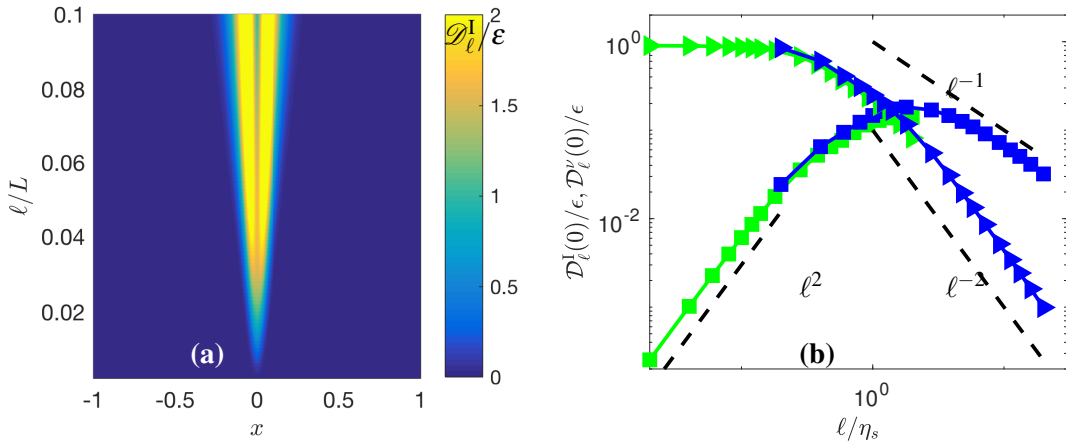


Figure 10.3: a) Space/scale diagram of the non-dimensional local energy transfer $\mathcal{D}_\ell^I/\epsilon$ for the viscous solution of Burgers equation with $\nu = 1/10$. The intensity of $\mathcal{D}_\ell^I/\epsilon$ is coded in colour, following the colorbar. b) Universal local energy budget as a function of the scale for the viscous solution of Burgers equation with $\nu = 1/10$ (green symbols) and $\nu = 1/100$ (blue symbols). Square: $\mathcal{D}_\ell^I(0)/\epsilon$; Triangle: $\mathcal{D}_\ell^V(0)/\epsilon$.

10.3 WKHM and intermittency

10.3.1 Spatial distribution of energy transfers and dissipation

Let us go back to real turbulence and try to compute \mathcal{D}_ℓ^I and \mathcal{D}_ℓ^V on a velocity field measured in the von Karman flow. An example is shown in figure 10.4, for scales of the order of $\ell \sim 100/\eta$. We see that \mathcal{D}_ℓ^I is inhomogeneous in space. In scale, the maxima of \mathcal{D}_ℓ^I are distributed along thinning lines, that point toward the location of maxima of \mathcal{D}_ℓ^I at the resolution scale $\Delta x = 120\eta$. This picture is reminiscent of what we observe for the Burgers velocity field, where we know that the point of convergence of the thickening lines of maxima is the shock i.e. the velocity field singularity regularized by viscosity at the Kolmogorov scale. To check that this picture is also valid in the von Karman case and study properties of corresponding quasi-singularities or singularities, we need to zoom into the flow, to decrease ℓ down to the Kolmogorov scale.

Two examples are shown in figure 10.5, where the spatial distribution of \mathcal{D}_ℓ^V and \mathcal{D}_ℓ^I are plotted around a location of convergence of maxima lines in scale space for the experiment ANTI-3D, where the smallest accessible length of the order of the Kolmogorov scale. \mathcal{D}_ℓ^V is always positive, while \mathcal{D}_ℓ^I can take both positive and negative value, tracing both downscale (positive) and upscale (negative) energy transfers. At this scale, downscale energy transfers clearly dominate, however, as one goes towards larger and larger scale, this difference weakens and upscale energy transfers become more numerous [15]. One sees that the largest values of \mathcal{D}_ℓ^I are located in a coherent structure, that is connected with a shock structure in the velocity field. Outside such structures, the value of \mathcal{D}_ℓ^I is much smaller. The viscous dissipation \mathcal{D}_ℓ^V is also highest within the coherent structure, but does not follow exactly the pattern of the local energy transfers \mathcal{D}_ℓ^I . It is conserved significant values in the region to the right of the shock, while it is negligible in the region left of the shock. This kind of structure might therefore be associated with the roll-up of a vorticity sheet viewed from above. They seem to be the most frequent structures encountered in the von Karman flow [61]. The shocks are not the only coherent structures that are associated with large values of \mathcal{D}_ℓ^I . The latter can also be associated with a "spiral" like structure in the velocity (a vortex), like illustrated in figure 10.5-b. In this case, the energy transfer \mathcal{D}_ℓ^I can be both positive and negative within the core of the vortex and negligible elsewhere, while the viscous dissipation \mathcal{D}_ℓ^V is

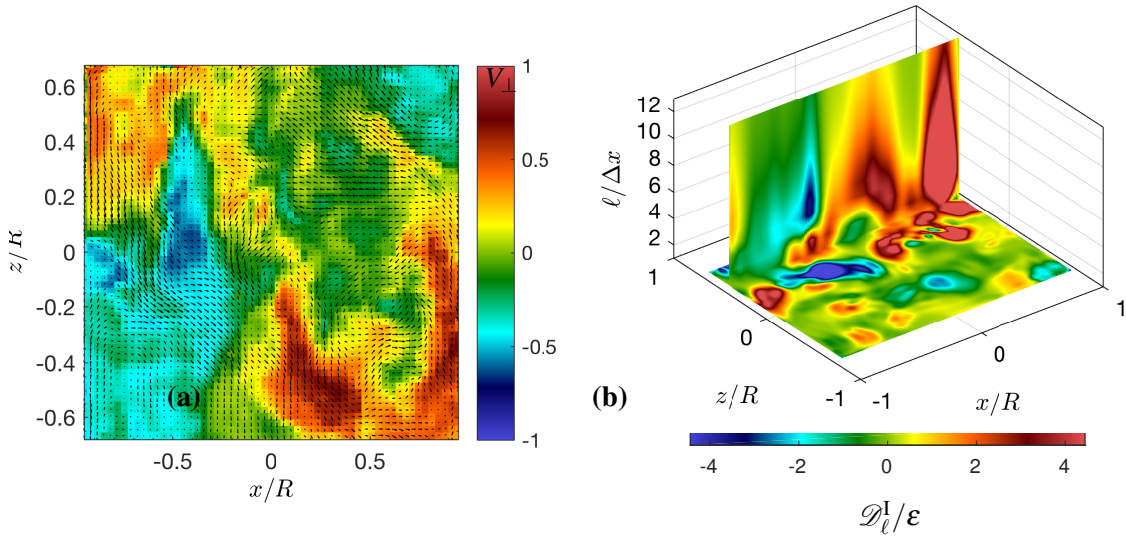


Figure 10.4: a) Example of an instantaneous velocity field, measured in a plane containing the rotation axis, in the von Karman experiment with parameters similar to experiment ANTIG, at resolution $\Delta x = 1.2\text{mm}$. The arrows code the in-plane velocity, the color codes the out-of-plane velocity, V_\perp . The velocities and axis are non-dimensional. The units of length and time are taken as R , the cylinder radius, and $1/2\pi F$, the rotation period of the impellers. b) Example of an instantaneous measurement of the local energy transfer \mathcal{D}_ℓ^I in experiment ANTIG, as a function of space and scale, in a plane containing the rotation axis. The local energy transfer is expressed in units of ε and is coded with color. The scale is expressed as a unit of the spatial resolution of the measurements.

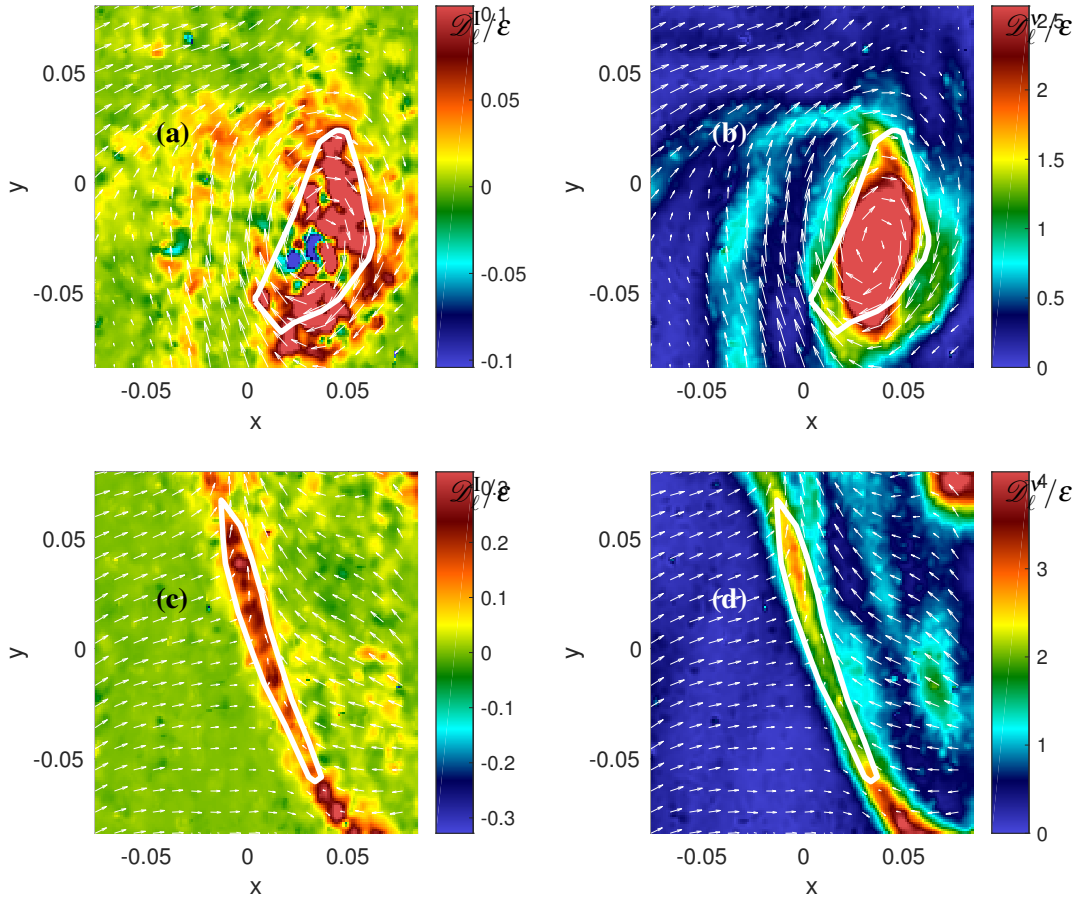


Figure 10.5: Examples of topology around an extreme value of the local energy transfer \mathcal{D}_ℓ^I at the dissipative scale $\ell \approx \eta$ in experiment CONC-3D. Around the event, coded in color, the velocity field, showed by white arrows display a "shock-like" (panel (a)) or "spiral-like" (panel (c)) structure. In panel (b) and (d), the local viscous energy dissipation \mathcal{D}_ℓ^V for the two types of events is provided, coded by color. The white contour delimits the area A1. The figures are drawn using unpublished data collected by the EXPLOIT collaboration (F. Daviaud, B. Dubrulle, P. Debue, V. Valori, J-P. Laval, J-M. Foucaut, Ch. Cuvier, Y. Ostovan), with permission. Adapted from [14].

strong within the core, and extends outside, forming spiral arms. Such structure could therefore be associated with the reconnection of two vortex tubes or the roll-up of a vortex sheet viewed from the side. Other type of coherent structures, observed less frequently, include "cusp" and "jet" [61].

10.3.2 Statistical properties of local energy transfers and dissipation

The spatial distribution of local energy transfers and dissipation is very inhomogeneous, at all scales. This is reflected in their statistics, shown in figure 10.6, to be compared to the statistics of the averaged energy transfers, studied in section 7.6 (figure 7.3). The distributions are similar in shape in both cases, but the tails of the distributions are fatter at small scale in the case of local energy transfers and dissipation. As the length is increased, the distributions tend to look increasingly like the distributions of the average, which is natural since $\mathcal{D}_L^I = \Pi_L^I$ and $\mathcal{D}_L^V = \Pi_L^V$. The self-similarity is broken, so that exponents of the structure functions $\Sigma_p^{DR} = \langle |\mathcal{D}_\ell^I|^p \rangle \sim \ell^{\xi_I(p)}$ and $\Sigma_p^V = \langle |\mathcal{D}_\ell^V|^p \rangle \sim \ell^{\xi_V(p)}$, shown in figure 10.7, do not follow a simple linear law, as can be seen on figure 8.6-b.

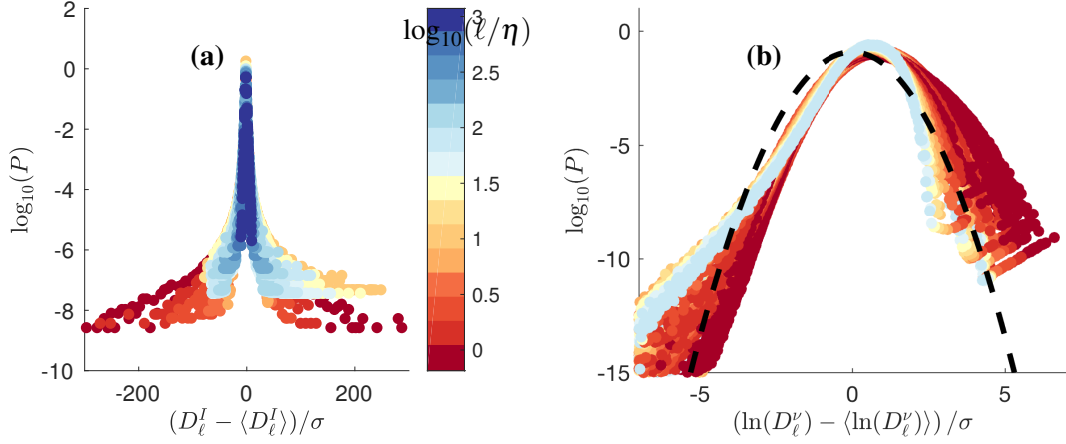


Figure 10.6: Centered and reduced PDF's of local energy transfers \mathcal{D}_ℓ^I (panel (a)) and log of local viscous dissipation \mathcal{D}_ℓ^ν (panel (b)) at different scales, coded by color, for experiments ANTIG and ANTIC-1 to ANTIC-4 (see figure 7.4-a and 12.2-b for corresponding mean and standard deviation and Table 1 for symbols).

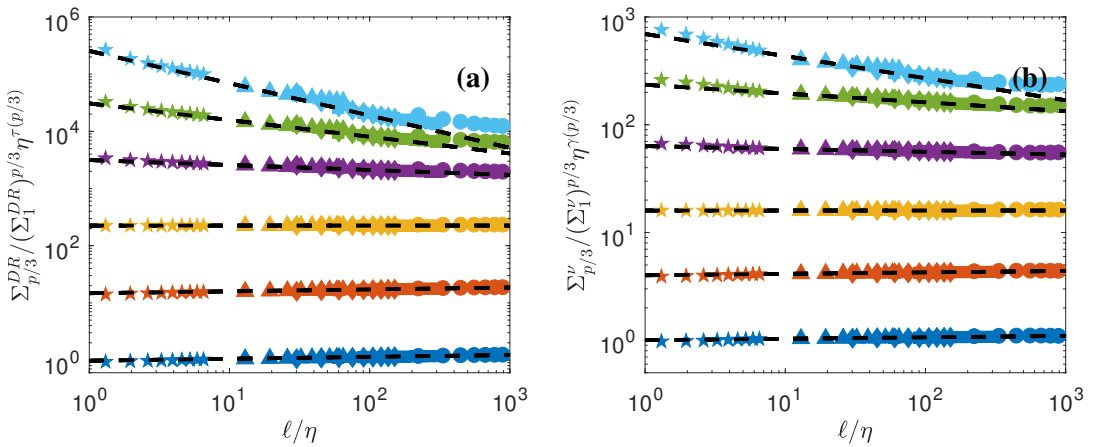


Figure 10.7: Scale variation of the non-dimensional structure function of order $p = 1/3$ to $p = 2$ of local energy transfers and dissipation for experiments ANTIG and ANTIC-1 to ANTIC-4. The structure functions have been shifted by arbitrary factors for clarity and are coded by color: $p = 1/3$: blue symbols; $p = 2/3$: orange symbols; $p = 1$: yellow symbols; $p = 4/3$: magenta symbols; $p = 5/3$: green symbols; $p = 2$: light blue symbols. a) Non-dimensional structure functions for \mathcal{D}_ℓ^I . b) Non-dimensional structure functions for \mathcal{D}_ℓ^ν . The dashed lines are power laws with exponents shown in figure 8.6-b. Adapted from [15].

10.3.3 Scaling of energy transfers and dissipation

When viewed in the scale space, the behavior of energy transfers and dissipation also reveals an interesting difference between regions outside or within "coherent" structures. Such structure are identified as connected regions where energy transfers have very strong values, and are delimited by a white line on figure 10.5 . Now, we can perform 3 kinds of conditional averages: i) average of \mathcal{D}_ℓ^I and \mathcal{D}_ℓ^V inside the coherent structure (A1); ii) average over the regions corresponding to the areas where \mathcal{D}_ℓ^I takes values larger than seventy percent of its maximum over the whole field (A2, strong energy transfers); iii) average over the regions corresponding to the areas where \mathcal{D}_ℓ^I takes values of the around than ten percent of its maximum over the whole field (A3, weak energy transfers). In choosing the threshold for the two cases, we have ensured that they include the same number of points (around 70), for a detailed comparison. The scaling of these conditional averages are shown in figure 10.8-a for the shock case, and 10.8-b for the spiral case. In all situations we observe similar trends: the term $\langle \mathcal{D}_\ell^I \rangle$ decreases with decreasing scale, with a clear change of slope at the point where it crosses the value of $\langle \mathcal{D}_\ell^V \rangle$ in the case of weak energy transfers. The term $\langle \mathcal{D}_\ell^V \rangle$ increases for decreasing scales, and then saturates towards a plateau, which defines the local energy dissipation in the corresponding region. We call ε this value for the weak energy transfers case (A3), and normalize all curves using this value, and its corresponding Kolmogorov scale $\eta = (v^3/\varepsilon)^{1/4}$. Note that ε is higher than ε_g , the global energy dissipation, corresponding to the total dissipation within the flow, and measured by torque-meters: about twenty percent higher in case (a), and 90 percent higher in case (b). Then, we find that dissipation is 5 times larger than ε within the spiral (A1 region case (b)), while it 2 times higher than ε within the shock (A1 region case (a)). Overall, the three curves look similar with the curves of the K41 theory (figure 7.1a), with a scaling close to ℓ^2 below η for $\langle \mathcal{D}_\ell^I \rangle$ and $\ell^{-4/3}$ above η for $\langle \mathcal{D}_\ell^V \rangle$. A closer inspection shows that case A1 and A2 behave identically with respect to A3: the corresponding $\langle \mathcal{D}_\ell^V \rangle$ are systematically steeper than for case A3 when $\ell > \eta$ and $\langle \mathcal{D}_\ell^I \rangle$ are systematically shallower than for case A3. Finally, the crossing between $\langle \mathcal{D}_\ell^V \rangle$ and $\langle \mathcal{D}_\ell^I \rangle$ occurs at a scale smaller in the cases A1 and A2 than in the case A3. Overall, the case A3 seems to be closer to the K41 picture, meaning that the turbulence is more "K41-like" within the regions of moderate local energy transfers and more "non Kolmogorov" within regions where local energy transfers are strong (A2 and A1 regions). Can we strengthen this affirmation?

10.3.4 Intermittency and energy transfers

Let us see how the strong energy transfers connect with intermittency, by conditioning the structure functions on the regions of high or low local energy transfers at the resolution scale. We implement this for the each data set by defining a special set of points \mathcal{A} corresponding to the locations of low of $|\mathcal{D}_{\Delta x}^I|$. To define it, we divide the PDF of $|\mathcal{D}_{\Delta x}^I|$ at the smallest scale of a given experimental data set into 10 deciles: the set of points forming the first decile (spatial regions with $|\mathcal{D}_{\Delta x}^I|$ being in the 10 per cent lower values of the inertial dissipation) are assigned to the set \mathcal{A} .

We compute the PDF of the wavelet velocity increments conditioned on the set \mathcal{A} . It is shown in figure 8.3-b. With respect to the non conditioned case, (figure 8.3-a), we see that the tails are slightly truncated, especially at smaller scales. This means that the large wavelet velocity increments are correlated with large events of $\mathcal{D}_{\Delta x}^I$, especially at small scale. This effect is more obvious when reducing and centering the distribution (insert figure 8.3-b1), which looks however not much more self-similar than the unconditioned one. We now turn to the scaling behavior of the mean and of the std of the conditioned distributions, plot on figure 8.4-a and -b. They appear to follow the $\ell^{1/3}$ as well as their unconditioned counter-part. A more stringent test of the quality of the self similarity is given by looking at the ratio of the std to the mean, provided in figure 8.1-b. If the distribution is self similar, this ratio should be constant. We see that this is not true for the unconditioned case, while it is approximately true for the conditioned case.

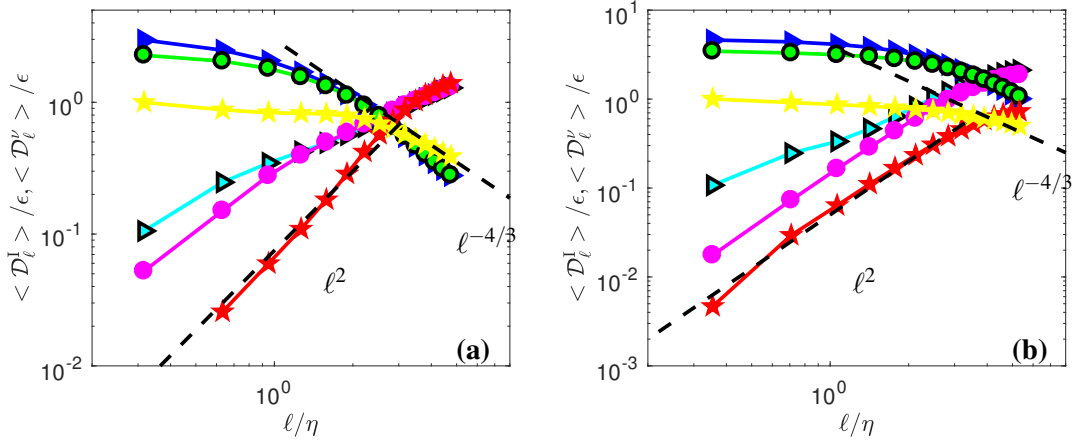


Figure 10.8: Local energy budget as a function of the scale for the two velocity fields of figure 10.5, average over different regions, coded by symbols: circle: A1/structure region; stars: A2/weak transfer region ; triangles: A3/strong transfer region. (a) shock case ; (b) spiral case: $\langle \mathcal{D}_\ell^I(0) \rangle / \epsilon$ averaged over region A1 (magenta circle), A2 (red stars), A3 (light blue triangles); $\langle \mathcal{D}_\ell^\nu(0) \rangle / \epsilon$ averaged over region A1 (green circle), A2 (yellow stars) and A3 (blue triangles). The figures are drawn using unpublished data collected by the EXPLOIT collaboration (F. Daviaud, B. Dubrulle, P. Debue, V. Valori, J-P. Laval, J-M. Foucaut, Ch. Cuvier, Y. Ostovan), with permission.

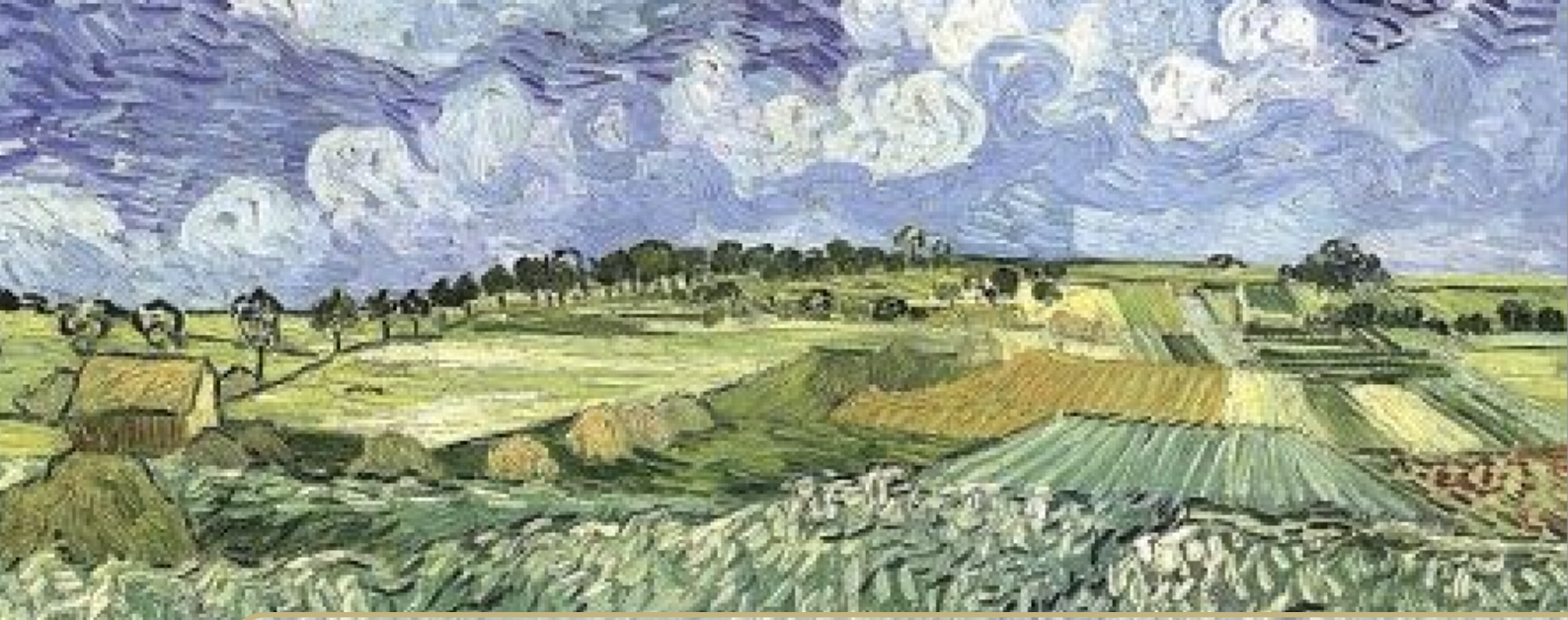
A more refined test of the self-similarity is provided by the scaling wavelet velocity structure functions. We compute them as

$$S_n^C(\ell) = \langle |\delta W(\mathbf{u})(\mathbf{x}, \ell)|^p \rangle_{\mathcal{A}}, \quad (10.24)$$

where the average is taken on the set \mathcal{A} . We show such structure functions in figure 8.5-b for orders $p \in [1, 6]$. From them, we compute the scaling exponent $\zeta_C(p)$. They are shown on figure 8.6-a. We see that $\zeta_C(p)$ is almost straight, lying very close to the Kolmogorov K41. The intermittency is reduced, meaning that the regions corresponding to the set \mathcal{A} are more self-similar. This shows that the intermittency is connected to the high events of the local energy transfers at the resolution scale. This suggests that the natural analog of the quantity ε_ℓ in K62, is \mathcal{D}_ℓ^I [15, 17] and that all intermittency corrections can be understood using the statistical scaling properties of the local energy transfers and dissipation defined through WKHM. The proper generalization involves the multi-fractal (MFR) formalism, first proposed by [30].

Application of Multifractals to Turbulence

- 11 Beyond Kolmogorov using multi-fractals 87**
 - 11.1 The multifractal model for turbulence
 - 11.2 The multifractal and Onsager's dissipative solutions
 - 11.3 Illustration: Burgers solution
 - 11.4 Interpretation of extreme events of local energy transfers
 - 11.5 Scaling range
 - 11.6 Scaling exponents and signs of \mathcal{D}_ℓ^I and \mathcal{D}_ℓ^V
- 12 Constraints on the multifractal spectrum 93**
 - 12.1 Theoretical constraints
 - 12.2 Observational Constraints on the MFR spectrum
- 13 Additional properties of Multifractals . . . 99**
 - 13.1 WKHM-Multifractal refined similarities
 - 13.2 Thermodynamical analogy
 - 13.3 Local multi-fractal analysis



11. Beyond Kolmogorov using multi-fractals

11.1 The multifractal model for turbulence

We have no compelling evidence that there are exact singularities in turbulence (meaning solutions which are Hölder continuous in the limit $\ell \rightarrow 0$), but we found evidence of existence of scaling behaviour for at least some range of scale. The multifractal model of turbulence therefore assumes that, in presence of viscosity, there exists a whole family of locally self-similar solutions, labelled by a scalar field $h(\mathbf{x}, t, \mathbf{r})$, such that

$$h(\mathbf{x}, t, \mathbf{r}) = \frac{\ln |\delta_{\mathbf{r}} \mathbf{u}(\mathbf{x}, t, \mathbf{r})|}{\ln(\ell/L)}, \quad \ell = |\mathbf{r}| \quad (11.1)$$

for a range of scale in a suitable "inertial range" $\eta_h \ll \ell \ll L$, where L is a characteristic integral length of scale and η_h a cut-off length scale. Such a definition of h is mathematically sound only for $0 \leq h \leq 1$. Using wavelet coefficients $\delta W(\mathbf{u})$ instead of velocity increments, one can extends the definition of h to values $h < 0$ [26, 51]. The local energy balance for such solutions helps us to understand the meaning of the cut-off scale η_h . Indeed, plugging (5.2) in the definitions (10.12) and (10.13), we see that $\mathcal{D}_I^\ell \sim \ell^{3h-1}$ and $\mathcal{D}_V^\ell \sim v \ell^{2h-2}$. These two terms balance at a scale $\eta_h \sim v^{1/(1+h)}$. This scale thus appears as a fluctuating cut-off which depends on the scaling exponent and therefore on \mathbf{x} . This is the generalization of the Kolmogorov scale $\eta_{1/3} \sim v^{3/4}$, and was first proposed in [56]. Below η_h , the viscous dissipation takes over and regularizes the flow, exactly like it did in the K41 solution or in the Burgers shock solution. The velocity increments then scale like $|\delta \mathbf{u}(\mathbf{x}, \ell)| \sim \ell$ so that \mathcal{D}_I^ℓ decreases to 0 like ℓ^2 , while \mathcal{D}_V^ℓ tends to a constant, equal to the local energy dissipation ε . This picture is thus a generalization of K41, and is schematized in figure 7.1-b. We note that the local energy transfer of the viscous Burgers solution (figure 10.3-b), exactly follows such scheme, with $h = 0$ being the Hölder exponent of the solution at zero viscosity, resulting in $v_s \propto v$.

11.2 The multifractal and Onsager's dissipative solutions

As long as $h > -1$, we have $\lim_{v \rightarrow 0} \eta_h = 0$. In that limit, the wavelet coefficients $\delta W(\mathbf{u}, \ell)$ are self-similar with exponent h at all scale, and the corresponding solution tends to a solution of

Euler equation with Hölder of exponent h . In this respect, we can interpret the corresponding multifractal solutions as (regularized) footprints of solutions of the Euler equation with Hölder of exponent h . As we have seen in section 10.2.4, such solution are able to dissipate energy for the Euler equation if $-1 < h \leq 1/3$. For this reason, we call multifractal solutions with $-1 < h \leq 1/3$ *dissipative quasi-singularities*, while the solutions with $1/3 < h \leq 1$ will be called *non-dissipative quasi-singularities*.

The multifractal solution for $h = -1$, if it exists, may be considered as an equivalent of Leray SS of Navier-Stokes. It is quite special, since $\eta_{-1} = \lim_{h \rightarrow -1} Re^{-1/(1+h)} = 0$ at any fixed $Re > 1$. For this exponent, there is no possibility of regularization by viscosity ($1/r$ is a zero mode of the Laplacian), so that $h = -1$ would correspond to a Navier-Stokes singularity which dissipates energy by non viscous mean.

The natural question that occurs now is: *how do these different solutions contribute to the total energy dissipation, and can they explain the dissipation anomaly?* To answer this question, we must first be able to count how often each of them occurs within the flow, i.e. what is their probability of occurrence. Does it mean that we have to be able to measure, with good precision, the velocity field at each point, compute its wavelet transform, fit locally an exponent, and do an histogram? Physically speaking, the procedure looks insane, because of noise issues. Mathematically speaking, it would be a complete nonsense, since the exponents $h(x)$ may be only defined on sets of zero measure (see e.g. [9]). Fortunately, there the large deviation theory enables to define the "probability of h " and provides a meaning to this kind of physical questions.

11.3 Illustration: Burgers solution

We have computed exactly the multifractal spectrum for the singular Khokhlov solution of the inviscid Burgers equation. When we consider the viscous solution instead, the scaling of the structure function given by (5.5) only holds for $\ell > \eta_s$. Below η_s , $\delta u \sim \ell$ because of regularity, and the structure function of order p scales like ℓ^p (figure 11.1-a). The multifractal spectrum $C(h)$ can nevertheless be computed using the scaling in the "inertial range" $\ell > \eta_s$ (figure 11.1-b) and provides the value of the ideal "inviscid" case (figure 11.1-b1). This case illustrates the methodology that is applied in real turbulence data.

11.4 Interpretation of extreme events of local energy transfers

We have now tools at hand to interpret the behaviour of local energy transfer and dissipation, measured in the von Karman flow (section 10.3). Typically, we observed that local energy transfers are very intermittent in space and time. Even at scales close or below the Kolmogorov scale, they exhibit locally intense events, than can exceed the global energy dissipation by several orders of magnitude (see figure 10.5 and [61]). In the multifractal picture of turbulence (figure 7.1-b), such events correspond to dissipative quasi-singularities ($h \leq 1/3$), that have not yet reached their dissipative cut-off η_h . The local energy budget of figure 10.8 can then be viewed as a (noisy!) realization of figure 7.1), with $h \sim 0.2$, obtained by fitting the scaling of \mathcal{D}_v^ℓ above the viscous cut-off. In contrast, the location where the local energy transfers are small above the Kolmogorov scale, correspond to non-dissipative quasi-singularities ($h > 1/3$). The dissipative quasi-singularities with $-1 < h \leq 1/3$ all eventually convert their local energy into viscous dissipation at η_h , the corresponding energy being transferred at a nearly constant rate towards smaller and smaller scales by the viscous term \mathcal{D}_v^ℓ , until it is ultimately converted into heat. In such picture, the value of the local energy dissipation is therefore provided by

$$\varepsilon = \mathcal{D}_v^{\eta_h} = \mathcal{D}_I^{\eta_h}. \quad (11.2)$$

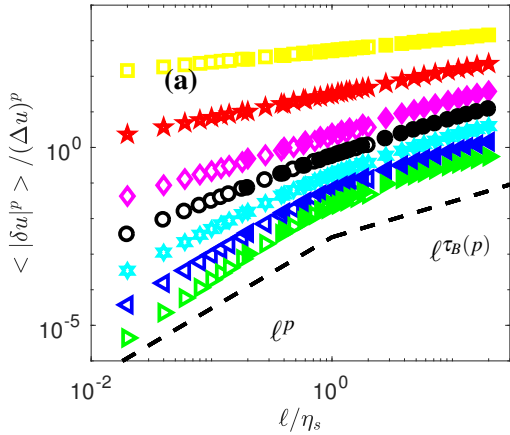


Figure 11.1: Multifractal analysis of viscous Burgers solutions. (a) Scale variation of the non-dimensional wavelet structure function computed using velocity fields $u^v(x, t)$ of figure 10.1 with $v = 1/100$ (open symbols) and $v = 1/10$ (filled symbols). The structure functions have been shifted by arbitrary factors for clarity and are coded by color: $p = 1/3$: yellow square; $p = 2/3$: red stars; $p = 1$: magenta diamonds; $p = 4/3$: black circles; $p = 5/3$: blue stars; $p = 2$: blue triangles; $p = 7/3$: green triangles. Note that because the structure functions scale like ℓ^p in the viscous range $\ell < \eta_s$, there is no scaling difference below and above η_s for $p \leq 1$.

Using the scaling $\mathcal{D}_I^\ell \sim \ell^{3h-1}$, and $\eta_h \sim Re^{-1/(1+h)}$, we thus get $\varepsilon \sim Re^{(1-3h)/(1+h)}$, which increases as Re increases or h decreases. This picture therefore predicts that the fluctuations of the energy dissipation become larger and larger and result from events occurring at smaller and smaller scale as Re is increased. It also means that if one truncates a numerical simulation at a scale Δx larger than $\eta_{h_{min}}$, the cut-off scale of the smallest Hölder exponent that can be observed in the flow, then one misses all the events of energy dissipation produced by quasi-singularities with $h_{min} \leq h \leq -1 - \ln Re / \ln(\Delta x / L)$. This explains why, increasing a numerical simulation from $\Delta x = \eta/2$ to $\eta/10$, the tails of the energy dissipation increase, as being noticed by [70]. The amount of energy dissipation lost by lack of resolution actually depends on h_{min} and on $C(h)$ that can either be measured (see section 8.5), or analytically computed on simple models, such as the Burgers solution (section 11.3).

11.5 Scaling range

The previous discussion shows that the notion of non trivial Hölder exponent $h < 1$ is only valid provided $\ell > \eta_h$. The notion of multifractal is thus rigorously only meaningful in the $Re \rightarrow \infty$ limit, where the limit $\ell \rightarrow 0$ can be taken. It is indeed in this limit only that all the properties deriving from large deviations, and Legendre property (such as convexity, etc) are valid. In the following, we will assume that Re is sufficiently large so that there exists an "inertial range" of scale $\eta_{1/3} \ll \ell \ll L$, in which the multifractal formalism applies. Since η_h is a decreasing function of h , this ensures that the condition $\eta_h \ll \ell$ holds for all $h \leq 1/3$ i.e. for all dissipative solutions.

11.6 Scaling exponents and signs of \mathcal{D}_ℓ^I and \mathcal{D}_ℓ^V

Once the multifractal spectrum $C(h)$ is given, one can use the small scale limits of section 10.2.3 to compute the scaling exponents of the wavelet velocity structure functions via $\zeta(p) = \min_h(ph + C(h))$, but also the scaling of other quantities appearing in WKHM. For example, since $\mathcal{D}_\ell^V \sim \ell^{2h-2}$

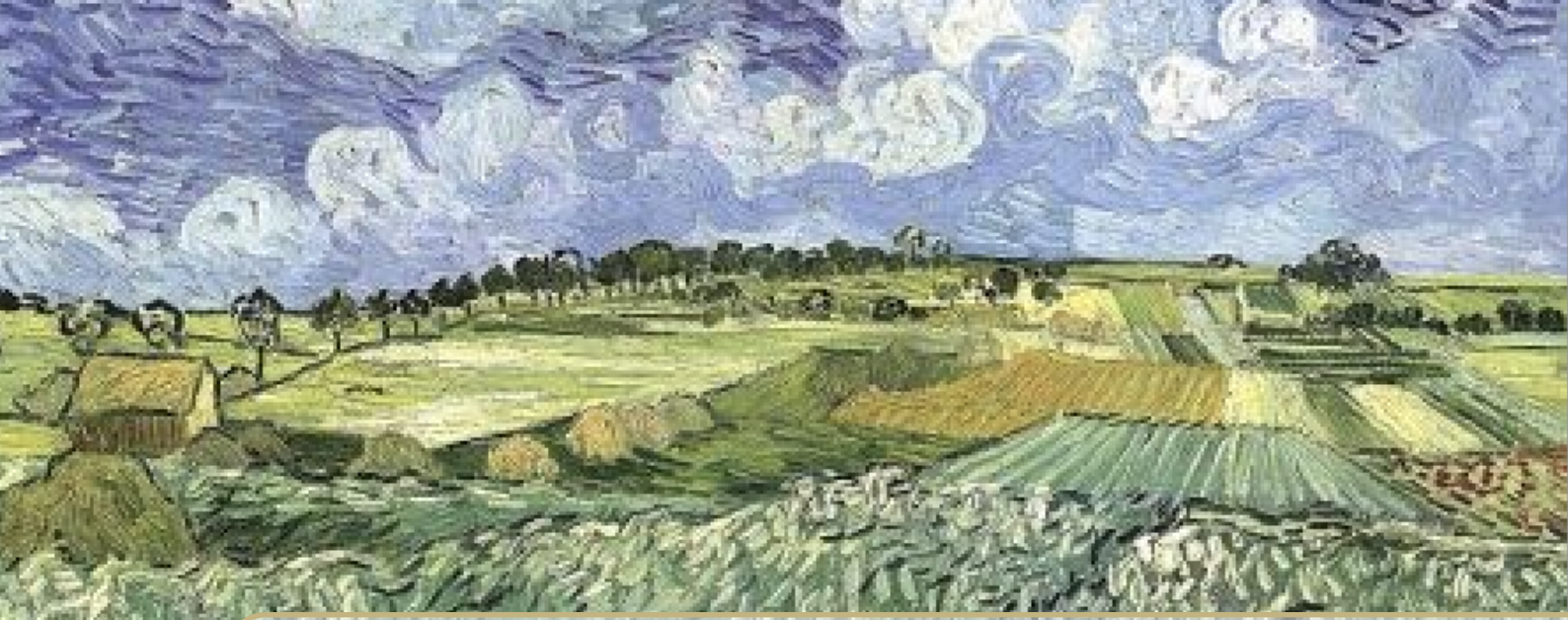
and $\mathcal{D}_\ell^I \sim \ell^{3h-1}$, we have:

$$\begin{aligned} \langle |\mathcal{D}_\ell^V|^p \rangle &\sim \ell^{\xi^V(p)}, \quad \xi^V(p) = \min_h (p(2h-2) + C(h)), \\ \langle |\mathcal{D}_\ell^I|^p \rangle &\sim \ell^{\xi^I(p)}, \quad \xi^I(p) = \min_h (p(3h-1) + C(h)). \end{aligned} \quad (11.3)$$

Using the regularity of the velocity at scale $\ell = \eta_h \sim Re^{-1/(1+h)}$, we can also get useful scalings with Reynolds number. Indeed, at $\ell = \eta_h$, we have $\delta_r \mathbf{u}(\mathbf{x}, t) = r_j \partial_j u_i$ so that we derive the following useful trace formula:

$$\begin{aligned} \mathcal{D}_{\eta_h}^V &\sim v Tr(SS^+), \\ \mathcal{D}_{\eta_h}^I &\sim \eta_h^2 Tr(S^+ S^2), \end{aligned} \quad (11.4)$$

where $S_{ij} = \partial_j u_i$. From this, we get a connection between the sign of the inertial or viscous energy transfers, and the topology of the coherent structures at the dissipative scale. Indeed, we have $Tr(SS^+) = \sum_{i=1,3} |\lambda_i|^2$, and $Tr(S^+ S^2) = \sum_{i=1,3} \lambda_i |\lambda_i|^2$, where λ_i are the eigenvalues of the tensor S . Using the incompressibility condition $\sum_i \lambda_i = 0$, we see that i) $Tr(SS^+)$ is positive; ii) if the eigenvalues of S are real with $\lambda_1 > \lambda_2 > \lambda_3$, then $Tr(S^+ S^2) = 3\lambda_1 \lambda_2 \lambda_3$. This means that $\mathcal{D}_{\eta_h}^V$ is positive and that $\mathcal{D}_{\eta_h}^I$ is zero for quasi two-dimensional flows ($\lambda_2 = 0$) or is positive for filaments like structures ($\lambda_2 > 0$), and negative for sheet like structures ($\lambda_2 < 0$).



12. Constraints on the multifractal spectrum

12.1 Theoretical constraints

12.1.1 For general boundary conditions

Turbulence properties impose some constraints on the multifractal spectrum $C(h)$. They are:

Normalization. The normalization of the pdf imposes $\langle |\delta W|^0 \rangle = 1$, so that

$$\zeta(0) = \min_h(C(h)) = 0. \quad (12.1)$$

Let us call h_* the value that realizes the minimum $C(h_*) = 0$. It corresponds to the exponent reached with the highest probability, i.e. the most probable exponent. In K41, we would have $h_* = 1/3$. However, intermittency effects produce a shift on this most probable exponent, as we illustrate in section 12.1.3.

Kolmogorov 4/3 law. Equation (7.8) implies $\zeta(3) = 1$. This implies $C(h) \geq 1 - 3h$, the equality being reached by the h_1 obeying

$$dC/dh|_{h_1} = -3, \quad \text{for } h_1 \text{ s.t. } C(h_1) = 1 - 3h_1. \quad (12.2)$$

Note however that this constraint strictly applies only to quantities built from ingredients that are involved in the 4/3rd law, i.e. third power of velocity increments, with *no absolute value*.

Anomalous dissipation. The condition $\langle \varepsilon \rangle = cte$ for $Re \rightarrow \infty$ imposes $\chi_\varepsilon(1) = 0$. Since $1 + h > 0$, this is achieved if $C(h) \geq 1 - 3h$, equality being achieved for $h = h_1$ defined via (12.2): the 4/3th law and the anomalous dissipation provide the same constraint on the multifractal spectrum. Since the 4/3th law is directly derived from the Navier-Stokes equation, one therefore concludes that the anomalous dissipation is a **consequence** of the 4/3th law and built into the Navier-Stokes equations.

12.1.2 Flows on a torus

Useful bounds on the multifractal spectrum can also be derived for flows on torus using Theorem 2.4.1. A correspondence between multifractal theory and the Navier-Stokes equations is more

appropriate for the stage when T in the time averages $\langle \cdot \rangle_T$ in (2.4.1) is large enough such that a Navier-Stokes turbulent flow has reached the fully developed stage. Multifractal theory enables us to obtain the scaling of $F_{n,m}$, defined in (??), as a function of v (in the limit $v \rightarrow 0$) via an h -dependent dissipation length scale η_h defined as that scale at which the local Reynold number $(\delta u)\ell/v = 1$ [PV1987, PV1987rev]. As explained in [BDB2019], this separates the scales into two domains ; a self-similar domain where $\delta u \sim \ell^h$ for $\ell > \eta_h$ and a laminar domain where δu is regular for $\ell < \eta_h$. Thus a balance occurs when

$$\eta_h \sim v^{\frac{1}{1+h}}. \quad (12.3)$$

Moreover, in the laminar domain, δu can be Taylor-expanded, resulting in $\delta u \approx \ell |\nabla \mathbf{u}|$. Matching with the self-similar domain at η_h then provides the scalings

$$|\nabla \mathbf{u}| \sim \eta_h^{h-1}, \quad \text{and} \quad |\nabla^n \mathbf{u}|^{2m} \sim \eta_h^{2m(h-n)}. \quad (12.4)$$

Then, forming the correspondence

$$L^{-3} \int_V |\nabla^n \mathbf{u}|^{2m} dV \longleftrightarrow \int_h \eta_h^{2m(h-n)} P_{\eta_h}(h) dh, \quad (12.5)$$

and using the scalings $\eta_h \sim v^{1/(1+h)}$ and $F_{n,m} \sim L^3 v^{\chi_{n,m}}$, in the limit $v \rightarrow 0$, we obtain

$$\chi_{n,m} = \min_h \left(\frac{2m(h+1) + C(h) - 2m(n+1)}{1+h} \right). \quad (12.6)$$

Using the definition of $F_{n,m}$ in (2.6) and comparing this with eq. (??), we therefore obtain

$$\lambda_{n,m}^{-(n+1)} \sim v^{\frac{\chi_{n,m}}{2m} - 1}. \quad (12.7)$$

Inserting this estimate into (??) of Lemma ??, and comparing powers of v , in the limit $v \rightarrow 0$, leads to the condition

$$\frac{\chi_{n,m}}{2m} - 1 \geq -\frac{3}{\alpha_{n,m}}. \quad (12.8)$$

In dimension d , the value of $\chi_{n,m}$ does not change and we have the more general condition

$$\frac{\chi_{n,m}}{2m} - 1 \geq -\frac{3}{(4-d)\alpha_{n,m,d}} = \frac{3}{4-d} \left[\frac{d}{2m} - (n+1) \right]. \quad (12.9)$$

Developing eqs. (12.6) and (12.9) leads to

$$C(h) \geq 2m(n+1) \left(1 - \frac{3(1+h)}{4-d} \right) + \frac{3d(1+h)}{4-d}, \quad \forall (n,m) \geq 1. \quad (12.10)$$

In the limit $(n,m) \rightarrow \infty$ the right hand side of equation (12.10) goes to infinity, unless $h \geq (1-d)/3$, which means that the only scaling exponents that have a nonzero probability are those greater than

$$h_{\min} = (1-d)/3. \quad (12.11)$$

When $d = 3$ we have the lower bound

$$h \geq -2/3, \quad (12.12)$$

the consequences of which will be discussed in §??.

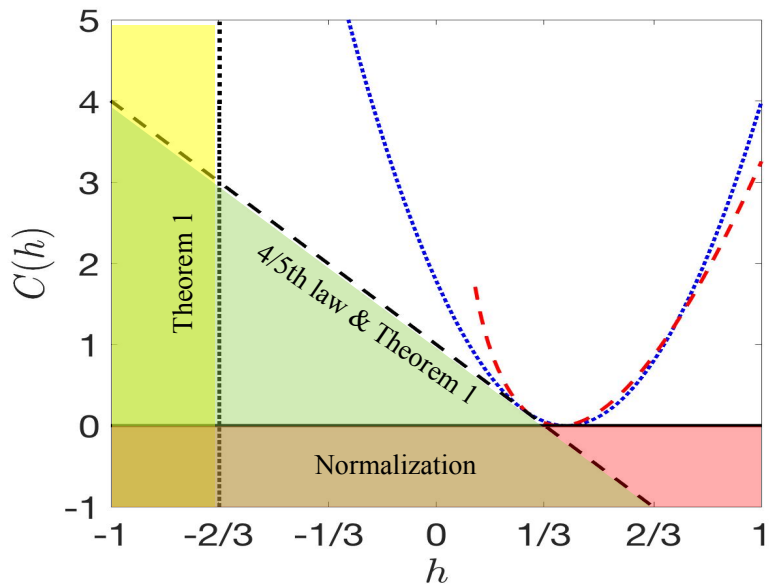


Figure 12.1: The figure is compiled from the various constraints, including $C(h) \geq 1 - 3h$, and displays the admissibility range of the multifractal spectrum when $d = 3$. The yellow zone left of the vertical dotted line is excluded as a result of Theorem 1. The red zone below the horizontal continuous line is excluded as a result of normalization of $C(h)$ [BDB2019]. The green zone below the black dashed-dotted line is excluded as a result of both Theorem 1 and the four-fifths law. A few classical models that fit turbulence measurements for $d = 3$ are also shown : blue dotted line : log-normal model with $b = 0.045$ [BDB2019]; red dashed line : log-Poisson model with $\beta = 2/3$ [SL94].

Returning to (12.10), for any $h \geq h_{min}$, the sharpest bound on $C(h)$, uniform in n, m comes from the values $m = n = 1$, leading to

$$C(h) \geq 1 - 3h, \quad \text{with} \quad C(h_{min}) \geq d. \quad (12.13)$$

The result $C(h_{min}) \geq d$ looks unusual but has a very low probability of occurrence. It is indeed one of the features allowed by Large Deviation Theory [26].

The first inequality in (12.13) is the same as that derived from the four-fifths law [BDB2019]. The second inequality $C(h_{min}) \geq d$ also provides a bound on the probability of observing the smallest exponent which has a very low probability of occurrence [CKN1982]. Note that that for $d = 3$, the condition for $n = m = 1$ reflects the fact that the energy dissipation is bounded, as stressed in [JDG2020]. Thus, we can say that while the hierarchy of bounds derived in Theorem 1 gives a lower bound¹ on h , which is expressed in (12.11), the lower bound $C(h)$ in (12.13) is no better than that derived from the four-fifths law. We see also that the exponent corresponding to Leray scaling, namely $h_{min} = -1$, is only achieved at the singular dimension $d = 4$. All the constraints on the multifractal spectrum are assembled in Fig. 12.1.

12.1.3 Illustration: the log-normal model

The simplest non-trivial convex function with a minimum equal to 0 is a parabola $C(h) = (h - a)^2/2b$, which satisfies the normalization condition (12.1). Performing the Legendre transform, we see that the corresponding structure function exponents are given by

$$\zeta(p) = ap - bp^2/2, \quad (12.14)$$

so that it corresponds to a log-normal law for the underlying process. In this case, the most probable exponent in dimension 3 is $h = a$, while $h_{min} = a - \sqrt{6b}$ and $h_{max} = a + \sqrt{6b}$.

Such a multifractal spectrum depends on two parameters a and b . To be a valid approximation for turbulence, it must satisfy the constraints of section 12.1.1. The 4/5th law condition (12.2) imposes $a = 1/3 + 3b/2$ so that the multifractal spectrum is given by

$$C(h) = \frac{(h - 1/3 - 3b/2)^2}{2b}. \quad (12.15)$$

One sees that the most probable exponent is shifted from $1/3$ by a term proportional to b , which therefore encodes all intermittency corrections. One more constraint only is needed in this approximation, to compute the intermittency parameter. For example, if one imposes $h_{min} = 0$, so that the strongest dissipative solution has the same Hölder regularity than a shock, one gets $b \approx 0.023$. On the contrary, if one imposes that $h_{max} = 1$, so that the multifractal spectrum extends all the way to the regular solutions, one gets $b \approx 0.056$. In the next section, we use our data to compute $C(h)$ from scaling exponents and get estimates of b .

12.2 Observational Constraints on the MFR spectrum

The bounds derived previously are currently the best we can do from a theoretical side, in the sense that no one succeeded to derive analytically the full shape of $C(h)$ from the NSE. One can then infer properties of $C(h)$ from measurements, either through numerical simulations or experiments. The way to do it is first to compute structure functions, then compute their scaling exponents, and

¹Paladin and Vulpiani [PV1987, PV1987rev] introduced the idea of an h -dependent dissipation scale η_h such that $L\eta_h^{-1} \sim R_e^{1/(1+h)}$. Comparing this with the estimate in (??) requires the assumption that their Reynolds number R_e is equivalent to Re of (??). Assuming this, we have $3(1+h) = (4-d)(n+1)\alpha_{n,m,d}$. Given that m, n vary across the ranges $1 \leq m \leq \infty$ and $n \geq 1$ we end up with $(1-d)/3 \leq h \leq \frac{1}{2}$, which is consistent with (12.11).

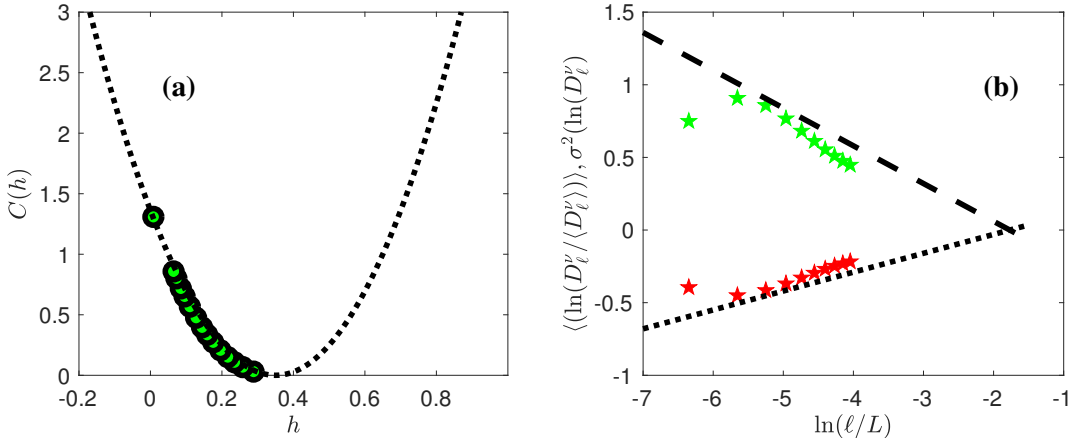


Figure 12.2: (a) Multifractal spectrum $C(h)$ for the experiments ANTIG and ANTIC-1 to ANTIC-4. The spectrum has been obtained by taking the inverse Legendre transform of the scaling exponents $\zeta(p)$ shown in figure 8.6-a. The dotted line is a parabolic fit $C(h) = (h - a)^2 / 2b$ with $a = 0.35$ and $b = 0.045$. (b) Further test of the WKHM-Multifractal refined similarity RSH2, showing that the mean and the variance of $\ln(\mathcal{D}_v^\ell / \langle \mathcal{D}_v^\ell \rangle)$ obey the same scalings than the mean and variance of $\ln(\epsilon_\ell)$. The dotted and dashed lines are the same fits than in figure 9.2-b.

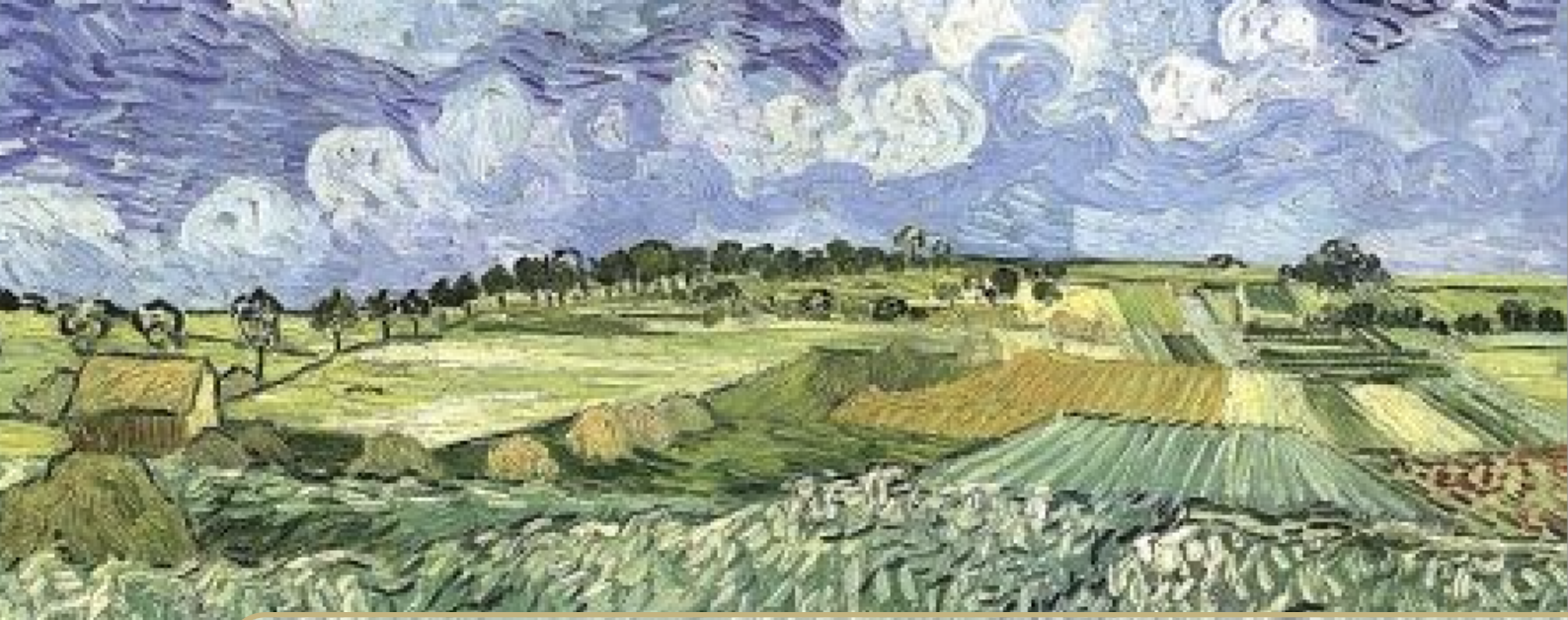
finally compute $C(h)$ from inverse Legendre transform. Doing that on the exponents of figure 8.6-a, we obtain the result provided in figure 12.2-a. One sees that it parabolic, and is well fitted by a parabola of the shape (12.15), with $b = 0.045$ and $a = 0.35$. We note that this does not satisfy $a = 1/3 + 3b/2$, because indeed, in our data, $\zeta(3) \approx 0.8$ (remember that we have considered absolute value of wavelet increments, that are not involved in the 4/3rd law). Extrapolated up to $C = 3$, we get $h_{\min} \approx -0.2$.

We can also substitute this value into (12.14) to check that it provides a good fit of the exponent $\zeta(p)$, shown in figure 8.6-a. We can also use them to compute the scaling exponent of the generalized skewness \mathcal{S}_p given by $\mathcal{S}_p = \langle |\mathcal{D}_\ell^I|^p \rangle / (\langle |\mathcal{D}_\ell^v|^{3p/2} \rangle)$. This exponent is $\xi^I(p) - \xi^v(3p/2) = 2p$, i.e. the same value found in section 8.2 for $(\Pi_\ell^I)^q / (\Pi_\ell^v)^{3q/2}$.

More stringent test can be done by considering other scaling exponents introduced previously. Indeed, in the log-normal approximation, we have

$$\begin{aligned} \xi^v(p) &= -\frac{4}{3}p + bp(3-2p), \\ \xi^I(p) &= \frac{9}{2}bp(1-p). \end{aligned} \quad (12.16)$$

These values are used to compute $\xi^v(p/3) - p/3$ and $\xi^I(p/3) - p/3$ and have been reported on figure 8.6-b. We see that they do not provide a good fit of the data, which seem better approximated by formulae 12.16, with $b = 0.065$. This puzzle will be explained in the next chapter, using the multifractal refined similarity hypothesis



13. Additional properties of Multifractals

13.1 WKHM-Multifractal refined similarities

From figure 8.6-b, we see already a striking feature: the intermittency exponent of velocity increment $\tau(p/3) = \zeta(p) - p/3$ does not coincide with the scaling exponent of ε_ℓ (failure of K62), and they look closer to that of \mathcal{D}_I^ℓ . However, if we consider now $\tau_{rsh} = \zeta(p) - \zeta(3)p/3$, we observe a very good coincidence: this means that a correct refined similarity hypotheses is

$$\begin{aligned} \frac{\langle |\delta W_\ell|^p \rangle}{\langle |\delta W_\ell|^3 \rangle^{p/3}} &= \frac{\langle |\mathcal{D}_I^\ell|^{p/3} \rangle}{\langle |\mathcal{D}_I^\ell| \rangle^{p/3}}, \\ &= C_p (\ell \varepsilon)^{p/3} \left(\frac{\ell}{L}\right)^{\xi^I(p/3)}, \end{aligned} \quad (13.1)$$

where ξ^I is given by (12.16), in the log-normal approximation for the MFR spectrum. This is in agreement with the remark by [40], since \mathcal{D}_I^ℓ is a quantity that traces local energy transfers. The physical interpretation was given in section 11.4, where we saw the connection between location of high energy transfers, and dissipative solutions with $h \leq 1/3$.

Does it mean that Kolmogorov's intuition was wrong, and that the energy dissipation is useless to characterize intermittency? In fact, no. If we observe further the figure 8.6-b, we see that the scaling exponents of ε_ℓ and $\mathcal{D}_v^\ell / \langle \mathcal{D}_v \rangle$ coincide. In fact, as shown in figure 12.2-b, the scaling properties of the mean and the variance of $\ln(\mathcal{D}_v^\ell / \langle \mathcal{D}_v \rangle)$ also coincide with that of $\ln(\varepsilon_\ell)$. This means that there is a refined similarity hypothesis involving ε_ℓ that states

$$\langle \left(\frac{\varepsilon_\ell}{\varepsilon}\right)^p \rangle = \langle \left(\frac{\mathcal{D}_v^\ell}{\langle \mathcal{D}_v^\ell \rangle}\right)^p \rangle. \quad (13.2)$$

This RHS imposes $\xi^v(p) - p\xi^v(1) = \tau_\varepsilon(p) = \mu p(1-p)$, or, using (12.16), $2b = \mu$. This relation is indeed well satisfied, since $\mu = 0.13/2 = 0.065$. So we can indeed deduce the intermittency corrections from the measurements of energy dissipation over a ball ℓ , provided we use the new refined similarity hypothesis (13.2).

13.2 Thermodynamical analogy

13.2.1 The large deviation formulation and thermodynamics

The original Parisi and Frisch formulation is very pedagogical, but a bit empirical. Eyink pointed out that the multi-fractal theory has a more rigorous formulation, in terms of large deviation theory [26]. This formulation is interesting, because it enables to build thermodynamical analogy to multi-fractals [**bohr1987entropy**, **rinaldo1996thermodynamics**, 51] that will be useful to replace the K41 universality which is broken in turbulence. For this, we consider again a scale dependent measure corresponding to the 3-measure (see section ??):

$$d\mu_3 = \frac{|W_\ell|^3}{\langle |W_\ell|^3 \rangle} d\mu_0. \quad (13.3)$$

One can check that $d\mu_3$ has the good properties of a measure: it is positive definite and $\int d\mu_3 = 1$ for any ℓ . Let us now assume that the measure μ_3 follows a large-deviation property as:

$$\mathbb{P}[\log(\mu_3) = E \log(\ell/\eta)] \sim e^{\log(\ell/\eta)S(E)}, \quad (13.4)$$

where $S(E)$ is the large deviation function of $\log(\mu_3)$.

The property given by Eq. 13.4 has a nice thermodynamic interpretation, where $S(E)$ represents of an entropy, $\log(\ell/\eta)$ has the meaning of a volume, and $\log(\mu_3)/\log(\ell/\eta)$ is an energy density.

The entropy is simply connected to the multi-fractal spectrum through $S(E) = C(3h - \zeta(3))$ [[**GFN+19**]]. We can also define a partition function Z associated to the variable $\log(\mu_3)$ through:

$$Z \equiv \langle e^{p \log(\mu_3)} \rangle = \frac{S_{3p}}{S_3^p}, \quad (13.5)$$

where p is a pseudo-inverse temperature $p = 1/kT$. Taking the logarithm of Z , we then get the free energy F as:

$$F \equiv \log(Z) = \log \left(\frac{S_{3p}}{S_3^p} \right). \quad (13.6)$$

By the Gärtner-Elis theorem, F is the Legendre transform of the energy S : $F = \min_E(pE - S(E))$. The thermodynamic analogy is summarized in Table 13.1.

	Thermodynamics	Turbulence
Temperature	$k_B T$	$1/p$
Energy	E	$\log(\mu_3)$
Entropy	S	$C(3h - \zeta(3))$,
Number of d.f.	N	$1/\beta(Re) \sim \log(Re)$
Volume	V	$\log(\ell/\eta)$
Free energy	F	$\log \left(\frac{S_{3p}}{S_3^p} \right)$.

Table 13.1: Summary of the analogy between the multi-fractal formalism of turbulence and thermodynamics.

13.2.2 Recovering universality

The thermodynamic analogy enables to recover a multi-fractal universality using basic properties of the free energy. Indeed, F a priori depends on the temperature T , on the volume V and on the

number of degrees of freedom system N . Further, extensivity of the free energy means that F should follow the homogeneous scaling:

$$F(T, V, N) = NF\left(T, \frac{V}{N}, 1\right). \quad (13.7)$$

Using the analogy of Table 13.1, and introducing the function $\beta = 1/N$, we see that for extensivity to be valid, the structure function should follow the generalized universality law:

$$\beta \log\left(\frac{S_p}{(S_3)^{p/3}}\right) = \mathcal{F}(\beta \log(\ell/\eta)), \quad (13.8)$$

At this point, β is a free parameter. Theories of turbulence usually assume that the number of degree of freedom of turbulence depends on the Reynolds number only i.e. $\beta(Re)$. Vergassola and Frisch [[VF91]] used properties of the dissipative range in the multi-fractal picture to infer that a relation like Eq. 13.8 should hold for the energy spectrum (Fourier transform of S_2), with β depending on the width of the inertial range like: $\beta \sim 1/\log(L/\eta)$, where L is the largest scale of the system. This universal representation is shown in the insert of Figure 13.1-b, and indeed provides a good collapse of the spectra. Since we have $L/\eta \sim Re^{3/4}$, this gives $\beta(Re) \sim 1/\log(Re)$. A few years later, Castaing and his collaborators [[CGM93]] checked empirically the veracity of Eq. 13.8 in turbulent jet by a best collapse procedure, and confirmed this scaling. More recently, Geneste et al. [[GFNV+19]] also check multi-fractal universality using the numerical and experimental data of Figure 2-a. They confirmed that the best collapse is indeed obtained for a function $\beta \sim 1/\log(Re)$. Their result is shown in Figure 2-b. Indeed, it is quite spectacular that see that all data from the 5 different DNS and 5 different experiments at Re between 6×10^2 and 3×10^5 (R_λ between 25 and 2000) indeed collapse on universal curves depending only on the pseudo-temperature $1/p$.

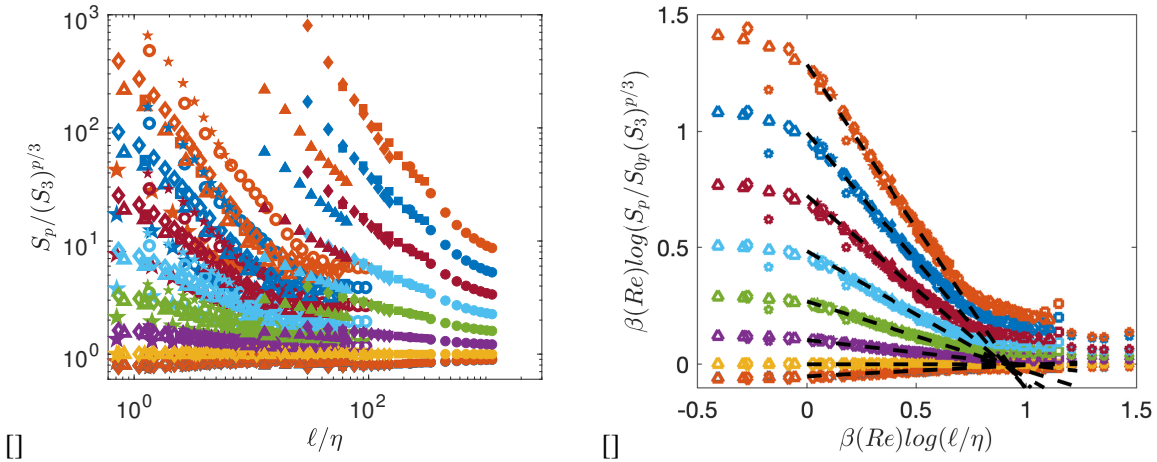


Figure 13.1: Test of universality using structure function based on wavelet transform. **(a)** K41 universality, given by Equation (??); **(b)** multi-fractal universality, given by Equation (13.8). DNS are shown with open symbols, while experiments are shown with filled symbols. The structure functions have been shifted by arbitrary factors for clarity and are coded by color: $p = 1$: blue symbols; $p = 2$: red symbols; $p = 3$: orange symbols; $p = 4$: magenta symbols; $p = 5$: green symbols; $p = 6$: light blue symbols; $p = 7$: dark red symbols; $p = 8$: blue symbols; $p = 9$: red symbols. Note that on that graph, the $p = 1$ symbols are hidden behind the $p = 2$ symbols, because both have very weak intermittency. For K41 universality to hold, all the function should be constant with p , with a level depending on p . The dashed lines are power laws with exponents $\zeta(p) - \zeta(3)p/3$. Figure adapted from Geneste et al. [[GFNV+19]].

Such universality ensures that the relative scaling exponent $\zeta(p) - p\zeta(3)/3 = \mathcal{I}(p) - \mathcal{I}(3)$ - computed as the slope of the dotted line in Figure 2-b- are universal in the sense that they do not depend on Reynolds number nor on boundary conditions. This provides a certain degree of universality to the multi-fractal spectrum, up to a translation by $\zeta(3)$ (which could be not universal, see discussion in Geneste et al. [[GFNV+19]]).

13.3 Local multi-fractal analysis

The multi-fractal formalism summarized in the previous section is essentially global: one is only interested in the probability of having a certain scaling exponent h within the whole volume of the fluid, without trying to localize exactly where the given behaviour takes place. As explained previously, this is essential because there is not such a thing a superposition of self-similar solutions, nor existence of a well given space and/or time location where a self-similar behaviour develops, since this is precluded by several mathematical theorems [11]. Yet, the very phenomenon of intermittency is based on physical processes which are well defined and localized in space and time: they are due to large velocity gradients, arising in an intermittent way, following non-linear dynamics of NSE. If the velocity field were locally self-similar with exponent h , there would however exist a correspondance between this exponent, and the value of velocity gradients smoothed at a fixed scale, since the wavelet coefficient W_ℓ/ℓ^p is nothing more than, within a multiplicative constant, the norm of the smoothed value of the derivative $\nabla^p u$ with respect to a Gaussian. The multiplicative constant is troublesome, in the sense that it forbids the simple identification of h with $\log_\ell W_\ell$. In this section, we summarize how it is possible to use information theory (and the knowledge of $P(h, \ell)$) to derive a one-to-one mapping between the value of the smoothed derivative of u at a given scale, and the value of the corresponding scaling exponent, h . This relies heavily on a work done by Cheskidov and Shvydoy [CS22], that we rephrase in a physical langage, more appropriate for practical applications [[NLKC+19]].

13.3.1 Active regions and the nested (concentration) volume interpretation

To start with, one needs to define what is an intermittent region, or "active" region. This is defined as a region where the magnitude of W_ℓ is large. Then, we consider these velocity wavelet coefficients as "source of information", whose concentration in active regions, A_q is measured by concentration volumes, with well defined co-dimension. The precise definition of A_q is given by:

$$A_q = \{x : b_q \ell^{h(q)} \leq W_\ell\}, \quad (13.9)$$

where the constant b_q at this stage is undefined, and $h(q)$ is a local exponent, playing the role of a Hölder exponent, that is defined according to Eq. (??) as:

$$h(q) = \frac{\langle \log_\ell (W_\ell) (W_\ell)^q \rangle}{\langle (W_\ell)^q \rangle}. \quad (13.10)$$

The volume of active regions is simply given by:

$$V_q = \langle 1_A \rangle \sim \ell^{C^\dagger(q)}, \quad (13.11)$$

where $C^\dagger(q)$ is the co-dimension of the active volume. These definitions guarantee that active volume are *nested*, ie $V_q \subset V_r$ for $q < r$.

13.3.2 Connection with multi-fractal formalism and construction of local exponents

For multi-fractal fields obeying $\langle (W_\ell)^q \rangle \sim \ell^{h(q)}$, we see that $h(q) = d\zeta(q)/dq$, in agreement with the Legendre transform property Eq. (??). This construction shows that the multi-fractal sets of

Parisi and Frisch are necessarily nested, like Russian dolls. It also shows that one can calibrate the values of b_q defining the active regions, by *imposing* that $C^\dagger(q)$, the co-dimension of the volume of the active regions, precisely matches the multi-fractal spectrum $C(h(q))$ which can be *computed* from the whole set of data.

The philosophy of this construction is therefore as follows: one first performs a classic multi-fractal analysis on the data set, to obtain the value of $C(h)$; then, one calibrates the constant b_q so that the co-dimension of the active volume matches the multi-fractal spectrum; this provides a one-to-one correspondance between W_ℓ and a local scaling exponent h , for a given data set. All details are given in [[NLKC+19]]. Figure 13.2-a shows example of a map of local scaling exponent obtained using this procedure on an experimental data set. As expected, isovalues of h are nested. In this example, the procedure is applied for a field resolved at the Kolmogorov scale $\Delta x = \eta$, so that the underlying velocity field is already very smooth. Yet, there are still a few places where h is below 1 (see 13.2-b), so that the field is non-differentiable. The same procedure has been repeated for velocity fields in the inertial range, resulting in values of h even smaller than $h = 1/3$, see [NLD20]. The probability distribution function for h that one can get from such plots (Figure 13.2-b) coincides by construction with $(\Delta x)^{C(h)}$.

Of course, if one changes the precision of the data set, one can get other estimates of $C(h)$, and the whole procedure has to be repeated, providing possibly another mapping. In the same way, if one increases the size of the data set, one can extend the multi-fractal spectrum to lower values of h , and extend the mapping between W_ℓ and h accordingly. In this sense, this local procedure is clearly an information-based procedure.

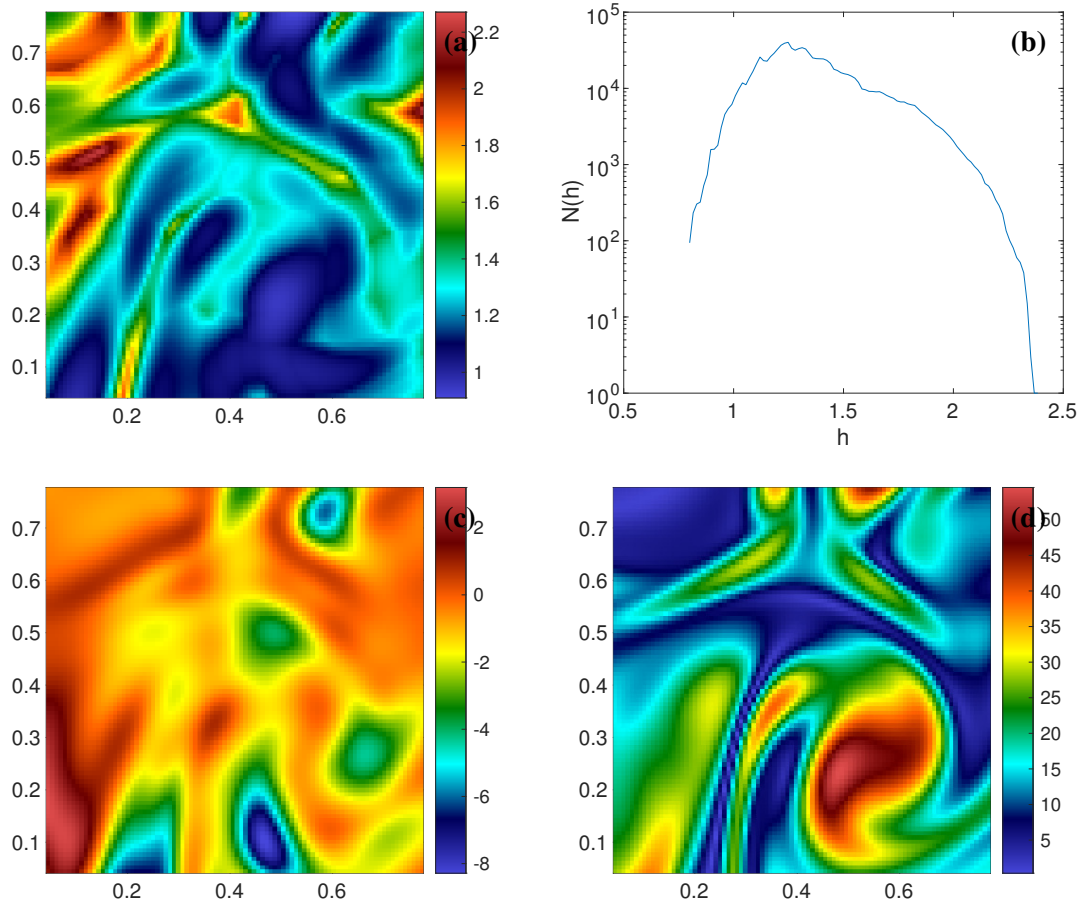


Figure 13.2: Local Holder exponents for experimental data at resolution $\Delta x = \eta$. (a) Map of local Holder exponent. (b) Histogram of values of h in the field of view (a). Most of the values are above $h = 1$ but there are a few events where $h < 1$, meaning non-differentiability. Note that for $h < 2$, the field is not twice differentiable, meaning we cannot define a dissipation. (c) Local-energy transfert for the velocity field corresponding to (a). (d) Vorticity field corresponding to (a).



Modelling turbulence

14	Generalities on Turbulent transport	107
14.1	Introduction	
14.2	Approche Lagrangienne	
14.3	Approche Eulérienne	
14.4	En guise de conclusion	
15	Closures and Computation of turbulent transport coefficients	129
15.1	Basic equations and definitions	
15.2	RANS	
15.3	Large eddy simulations	
15.4	Rapid Distortion Theory	
15.5	Beyond eddy-viscosity models	



14. Generalities on Turbulent transport

14.1 Introduction

14.1.1 Transport turbulent?

Nous avons tous sans le savoir été confrontés à la diffusivité turbulente. En effet, imaginons une pièce dans laquelle quelqu'un allumerait une cigarette. Au bout d'une minute environ, toute la pièce serait envahie par la fumée, au grand dam des associations anti-tabac. Cette simple observation cache en fait un grand mystère. Le processus responsable du "transport" de la fumée dans la pièce est la diffusion, liée à l'agitation des molécules d'air. Elle est caractérisée par un coefficient de diffusivité κ (appelé à partir de maintenant diffusivité) qui vaut, dans l'air, environ $0.1 \text{ cm}^2\text{s}^{-2}$. Le temps de diffusion typique associé à une telle diffusivité, sur une échelle de l'ordre de $L = 10 \text{ m}$ (la taille d'une pièce) est de $T_{diff} = L^2 / \kappa \sim 10^7 \text{ s}$, c'est à dire environ 4 mois! Pour expliquer la diffusion de la fumée dans la pièce sur une échelle d'une minute, on est donc amené à invoquer l'existence d'une diffusivité additionnelle, cent mille fois plus grande que la diffusivité moléculaire, appelée diffusivité turbulente. En effet, comme nous allons le voir, cette diffusivité est engendrée par les mouvements turbulents de l'air dans la pièce. Elle possède certaines propriétés remarquables que nous allons maintenant explorer.

14.1.2 Propriétés générales du transport turbulent

Importance du transport moléculaire

Pour découvrir le mécanisme caché derrière cette diffusivité turbulente, examinons plus en détails l'évolution de la tache de fumée (Fig. 14.1). Sous l'action des mouvements turbulents, la tache perd progressivement sa régularité initiale, pour devenir de plus en plus circonvoluée et tourmentée, avec apparition de petites volutes de plus en plus fines, dans lesquelles la diffusion moléculaire est très efficace, à cause de la présence de forts gradients de vitesse. On voit donc que le rôle essentiel de la turbulence n'est pas de "diffuser" elle-même la fumée, mais de produire dans la tache des échelles assez petites pour que la diffusion moléculaire puisse agir efficacement. On peut résumer ceci en disant que la turbulence ne crée que des petites échelles, alors que la diffusion finale n'est due qu'à la diffusivité moléculaire. Il n'y a donc pas de diffusion turbulente sans diffusion moléculaire! Cette règle est aussi vraie pour la viscosité turbulente: celle-ci est le résultat des transferts d'énergie



Figure 14.1: Evolution d'une tache de fumée sous l'action des mouvements turbulents.

(au cours de la “cascade”) des échelles les plus grandes vers l’échelle dissipative, où la viscosité moléculaire entre en jeu.

Importance de la séparation d'échelle

L’observation de la figure 14.1 nous permet de découvrir une autre caractéristique de la notion de transport turbulent. On peut remarquer en effet que la taille des volutes créées est beaucoup plus petite que l’échelle totale à laquelle se produit le phénomène de diffusion (la taille de la tache, ou de la pièce). Cette séparation d’échelle entre le processus responsable de la diffusion (la turbulence) et l’échelle caractéristique de la diffusion résultante est un des éléments essentiels de toute théorie de transport. Elle se retrouve aussi dans la simple diffusivité moléculaire: cette dernière est le résultat à l’échelle macroscopique des chocs entre particules d’air se produisant sur des échelles de l’ordre du libre parcours moyen. Comme nous le verrons par la suite, cette séparation d’échelle inhérente à tout processus de transport peut et doit être utilisée dans le calcul effectif des coefficients de transport. En principe, on ne peut bâtir une théorie raisonnable sans faire appel à elle.

Différence générique entre diffusivité et viscosité

Une tache de fumée s’étale toujours. C’est la conséquence d’une propriété bien connue du transport de quantité *scalaire*: il est toujours diffusif, avec un coefficient de diffusivité positif. Nous démontrerons cette propriété en section 3.1.2. Par contre, le transport de quantité *vectorielle* n’obéit pas à des propriétés aussi simples. Pour mettre en évidence les difficultés conceptuelles apparaissant dans le cadre du transport de quantité de mouvement, il est pratique d’utiliser un formalisme dû à Reynolds et utilisant la propriété de séparation d’échelles. Considérons un écoulement turbulent v , correspondant au signal représenté en figure 14.2, et obéissant à l’équation de Navier-Stokes

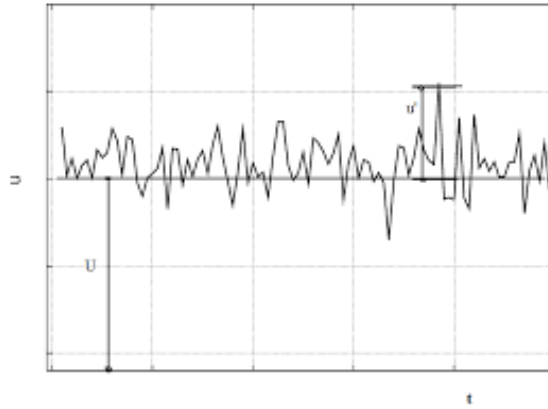


Figure 14.2: Un signal turbulent typique, avec une composante moyenne et une composante aléatoire, de moyenne nulle.

incompressible forcée par une force f s’annulant en moyenne sur une période τ :

(14.1)

$$\text{grad} \cdot \mathbf{v} = 0 \quad (14.2)$$

$$\partial_t \mathbf{v} + (\mathbf{v} \cdot \partial) \mathbf{v} = -\partial p + \nu \partial^2 \mathbf{v} + \mathbf{f}. \quad (14.3)$$

On voit en figure 14.2 que le signal turbulent est fait de deux composantes distinctes: une composante variant sur une échelle de temps courte, $u(\tau)$, appelée fluctuation et qui s’annule en moyenne sur une échelle de temps plus grande que τ ; une composante variant sur une échelle de temps plus longue $W(T)$ et qui définit l’écoulement turbulent moyen aux temps longs. Nous écrirons donc:

$$\mathbf{v} = \mathbf{u}(\tau) + \mathbf{W}(T), \quad \langle \mathbf{u} \rangle = 0, \quad \langle \mathbf{v} \rangle = \mathbf{W} \quad (14.4)$$

où le symbole $\langle \rangle$ signifie moyenne sur des temps du même ordre où plus long que τ . En injectant la décomposition (16.9) dans l’équation de Navier-Stokes et en moyennant, on peut trouver l’équation gouvernant l’évolution de la composante moyenne de l’écoulement, qui s’écrit:

$$\partial_t W_i + W_j \partial_j W_i = -\partial_i \langle p \rangle + \nu \partial^2 W_i - \partial_j \langle u_i u_j \rangle. \quad (14.5)$$

On reconnaît là une équation de Navier-Stokes, forcée par le terme $-\partial_j \langle u_i u_j \rangle$. Les quantités $\langle u_i u_j \rangle$, qui représentent l’action des fluctuations turbulentes à petite échelle sur l’écoulement moyen, sont appelées tensions de Reynolds. Pour déterminer précisément l’action de ces tensions de Reynolds, il faut arriver à les exprimer en fonction de l’écoulement moyen. C’est le problème bien connu de “cloture” des équations moyennes. Pour cela, nous pouvons utiliser des arguments généraux de type champs moyen, en utilisant la séparation d’échelle. En effet, les gradients successifs de \mathbf{W} sont d’ordre $\partial^n \mathbf{W} = O((\tau/T)^n)$. A cause de la séparation d’échelle, $\tau/T \ll 1$, et il semble alors naturel de faire un développement des tensions de Reynolds en gradient de \mathbf{W} :

$$\langle u_i u_j \rangle = -\alpha_{ij\ell} W_\ell - \nu_{ij\ell m} \partial_\ell W_m + O(\partial^2 W), \quad (14.6)$$

où $\alpha_{ij\ell}$ et $\nu_{ij\ell m}$ sont deux tenseurs dépendant des fluctuations, et qu’il faudrait calculer explicitement pour clore le problème. Nous verrons en section 3 une méthode systématique permettant le calcul explicite de ces deux tenseurs. Nous pouvons cependant dès à présent faire quelques remarques

générales liées uniquement à la forme de développement (14.6). Pour cela, nous pouvons remplacer (14.6) dans (14.5), pour obtenir:

$$\partial_t W_i + W_j \partial_j W_i = -\partial_i < p > + \alpha_{ij\ell} \partial_j W_\ell + (\nu \delta_{im} \delta_{kl} + v_{iklm}) \partial_k \partial_\ell W_m. \quad (14.7)$$

On reconnaît dans le dernier terme de (14.7) un terme diffusif, représentant la “viscosité turbulente”. Cependant, la présence du terme proportionnel au gradient de \mathbf{W} peut induire un effet bien différent d'un simple effet diffusif, et qui domine en général l'effet de viscosité turbulente (ordre $O(\tau/T)$ au lieu de $O((\tau/T)^2)$). Cet effet, connu sous le nom de Anisotropic Kinetic Alpha (effet AKA), est l'équivalent hydrodynamique du célèbre effet alpha en magnétohydrodynamique [63][31][64][50]. Il donne lieu à des transferts d'énergie des petites échelles vers les grandes échelles par des cascades inverses [31][64]. Cela conduit à la formation de grandes structures dans un écoulement turbulent, comme la génération de tourbillons à grande échelle dans un disque d'accrétion [35]. La présence ou non de cet effet (et donc le comportement diffusif ou non) est reliée aux symétries de l'écoulement. Cet effet est étudié plus en détail en section 3.2.1.

Importance des symétries

Il existe un certain nombre de cas simples où l'effet AKA disparaît, et où le comportement du système à grande échelle est de type diffusif. Ces cas, correspondants à des écoulements avec des symétries particulières, comprennent:

N1) les écoulements isotropes; en effet, il n'existe pas de tenseurs isotropes du troisième ordre, ce qui rend le tenseur $\alpha_{ij\ell}$ forcément nul dans ce cas.

N2) les écoulements invariants de parité, c'est à dire qui possèdent un centre de symétrie; en effet, le tenseur $\alpha_{ij\ell}$ est un pseudo-scalaire, qui s'annule dans ce cas précis (voir section 3.1.3.).

N3) les écoulements cisailés, c'est à dire ne dépendant que de la variable orthogonale à leur direction. L'exemple le plus simple est donné par un écoulement bi-dimensionnel,

$$\mathbf{u} = u(x) \mathbf{e}_y.$$

A l'inverse, on peut suspecter la présence d'un effet AKA dès que les deux conditions suivantes sont **simultanément** satisfaites:

O1) le système est soumis à une force extérieure (gravité, champs magnétique, force de Coriolis); en effet, la présence de cette force entraîne une brisure de l'invariance galiléenne, nécessaire pour justifier le premier terme du développement de (14.6).

O2) le système est anisotrope (cf condition N1). Cette anisotropie peut être créée par divers processus, comme la stratification, ou la rotation.

Importance du caractère tensoriel

En parlant de diffusivité ou viscosité turbulente, on commet un abus de langage, qui masque une propriété essentielle de ces deux quantités: en fait, ce sont toutes les deux des tenseurs, respectivement du second et du quatrième ordre. En tant que tels, elles ne sont pas forcément isotropes, c'est à dire qu'elles ne peuvent pas toujours s'exprimer par un seul coefficient. Par exemple, dans un système en rotation, le transport dans le plan perpendiculaire à l'axe de rotation est beaucoup moins efficace que le transport le long de l'axe de rotation, et il faut au moins deux coefficients pour tenir compte de cet effet [21].

D'autres effets exotiques sont liés au caractère tensoriel. Par exemple, alors que les diffusivités turbulentes sont toujours positives (nous le démontrerons en section 3.1.2), les viscosités turbulentes peuvent être négatives [23, 33], voire imaginaires [69]! En effet, à toute viscosité turbulente est associée une matrice carrée de dimension la dimension du système, grâce à la décomposition en ondes planes:

$$W_i = W_{i0} \exp(-\sigma t + q_j x_j). \quad (14.8)$$

Si W_i obéit à l'équation de diffusion:

$$\partial_t W_i = v_{ik\ell m} \partial_k \partial_\ell W_m, \quad (14.9)$$

on peut alors écrire:

$$\sigma W_{i0} = N_{im} W_{m0}, \quad (14.10)$$

où N est la matrice $N_{im} = v_{ik\ell m} q_k q_\ell$. La viscosité négative ou imaginaire correspond au cas où N a une ou plusieurs valeurs propres négatives ou imaginaires. Cela engendre des taux de croissance positifs ou imaginaires, c'est à dire des instabilités ou des comportements oscillants ("élastiques"). L'instabilité visco-négative est discutée plus en détails en section 3.2.2.

Calcul dimensionnel

La viscosité et la diffusivité ont la dimension du produit d'une vitesse par une longueur. On pourra donc toujours écrire, en ordre de grandeur:

$$\kappa_t, v_t = Cv_t l_t, \quad (14.11)$$

où v_t et l_t sont une vitesse et une longueur caractéristiques de l'écoulement, et C une constante à calculer. Si on choisit bien v_t et l_t (c'est à dire qu'ils représentent bien les mouvements responsables de la viscosité ou de la diffusivité), on peut s'attendre à ce que C ne prenne pas des valeurs archipetites 10^{-8} , ou archi-grandies 10^8 . Cela ne veut pas dire cependant que C est forcément d'ordre unité! Des valeurs de 10^{-2} par exemple, ne sont pas à exclure (cf [19]). En fait, seul un calcul explicite, selon la méthode développée en section 3 par exemple, permet de déterminer la valeur de C . Cette valeur dépend de l'écoulement considéré (elle peut même être négative!), et en particulier des forces extérieures en présence (rotation, gravité...) [21].

On voit que le raisonnement dimensionnel appliqué à l'estimation de la viscosité ou diffusivité turbulente a des limites infranchissables. Il permet cependant d'expliquer qualitativement certains faits observationnels. Par exemple, Richardson a remarqué que la diffusivité turbulente dans certains systèmes géophysiques (océan, atmosphère) suivaient une loi simple dépendant de l'échelle d'observation, ℓ (cf Figure 14.3):

$$\kappa_t(\ell) = C_R \ell^{4/3}. \quad (14.12)$$

Cette loi, dite "loi de Richardson", peut s'expliquer simplement par un argument dimensionnel appliqué à la turbulence isotrope homogène. Selon la théorie phénoménologique de Kolmogorov, un tel système est caractérisé par la conservation de la dissipation de l'énergie $\varepsilon = d_t(v^2)$ le long de la cascade (i.e. ε est indépendant de l'échelle). Comme dimensionnellement, le temps de dissipation de l'énergie est d'ordre un temps de retournement $\tau = l/v$, on obtient $v^3/l = \varepsilon = cte$, soit $v = \varepsilon^{1/3} l^{1/3}$. Cette loi simple de variation de la vitesse typique en fonction de l'échelle permet de retrouver le fameux spectre d'énergie en $k^{-5/3}$ caractéristique des systèmes turbulents. Appliquée à l'évaluation de la diffusivité $\kappa_t = Cv_t l_t$, elle permet d'obtenir $\kappa_t = C\varepsilon^{1/3} l_t^{4/3}$, ce qui est exactement la loi de Richardson. En particulier, cela montre que le coefficient C_R intervenant dans la loi de Richardson n'est pas universel et dépend de la quantité d'énergie injectée dans le système.

14.1.3 Comment modéliser le transport turbulent?

Il existe a priori deux méthodes pour modéliser le transport turbulent. L'une, basée sur une approche que je qualifierais abusivement de lagrangienne, car elle consiste à suivre la trajectoire d'une particule, est plus souvent utilisée pour décrire le transport lié aux ondes [36]; l'autre, basée sur une approche eulérienne, est couramment utilisée dès que l'on décrit le transport dû à la turbulence. Je vais commencer par décrire brièvement ces deux méthodes, et montrerai ensuite qu'elles sont équivalentes et complémentaires.

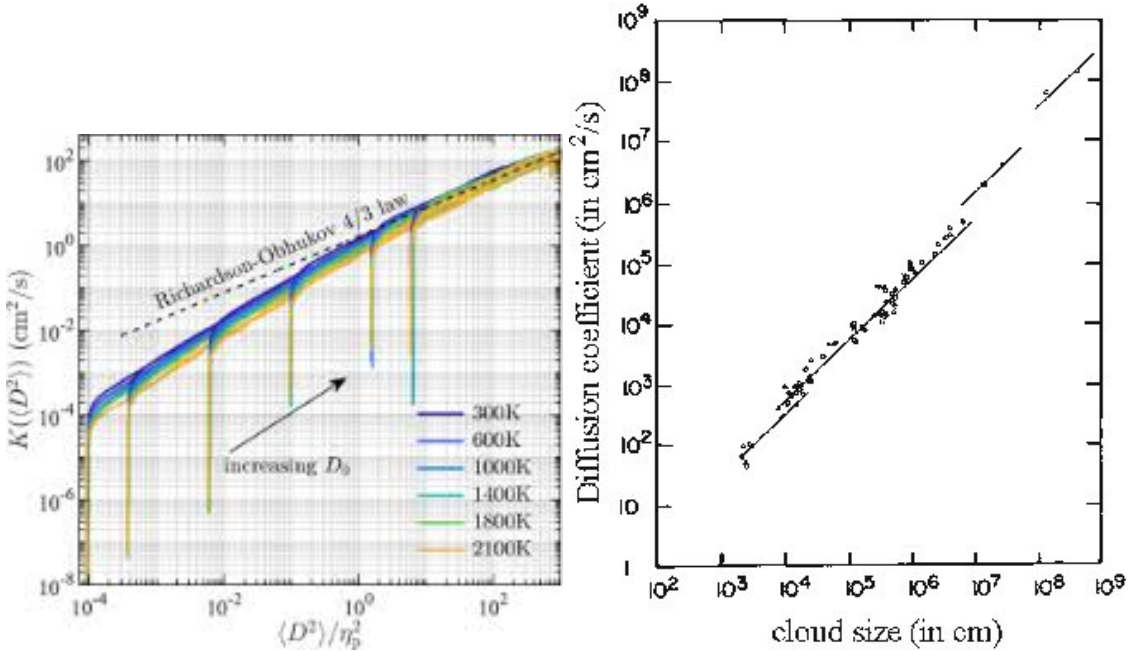


Figure 14.3: Loi de Richardson (a) dans une expérience de combustion; (b) dans les nuages: la diffusivité turbulente varie comme $l^{4/3}$.

Approche "lagrangienne"

Dans cette approche, on s'intéresse aux trajectoires d'une particule placée dans un écoulement donné, caractérisé par la donnée (analytique ou numérique) de sa vitesse en tout point et en tout temps $u(x, t)$. La particule placée en position x obéit alors simplement à l'équation du mouvement (traduisant que la particule "suit" le fluide):

$$\dot{x} = u(x, t). \quad (14.13)$$

La diffusion dans cette approche est obtenue en étudiant la dispersion d'un nuage de particules au cours du temps. Pour cela, on définit une moyenne d'ensemble, en faisant une moyenne sur les conditions initiales, ou, cela revient au même, sur le numéro de la particule appartenant au nuage initial. Ainsi, on aura, pour un nuage composé de N particules, suivant une trajectoire donnée par $x_i(t)$, $i = 1 \dots N$:

$$\langle x \rangle = \frac{1}{N} \sum_{i=1}^N x_i(t). \quad (14.14)$$

Le coefficient de diffusion κ sera alors simplement obtenu grâce à:

$$\kappa t = \langle x^2 \rangle - \langle x \rangle^2. \quad (14.15)$$

Approche "eulérienne"

Dans cette approche, on définit une fonction de distribution $\rho(x, t)$ décrivant la concentration des particules en un point x , au temps t . Cette fonction de distribution obéit à l'équation de diffusion:

$$\begin{aligned} \partial_t \rho + \partial_x(u\rho) &= \partial_x(\kappa \partial_x \rho), \\ \rho(x, 0) &= \rho_0(x). \end{aligned} \quad (14.16)$$

Ici, le paramètre κ mesure l'étalement de la distribution au cours du temps. En définissant cette fois la moyenne par:

$$\langle x \rangle = \int \rho(x, t) x dx, \quad (14.17)$$

on a toujours la relation (14.15).

Lien entre les deux approches

De par l'existence de la relation (14.15) dans les deux cas, on se doute que les deux approches sont en fait étroitement liées. Ceci est dû à un résultat bien connu, permettant d'associer une équation de Focker-Planck à tout processus de Langevin. Un tel processus décrit le mouvement d'une particule soumise d'une part à une force de friction solide $-\gamma u$, et de l'autre à un mouvement d'agitation brownien $\zeta(t)$, défini complètement par sa fonction d'autocorrélation:

$$\langle \zeta(t) \zeta(t + \tau) \rangle = 2\kappa \delta(t - \tau).$$

La particule obéit alors à l'équation:

$$\dot{x} = -\gamma u + \zeta(t). \quad (14.18)$$

On peut alors montrer qu'il existe un fonction de distribution $\rho(x, t)$, décrivant la probabilité de présence d'une particule au point x , au temps t , et qu'elle obéit à l'équation de Focker-Planck:

$$\partial_t \rho + \partial_x (-\gamma u \rho) = \partial_x (\kappa \partial_x \rho). \quad (14.19)$$

On voit donc que l'approche lagrangienne est reliée à une description Langevin, alors que l'approche eulérienne est reliée à une description Focker-Planck, qui sont en fait équivalentes. Dans la suite du cours, nous allons aborder les deux approches, pour montrer ce qu'on peut retirer de chacune des approches.

14.2 Approche Lagrangienne

14.2.1 Particules neutres

Les particules neutres sont des particules qui suivent exactement un écoulement donné $u(x, t)$. Une particule neutre placée initialement en x_0 suit donc une trajectoire définie par

$$\begin{aligned} \dot{x} &= u(x, t), \\ x(t=0) &= x_0. \end{aligned} \quad (14.20)$$

Les propriétés de la trajectoire suivie par une particule neutre dépendent bien évidemment des propriétés de l'écoulement dans lequel la particule est plongée. En particulier, nous verrons que les structures cohérentes (tourbillons) présentes dans l'écoulement jouent un rôle essentiel. Par contre, le lien entre les trajectoires des particules neutres et les propriétés de l'écoulement n'est pas toujours direct. Cela oblige à une certaine prudence lorsqu'on veut par exemple étudier un écoulement en l'ensemencant avec des particules neutres, et en étudiant les trajectoires suivies. Par exemple, il n'y a pas de lien direct entre le chaos des trajectoires et les propriétés chaotiques de l'écoulement de base. Cette particularité des trajectoires des particules neutres a été étudiée en détail par Babiano et al. [4] en utilisant la méthode des exposants de Lyapunov. Une des propriétés essentielle du chaos est la sensibilité du résultat par rapport aux conditions initiales, qui est elle même reliée à la divergence des trajectoires proches: deux trajectoires x_A et x_B , initialement infiniment proches dans l'espace des phases (conditions initiales quasiment identiques) divergent au cours du temps avec une séparation croissant exponentiellement $|x_A - x_B| \sim \exp(\Lambda t)$. Le coefficient Λ caractérisant la

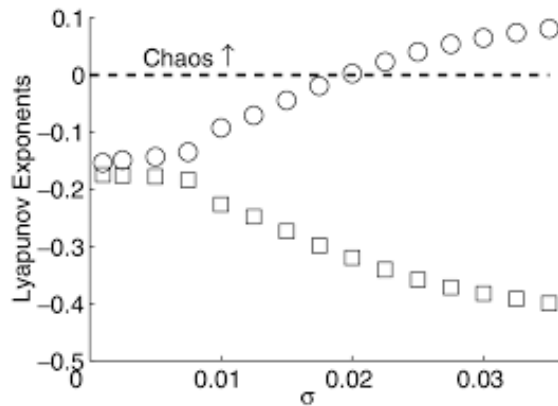


Figure 14.4: Lyapunov exponent in a chaotic and laminar fluid.

rapidité de divergence des trajectoires est appelé exposant de Lyapunov. Lorsqu'il est positif, les trajectoires sont chaotiques.¹ Babiano et al. ont donc mesuré cet exposant de Lyapunov pour deux types d'écoulement: un écoulement régulier, sans chaos, et un écoulement chaotique (imprédictible) (Figure ??).

Dans les deux cas, les trajectoires suivies par les particules se divisent en deux classes: les trajectoires de type "régulières", pour lesquels on ne peut définir un exposant de Lyapunov (il décroît comme $1/t$); les trajectoires "chaotiques", caractérisées par un exposant de Lyapunov positif (Figures ??). La division entre les deux classes ne dépend que de la position initiale de la particule, et non de l'écoulement de base: si la particule a été placée initialement proche du cœur d'un tourbillon, sa trajectoire sera régulière; en revanche, si la particule a été placée dans le "marécage", loin de tout tourbillon, sa trajectoire sera chaotique. Cette propriété, démontrée ici pour des écoulements déterministes, peut aussi être vérifiée pour des écoulements turbulents. Cela a des conséquences importantes sur la diffusion dans un écoulement donné. En effet, la diffusion est d'autant plus importante que la capacité à diverger des trajectoires est grande (la dispersion augmente!). On s'attend donc à observer une plus grande diffusion dans les zones où les trajectoires sont chaotiques, c'est à dire entre les tourbillons. En effet, lorsque on ensemence un nuage de particule dans le marécage entre plusieurs tourbillons, il prend rapidement une forme de plus en plus compliquée, traduisant une diffusion.

A l'inverse, un ensemencement au cœur d'un tourbillon ne produit aucun effet sur la forme du nuage de point, qui se déplace juste erratiquement en suivant le tourbillon (Figure 14.5).

L'ensemencement d'un écoulement turbulent bi-dimensionnel est tout aussi spectaculaire (Figure 14.6). On voit que les particules ont peu à peu tendance, sous l'action de la diffusion, à envahir tout l'espace entre les tourbillons, sans pénétrer dans les coeurs des tourbillons. Ces derniers agissent comme des pièges, en maintenant capturées les particules placées initialement dedans. Cette propriété de piégeage, qui s'oppose à la diffusion, peut provoquer dans l'écoulement une diffusion dite "anormale".

14.2.2 Diffusion anormale

En général, la diffusion s'accompagne d'une dispersion augmentant avec le temps comme (voir introduction):

$$\langle x^2 \rangle - \langle x \rangle^2 = \kappa t, \quad (14.21)$$

¹Bien sur, si l'on mesure un Lyapunov effectif décroissant comme $1/t$, alors la divergence des trajectoires n'est pas exponentielle et les trajectoires ne sont pas chaotiques!

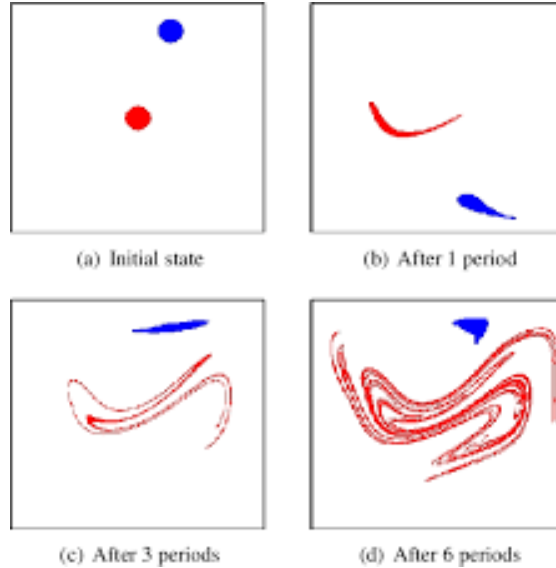


Figure 14.5: Evolution temporelle d'un ensemble de particules ensemencées initialement dans le cœur d'un tourbillon (en bleu) et à côté du tourbillon (en rouge).

où κ est le coefficient de diffusivité. Dans certains cas, cependant, la diffusion s'accompagne d'une dispersion variant avec le temps comme;

$$\langle x^2 \rangle - \langle x \rangle^2 \sim t^{1+\mu}, \quad \mu \neq 0. \quad (14.22)$$

On parle alors de diffusion "anormale". Si $\mu > 0$, la dispersion est plus rapide que au cours d'une diffusion classique. On a affaire à une hyperdiffusion. Dans le cas contraire ($\mu < 0$), on a une sous-diffusion.

Un des exemples les plus classiques de diffusion anormale est celle dont la diffusivité suit la loi de Richardson (14.12). En effet, la dispersion correspondante va comme $\kappa t = C_R \ell^{4/3} t$. D'après la loi de Kolmogorov, le temps et l'échelle sont reliés par $t \sim \ell/v \sim \ell^{2/3}$. La dispersion augmente donc comme t^3 . C'est une hyperdiffusion. Un autre exemple de diffusion anormale est obtenu en considérant la diffusion dans un système convectif [6]. Dans ce cas, on observe une sous-diffusion, avec un coefficient μ dépendant des conditions aux limites: $\mu = -1/2$ dans le cas de frontières libres (vitesse constante aux parois); $\mu = -1/3$ dans le cas de frontières sans glissement (vitesse nulle aux parois).

Dans la plupart des cas, la diffusion anormale s'explique soit par des corrélations dans le champs de vitesse de l'écoulement $\langle u(x+l)u(x) \rangle \sim l^\alpha$, soit par un piègeage des particules. La démonstration du lien entre corrélations de vitesse et diffusion anormale (cas Richardson par exemple) est un peu compliquée et fait appel à des notions de groupe de renormalisation. On pourra la trouver dans Bouchaud et Georges [6]. Par contre, la démonstration dans le cas du piègeage est plus simple et fort illustrative des processus mis en jeu. Nous allons donc l'esquisser ici. Plaçons nous pour simplifier dans le cas unidimensionnel. On peut alors schématiser un processus de diffusion en considérant que les particules se déplacent par bonds discrets successifs de longueur ℓ_n , effectués chacun après un temps d'attente τ_n (voir figure 14.7). On suppose de plus que les longueurs successives ne sont pas corrélées entre elles, et sont caractérisées par une distribution de moyenne nulle, et de variance finie $\langle \ell^2 \rangle$. Enfin, on suppose que les temps d'attente sont caractérisés par une distribution $\psi(\tau)$. Au bout de N sauts, la distance parcourue par une particule

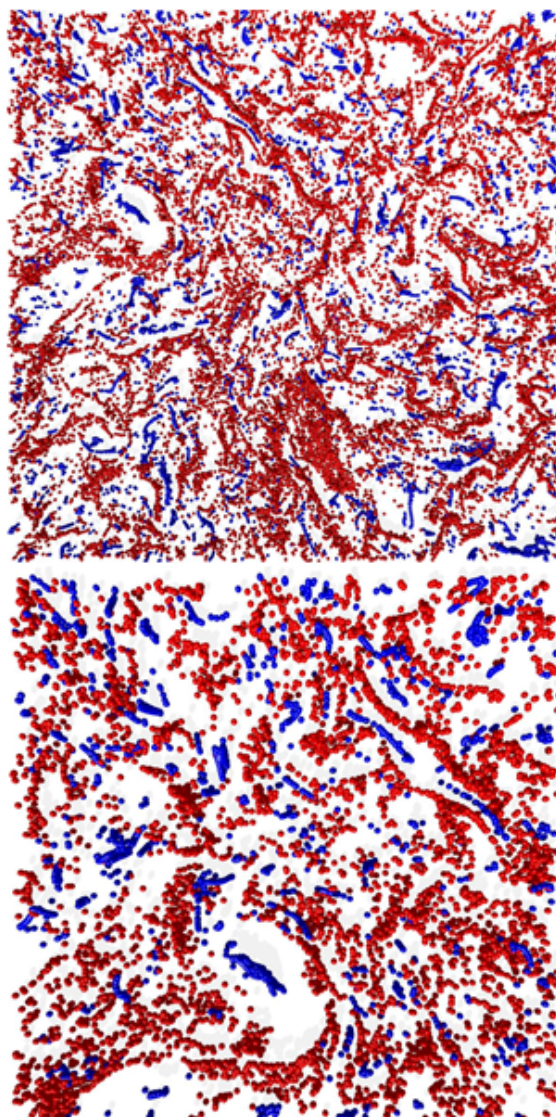


Figure 14.6: Evolution temporelle d'un ensemble de particules ensemencées initialement dans un écoulement turbulent :top particules lourdes; bas: particules legeres.

est:

$$x_N = \sum_{n=1}^N \ell_n. \quad (14.23)$$

Cette distance a été parcourue en un temps:

$$t_N = \sum_{n=1}^N \tau_n. \quad (14.24)$$

En moyennant les expressions ci-dessus, on obtient donc:

$$\begin{aligned} \langle x_N \rangle &= 0, \\ \langle x_N^2 \rangle &= N \langle \ell^2 \rangle. \end{aligned} \quad (14.25)$$

Si la distribution des temps d'attente est caractérisée par une moyenne finie, $\langle \tau \rangle$, le temps moyen t nécessaire pour obtenir (14.25) est:

$$t = N \langle \tau \rangle, \quad (14.26)$$

et donc la dispersion obéit à une loi de diffusion classique:

$$\langle x^2 \rangle - \langle x \rangle^2 = \kappa t,$$

avec $\kappa = \langle \ell^2 \rangle / \langle \tau \rangle$. C'est le cas Brownien usuel. Imaginons maintenant que la distribution des temps d'attente soit "large", correspondant à une loi:

$$\psi(\tau) = \tau_0^\beta \tau^{-(1+\beta)}, \quad 0 \leq \beta < 1. \quad (14.27)$$

Dans ce cas, la moyenne des temps d'attente est infinie: $\langle \tau \rangle = \int \tau \psi(\tau) d\tau = \infty$. Cela correspond à une situation où la probabilité qu'une particule reste infiniment longtemps à un même site est non nulle: il y a piégeage de certaines particules. On peut néanmoins calculer la loi de dispersion des particules en considérant $\tau_c(N)$, le plus grand temps d'attente obtenu en N sauts. Par définition, on remarque que cela veut dire qu'il y a au plus une valeur du temps d'attente plus grande que τ_c en N sauts. On peut donc écrire:

$$N \int_{\tau_c}^{\infty} \psi(\tau) d\tau = 1, \quad (14.28)$$

ce qui nous donne, en utilisant (14.27),

$$\tau_c(N) \sim \tau_0 N^{1/\beta}. \quad (14.29)$$

On peut alors écrire, puisqu'il n'y a pas de valeurs de τ plus grandes que τ_c :

$$t \sim N \int_0^{\tau_c(N)} \tau \psi(\tau) d\tau = \tau_0 N^{1/\beta}. \quad (14.30)$$

On voit donc que la dispersion obéit à :

$$\langle x^2 \rangle - \langle x \rangle^2 \sim t^\beta.$$

C'est une sous-diffusion: comme on pouvait s'y attendre, le piégeage diminue l'efficacité de la diffusion.

Figure 14.7: Modèle de diffusion par sauts sur réseaux. La particule saute de noeuds en noeuds, situés à des distances l_n , après un temps d'attente τ_n .

14.2.3 Particules lourdes/légères

Jusqu'à présent, nous n'avons considéré que des particules de même densité que le fluide les transportant. Un modèle plus réaliste consiste à prendre en compte la possibilité que les particules soient plus denses (particules "lourdes") ou moins denses (particules "légères") que le fluide. On peut ainsi décrire le comportement de bouées dans l'océan, des aérosols dans l'atmosphère ou des particules de poussière dans la nébuleuse protoplanétaire. Au lieu d'être advectées passivement, les particules lourdes ou légères sont soumises à deux forces principales: une force qui tend à les mettre en mouvement en suivant le fluide par l'intermédiaire principalement des forces de pression; une force de frottement des particules sur les particules fluides. L'équation du mouvement d'une particule lourde ou légère de densité ρ_p et de taille a , indiquée par $x(t)$, dans un fluide de vitesse $u(x,t)$ donnée et de densité ρ_f est alors:

$$\rho_p \frac{d^2x}{dt^2} = \rho_f \frac{du}{dt} - \frac{9\mu}{2a^2} \left(\frac{dx}{dt} - u \right). \quad (14.31)$$

Le premier terme représente l'accélération de la particule. Le second, la force exercée par le fluide. Le troisième est la force de friction solide, dite friction de Stokes, valable pour des petites particules. Cette force tend principalement à ramener la vitesse des particules proche de celle du fluide. μ est un coefficient dépendant de la vitesse du son. On peut encore réécrire cette équation en introduisant le paramètre $\delta = \rho_f/\rho_p$, qui dépend du type de la particule (δ vaut 1 pour les particules neutres, et est plus grand que un pour les particules légères, et plus petit que un pour les particules lourdes):

$$\frac{d^2x}{dt^2} = \delta \frac{du}{dt} - \gamma \left(\frac{dx}{dt} - u \right). \quad (14.32)$$

γ , homogogène à l'inverse d'un temps, est le coefficient de friction. Le comportement d'une particule dépend donc de deux paramètres, δ et γ . On peut facilement vérifier que, pour $\delta = 1$ (particule neutre), la vitesse de la particule s'ajuste à la vitesse du fluide en un temps de l'ordre de $1/\gamma$, et on est alors ramené à la situation décrite en section 2.1. Par contre, pour δ différent de un, on peut s'attendre à des comportements variés. Crisanti et al [13] ont étudié ces comportements en intégrant numériquement l'équation du mouvement (14.32) pour divers champs de vitesse et diverses valeurs de γ et δ . Encore une fois, les trajectoires sont fortement influencées par la présence de structures cohérentes dans l'écoulement. On trouve ainsi que les particules lourdes ($\delta < 1$) sont "capturées" par les tourbillons, alors que les particules légères ($\delta > 1$) sont éjectées des tourbillons et se répartissent de façon homogène dans le marécage (Figure ??).

Notons cependant que ce résultat peut être modifié sous l'influence de forces extérieures. Par exemple, Tanga et al [65] ont étudié le comportement de particules lourdes et légères dans un fluide en rotation. Il faut alors tenir compte de la force de Coriolis, et l'équation du mouvement s'écrit:

$$\frac{d^2x}{dt^2} = \delta \frac{du}{dt} - \gamma \left(\frac{dx}{dt} - u \right) + 2\Omega \left(\delta u - \frac{dx}{dt} \right). \quad (14.33)$$

Dans ce cas, toutes les particules sont capturées par les tourbillons, mais correspondant à des sens de rotation différents: les particules lourdes sont capturées par les tourbillons anti-cycloniques, alors que les particules légères sont capturées par les tourbillons cycloniques. Cette observation pourrait avoir des conséquences importantes en géophysique (le trou d'ozone) ou en astrophysique, notamment dans le cadre de la formation du système solaire. Elle permet notamment d'expliquer la formation des planètes par capture des poussières dans les tourbillons (cf Tanga et al pour plus de détails).

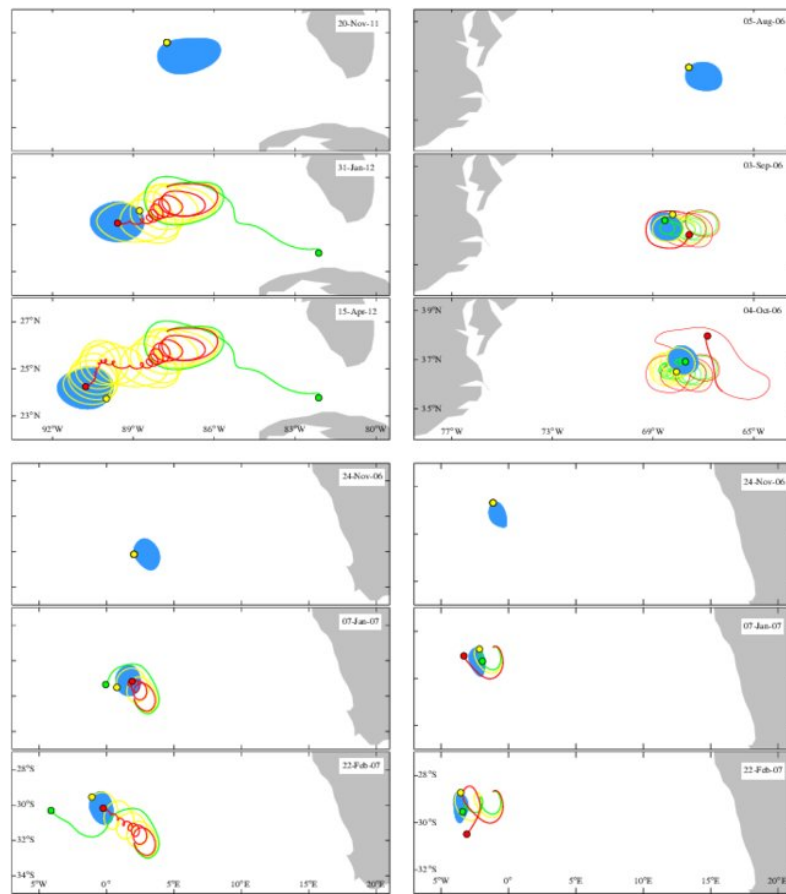


Figure 14.8: Trajectoires des particules lourdes (red), legeres (vertes) et neutres (jaunes) dans un tourbillon oceânique à meso échelle (en bleu).

14.3 Approche Eulérienne

A partir de maintenant, nous allons nous concentrer sur la description du transport par des équations type Fokker-Planck. Je vais décrire une méthode systématique de calcul des coefficients de transport (dont certaines propriétés ont déjà pu être par ailleurs étudiées par des arguments généraux de symétries). Cette méthode s'applique en principe aussi bien aux écoulements connus analytiquement, que ceux donnés numériquement. Elle possède donc un champ d'application très vaste.

14.3.1 La méthode multi-échelle

Esprit de la méthode

Nous avons vu en introduction qu'une des propriétés fondamentale associée à la notion de transport turbulent était la séparation d'échelle: un écoulement turbulent, d'échelle caractéristique l_t , provoque une diffusion à une échelle L beaucoup plus grande $l_t/L \ll 1$. Nous voyons donc apparaître un paramètre naturel de développement, la séparation d'échelle $\varepsilon = l_t/L$. Plus nous serons dans les conditions d'application de la théorie de transport, plus la séparation d'échelle sera satisfaite, et plus ε sera petit. Il paraît alors naturel d'exploiter ce petit paramètre, et d'effectuer des développements asymptotiques, en ε , des quantités physiques associées au problème (température, concentration, quantité de mouvement). L'originalité de la méthode multi-échelle est de prendre aussi en compte les différentes échelles de variation de ces quantités (l_t et L , plus les temps associés), en développant aussi les opérateurs (∂_t et ∂_x). Cela est équivalent à considérer l'existence de deux sortes de variables indépendantes dans le problème: les variables rapides x et t , caractéristiques de l'écoulement de base produisant le transport, et les variables lentes, X et T , à l'échelle desquelles se produit le transport. Cette hypothèse qui peut paraître un peu choquante (on a du mal à voir comment l'échelle du transport serait indépendante de l'échelle de l'écoulement de base!) peut en fait se justifier par des arguments théoriques basés sur des développements en mode de Fourier (Frisch, résultat non publié).

Avant de passer à l'application de ce principe de base simple, il est bon de faire un petit rappel mathématique d'algèbre linéaire². Au cours de la mise en œuvre de la méthode, nous nous retrouverons en effet confrontés au problème de trouver des solutions à des équations de type

$$A\Psi = \Phi, \quad (14.34)$$

où A est un opérateur différentiel linéaire et Φ une fonction (un élément d'un espace vectoriel). Une telle équation n'a de solution que si Φ appartient à l'image de A . On voit alors que la solution Ψ n'est définie qu'à un élément du noyau de A près. Lorsque l'espace vectoriel est muni d'un produit scalaire, une condition équivalente à l'existence d'une solution est que Φ appartienne à l'orthogonal du noyau de l'adjoint de A , noté A^\dagger .

Dans le cas où l'espace vectoriel considéré est formé des fonctions qui sont périodiques en temps et en espace (qui est le cas qui va nous intéresser), cette condition équivalente prend une forme très simple. Le produit scalaire de deux fonctions périodiques Φ et Ψ est en effet égal à:

$$\begin{aligned} \Psi \cdot \Phi &\equiv \int_0^{l_0} dx \int_0^{t_0} dt \Psi(x, t) \Phi(x, t) \\ &= \langle \Phi \Psi \rangle, \end{aligned} \quad (14.35)$$

où l_0 et t_0 sont les deux périodes, et le symbole $\langle \rangle$ représente une moyenne spatio-temporelle sur une période. De plus, les opérateurs A que nous allons considérer seront tous tels qu'ils auront

²Il est fortement conseillé, si on veut comprendre ce qui suit, de repasser un cours d'algèbre linéaire si on a oublié ce qu'était un espace vectoriel, un noyau, un adjoint, un produit scalaire.... Mais on peut aussi accepter bêtement les résultats et les appliquer comme des recettes lors de la mise en application de la méthode multi-échelle.

toujours des opérateurs différentiels agissant à gauche (exemple: $A = \partial_t + \partial_i u_i - \kappa \partial_i \partial_i$). En utilisant la définition de l'opérateur adjoint à partir du produit scalaire et en effectuant une intégration par partie, on voit alors que l'opérateur adjoint sera tel qu'il aura toujours des opérateurs différentiels agissant directement à droite (exemple: $A^\dagger = -\partial_t - u_i \partial_i - \kappa \partial_i \partial_i$). On peut alors facilement vérifier que toutes les fonctions constantes sont dans le noyau de A^\dagger . En fait, si le système n'est pas instable à petite échelle (auquel cas, il n'y a plus de sens à regarder ses propriétés à grande échelle), le noyau de A^\dagger est constitué uniquement des fonctions constantes. On voit donc que la condition nécessaire et suffisante de solubilité de l'équation (14.34) est que pour toute fonction constante f , on ait

$$\langle f\Phi \rangle = 0$$

c'est à dire tout simplement que Φ soit de moyenne nulle:

$$\langle \Phi \rangle = 0. \quad (14.36)$$

On peut alors exprimer simplement les solutions de l'équation (14.34) en fonction de la restriction \tilde{A} de l'opérateur A aux fonctions périodiques de moyenne nulle. Cet opérateur est alors inversible, et son inverse sera noté \tilde{A}^{-1} . La solution de l'équation (14.34) dont la condition de solubilité (14.36) est satisfaite sera alors donnée par:

$$\Psi = \tilde{A}^{-1}\Phi + (I - \tilde{A}^{-1}A) \langle \Psi \rangle, \quad (14.37)$$

où la fonction moyenne (i.e. constante) $\langle \Psi \rangle$ est arbitraire (c'est un représentant du noyau de A).

En prenant en particulier $\Phi = 0$, nous pouvons aussi obtenir la représentation générale des fonctions appartenant au noyau de A . C'est:

$$\Xi = (I - \tilde{A}^{-1}A) \langle \Xi \rangle, \quad (14.38)$$

où $\langle \Xi \rangle$ est une fonction arbitraire.

Diffusivité turbulente

Calcul

Nous allons maintenant appliquer la méthode multi-échelle pour déterminer la diffusivité turbulente créée par un écoulement $u(x, t)$ donné. Pour simplifier le calcul, nous supposerons que cet écoulement est périodique en espace et en temps³. Nous supposerons également que $u(x, t)$ est incompressible, et que sa moyenne spatio-temporelle sur une période est nulle, ceci afin d'éviter des effets de pure advection. Nous nous intéressons alors à la diffusion d'une quantité scalaire θ (température, concentration..) placée dans cet écoulement. Elle satisfait à l'équation:

$$\begin{aligned} \partial_t \theta + \partial_i(u_i \theta) &= \kappa_m \partial_i \partial_i \theta, \\ \partial_i u_i &= 0, \\ \langle u_i \rangle &= 0, \end{aligned} \quad (14.39)$$

où κ_m est la diffusivité moléculaire, et où le symbole $\langle \rangle$ signifie moyenne spatio-temporelle. Nous nous intéressons aux effets de diffusion de cette quantité sur une échelle spatiale L grande devant l'échelle de l'écoulement de base (l_0 , sa période spatiale), $L = l_0/\varepsilon$. On s'attend à ce que cet effet se produise sur une échelle temporelle d'ordre $T = t_0/\varepsilon^2$, où t_0 est la période temporelle de

³Mais le calcul se généralise aussi au cas où $u(x, t)$ est un champs aléatoire homogène et stationnaire.

l'écoulement. On introduit donc les variables rapides x, t et les variables lentes $X = x/\varepsilon, T = t/\varepsilon^2$ et on déroule la machinerie multi-échelle. On écrit donc:

$$\begin{aligned}\theta &= \theta^{(0)}(x, t, X, T) + \varepsilon\theta^{(1)}(x, t, X, T) + \dots, \\ \partial_i &= \partial_i + \varepsilon\nabla_i, \\ \partial_t &= \partial_t + \varepsilon^2\partial_T,\end{aligned}\tag{14.40}$$

où ∂_i et ∇_i représentent les dérivées spatiales par rapport aux variables rapides et lentes. En reportant ce développement dans l'équation (14.39) et en séparant en puissance de ε on obtient une hiérarchie d'équations. La remarque cruciale ici est que A ne dépend que des variables rapides. Cette hiérarchie d'équations prendra alors toujours la forme (14.34) discutée en section 3.1.1., pourvu que l'on considère la dépendance en les variables lentes comme paramétrique. A partir de maintenant, l'opération de moyennage ne sera toujours faite que sur les variables rapides.

A l'ordre 0 en ε , on trouve:

$$A\theta^{(0)} = 0,\tag{14.41}$$

où A est l'opérateur différentiel

$$A : f \rightarrow Af = \partial_t f + \partial_i(u_i f) - \kappa_m \partial_i \partial_i f.\tag{14.42}$$

D'après les résultats de la section précédente, on voit que (14.41) signifie que $\theta^{(0)}$ appartient au noyau de A . Il s'écrit donc:

$$\theta^{(0)} = (I - \tilde{A}^{-1}A) \langle \theta^{(0)} \rangle(X, T),\tag{14.43}$$

où \tilde{A} est la restriction de A aux fonctions de moyenne nulle. Comme $\langle \theta^{(0)} \rangle$ ne dépend que des variables lentes, son image par A est nulle (à cause de la condition d'incompressibilité), et (14.43) se simplifie en

$$\theta^{(0)} = \langle \theta^{(0)} \rangle(X, T).\tag{14.44}$$

A l'ordre un en ε , on obtient l'équation:

$$A\theta^{(1)} = -u_i \nabla_i \langle \theta^{(0)} \rangle.\tag{14.45}$$

La condition de solubilité est que la moyenne du second membre est nulle. Cela est satisfait car la moyenne de u est nulle par hypothèse. La solution de (14.45) est alors:

$$\begin{aligned}\theta^{(1)} &= \tilde{A}^{-1}(-u_i \nabla_i \langle \theta^{(0)} \rangle) + \langle \theta^{(1)} \rangle \\ &\equiv \xi_i \nabla_i \langle \theta^{(0)} \rangle + \langle \theta^{(1)} \rangle,\end{aligned}\tag{14.46}$$

où ξ_i est solution de:

$$A\xi_i = -u_i.\tag{14.47}$$

A l'ordre deux en ε , on obtient l'équation:

$$\begin{aligned}A\theta^{(2)} &= -\partial_T \langle \theta^{(0)} \rangle - \nabla_i u_i \theta^{(1)} \\ &\quad + \kappa_m \nabla_i \nabla_i \langle \theta^{(0)} \rangle + 2\kappa_m \partial_i \nabla_i \theta^{(1)}.\end{aligned}\tag{14.48}$$

La condition de solubilité s'écrit:

$$\partial_T \langle \theta^{(0)} \rangle + \nabla_i \langle u_i \theta^{(1)} \rangle = \kappa_m \nabla_i \nabla_i \langle \theta^{(0)} \rangle.\tag{14.49}$$

En utilisant l'expression de $\theta^{(1)}$ donnée en (14.46), on voit que cette condition de solubilité nous donne en fait une équation de diffusion pour $\langle \theta^{(0)} \rangle$

$$\partial_T \langle \theta^{(0)} \rangle = \left(\kappa_m \delta_{ij} + \kappa'_{ij} \right) \nabla_i \nabla_j \langle \theta^{(0)} \rangle, \quad (14.50)$$

avec un coefficient de diffusion provenant de deux contributions: la contribution moléculaire, donnée par κ_m , et la contribution turbulente, κ'_{ij} , qui s'exprime en fonction de l'écoulement de base selon:

$$\kappa'_{ij} = -\frac{1}{2} \left(\langle u_i \xi_j \rangle + \langle u_j \xi_i \rangle \right), \quad (14.51)$$

où ξ est le vecteur solution de l'équation linéaire non homogène (14.47).

Remarques

Plusieurs remarques peuvent être faites à ce point. D'abord, on peut remarquer que la moyenne de $\theta^{(1)}$, qui était à priori arbitraire, n'intervient pas. Ainsi, on n'obtient bien qu'une seule solution possible pour la diffusion turbulente, même si l'il y a une infinité d'étapes intermédiaires possibles. Cela permet de ne pas se préoccuper des constantes dans la résolution des problèmes auxiliaires. On peut aussi remarquer que la diffusion turbulente est bien décrite par un tenseur, qui n'est pas forcément isotrope (ça dépendra de l'écoulement de base!). Enfin, à partir de l'expression (14.51), on peut démontrer que κ' est un tenseur défini positif, et que donc la diffusion est toujours augmentée par la turbulence. En effet, considérons l'équation obéie par ξ . En prenant les équations des i^{eme} et j^{eme} composantes et en les multipliant respectivement par ξ_j et ξ_i , en additionnant les équations résultantes, puis en prenant la moyenne, on trouve:

$$-\frac{1}{2} \left(\langle u_i \xi_j \rangle + \langle u_j \xi_i \rangle \right) = \kappa_m \langle \partial_k \xi_i \partial_k \xi_j \rangle. \quad (14.52)$$

On peut facilement vérifier que le tenseur apparaissant dans le second membre de (14.52) est défini positif, par exemple en calculant les valeurs propres, toujours positives. Notons qu'on peut aussi démontrer que la diffusion turbulente produit des corrections toujours plus petites que $\kappa_m Pe^2$ où Pe est le nombre de Péclet $Pe = \langle (\text{rot } u)^2 \rangle^{1/2} / \kappa_m$ [68]⁴.

Application: cas des écoulements cisaillés 2D

On peut obtenir une forme analytique explicite de la diffusivité turbulente dans certains cas simples, comme par exemple les écoulements cisaillés bi-dimensionnels. Ce sont des écoulements ne variant que dans la direction orthogonale au sens de l'écoulement. On peut les mettre sous la forme:

$$\begin{aligned} u_x &= 0, \\ u_y &= -\partial_x \psi, \end{aligned} \quad (14.53)$$

où $\psi(x)$ est la fonction de courant. L'opérateur A dans ce cas s'écrit simplement $A = -\kappa_m \partial_x \partial_x$ et la solution de l'équation (14.47) est donc donnée simplement par:

$$\begin{aligned} \xi_x &= 0, \\ \xi_y &= -\frac{1}{\kappa_m} \partial_x^{-1} \psi. \end{aligned} \quad (14.54)$$

⁴Attention! Tous les résultats mentionnés dans ce paragraphe ne sont valables que dans le cas des écoulements incompressibles. On pourrait par exemple très bien trouver des diffusivités turbulentes négatives dans un écoulement compressible [18].

Le tenseur de diffusivité turbulente n'a alors qu'une composante non nulle, donnée par

$$\kappa_{yy}^t = \langle u_y \xi_y \rangle = \frac{1}{\kappa_m} \langle \psi^2 \rangle. \quad (14.55)$$

On a utilisé une intégration par partie pour obtenir le résultat ci-dessus. On peut ici vérifier directement que la diffusivité turbulente est positive et donne une contribution inférieure ou égale à $\kappa_m Pe^2$.

14.3.2 Quelques compléments

Effet AKA

Exemple

L'effet AKA ne peut apparaître que dans un système anisotrope et soumis à une force extérieure. Un bon exemple, étudié par Kitchanov et al. [35], est celui du disque d'accrétion. C'est un disque de matière en rotation autour d'un objet central compact (trou noir, étoile). La force extérieure dans ce cas est la gravité due à l'objet central, et l'anisotropie est créée par la rotation. Prenons pour direction z l'axe de rotation du disque et considérons pour simplifier une perturbation à grande échelle de la forme:

$$\begin{aligned} P &= P(Z), \\ W_x &= U(Z), \\ W_y &= V(Z), \\ W_z &= 0. \end{aligned} \quad (14.56)$$

Par des considérations de symétrie (voir [35]), on peut montrer que les seuls composantes non nulles du tenseur AKA sont α_{132} et α_{231} , qui peuvent s'écrire:

$$\alpha_{132} = -\alpha_{231} = -\gamma\Omega, \quad (14.57)$$

où Ω est la rotation du disque et γ un coefficient qui dépend de la turbulence à petite échelle. Les équations du mouvement pour la perturbation à grande échelle, sont:

$$\begin{aligned} \partial_T U - 2\Omega V &= -\nabla_Z(\gamma\Omega V) + v\nabla_Z\nabla_Z U, \\ \partial_T V + 2\Omega U &= \nabla_Z(\gamma\Omega U) + v\nabla_Z\nabla_Z V, \end{aligned} \quad (14.58)$$

où v est la viscosité, incluant éventuellement la composante turbulente. La stabilité de l'écoulement à grande échelle peut s'étudier en introduisant la vitesse complexe $W = U + iV$, et en la décomposant en ondes planes:

$$W = W_0 \exp(ikZ + \sigma T). \quad (14.59)$$

En reinjectant dans (14.58), on trouve l'équation de dispersion:

$$\sigma = -vk^2 - 2i\Omega - k\gamma\Omega. \quad (14.60)$$

Cette relation fait apparaître plusieurs effets: un effet stabilisant, dû à la viscosité, un effet de déphasage pur dû à la rotation, et un effet déstabilisant dû à l'effet AKA pour tout nombre d'onde tel que $k\gamma < 0$. On assiste alors à une instabilité à grande échelle, pour des nombres d'ondes plus petits que $|\gamma\Omega|/v$.

Instabilité et saturation

L'instabilité AKA n'a pas été étudiée en détails dans le système précédent, mais on s'attend qualitativement à ce qu'elle suive le scénario observé numériquement par Frisch et al. [31]: d'abord

Figure 14.9: Evolution temporelle d'une instabilité liée à l'effet AKA (d'après Frisch et al. 1987).

une phase de croissance linéaire, suivie d'une phase de saturation (voir figure 14.9) due à un effet rétroactif de l'écoulement à grande échelle sur l'instabilité, qui modifie le coefficient AKA.

Ce dernier devient proportionnel, dans le régime non linéaire à $1/(1 + W^2)$, et devient négligeable quand l'énergie à grande échelle devient assez grande. L'état final atteint dans le cas du disque d'accrétion pourrait alors ressembler à la célèbre image des tourbillons hiérarchiques de von Weisäcker (Fig. 14.10), introduite dans le cadre de la théorie de formation du système solaire (voir Tanga et al. [65]): à grande échelle, on aurait alors une structure de gros tourbillons quasi bi-dimensionnels, nourris par l'instabilité AKA, et à petite échelle, la turbulence 3D ordinaire.

Figure 14.10: Hiérarchie de tourbillons dans un disque d'accrétion soumis à l'effet AKA.

Viscosités négatives

Fréquence et isotropie

Nous avons vu en section 3.1.3. un exemple d'écoulement possédant une viscosité négative. C'est un écoulement très particulier, car fortement anisotrope, et engendrant une viscosité elle aussi très anisotrope. On peut alors se poser deux questions: (i) est-ce que les viscosités négatives sont fréquentes, ou uniquement liées à des configurations très particulières? (ii) est-il possible de trouver des écoulements produisant des viscosités turbulentes isotropes? La réponse à ces deux questions a été apportée par Gama et al. [33] et par Vergassola et al. [45]. Ils ont d'abord trouvé que le phénomène de viscosité négative est assez courant en dimension 2: environ un tiers des écoulements semblent engendrer une viscosité négative. Un exemple typique d'un tel écoulement est donné en figure 14.11.

On voit que cet écoulement est caractérisé par une zone locale de cisaillement intense, qui a une structure identique à l'écoulement (14.53). On peut se demander si ce n'est pas là une condition nécessaire et suffisante pour obtenir une viscosité négative. Cependant, au cours de leur étude,

Figure 14.11: Un des nombreux écoulements 2D produisant une viscosité négative (d'après Gama et al. 1994).

Gama et al. ont exhibé un exemple explicite d'écoulement menant à une viscosité négative et isotrope, ce qui montre bien que cette condition locale ne peut rien permettre d'apprendre sur la structure globale du tenseur de viscosité résultant.

Instabilité et saturation

Nous avons vu que les viscosités négatives entraînent une instabilité à grande échelle. Cette instabilité a été étudié numériquement dans le cas d'un écoulement bi-dimensionnel par Gama et al. [32]. L'instabilité croît linéairement selon un processus s'apparentant à un phénomène de cascade inverse: croissance des modes à nombre d'onde de plus en plus petits, avec prédominance finale du mode correspondant au nombre d'onde le plus bas (Figure 14.12 et 14.13).

Figure 14.12: Croissance linéaire d'une instabilité visco-négative (d'après Gama et al. 1991).

Figure 14.13: Spectre d'énergie en phase finale. Noter le pic correspondant au nombre d'onde le plus bas (d'après Gama et al. 1991).

On peut alors se demander si et comment cette instabilité peut atteindre une phase de saturation, conduisant à un nouvel équilibre. La réponse semble dépendre de la dimension, comme l'a montré une étude de Gama et al. [32]. La saturation doit être décrite a priori en tenant compte de deux effets: (i) le fait qu'au voisinage de la bifurcation où la viscosité devient négative (c'est à dire en passant par la valeur zéro), il faille prendre en compte les termes d'ordre supérieurs dans le développement (14.6); il faut alors introduire un terme d'hyper-viscosité, en $-\mu\partial^4$; (ii) le fait que lorsque l'instabilité survient, la perturbation croît, et les termes non-linéaires deviennent importants. On peut aisément se convaincre que de ces deux effets, seul le second peut aboutir à une saturation. En effet, l'hyper-viscosité agit à des échelles beaucoup plus petites que la viscosité, et ne peut donc stabiliser que les nombres d'ondes les plus petits. L'équation décrivant la dynamique de l'instabilité visco-négative peut donc s'écrire, dans le cas le plus simple:

$$\begin{aligned} \partial \cdot \mathbf{u} &= 0 \\ \partial_t \mathbf{u} + (\mathbf{u} \cdot \partial) \mathbf{u} &= -\partial p - \nu \partial^2 \mathbf{u} - \mu \partial^4 \mathbf{u}. \end{aligned} \tag{14.61}$$

A une dimension, cette équation est l'équation de Kuramoto-Sivashinsky, qui décrit la dynamique

des fronts de flamme. Dans ce cas, les effets non-linéaires peuvent contrer l'instabilité et on observe une saturation sous forme de solutions "cellulaires" de type soliton. Par contre, à deux dimensions, la situation est moins réjouissante, comme l'on démontré Gama et al.[32]. En effet, l'instabilité se développe de manière à tuer l'action des termes non-linéaires. Ce phénomène, bien connu en dynamique bi-dimensionnel, peut se produire lorsque la vorticité devient une certaine fonctionnelle de la fonction de courant ψ . En effet, la vorticité est donnée par $\partial^2\psi$ et les termes non-linéaires par:

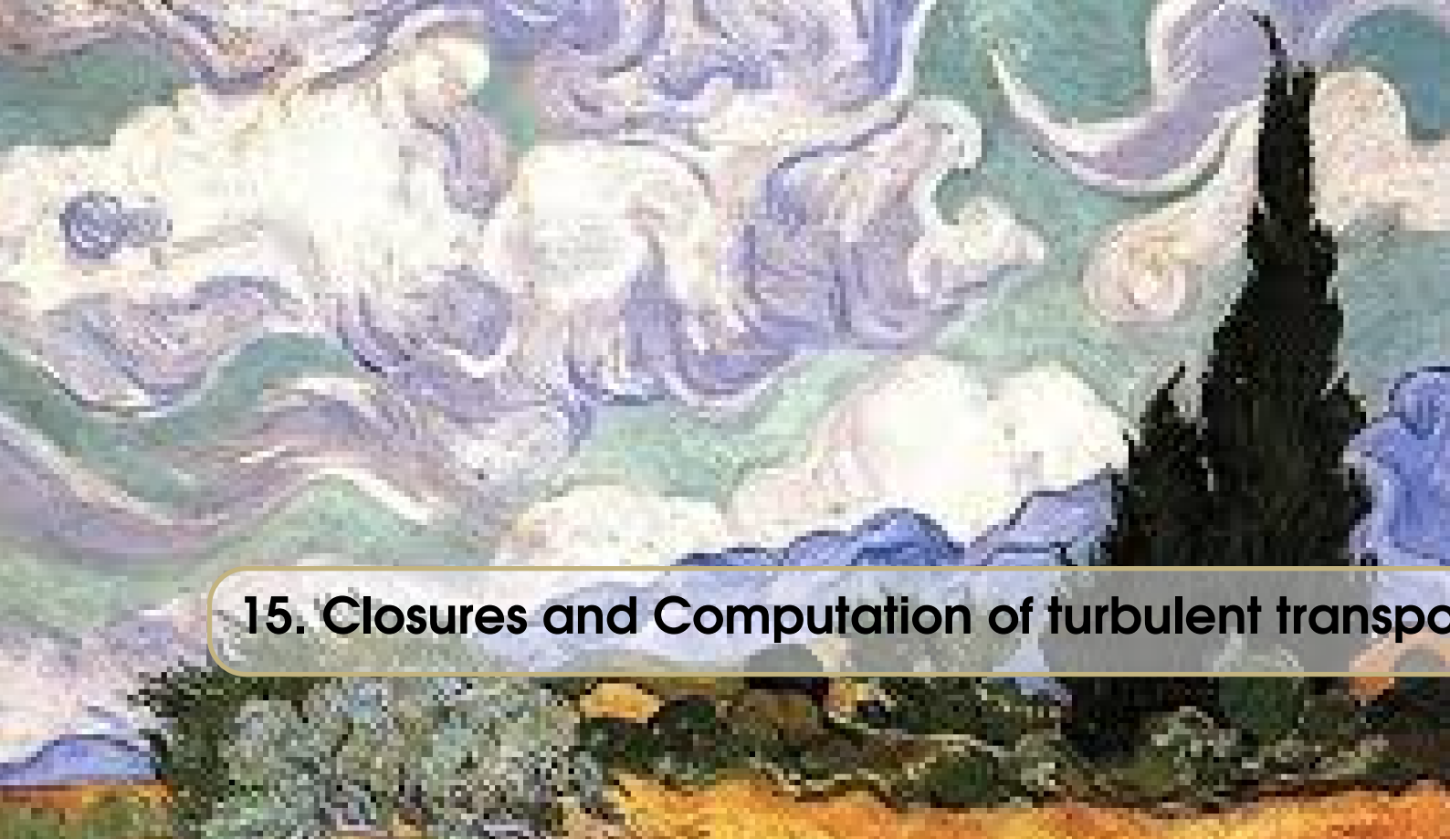
$$NL = J(\psi, \partial^2\psi) = \partial_x\psi\partial_y\partial^2\psi - \partial_y\psi\partial_x\partial^2\psi.$$

Cette expression s'annule dans le cas où $\partial^2\psi = F(\psi)$. On observe alors une croissance continue de l'instabilité, accompagnée d'une cascade inverse d'énergie (Figure 14.14). Il se pourrait donc bien que ce mécanisme explique la cascade inverse d'énergie observée en turbulence bi-dimensionnelle. Notons qu'en trois dimension, ce mécanisme de "déplétion des non-linéarités" n'existe plus. Il serait donc intéressant de poursuivre cette étude en dimension trois, afin d'observer la saturation éventuelle.

Figure 14.14: Cascade inverse d'énergie dans l'instabilité visco-négative bi-dimensionnelle par appariement de tourbillons (d'après Gama et al., 1991)

14.4 En guise de conclusion

Nous avons passé en revue quelques unes des propriétés essentielles du transport turbulent. J'insisterai en particulier sur la complémentarité des descriptions Lagrangienne et Eulérienne, et sur la différence de comportement entre le transport d'une quantité scalaire, comme la température, et vectorielle, comme la quantité de mouvement (possibilité d'effet AKA, de viscosité négative, ...). Nous avons aussi vu qu'il existait des moyens systématiques de décrire ce transport turbulent, en utilisant en particulier le formalisme multi-échelle. Même si certains des résultats et des méthodes décrites ont pu paraître au lecteur un peu théoriques et ardues, je pense qu'ils valent la peine d'un investissement plus important de la part des astrophysiciens, et qu'ils pourraient permettre de progresser dans certains domaines. Par exemple, ils ont permis de mettre au point un scénario complet et cohérent de la formation du système solaire dans une nébuleuse turbulente [20, 22, 65]. Le soleil ou la structure interne des étoiles pourraient bien être le prochain domaine d'application de ces techniques!!!



15. Closures and Computation of turbulent transport

From the work of Kolmogorov on turbulence [K41], hereafter referred to as the K41 theory of turbulence, we know that the balance between forcing and dissipation results in a self-similar organization of the fluid. Kinetic energy is injected at scale L_f and is transferred at a constant rate ε by the energy flux $\overline{\Pi_\ell^I}$ down to the scale η where the energy flux becomes compensated by the viscous flux, with $\eta = (\nu^3/\varepsilon)^{1/4}$ and ν is the viscosity. At smaller scales, the energy flux is transported by the viscous processes to the smallest hydrodynamic scale, where it is dissipated into heat. A turbulent flow then displays vortices of all sizes in between L_f and η , and its energy spectrum scales like $E(k) \sim \varepsilon^{2/3} k^{-5/3}$. This means that if we want to capture the flow physics (e.g; location of vortices and their dynamics in the flow, energy dissipation, interplay between vortices at different scales), we need to discretize the Navier-Stokes equations on a grid that is $(L_f/\eta) \times (L_f/\eta) \times (L_f/\eta)$, containing *a priori* $N \sim (L_f/\eta)^3$ degrees of freedom (as we shall discuss later, the actual number may even be larger!) . If we put numbers corresponding to the atmosphere ($L = 10^3$ km, $\eta = 10$ mm), we get an astronomical number: $N \sim 10^{24}$, larger than the Avogadro number. Reading-in or writing out this volume of data at each time-step to advance the flow would take 73 billion years of CPU time at the pace of the fastest massively parallel computers! We are then led by necessity to simulate much fewer degrees of freedom, typically a few thousands in the atmosphere or ocean for recent climate models.

How reasonable is this drastic reduction of the number of degrees of freedom? It now depends on the flow physics: the self-similar energy spectrum is an indication that some scales or modes may play a more prominent role than others. So, maybe, the theoretical $N \sim (L_f/\eta)^3$ figure overestimates the actual number of modes that is needed to represent the flow dynamics, and we could circumvent the computational obstacle by a clever selection of grid points or modes. This chapter presents several classical or more modern procedures.

15.1 Basic equations and definitions

15.1.1 Filters

Making a selection of modes ("decimating" modes) can be achieved via filtering, that is, instead of considering the full velocity field \mathbf{u} one considers instead $\langle \mathbf{u} \rangle$ where the brackets describes the filtering procedure. The nature and the properties of such filtering procedure determines the decimating technique. Three 3 main procedure I will discuss here are:

- (i) a statistical filtering; this case will correspond to Random Average Navier Stokes method (RANS)
- (ii) a global scale filtering; this case will correspond to Large Eddy Simulation (LES) method;
- (iii) a local scale filtering; this case will correspond to Rapid Distortion (RDT) method.

Using this filter, we can now decompose the velocity field into its "mean" and its "fluctuating" contribution, via:

$$\begin{aligned}\mathbf{u}(\mathbf{x}, t) &= \mathbf{U}(\mathbf{x}, t) + \mathbf{u}'(\mathbf{x}, t), \\ \mathbf{U}(\mathbf{x}, t) &= \langle u \rangle.\end{aligned}\quad (15.1)$$

An important property of all the filters will be that they commute with space and time derivative:

$$\begin{aligned}\langle \partial_t f \rangle &= \partial_t \langle f \rangle, \\ \langle \partial_x f \rangle &= \partial_x \langle f \rangle.\end{aligned}\quad (15.2)$$

Depending on the filter, it can be involutif, that is:

$$\langle\langle u \rangle\rangle = \langle u \rangle. \quad (15.3)$$

In this case, we have $\langle u' \rangle = 0$: fluctuations defined through involutive filters have zero mean .

15.1.2 Equations

The equation for the "mean" flow can be easily found by applying the filtering on the Navier-Stokes equations. One finds then the following equation for \mathbf{U} :

$$\begin{aligned}\nabla \cdot \mathbf{U} &= 0, \\ \partial_t \mathbf{U} + \mathbf{U} \cdot \nabla \mathbf{U} &= -\nabla P + \nu \Delta \mathbf{U} + \nabla \cdot \boldsymbol{\tau};\end{aligned}\quad (15.4)$$

where $\boldsymbol{\tau}_{ij} = U_i U_j - \langle u_i u_j \rangle$ is the Reynolds stress tensor. The equation for the mean flow therefore looks very similar to the original equation, except for the additional term involving the Reynolds stress. To be able to simulate the evolution of the mean flow, one need to be able to express Reynolds stress tensor as a function of the mean flow only. This is the so-called closure problem. Obviously, the only troublesome term is the term $\langle u_i u_j \rangle$ which represent the contribution of all the decimated modes.

The goal of any modelling of turbulence is to represent this term in function of only the "mean flow" and its derivatives.

15.2 RANS

In this case, the filter applied is a statistical mean (over realizations). In practice, if we assume that turbulence is ergodic (a property that has never been proved to my knowledge), we may substitute this statistical mean by spatio or temporal average.

15.2.1 Equations

RANS model do not usually arbitrarily prescribe how $\langle u_i u_j \rangle$ depends on U and its derivatives, but rather compute it dynamically through an equation that is derived from Navier-Stokes, and closed through simple assumptions. Indeed, taking the difference between Navier-Stokes equations and the equation or the mean Eq. (15.4), we obtain an equation for the fluctuation as:

$$\begin{aligned} \nabla \cdot \mathbf{u}' &= 0, \\ \partial_t \mathbf{u}' + \mathbf{U} \cdot \nabla \mathbf{u}' + \mathbf{u}' \cdot \nabla \mathbf{U} + \mathbf{u}' \cdot \nabla \mathbf{u}' &= -\nabla p' + \nu \Delta \mathbf{u}'; \end{aligned} \quad (15.5)$$

To obtain an equation for the Reynolds stress, we take i component of this equation, multiply it by j component of u' , repeat process while inverting i and j , sum the two resulting equations, and take average. We obtain:

$$\begin{aligned} \partial_t \langle u'_i u'_j \rangle + U_k \partial_k \langle u'_i u'_j \rangle &= - \langle u'_i u'_j \rangle \partial_k U_k + \nu \partial_k \langle u'_i u'_j \rangle + T_{ij}, \\ T_{ij} &= \langle p'(S_{ij} + S_{ji}) \rangle - \nu \langle S_{ik} S_{kj} \rangle - \partial_k (\langle u'_i u'_j u'_k \rangle + \langle p' u_i \rangle \delta_{kj} + \langle p' u'_j \rangle \delta_{ki}) \end{aligned}$$

where $S_{ij} = \partial_j u'_i$. The term that needs to be modelled is T_{ij} . It depends on triple correlation of u' and on correlation of p' with u' and its derivatives, that are also third order quantities (because p' can be found by inverting a poisson equation that depends on double correlations of u'). If we were thinking about deriving an equation for T_{ij} from Navier-Stokes equation, we would find that such equation depends on fourth correlation of u' and so on. This means that if we want to solve exactly the equation from Navier-Stokes, we have to solve an infinite hierarchy of equations. To avoid that, we must at some level, prescribe the way the "nth" correlation depends on the $(n-1)th$ correlations. For example, the simplest choice is to take:

$$T_{ij} = \nu_T \partial_k \partial_k \langle u'_i u'_j \rangle, \quad (15.7)$$

where ν_T is a turbulent viscosity that need to be prescribed. Usual RANS of turbulence use more elaborate models, taking into account pressure fluctuation. Their success can be measured by the fact that planes flight! However, from a theoretical point of view, none of them is completely satisfying, because they introduce many adjustable parameters (similar to ν_T) that need to be calibrated on experiments. This is what engineers have been doing in the past in the wind tunnels, and explain why their models is so good. However, constants calibrated in one situation cannot be used in another situation, for example if I change the forcing, or boundary conditions, etc, so there is some kind of arbitrariness that remains. In some case, when constant cannot be calibrated, like in the case of climate model, this is worrisome: think that present climate model have more than 100 adjustable parameters... Can we trust their predictions? This is why, there is till a large ongoing activity to devise turbulent modeling. below, I describe briefly some of them.

15.3 Large eddy simulations

15.3.1 Filter properties

In the LES case, the filter removes all the scale that are smaller than a certain scale ℓ_c . Such filtering can easily be achieved in any dimension d by convolution with a filtering function ϕ , so that:

$$U(x) \equiv \int \phi(y/\ell_c) u(x-y) d^d y / \ell_c^d. \quad (15.8)$$

To be admissible, ϕ must be positive, of unit integral, and be decaying sufficiently fast an infinity so hat the integral converges for any smooth function. A good filter is for example $\phi(x) = e^{-x^2/2}$. Note that the filtering can be easily achieved by going into the Fourier space, so that:

$$U(k) \equiv \phi(k\ell_c) u(k), \quad (15.9)$$

which is equivalent to remove all wave-numbers larger than $k = 2\pi/\ell_c$ if the filter is sharp, otherwise the decimation is gradual. This filter is non involutif, so that fluctuations do contribute to the mean.

15.3.2 Physical constraints on the closure

The simplest closure would be to disregard any action of the fluctuations and take $\tau_{ij} = 0$. Basic turbulence energetics however tells us that it is a bad idea: under the action of the forcing, the turbulent flow absorbs a power Π given by the work of the force. Such power is dissipated through the viscosity as $-\nu(\nabla u)^2$, resulting in Fourier space in a term $\int dk \nu k^2 E(k)$ in the energy balance. For a Kolmogorov like turbulence, $E(k) \sim k^{-5/3}$ so that the dissipative term is dominated by the contribution of the largest wavenumber of the inertial range, k_c , resulting in a dissipation rate of the order of $\nu k_c^{4/3}$. In a direct simulation, all the scales down to the dissipative scale are resolved, so that $k_c = k_d$ and the dissipation rate balances the work of the force, enabling steady state. In a filtered equation with no closure, $k_c = Ak_d$ so that the dissipated energy is only a small fraction of the power input $\Pi_{diss} = (k_c/k_d)^{4/3}\Pi$, and we observe a runaway of the simulation. The primary goal of the closure is therefore to model τ_{ij} so as to dissipate the missing fraction of dissipated power.

15.3.3 Eddy viscosity models

The simplest solution to solve the closure problem in homogeneous isotropic turbulence is of course to introduce an isotropic eddy-viscosity tensor with intensity ν_{ijkl}^T and write $\tau_{ij} = \nu_{ijkl}^T \nabla_k U_l$. Some more refined models build an eddy viscosity that is proportional for example to the large-scale velocity gradients (Smagorinsky model) (citer tous les trucs de Meneveau- , or derived by similarity arguments thanks to Germano identity (Germano). Other non-isotropic eddy viscosity tensors can also be derived from asymptotic expansions performed on the Navier-Stokes equations using strong hypothesis such as scale separation (see next subsection. In all cases, the procedure guarantees that there is no energy pile-up at the coarse-grid scale. In climate simulations, for example, this amounts to simulate the atmosphere using peanut butter, while the ocean is made of honey. This appears to be sufficient to reproduce the large-scale structure of the flows involved in climate research. However, the damping of the fluctuation by the viscosity is an annoying side effects of the procedure, given the recent revival of "tipping point" scenarios in climate model.

15.3.4 Homogenization

Nous allons maintenant appliquer la méthode multi-échelle au calcul de la viscosité turbulente. Le formalisme et la méthodologie sont très similaires à ceux employés pour le calcul de la diffusivité turbulente, mais quelques modifications sont introduites par le fait que l'on s'intéresse à une quantité vectorielle plutôt que scalaire. Nous verrons que cela alourdit un peu les notations, mais pas la mise en œuvre de la procédure. Le calcul qui suit est adapté de l'article Dubrulle-Frisch [23] que l'on pourra consulter pour plus de détails.

Viscosité turbulente

Calcul

Considérons un écoulement incompressible turbulent (p, \mathbf{u}) , où la pression p et la vitesse \mathbf{u} sont périodiques en espace x et en temps t . L'écoulement est solution des équations de Navier-Stokes D -dimensionnelles, avec une force \mathbf{f}

$$\begin{aligned} \partial \cdot \mathbf{u} &= 0 \\ \partial_t \mathbf{u} + (\mathbf{u} \cdot \partial) \mathbf{u} &= -\partial p + \nu \partial^2 \mathbf{u} + \mathbf{f}. \end{aligned} \tag{15.10}$$

La force dépend du temps et de la position et est périodique en l'espace et en temps. Sa moyenne sur les périodes, $\langle \mathbf{f} \rangle$, est nulle, de même que celle de l'écoulement. Enfin, afin d'éliminer tout

effet AKA (voir introduction), nous supposerons que l'écoulement possède un centre de symétrie, c'est à dire qu'il est invariant par la transformation

$$\mathbf{P} : \mathbf{x} \rightarrow -\mathbf{x}, \quad \mathbf{u} \rightarrow -\mathbf{u}, \quad p \rightarrow p. \quad (15.11)$$

Nous allons explorer comment cet écoulement modifie les propriétés de transport d'une perturbation à grande échelle (P, \mathbf{W}). Cette perturbation obéit à l'équation de Navier-Stokes linéarisée¹:

$$\begin{aligned} \partial \cdot \mathbf{W} &= 0, \\ \partial_t W_i + \partial_j(u_i W_j + u_j W_i) &= -\partial_i P + v \partial^2 W_i. \end{aligned} \quad (15.12)$$

Nous introduisons maintenant un formalisme matriciel, qui permet d'obtenir des équations très compactes et facilite le déroulement des calculs. Ainsi, nous réécrivons l'équation (15.12) sous la forme:

$$\mathcal{A} \begin{pmatrix} P \\ \mathbf{W} \end{pmatrix} u i v (\mathcal{A}_{PP} \mathcal{A}_{PW} \mathcal{A}_{WP} \mathcal{A}_{WW}) \begin{pmatrix} P \\ \mathbf{W} \end{pmatrix} = 0. \quad (15.13)$$

Nous avons ainsi rassemblé les D composantes de la perturbation de vitesse \mathbf{W} et la perturbation de pression en un vecteur de dimension $D+1$. L'opérateur linéaire de Navier-Stokes \mathcal{A} dans (15.13) est composé de blocs matriciels définis par:

$$\mathcal{A}_{PP} = 0, \quad \mathcal{A}_{PW_i} = \partial_i, \quad \mathcal{A}_{W_i P} = \mathcal{A}_{W_i W_j} = (\partial_t - v \partial^2) \delta_{ij} + \partial_k (\delta_{ij} u_k \bullet + \delta_{kj} u_i \bullet). \quad (15.14)$$

Ici, le gros rond \bullet indique la position de la fonction sur laquelle agit l'opérateur.

Pour plus de clarté, nous dénoterons par A la restriction de l'opérateur \mathcal{A} aux fonctions de même périodicité que l'écoulement de base (avec une notation similaire pour les blocs matriciels dont il est constitué, comme A_{PW}). Notons que l'opérateur A obéit aux propriétés décrites en section 3.1.1. De plus, du fait de l'invariance par parité de l'écoulement de base, ses blocs se transforment sous une transformation de parité (15.11) selon:

$$\mathbf{P} A_{PW} = -A_{PW}, \quad \mathbf{P} A_{WP} = -A_{WP}, \quad \mathbf{P} A_{WW} = A_{WW}. \quad (15.15)$$

Pour calculer la viscosité turbulente, nous déroulons maintenant la machinerie multi-échelle, en introduisant les variables rapides x et t , et les variables $X = x/\varepsilon, T = t/\varepsilon^2$, et développons tout en ε :

$$\begin{aligned} \partial_t &= \partial_t + \varepsilon^2 \partial_T, \\ \partial &= \partial + \varepsilon \nabla, \end{aligned}$$

$$\begin{pmatrix} P \\ \mathbf{W} \end{pmatrix} = \begin{pmatrix} P^{(0)} \\ \mathbf{W}^{(0)} \end{pmatrix} + \varepsilon \begin{pmatrix} P^{(1)} \\ \mathbf{W}^{(1)} \end{pmatrix} + \varepsilon^2 \begin{pmatrix} P^{(2)} \\ \mathbf{W}^{(2)} \end{pmatrix} + O(\varepsilon^3). \quad (15.16)$$

La substitution de (15.16) dans (15.12) donne une hiérarchie d'équations. Au premier ordre en ε , on obtient:

$$A \begin{pmatrix} P^{(0)} \\ \mathbf{W}^{(0)} \end{pmatrix} = 0. \quad (15.17)$$

¹ On peut également mettre en œuvre la méthode multi-échelle sur l'équation non-linéaire. Cela permet d'obtenir la forme des couplages non-linéaires pour la perturbation, qui ne sont pas toujours du type Navier-Stokes (voir [68]).

Cette équation traduit que $(P^{(0)}, \mathbf{W}^{(0)})$ est dans le noyau de A . On a donc directement par (14.38),

$$\begin{pmatrix} P^{(0)} \\ \mathbf{W}^{(0)} \end{pmatrix} = (I - \tilde{A}^{-1}A) \begin{pmatrix} < P^{(0)} > \\ < \mathbf{W}^{(0)} > \end{pmatrix}. \quad (15.18)$$

Au deuxième ordre en ε , on obtient

$$A \begin{pmatrix} P^{(1)} \\ \mathbf{W}^{(1)} \end{pmatrix} + B \begin{pmatrix} P^{(0)} \\ \mathbf{W}^{(0)} \end{pmatrix} = 0, \quad (15.19)$$

où l'opérateur B est donné sous forme de blocs par:

$$B = \begin{pmatrix} 0 & B_{PW} \\ B_{WP} & B_{WW} \end{pmatrix}, \quad (15.20)$$

avec

$$B_{PW_i} = \nabla_i, \quad B_{W_i P} = \nabla_i, \quad B_{W_i W_j} = -2\nu\delta_{ij}\partial_k \nabla_k + \nabla_k (\delta_{ij}u_k \bullet + \delta_{jk}u_i \bullet). \quad (15.21)$$

Comme B est linéaire en les dérivées par rapport aux variables lentes, il peut être encore décomposé en

$$B = B^\ell \nabla_\ell, \quad B_{PW_i}^\ell = B_{W_i P}^\ell = \delta_{i\ell}, \quad B_{W_i W_j}^\ell = -2\nu\delta_{ij}\partial_\ell + \delta_{ij}u_\ell \bullet + \delta_{j\ell}u_i \bullet. \quad (15.22)$$

Cette décomposition est le pendant de la décomposition (14.47). En reinjectant la solution (15.18), cette équation s'écrit

$$A \begin{pmatrix} P^{(1)} \\ \mathbf{W}^{(1)} \end{pmatrix} + B(I - \tilde{A}^{-1}A) \begin{pmatrix} < P^{(0)} > \\ < \mathbf{W}^{(0)} > \end{pmatrix} = 0. \quad (15.23)$$

Cette équation pour $(P^{(1)}, \mathbf{W}^{(1)})$ n'aura de solution que si la conditions de solvabilité est réalisée, c'est à dire que le second membre est de moyenne nulle:

$$< B(I - \tilde{A}^{-1}A) \begin{pmatrix} < P^{(0)} > \\ < \mathbf{W}^{(0)} > \end{pmatrix} > = 0. \quad (15.24)$$

Cette condition peut se réécrire sous une forme plus sympathique, en utilisant la décomposition en blocs de B et la relation (15.22), et en utilisant plusieurs astuces: (i) que le bloc B_{WW} ne dépend que des variables rapides; (ii) que la moyenne de toute quantité ayant un opérateur \tilde{A}^{-1} à gauche est nulle, puisque ce dernier n'agit que dans l'espace des fonctions de moyenne nulle; (iii) que les dérivées lentes ∇ commutent avec les opérateurs de dépendant que des variables rapides. On trouve alors que la condition de solvabilité se réduit à:

$$\begin{aligned} \nabla_j < W_j^{(0)} > &= 0 \\ \nabla_i < P^{(0)} > - \alpha_{ij\ell} \nabla_j < W_\ell^{(0)} > &= 0, \end{aligned}$$

où

$$\alpha_{ij\ell} = - < B_{W_i W_n}^j (I - \tilde{A}^{-1}A) >_{w_n w_\ell}. \quad (15.25)$$

Dans (15.25), nous avons introduit une nouvelle notation: étant donné un opérateur M , sa moyenne $\langle M \rangle$ est définie comme un opérateur n'agissant que sur les fonctions indépendantes des variables rapides:

$$\langle M \rangle \langle \Psi \rangle uiv \langle M \rangle \langle \Psi \rangle = . \quad (15.26)$$

On reconnaît dans la première condition de (??) la condition d'incompressibilité pour $\langle \mathbf{W}^{(0)} \rangle$. La deuxième condition traduit la non-existence de l'effet AKA. On peut en effet vérifier que le tenseur $\alpha_{ij\ell}$ apparaissant dans (??) est le même que celui décrit en introduction. Si cet effet ne disparaît pas, on ne peut continuer l'analyse jusqu'à l'ordre ε^2 , auquel le comportement diffusif intervient. Physiquement, cela traduit le fait que l'effet AKA a une dynamique du premier ordre en temps et en l'espace, qui se produit à des temps de l'ordre de $T = \varepsilon t$. Il faudrait donc recommencer l'analyse avec cette nouvelle échelle, et l'équation (??) nous permettrait alors de déterminer la dynamique de la perturbation $\langle \mathbf{W}^{(0)} \rangle$ en présence de l'effet AKA. Cependant, lorsque nous ne considérons que des écoulements invariants de parité, le tenseur $\alpha_{ij\ell}$ s'annule identiquement. On peut en effet vérifier cela en remarquant que $B_{WW_h}^j$ défini dans (15.22) change de signe dans une opération de parité, alors que par (15.15) $(I - \tilde{A}^{-1}A)_{w_n w_\ell}$ reste invariant. On peut alors réécrire la condition de solubilité associée à l'équation (15.19) sous la forme

$$\nabla_j \langle W_j^{(0)} \rangle = 0 \quad (15.27)$$

et

$$\nabla_i \langle P^{(0)} \rangle = 0. \quad (15.28)$$

On déduit de (15.28) que $\langle P^{(0)} \rangle$ ne dépend pas des variables spatiales. Comme la pression n'apparait que dans un gradient, nous pouvons, sans perte de généralité, la prendre égale à zéro (en lui rajoutant une fonction ne dépendant que du temps). La condition de solubilité réalisée, nous pouvons ainsi écrire la solution de (15.19), en utilisant (14.37)):

$$\begin{pmatrix} P^{(1)} \\ \mathbf{W}^{(1)} \end{pmatrix} = -\tilde{A}^{-1}B(I - \tilde{A}^{-1}A)\begin{pmatrix} \langle P^{(0)} \rangle \\ \langle \mathbf{W}^{(0)} \rangle \end{pmatrix} + (I - \tilde{A}^{-1}A)\begin{pmatrix} \langle P^{(1)} \rangle \\ \langle \mathbf{W}^{(1)} \rangle \end{pmatrix}, \quad (15.29)$$

où $\langle P^{(1)} \rangle$ and $\langle \mathbf{W}^{(1)} \rangle$ sont des fonctions arbitraires des variables lentes.

Pour obtenir la viscosité turbulente, nous considérons maintenant l'ordre $O(\varepsilon^2)$. Il s'écrit:

$$A\begin{pmatrix} P^{(2)} \\ \mathbf{W}^{(2)} \end{pmatrix} + B\begin{pmatrix} P^{(1)} \\ \mathbf{W}^{(1)} \end{pmatrix} + C\begin{pmatrix} P^{(0)} \\ \mathbf{W}^{(0)} \end{pmatrix} = 0, \quad (15.30)$$

où l'opérateur C est donné sous la forme

$$C = \begin{pmatrix} 0 & 0 \\ 0 & C_{WW} \end{pmatrix}, \quad (15.31)$$

avec:

$$C_{W_i W_j} = (\partial_T - v \nabla^2) \delta_{ij}. \quad (15.32)$$

La condition de solubilité de (15.30) s'écrit, en utilisant (15.18) et (15.29):

$$\begin{aligned} & \langle B\tilde{A}^{-1}B(I - \tilde{A}^{-1}A) \rangle \left(\begin{pmatrix} \langle P^{(0)} \rangle \\ \langle \mathbf{W}^{(0)} \rangle \end{pmatrix} \right) - \langle B(I - \tilde{A}^{-1}A) \rangle \left(\begin{pmatrix} \langle P^{(1)} \rangle \\ \langle \mathbf{W}^{(1)} \rangle \end{pmatrix} \right) \\ & - \langle C(I - \tilde{A}^{-1}A) \rangle \left(\begin{pmatrix} \langle P^{(0)} \rangle \\ \langle \mathbf{W}^{(0)} \rangle \end{pmatrix} \right) = 0. \end{aligned} \quad (15.33)$$

Cette condition peut se réécrire sous une forme plus familière en la décomposant en ses composantes P et \mathbf{W} , et en utilisant les même astuces que pour (15.24) et le fait que les moyennes de la forme $\langle B_{PW} \tilde{A}^{-1} \dots \rangle$ and $\langle C \tilde{A}^{-1} \dots \rangle$ s'annulent parce que B_{PW} and C ne dépendent pas des variables rapides. On obtient alors:

$$\nabla_j \langle W_j^{(1)} \rangle = 0 \quad (15.34)$$

et

$$\nabla_j \langle W_j^{(0)} \rangle = 0 \quad (15.35)$$

$$\partial_T \langle W_i^{(0)} \rangle = v_{ij\ell m} \nabla_j \nabla_\ell \langle W_m^{(0)} \rangle - \nabla_i \langle P^{(1)} \rangle, \quad (15.36)$$

où

$$v_{ij\ell m} = v \delta_{j\ell} \delta_{im} + \left\langle \left(B^j \tilde{A}^{-1} B^\ell (I - \tilde{A}^{-1} A) \right)_{W_i W_m} \right\rangle. \quad (15.37)$$

d'équation On reconnaît dans le système d'équations (15.36) une équation de diffusion pour $\langle \mathbf{W}^{(0)} \rangle$, avec un tenseur de viscosité turbulente $v_{ij\ell m}$ donné par (15.37). Remarquons que l'on a répété la condition d'incompressibilité venant de la condition de solubilité à l'ordre un en ε .

Remarques

L'équation (15.37) nous donne une expression compacte mais non explicite de la viscosité turbulente, sous forme d'un tenseur du quatrième ordre. On ne peut obtenir une valeur analytique ou numérique qu'au prix de la résolution de deux problèmes auxiliaires du type $A\Psi = \Phi$. C'est pour cela qu'apparaissent deux opérateurs \tilde{A}^{-1} dans l'expression de la viscosité. Cette résolution n'est pas toujours possible analytiquement. Il faut dans la plupart des cas envisager une résolution numérique ou perturbative (en puissance du nombre de Reynolds par exemple, voir [23]). Il existe cependant des solutions analytiques pour des écoulements simples, qui permettent d'obtenir des résultats intéressants. C'est le cas des écoulements cisaillés bi-dimensionnels du type (14.53) soumis à des perturbations transverses:

$$\begin{aligned} P &= P(x, t, Y, T), \\ W_x &= W(x, t, Y, T), \\ W_y &= 0. \end{aligned} \quad (15.38)$$

Dans ce cas, on peut vérifier que le tenseur de viscosité turbulente n'a alors qu'une composante non nulle, donnée par

$$v_{xyyx}^t = -\frac{1}{v} \langle \psi^2 \rangle. \quad (15.39)$$

Si l'on compare avec l'expression obtenue pour la diffusivité turbulente dans le même cas (eq. (14.55)), on voit que le signe est **inverse**. En déroulant explicitement le calcul, on peut démontrer que cette différence est liée à un effet de pression. L'importance de ce changement de signe peut se comprendre aisément en écrivant l'équation de diffusion pour W_x :

$$\partial_T W_x = (v - \frac{1}{v} \langle \psi^2 \rangle) \nabla_Y \nabla_Y W_x.$$

On voit que pour v inférieur à une valeur critique $v_c = \sqrt{\langle \psi^2 \rangle}$ (c'est à dire pour un nombre de Reynolds assez grand), la viscosité totale devient négative. On observe alors une instabilité au cours de laquelle l'écoulement à grande échelle croît au détriment de l'écoulement à petite échelle. Cette instabilité visco-négative, très fréquente dans les écoulements cisaillés, est étudiée en section

3.2.2. Remarquons finalement que cette instabilité est présente même dans le cas plus général des perturbations non-transverses (c'est à dire avec une composante W_Y non nulle, et qui dépend à la fois de X et Y). Dans ce cas, l'instabilité se produit dans une direction faisant un angle non nul avec la direction x et pour une valeur de la viscosité légèrement différente (voir [23]). Ceci démontre le caractère général de cette instabilité, dans le cas des écoulements cisaillés.

15.4 Rapid Distortion Theory

Instead of deriving a model for the sub-grid scale tensor directly, one can directly derive a model for the sub-grid scales, from which the sub-grid scale tensor can be easily built. This type of approach started to be popular in the late 1990's. Several approaches were followed, including the deconvolution procedures on large-scale flow, or estimates obtained by expanding the resolved large-scale velocity field to sub-grid-scales two times smaller than the grid scale [DA02]. The problem with such approach is that small scales are extrapolated from values near the cutoff, and cannot represent realistic fluctuations occurring at or below the Kolmogorov scales, since the self-similarity is lost when leaving the inertial range of scale. To overcome , such difficulty, I have devised with my collaborators a dynamical procedure that allows to compute realistic small scales from the large-scale flow, using a combination of the Rapid Distortion Theory (RDT) and a WKB approach [XXX].

15.4.1 Filtering

In a typical situation, the forcing is provided by some boundary conditions (experiments) or externally fixed, e.g. by keeping a fixed low-wavenumber Fourier mode at a constant amplitude (numerical simulation). This situation typically gives rise to quasi-Gaussian large-scale velocity fields, while smaller-scale velocities display increasingly non-Gaussian statistics. Presence of the forcing guarantees existence of a stationary steady state in which the total energy is constant. In absence of forcing, the turbulence energy decays steadily, due to losses through viscous effects. However, starting from a quasi-Gaussian large-scale field, one can still observe development of increasingly non-Gaussian small scales in the early stage of the decay. We will study the effect of the non-local interactions on the statistics of such non-Gaussian small scales. For this, we introduce a filter function $G(\mathbf{x})$ in order to separate the large and small scales of the flow. In our numerical procedure, the filter G will be taken as a cut-off. We have checked that the results are insensitive to the choice of the filter, provided the latter decays fast enough at infinity.

Properties

Note that we are doing here a "scale filtering", and not a statistical filtering via the usual ensemble averaging. This scale filtering is in the spirit of Large Eddy Simulations, where large and small scales are modelized separately for improving the computational efficiency. In the present case, the small and large scale separation is dictated by physical considerations (Section III.A) which only apply because of the scale difference (scale separation) between the two components. This means that our hypothesis might not be valid for statistical average. This also means that to be a little cautious in our averaging, since for example the filtering of the product of two filtered quantities is not necessarily the product of this filtered quantities: $\langle\langle u \rangle\langle v \rangle\rangle \neq \langle u \rangle\langle v \rangle$. This is because the beating of two small (intermediate) wavenumbers can produce a large wavenumber, if the scale separation between the large and the small scale is not enough. In the same way, the filtering of a product of a small scale quantity and a large scale filtered quantity is not necessarily zero, since the beating of a large wavenumber and a small (intermediate) one can produce an intermediate wavenumber. As we shall see, this difference produces additional terms in the averaged equations with respect to the standard Reynolds stresses phenomenology, based upon statistical averaging, and which underlies all the closure models of the PSL [MellYama74, MellYama82].

Another important difference between the LES filtering and the statistical average is in the combination of derivatives and averaging: for statistical averaging, derivatives and averaging commute. For LES filtering, this is not the case in general. To see that, consider the average of some derived quantity, say $\partial_1 u$, and let us integrate by parts over x'_1 . We get:

$$\begin{aligned} \langle \partial_1 u \rangle &= \int g(\mathbf{x} - \mathbf{x}') \partial_{x'_1} u(\mathbf{x}') d\mathbf{x}', \\ &= \int dx_2 dx_3 [g(\mathbf{x} - \mathbf{x}') u(\mathbf{x}')]_{x'_1}^{x'^{\max}} - \int (\partial_{x'_1} g(\mathbf{x} - \mathbf{x}')) u(\mathbf{x}') d\mathbf{x}'. \end{aligned} \quad (15.40)$$

By symmetry, the derivative over x'_1 in the second term of the r.h.s. of (15.40) can be changed into minus a derivative over x_1 , which can then be taken out of the integral, giving a term $\partial_1 \langle u \rangle$. We then see that average and derivative commute *only provided the surface term (the first term in the r.h.s.) is zero*. If not, this term has to be taken into account in the derivation of LES equations. When dealing with unbounded systems, this problem of commutativity is not important, for one usually consider physical quantities which tends to zero at infinity. The non-commutativity shows up when dealing with finite size systems, where boundary conditions may reflect some physical processes.

15.4.2 Gabor transform

Definition

Our ultimate goal is to write an equation for the small (subgrid) scales, as a function of the large (resolved) scales. However, we would like to take into account the fact that the small scales are strongly inhomogeneous. A good way of dealing inhomogeneous fields is to decompose them into wave packets, using e.g. a Gabor transformation [NKD98]:

$$\hat{u}'(\mathbf{x}, \mathbf{k}, t) = \int f(\mathbf{x} - \mathbf{x}') e^{i\mathbf{k} \cdot (\mathbf{x} - \mathbf{x}')} \mathbf{u}'(\mathbf{x}', t) d\mathbf{x}'. \quad (15.41)$$

For reasons of convenience which will appear later, we choose here $f(\mathbf{x}) = \sqrt{g(\mathbf{x})}$ (since g is a positive function, this is always possible). We could also have achieved the same decomposition using a wavelet transformation [AMR97], but they are less handy to use in analytical computations.

Useful properties of the Gabor transform

A few properties of the Gabor transformation (15.41) are worth mentioning at this point. First, the inverse Gabor transform is easily obtained by an integration over \mathbf{k} :

$$f(0) \mathbf{u}'(\mathbf{x}, t) = \frac{1}{(2\pi)^D} \int \hat{\mathbf{u}}'(\mathbf{x}, \mathbf{k}, t) d\mathbf{k}. \quad (15.42)$$

Second, we note that like for the filtering, the commutation of Gabor transform and partial derivative is subject to surface terms depending on boundary conditions. The proof is analog to the one given in Section II.A.2. Also, there is an interesting approximation to the derivative of the Gabor transform, according to:

$$\partial_i \hat{\mathbf{u}}' \approx i k_i \hat{\mathbf{u}}' + O(1/(Lk)), \quad (15.43)$$

where L is the typical scale of the large scale flow. Technically speaking, $\varepsilon = 1/(kL)$ labels the "scale separation" between the large scale and the small scales. It is a parameter much less or less than one. Rigorous expansions in terms of this parameter are possible [DubrNaza98, NKD98] but for pedagogical reasons, we shall give here more heuristic derivations of the equations. Thirdly,

it is interesting to consider the Gabor transform of a quantity involving the product of a function varying over large scales (e.g. \mathbf{U}) and a function varying over small scales (e.g. \mathbf{u}'):

$$\widehat{\mathbf{U}\mathbf{u}'} = \int f(\mathbf{x} - \mathbf{x}') e^{i\mathbf{k} \cdot (\mathbf{x} - \mathbf{x}')} \mathbf{U}(\mathbf{x}', t) \mathbf{u}'(\mathbf{x}', t) d\mathbf{x}'. \quad (15.44)$$

Because the kernel f varies over scales of the order of $1/k_c$, while U varies over scales of the order L , one can Taylor expand the function U around the point \mathbf{x}' as a function of ε . To first order in ε , and after integration by parts, we then get:

$$\widehat{\mathbf{U}\mathbf{u}'}(\mathbf{x}, \mathbf{k}, t) = \mathbf{U}(\mathbf{x}, t) \hat{\mathbf{u}'} + i \nabla_i (U_j(\mathbf{x}, t)) \nabla_{k_i} \hat{\mathbf{u}}'. \quad (15.45)$$

This expansion will be useful in our derivations.

Finally, it is interesting to consider the average of the product of two small scale quantity, e.g. the Reynolds stress $\langle u'_i u'_j \rangle$. Using our definition of filtering (16.9) and the fact that $(2\pi)^D \delta(x' - x'') = \int e^{ik(x-x')} e^{-ik(x-x'')} dk$ and $f^2 = g$, we can write the Reynolds stress at point \mathbf{x} and time t as a function of the Gabor transform:

$$\begin{aligned} \langle u'_i u'_j \rangle &= \frac{1}{2(2\pi)^D} \int \{ \hat{u}'_i(\mathbf{k}, \mathbf{x}, t) \hat{u}'_j(-\mathbf{k}, \mathbf{x}, t) \\ &\quad + \hat{u}'_i(-\mathbf{k}, \mathbf{x}, t) \hat{u}'_j(\mathbf{k}, \mathbf{x}, t) \} d\mathbf{k}. \end{aligned} \quad (15.46)$$

15.4.3 Derivation of the dynamical equation

Using the filter, we decompose the velocity field into large scale and small scale components:

$$\begin{aligned} \mathbf{u}(\mathbf{x}, t) &= \mathbf{U}(\mathbf{x}, t) + \mathbf{u}'(\mathbf{x}, t), \\ \mathbf{U}(\mathbf{x}, t) \quad uiv \quad \bar{u} &= \int G(\mathbf{x} - \mathbf{x}') \mathbf{u}(\mathbf{x}', t) d\mathbf{x}'. \end{aligned} \quad (15.48)$$

Equations for the large scales of motion are obtained by application of the spatial filter (16.9) to the individual terms of the basic equations (??). They are:

$$\begin{aligned} \partial_j U_j &= 0, \\ \partial_t U_i + \partial_j \overline{U_i U_j} + \partial_j \overline{U_i u_j} + \overline{U_j u_i} + \partial_j \overline{u_i u_j} &= \\ -\partial_i P + v \Delta U_i + F_i, \end{aligned} \quad (15.49)$$

In these equations, we have dropped primes on subgrid components for simplicity; this means that from now on, any large-scale quantities are denoted by a capital letter, while the small-scale quantities are denoted by a lower case letter. Equation for the small-scale component is obtained by subtracting the large-scale equation from the basic equations (??); this gives

$$\begin{aligned} \partial_j u_j &= 0, \\ \partial_t u_i + \partial_j ((U_i + u_i)(U_j + u_j) - \overline{(U_i + u_i)(U_j + u_j)}) &= \\ -\partial_i p + v \Delta u_i + f_i, \end{aligned} \quad (15.50)$$

Several terms contribute to the interaction of scales: *non-local* terms, involving the product of a large scale and a small scale component, and *local* term, involving two small-scale components. One way to study the dynamical effect of these contributions at small scale, is to integrate numerically a set of two coupled equations, in which the local small scale interactions have been switched off at

the small scale². This corresponds to the following set of equations,

$$\begin{aligned} \partial_t U_i + \partial_j \overline{U_i U_j} &= -\partial_j \overline{U_i u_j} - \partial_j \overline{U_j u_i} - \partial_j \overline{u_i u_j} \\ &\quad - \partial_i P + v \Delta U_i + f_i \end{aligned} \quad (15.51)$$

$$\begin{aligned} \partial_t u_i + \partial_j (U_i u_j) + \partial_j (u_i U_j) &= -\partial_i p + v \Delta u_i + \sigma_i, \\ \partial_j U_j = \partial_j u_j &= 0, \end{aligned} \quad (15.52)$$

where

$$\sigma_i = \partial_j (\overline{U_i U_j} - U_i \overline{U_j} + \overline{u_j U_i} + \overline{U_j u_i}). \quad (15.53)$$

The later describes a forcing of the small scales by the large scales via the energy cascade mechanism. This term is always finite even when the external forcing \mathbf{f} (which is always at large scales) is absent. The small scale equation is linear and it resembles the equations of the Rapid Distortion Theory [townsend76]. We shall therefore refer to this new model as the RDT model.

15.4.4 Interest of RDT model

From a theoretical point of view, such model enables analytic derivation of the law of the wall [DLNK], or of the heat transport in Rayleigh-Bénard convection [D], that appear to be in good agreement with available data. From a numerical point of view, the RDT-WKB model enables to produce a model in 2D that produces the same results than a DNS in a time reduced by two orders of magnitudes (Figure 1). However, it gave disappointing results in 3D for 2 main reasons: i) the non-local hypothesis is very good in 2D [LDN], but not in 3D, so that an eddy viscosity (with adjustable parameter) has to be added anyway to maintain good energy balance [LDM]. ii) the wave packets have $2 \times D$ degrees of freedom (D for position, D for wavenumber). In 3D, this amounts to keep track of $6 \times N$ degrees of freedom, where N is the number of wave-packets. In order to get scales that reach the Kolmogorov scale, we need N to be of the order of a power of the Reynolds number [Laval,Dolganov]. In practice, the gain with respect to a fully resolved DNS then becomes negligible, regarding the complexity of the procedure.

15.5 Beyond eddy-viscosity models

The K41 energy cascade picture is at the basis of many subgrid-modelling of turbulence, to simulate flows at finite resolution $\Delta x > \eta$. For example, the "eddy-viscosity" model relies on the idea that any energy transfer at a given scale ℓ will eventually result in an energy dissipation at the Kolmogorov scale. One thus replaces the energy transfer by a viscous term, with a viscosity tuned to provide an energy dissipation equal to the energy transfer. If $\Delta x \gg \eta$, the velocity gradients at this scale $\Delta u / \Delta x$ are much lower than what they would be at scale η . The turbulent viscosity is therefore increased by a huge factor (of the order of $(\Delta u / \Delta(\partial u))^2$) with respect to the molecular viscosity. While this approach has enabled a successful computation of large scale flows in many fields of interest (aeronautical, geophysics, astrophysics), it is not very appropriate to account for the small scale inhomogeneity that results from the true multifractal local cascade. This is problematic in combustion or in problem involving phase transition (like rain or cloud formation), since chemical reactions preferably occur at location of high energy dissipation, where due to energy release the temperature locally increases. This cannot be captured by an eddy-viscosity model, that spread out homogeneously all dissipation over a cell of size Δx .

The issue is to find a subgrid model that capture the localization and energy dissipation focusing property evidenced by the WKHM-MFR approach. I know of several approaches that appear

²We do not switch off the local interactions at the large scales: this would hinder the cascade mechanism and prevent small scale generation from an initial large scale field.

promising in this context. The first one is to use simple random multiplicative models, introduced originally by [48, 49]. Such models naturally localize and concentrate energy dissipation. Then, by adjusting the probabilities, one can produce statistically realistic energy dissipation events. A more realistic but more complex version of this idea is to use multiplicative chaos (exponential of random matrices) to produce synthetic small scale velocity fields [57]. A third approach, developed by [54] is to introduce an "entropy viscosity", that locally adds a diffusion depending on the unbalance in the energy equation at scale Δx . This method is therefore "rooted" in the WKHM picture, and produces a viscosity that behaves differently depending on the local regularity of the flow: it is smaller than the order of consistency of the method in regions where the solution is smooth and well resolved and does not perturb the approximation. On the other hand, in regions where the solution is not well approximated due to the presence of large gradients that cannot be represented by the coarse mesh, the entropy viscosity adds a diffusion proportional to the unbalance in the energy equation so the resulting approximation dissipates energy.

15.5.1 Viscosity-entropy method

To avoid the accumulation of energy at the grid scale at high Reynolds numbers when the grid is not fine enough to resolve the Kolmogorov scale, we use a LES-like technique called entropy viscosity. This method, developed in [**Gu_Ma_Qu_2005**, **Guermond_pasquetti_popov_JCP_2011**, **Guermond_pasquetti_popov_suitable**], consists of adding a local artificial viscosity made proportional to the residual of the kinetic energy balance. This artificial viscosity is added on the right-hand side of (??) in the form $\nabla(v_E \nabla \mathbf{u})$. This induces a nonlinear diffusion proportional to the local energy imbalance that in turn allows the unresolved scales to be better accounted for. The method has its roots in the notion of suitable weak solutions introduced by [**MR88i:35137**] and which has been shown by [**MR84m:35097**] to be the only reasonable notion of solution currently available for the 3D Navier-Stokes equations.

We now give some technical details on the computation of the entropy viscosity. Since the approximation mixes finite elements and Fourier approximation, we construct a three-dimensional mesh by considering the tensor product of the finite element mesh in the meridian section with the uniform azimuthal one-dimensional mesh induced by the Fourier approximation. Denoting by M the number of complex azimuthal Fourier modes, the mesh size in the azimuthal direction at the radius r is $2\pi r/(2M - 1)$. For each two-dimensional finite element cells K , we denote by $h_K = \min(\min_{\mathbf{x} \in K} \frac{2\pi r}{2M-1}, \text{diam}(K))$. Assuming that $n \geq 2$, we define the residual of the momentum equation as follows:

$$\begin{aligned} \text{Res}_{\text{NS}}^n &= \frac{\mathbf{u}^n - \mathbf{u}^{n-2}}{2\tau} + (\mathbf{u}^{n-1} \cdot \nabla) \mathbf{u}^{n-1} \\ &\quad - \frac{1}{2} \mathbf{u}^{n-1} + \nabla p^{n-1} - \mathbf{f}^{n-1}. \end{aligned} \tag{15.54}$$

This residual is then computed at each time step and over every mesh cell in the real space. The local artificial viscosity is defined on each cell K by:

$$v_{R|K}^n = \frac{h_K^2 \|\text{Res}_{\text{NS}}^n \cdot \mathbf{u}^n\|_{\infty(D_K)}}{\|\mathbf{u}^n\|_{\infty(D_K)}^2}. \tag{15.55}$$

where D_K is the patch composed of the cells sharing one face with the cell K in the real space. The quantity $v_{R|K}^n$ is expected to be as small as the consistency error in smooth regions and to be large in the regions where the Navier-Stokes equations are not well resolved. To be able to run with CFL numbers of order $\mathcal{O}(1)$, we finally define the entropy viscosity as follows:

$$v_{E|K}^n = \min \left(c_{\max} h_K \| \mathbf{u}^n \|_{\infty(D_K)}, c_e v_{R|K}^n \right), \quad (15.56)$$

where $c_{\max} = \frac{1}{8}$ and c_e is a tunable constant $\mathcal{O}(1)$. In classical codes, the entropy viscosity scales like $\mathcal{O}(h_K^3)$ in smooth regions and scales like $\mathcal{O}(h_K)$ in regions with very large gradients.

This LES technique has been validated with $c_{\max} = \frac{1}{8}$ and $c_e = 1$ in [**cappanera2016two**] for flows in precessing cylinders and in [**wang2019entropy**] for turbulent flows in a flexible pipe (notice that the parameter α , defined therein in equation (2.13), is equal to $c_e/2$). We have used this method in [**nore_castanon_quiroz_cappanera_guermond_2018**] to perform high Reynolds number computations in a magnetohydrodynamics version of the von Kármán experiment.

15.5.2 REWA models

REduced Wavenumber Approximation (REWA) models are models based on a Fourier representation of the Navier-Stokes equation:

$$\begin{aligned} ik_n \cdot \hat{u}_n &= 0, \\ \partial_t \hat{u}_n + (\hat{u} * \hat{u})_n &= -Ik_n \hat{p}_n - \nu k_n^2 \hat{u}_n, \end{aligned} \quad (15.57)$$

where \hat{u}_n represents the n_{th} mode of the Fourier decomposition $u(x,t) = \sum_n e^{ik_n x} \hat{u}_n(t)$, k_n is the wavenumber and $*$ stands for the convolution product in Fourier space:

$$(f * g)_n = \sum_{k_n = k_p + k_q} f_p g_q. \quad (15.58)$$

In the exact Fourier representation, k_n follows a linear progression: $k_n = n\Delta k$ and the spacing between two wavenumber is constant. With such assignment, it is equivalent to solve Navier-Stokes equation in the physical space (using $u(x,t)$) or in the Fourier space (using \hat{u}_n) for fluids on torus. However, the cost is very large, whenever the fluid is turbulent. A somewhat drastic simplification that leads to a huge saving of computational cost is to keep only a reduced subset of Fourier modes following a geometric progression of step λ [refs]. This can be seen as the equivalent of a discretization over a log-grid, since it takes only $M \sim (\log(Re)/\log\lambda)^3$ modes to span the whole range of scales between the injection scale and the dissipation scale. The geometric decimation in Fourier space implies a substantial loss of accuracy for the description of the flow in the physical space. This makes these models more suitable to estimate statistical fluctuations of global quantities (such as heat transport, mean temperature, energy spectra), that to reproduce spatial distributions of these quantities. Moreover, the raw REWA mode reduction implies a destruction of the basic laws of the flow: since some modes are arbitrarily left out, there is no guarantee that the energy balance is correct, and that energy (and other quantities like helicity, or angular momentum) is conserved in the inviscid limit. To overcome such limitation, one needs an additional modelling.

GOY Model

A clever way to constrain energy conservation is to tune the nonlinear interaction between Fourier modes to avoid energy losses. The corresponding 1D models are called GOY shell model [] and have been generalized to any space dimension by [**campolino**]. In GOY shell models, the velocity field corresponding to the wavenumber $k_n = k_0 2^n$ is represented by one complex mode u_n that can only interact with adjacent wavenumbers. The evolution equation is then

$$d_t u_n = -D_n + IC_n + F_n, \quad (15.59)$$

where I is the imaginary number, and the dissipation D_n , forcing F_n and interaction term C_n are given by

$$\begin{aligned} D_n &= -\nu k_n^2 u_n, \\ F_n &= f \delta_{n4}, \\ C_n &= k_n u_{n+1}^* u_{n+2}^* + b k_{n-1} u_{n-1}^* u_{n+1}^* + c k_{n-2} u_{n-1}^* u_{n-2}^*, \end{aligned} \quad (15.60)$$

where u_n^* stand for the complex conjugate of u_n , and b and c are two free parameters that can be tuned to select the shape of the two inviscid invariants of equation (2). For example, the choice $c = -(1 - b)$ guarantees that one of the inviscid invariant is equal to the energy $E = \sum_n |u_n|^2$ [Bifetc]. To guarantee the conservation of the helicity, $H = \text{sum}_n (-1)^n k_n^2 |u_n|^2$, one must further impose that $b = -1/2$. From this equation, one sees that while D_n is the "normal" Fourier representation of the dissipation in Fourier space, C_n , which represents the convolution, only keeps interactions between the nearest modes, which is a big approximation with respect to the Fourier convolution. More over, this model is only 1D,. A more general way to approximate the convolution that holds for any dimension is done in log-lattices.

15.5.3 Log-lattices

In this model, the modes are evenly spaced points in log space ("logarithmic lattices" or "Log grids") of step λ : they are labelled by 3 integer (m, n, p) such that a mode k is given by $k = (q_0 \lambda^m, s_0 \lambda^n, t_0 \lambda^p)$. LogLattice modes are interacting via nonlinear equations that are derived from the fluid equations by substituting for the convolution product a new operator, that can be seen as a convolution on the log-lattice, and preserves all symmetries of the original equations. It was shown by Campolina and Mailybaev that if we impose that the convolution product is still given by Eq. (convorodinaire, but with k_n , k_p and k_q forced to live the log-grid, then the log-lattice spacing can only take special values so that either $\lambda = 2$ or $\lambda = 1.05$, or λ is solution of $1 = \lambda^a + \lambda^b$ where $0 < a < b$ are mutually prime integers number no larger than 62. In that case, the values of a and b govern the number of possible interacting triads. Such model was shown to exhibit known features of Burgers, Euler and Navier-Stokes equation in the Fourier space (energy spectrum, energy transfers), over an unprecedented wide range of scales [campolina20], see figure 15.1. The model is valid for all dimensions. In 1D, it was shown to correspond [campolina20] to the Sabra shell model of turbulence[gloaguen85, biferale03].

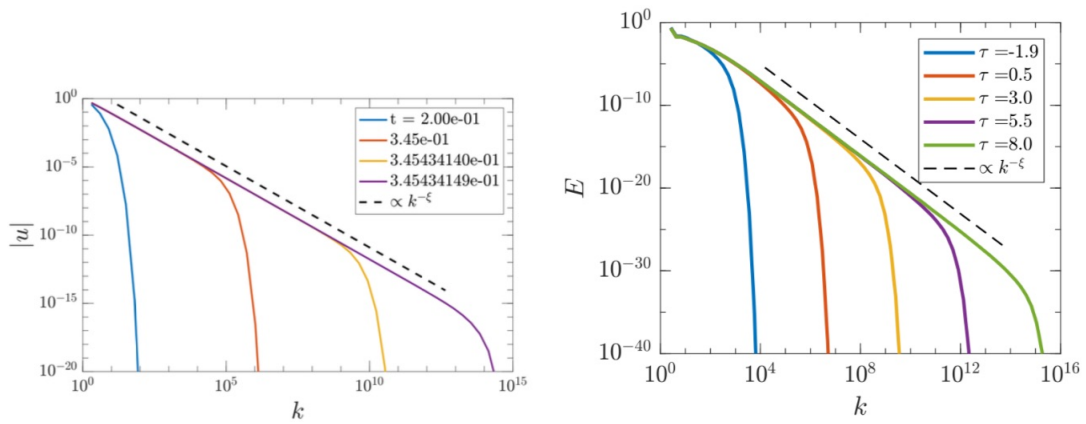


Figure 15.1: Energy spectra obtained by log-lattice method by Campolina and Mailybaev for times before blow-up: (a) Burgers equation, slope $\xi = 1.19$ (1D); (b) Euler equation (3D) slope $\xi = 2.26$. Note the unprecedented range of wavenumbers with respect to a DNS (see figure xx).

Beyond incompressible turbulence

16	Rayleigh-Benard Convection	147
16.1	Phenomenology	
16.2	Equations	
16.3	Physics of Convection	
16.4	Convection onset	
16.5	Scaling laws in convection	
	Bibliography	155
	Articles	
	Books	
	Index	161

16. Rayleigh-Benard Convection

16.1 Phenomenology

16.1.1 Description

In fluid mechanics, the Rayleigh-Benard (RB) equations describe the dynamics of a fluid enclosed in a volume, in which thermal energy is injected at the bottom via imposed heat flux or temperature gradient. The simplest set-up is made of a fluid enclosed in a cell heated from below and cooled from above see Figure 16.1. The temperature difference ΔT is maintained by two conducting parallel and horizontal plates, separated by a distance H . In most studies, the plates are orthogonal to the uniform gravitational field $\mathbf{g} = -g \mathbf{e}_z$. (figure 16.1).

16.1.2 Observations

As the fluid temperature changes, density differences arises. Hot sections at the bottom expand while cooled parts at the top contract. If ΔT is kept small the fluid will stay almost motionless, and

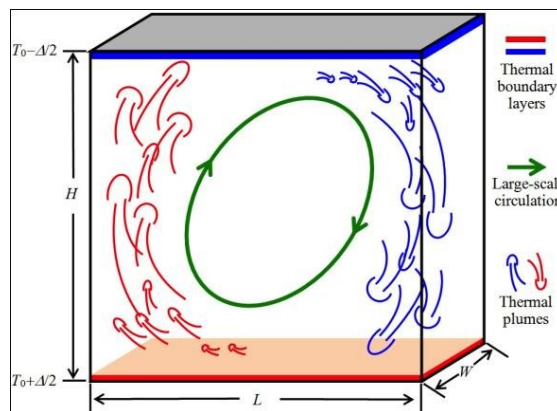


Figure 16.1: Sketches of a Rayleigh-Benard cell and the resulting convection.

the heat transfer will happen only through diffusion with a linear temperature gradient. But if ΔT is raised over a critical value, the buoyancy from the fluid density differences will transfer the heat faster than diffusion, giving rise to convection.

Convection manifests itself in the temperature field by the presence of plumes, i.e. very thin temperature structures that detach from the boundaries: hot plumes, that detach from the bottom boundary and rise to bring hot temperature to the top plate; conversely, cold plume detach from the top boundary and plunge towards the bottom to bring cold temperature to the bottom. Overall, temperature mixing occurs inside the core, while a large scale circulation develop within the cell. The mixing ensures that in the bulk of the fluid, the temperature is homogeneous, being equal to the mean temperature between the top and the bottom. Near boundaries, very thin boundary layers develop, to enable the fluid to catch up with boundary conditions at the top and the bottom. The size of these boundary is controlled by the diffusivity κ . Inside the boundary, the temperature profile is linear.

The geometry of the structures depend on the ratio $Pr = v/\kappa$: when it is very small, like in liquid sodium, the plume are thick, and and very smooth, while the fluid itself develops very small vorticity structures, characteristic of a turbulent fluid. When Pr is of order one, like in the air, the plumes and the temperature field are also very convoluted and complex, and organize itself around turbulent vorticity structures.

16.2 Equations

It is commonly assumed that the fluid's flow can be described using the Oberbeck-Boussinesq approximation [Rieutord2014] which consists to assume that the fluid is Newtonian, mechanically incompressible (i.e. the divergence of the velocity field is zero) but thermally compressible (i.e. the variation of temperature induces a variation of density), and that we can neglect the effect of viscous dissipation heating. More precisely, we assume that the fluid motions are described by the following equations

$$\nabla \cdot \mathbf{u} = 0, \quad (16.1)$$

$$\frac{\partial \mathbf{u}}{\partial t} + \mathbf{u} \cdot \nabla \mathbf{u} = -\frac{1}{\rho_0} \nabla p + v \Delta \mathbf{u} + \alpha(T - T_0)g \mathbf{e}_z, \quad (16.2)$$

$$\frac{\partial T}{\partial t} + \mathbf{u} \cdot \nabla T = \kappa \Delta T, \quad (16.3)$$

where ρ_0 is the reference volumic mass of the fluid, v is the kinematic viscosity, κ is the thermal diffusivity, $\mathbf{u} = (u_x, u_y, u_z)$ is the velocity, p is the pressure variation about the hydrostatic equilibrium profile, and T the temperature. The last equations constitute the simplest description of heat convection. The Oberbeck-Boussinesq approximation is valid when the thermodynamical properties do not vary significantly in the flow [Gray1976]. We focus on the case where $H_x \simeq H_y \simeq H_z \equiv H$ so the aspect ratio of the container $\Gamma \equiv H_x/H_z$ is near unity. When we scale the temperature by ΔT , the velocity by the free fall velocity $U \equiv \sqrt{\alpha \Delta T g H}$, the lengths by H and the time by H/U , the dimensionless equations of motions are

$$\tilde{\nabla} \cdot \tilde{\mathbf{u}} = 0, \quad (16.4)$$

$$\frac{D\tilde{\mathbf{u}}}{Dt} = -\tilde{\nabla} \tilde{p} + \sqrt{\frac{Pr}{Ra}} \tilde{\Delta} \tilde{\mathbf{u}} + \tilde{T} \mathbf{e}_z, \quad (16.5)$$

$$\frac{D\tilde{T}}{Dt} = \frac{1}{\sqrt{RaPr}} \tilde{\Delta} \tilde{T}, \quad (16.6)$$

where \tilde{T} is the dimensionless temperature, $\tilde{\mathbf{u}} = (\tilde{u}_x, \tilde{u}_y, \tilde{u}_z)$ is the dimensionless velocity, \tilde{p} is the dimensionless pressure perturbation, $Ra \equiv \alpha g \Delta T H^3 / \nu \kappa$ is the Rayleigh number, and $Pr = v/\kappa$

is the Prandtl number. We define the Reynolds number $Re \equiv UH/v = \sqrt{Ra/Pr}$ and the Peclet number $Pe \equiv UH/\kappa = \sqrt{RaPr}$, and we will focus on the case where $Re, Pe \gg 1$.

Within the Oberbeck-Boussinesq approximation, convection is therefore controlled by Ra , Pr , Γ , and the boundary conditions which are basically: no slip boundary conditions for the velocity, adiabatic conditions on the lateral sides of the cell, and imposed temperature on the top and bottom plates. The key response of the system is the vertical heat flux, quantified by the so called Nusselt number

$$Nu \equiv \frac{JH}{\kappa\Delta T}. \quad (16.7)$$

It represents the ratio between J , the total heat flux ensured by the fluid divided by the laminar heat flux $\kappa\Delta T/H$.

16.3 Physics of Convection

16.3.1 Energy budget

Using the Boussinesq equation, it is possible to infer exact energy balance law for the convection. For this, we multiply the velocity equation by u and the temperature equation by T . Taking space and time average, we get:

$$\begin{aligned} \partial_t \frac{\langle u^2 \rangle}{2} &= -\sqrt{\frac{Pr}{Ra}} \langle (\nabla u)^2 \rangle + Nu - 1, \\ \partial_t \frac{\langle T^2 \rangle}{2} &= -\frac{1}{\sqrt{RaPr}} \langle (\nabla T)^2 \rangle + Nu. \end{aligned} \quad (16.8)$$

The negative terms correspond to "sink" of energy, due to viscosity and diffusivity. The term in Nu represent a coupling term between the kinetic energy $E_k = \langle u^2 \rangle / 2$ and the "potential" or "thermal" energy $E_p = \langle T^2 \rangle / 2$. When we heat the bottom boundary, we inject energy into the thermal component, that is then converted into kinetic energy via the Nu term. Therefore, convection is just a process by which thermal energy is converted into kinetic energy (the large scale circulation): it is a thermal engine.

16.3.2 Example: the Earth climate as a thermal engine

The Earth climate is very complicated, and depends on many processes: atmosphere, ocean, volcanoes, vegetation, albedo, etc etc. However, to first order, it may be understood using the same physics than convection. Interestingly enough, the word "climate" comes from a greek word "klima", that means inclinaison. Indeed, the inclinaison of the axis of rotation of the Earth with respect to the ecliptic plane (the plane containing the Sun and the planets) plays a major role in defining a climate, becomes it controls all the insolation that is received by the North and the South hemisphere during the year. In winter, the sun rays are mainly perpendicular to the ground in the south hemisphere, while they are more tangential in the north hemisphere. As a result, the south hemisphere receives more heat from the Sun than the North, the converse being true in summer. Moreover, in general, sun rays are more tangential at the pole than at the equator. As a result, there is more heat reaching the ground at the equator than at the pole, resulting in a temperature difference between equator and the two poles: in some sense, the Earth is like a double Rayleigh Benard cell, glued together, with the temperature difference being piloted by the season. Due to the temperature imbalance, large scale circulations are created in the atmosphere and in the ocean, that help transporting heat from the equator to the pole. These large scale circulations have famous names, like "alizs" for the wind, or "gulf-stream" for the ocean.

Note that there is an additional subtleties for the climate, as the inclination of the rotation axis of the Earth is not constant, but is periodically modulated over a period of about 23 000 years, due to precession of the equinox. This modulates the solar flux by about 10%, a seemingly small number that is enough to induce a severe change in the climate, as it is responsible for the alternation of "glacial periods", and inter-glacial period. The difference in mean temperature between the two types of regimes is only 5 degrees, but it is sufficient to make half of the north hemisphere covered with ice! This shows how sensitive the climate is, and why it is not such a great idea to perturbate it with CO₂.

16.4 Convection onset

16.4.1 Non-rotating case

Convection is an instability, so it sets-up at a certain critical value of the parameter Ra_c . The value of this parameter depends on the boundary conditions. It is easy to do in the case of periodic boundary conditions, for the so-called "homogeneous" Rayleigh Benard convection (HRB). In that case, we write $T = -\Delta T z / H + \theta$, and assume that both u and θ are periodic. To estimate the convection threshold, we will then do 2 approximation: first, we assume that we are very near the threshold, so that deviations from the "equilibrium state" $u = \theta = 0$ are small. This will allow us to neglect all non linear terms in the equations. Then, because of periodicity, we can work in the Fourier space, and decompose the field into "plane waves":

$$\begin{aligned} \mathbf{u}(x, t) &= \sum_k (u(k), v(k), w(k)) e^{\sigma t + ikx}, \\ p(x, t) &= \sum_k p(k) e^{\sigma t + ikx}, \\ \theta(x, t) &= \sum_k \theta(k) e^{\sigma t + ikx}, \end{aligned} \quad (16.9)$$

where $k = (k_x, k_y, k_z)$ is the wave vector, and σ is the growth rate of the instability: if σ has a negative real part, then all perturbation decay, while the instability develop when the real part of $\sigma > 0$. Plugging this decomposition into the equations (16.5) and (16.6) and neglecting non-linear terms we get:

$$\begin{aligned} ik_x u + ik_y v + ik_z w &= 0, \\ \sigma u &= -ik_x p - \sqrt{\frac{Pr}{Ra}} k^2 u, \\ \sigma v &= -ik_y p - \sqrt{\frac{Pr}{Ra}} k^2 v, \\ \sigma w &= -ik_z p - \sqrt{\frac{Pr}{Ra}} k^2 w + \theta, \\ \sigma \theta &= w - \frac{1}{\sqrt{RaPr}} k^2 \theta. \end{aligned} \quad (16.10)$$

This represent a linear, homogeneous system of equations in the variable (u, v, w, p, θ) . If we want this system to have other solutions than $(0, 0, 0, 0)$, we must impose the determinant of the system to be zero, which provides us with an expression linking σ , k and the parameters of the system, namely:

$$\sigma^2 + 2k^2 Ra^{-1/2} \sigma + \frac{k^4}{Ra} - \frac{1}{1 + \mu^2} = 0, \quad (16.11)$$

where $\mu^2 = k_z^2/(k_x^2 + k_y^2)$. This is a second order equation for σ , there are therefore two solutions. Since the prefactor of σ is positive, it means that the sum of the two solution is negative. To ensure that there exist at least one solution with a positive real part, we must then ensure that the product of the solution, given by $\frac{(1+\mu^2)k^4}{Ra} - 1$ is negative. Since $(1+\mu^2)k^4 > k_{min}^4$, where k_{min} is the minimal wavenumber, this is achieved whenever $Ra > k_{min}^4 = Ra_c$. Since $k_{min} \sim 2\pi$, this gives $Ra_c \sim 1558$.

16.4.2 Rotating case

Using this technique, we can also infer the influence of rotation on the convection threshold. In the sequel, we assume $Pr = 1$ for simplicity. In the presence of a rotation around the vertical axis, with intensity Ω , we have to add a term $2\Omega e_z \times \mathbf{u}$ corresponding to the Coriolis force to the l.h.s. of equation (16.5). In non-dimensional units, this makes a term $1/Roe_z \times \mathbf{u}$, where $Ro = \sqrt{RaE}$ is the Rossby number, written in term of the Ekman number $E = v/\Omega H^2$. Using the same technique than before, we see that the linearized equation of motion become:

$$\begin{aligned} ik_x u + ik_y v + ik_z w &= 0, \\ \sigma u - \frac{v}{Ro} &= -ik_x p - \sqrt{\frac{Pr}{Ra}} k^2 u, \\ \sigma v + \frac{u}{Ro} &= -ik_y p - \sqrt{\frac{Pr}{Ra}} k^2 v, \\ \sigma w &= -ik_z p - \sqrt{\frac{Pr}{Ra}} k^2 w + \theta, \\ \sigma \theta &= w - \frac{1}{\sqrt{RaPr}} k^2 \theta. \end{aligned} \quad (16.12)$$

Imposing that the determinant of the system is zero, we can check that we still find a second order equation for σ , that writes:

$$\sigma^2 + 2k^2 Ra^{-1/2} \sigma + \frac{k^4}{Ra} + (1 + \mu^2)^{-1} \left(\frac{\mu^2}{Ro^2} - 1 \right) = 0, \quad (16.13)$$

where $\mu^2 = k_z^2/(k_x^2 + k_y^2)$. In the limit of large rotation, $Ro \rightarrow 0$ and the condition for instability now reads: $\frac{\mu^2}{Ro^2} - 1 < 0$. The minimal value of μ^2 is obtained when k_z takes its smallest possible value $k_z = 2\pi$, while $k_x^2 + k_y^2$ takes its largest possible value, ie $k_x^2 + k_y^2 \sim \sqrt{Ra}$ (above that, all is dissipated by viscosity. Taking into account that $Ro^2 \sim RaE^2$ we then get $Ra^{3/2} > 4\pi^2 E^{-2}$, giving a critical Rayleigh number scaling like $Ra_c \sim E^{-4/3}$. This means that the larger the rotation (the smaller E), the more difficult it is to get convection: rotation stabilizes the flow.

16.5 Scaling laws in convection

Despite its simplicity, Rayleigh-Benard set up is paradigmatic of convection, a process that governs heat transport and mixing in a variety of systems ranging from planetary and astrophysical flows to industrial devices. In that respect, a crucial question is how the heat flux in the system is connected with the temperature gradient. Near equilibrium, where both quantities are small, Fourier laws apply, and the heat flux is simply proportional to the temperature gradient. For larger values, the system enters in a non-linear, turbulent regime, where thermal energy is converted into mechanical energy, and the relation becomes nonlinear. The deviation from linearity are quantified by the relation between the Nusselt number, Nu , the ratio between the heat flux and its value near equilibrium, and the Rayleigh number, the non-dimensional temperature gradient between the two plates.

The phenomenology of homogeneous convection distinguishes several regimes for the behaviour of the heat flux, as a function of the forcing

16.5.1 Convection onset and Transitional regime

When $Ra \leq Ra_c$, we are in the laminar case. The fluid is at rest, $\langle u_z \theta \rangle = 0$ and the heat flux is only piloted by the Fourier law, so that $J = \kappa \Delta T / H$ and $Nu = 1$. Above the critical threshold for instability, when $Ra > \sim Ra_c$, convection sets in, $\langle u_z \theta \rangle$ starts becoming positif, and we have $Nu \sim (Ra - Ra_c)^\alpha$, where α is an exponent characterizing the (super)-critical transition to convection. Typically $\alpha \sim 1$.

16.5.2 Turbulent regime

Increasing Ra further, we reach a regime where the heat flux starts to depend non-linearly as a function of ΔT . As usual in turbulence, we shall assume that the dependance is via a power-law, and assume $Nu = Ra^\beta Pr^\gamma$. The problem is to find β and γ . There are two extreme cases where it is possible to infer α and β .

Boundary piloted heat transfer:Malkus regime

We first assume that there is a regime where the heat flux is entirely piloted by the boundary layer, of size $\delta \ll H$. This has two consequences: first, the heat flux corresponding to the dissipation of a temperature gradient ΔT over a layer of scale δ is juste $J \sim \kappa \Delta T / \delta$, resulting in $Nu = H / \delta$. Second, since the heat flux is entirely piloted by the boundary layer, it means that the scaling law between Nu and Ra cannot depend on the height H of the apparatus. Given that Nu is proportional to H , and Ra proportional to H^3 , this means that necessarily, $\beta = 1/3$ to be able to balance H from both sides of the relation. As noted by Malkus, this value of β also means that the boundary layer is just "critical": indeed, the Rayleigh number based on its width is constant, presumably equal to the critical Rayleigh number for transition to convection Ra_c . This means that $\alpha g \Delta T \delta^3 / \nu \kappa \sim Ra_c$, or $\delta / H \sim (Ra_c / Ra)^{1/3}$. Overall, we thus get:

$$Nu \sim Ra^{1/3}, \quad (16.14)$$

which is the so-called "Malkus regime" [[malkus1954heat](#)]. This regime is observed in many experiments (see [[ahlers2009heat](#)] for review).

Bulk piloted regime: Spiegel regime

We can also consider the "opposite situation", where all the heat flux is only piloted by what is going on "in the bulk", far from boundary layers. Given that the boundary layers are the only regions of the flow where viscous and thermal dissipation are relevant, this means that this regime is such the heat flux does not depends anymore on the viscosity or the diffusivity. With this assumption, it is easy to find what is the scaling, by simple dimensional argument. Assuming $Nu \sim Ra^\beta Pr^\gamma$ and counting powers of κ and ν , we get:

$$\text{power of } \nu: 0 = \beta - \gamma.$$

power of κ : $1 = \beta + \gamma$. The solution to this coupled equations is $\gamma = \beta = 1/2$. In that case, we have $Nu \sim (Ra Pr)^{1/2}$, also called "ultimate" or Spiegel regime [[spiegel1963generalization](#), [gl2000](#)], with possible logarithmic corrections [[kraichnan62](#)]. Experimental or numerical observations of the ultimate regime prove to be very difficult, and no final consensus has been reached so far about its existence in a pure RB setting [[chavanne97](#), [urban19](#), [doering96](#), [roche2020ultimate](#)], see Figure 16.2. It is believed that this regime only occurs that when Ra becomes very large, and when the boundary layers become fully turbulent. On the other hand, various modifications of the RB geometry aiming at suppressing the influence of the boundary layers result in experimental observation of a regime where $Nu \sim Ra^{1/2}$: use of highly elongated cells [[castaing17](#), [pawar16](#)], using rough [[ciliberto99](#), [rusaouen18](#), [zhu19](#), [kawano21](#)] or porous [[zou21](#)] boundaries, or radiatively heating the flow [[lepot18](#), [bouillaut19](#)].

Rotating regime Let us consider the case with rotation., which is a situation often met in geophysical or astrophysical situations. In that case, a term $2\Omega \times \mathbf{u}$ corresponding to the Coriolis

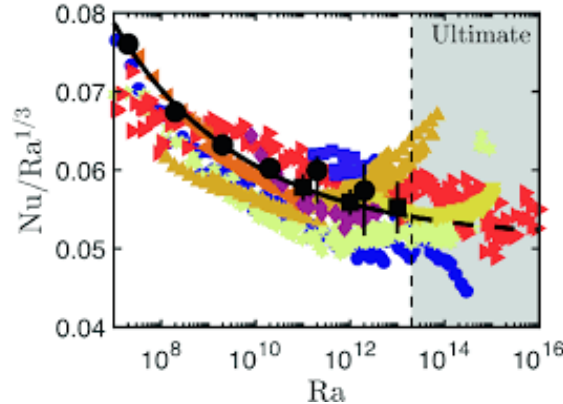


Figure 16.2: Compilation of experimental and numerical data for the compensated Nusselt versus Rayleigh numbers: the solid black line is the GL theory]; Experiments: blue bullets , purple squares, dark red diamonds, red right triangles, orange left triangles, yellow up triangles, yellow down triangles, yellow stars, ; Numerical simulations: black bullets, black squares (preliminary numerical simulations by Stevens (2019)).

force induced by a rotation of Ω has to be added to the l.h.s. of the velocity equation, (second equation of Eq. (equaRB)). In that case, a new non-dimensional parameter , the Ekman number $E = v/\Omega H^2$, has to be introduced.

As shown previously, the rotation has a stabilizing influence on the flow, so that the threshold for instability now increases with increasing rotation. Detailed studies show that $Ra_c \sim E^{-4/3}$. In addition, the rotation modifies the structure of the convective cells, that become align with the vertical axis in the case of strong rotation. This changes profoundly the heat transfer. To account for this effect xx suggests to perform the same phenomenology than in the non-rotating case, using $\tilde{Ra} = RaE^{4/3}$ instead of Ra . The ultimate regime is then found by stating that the relation between Nu and \tilde{Ra} and Pr should be such that Nu is independent of κ and v ;, resulting by the same reasoning than before to:

$$Nu \sim Ra^{3/2} E^2 Pr^{-1/2}. \quad (16.15)$$

This is the so-called geostrophic turbulent regime. This regime is difficult to achieved using direct numerical simulations. An interesting property of the geostrophic turbulent regime is that it can be expressed as a universal law, independent of the rotation and the Prandtl number, using the "turbulent" coordinates [qui]:

$$\begin{aligned} Nu_* &= \frac{NuE}{Pr}, \\ Ra_* &= \frac{RaNuE^3}{Pr^2}. \end{aligned}$$

In that case, the relation (16.15) becomes:

$$Nu_* \sim Ra_*^{3/5}. \quad (16.17)$$

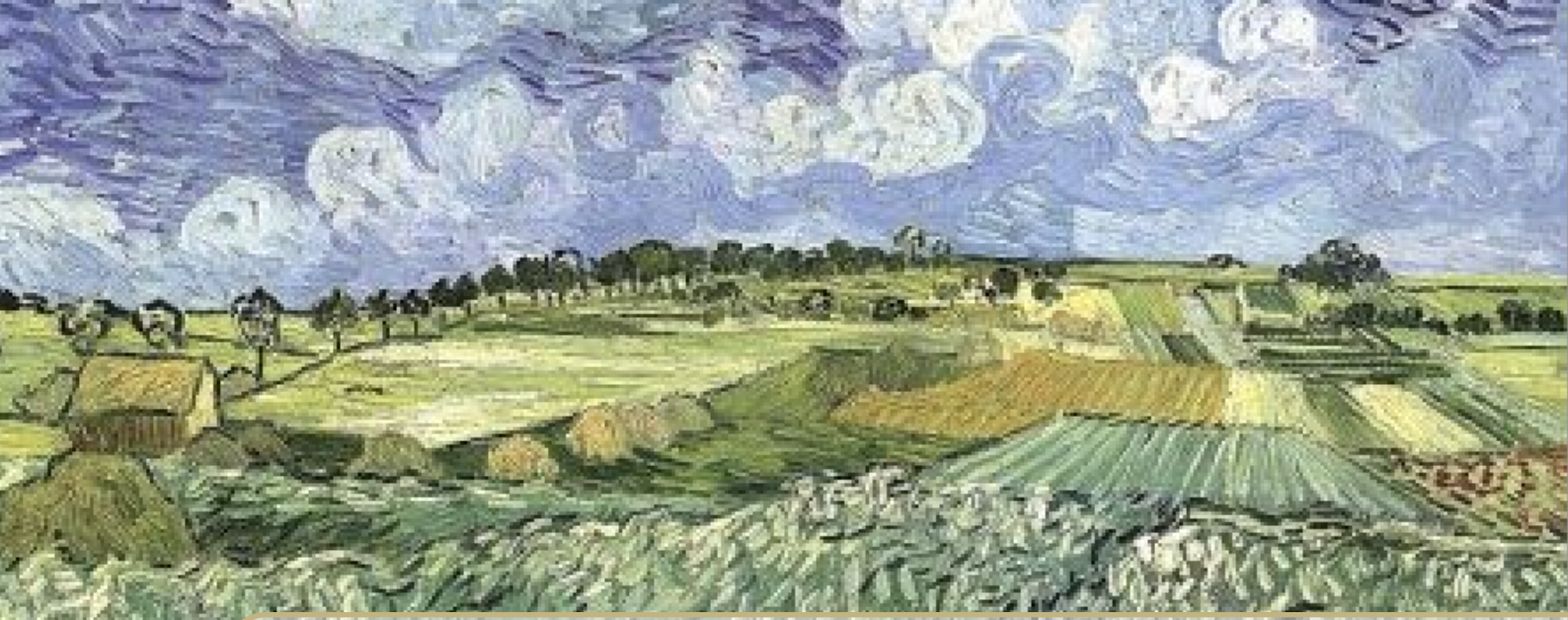
GL theory

A famous theory in convection is the Grossman-Lohse theory (hereafter GL theory) [**Grossmann-Lohse2000**, **Grossmann-Lohse2004**, **Grossmann-Lohse2011**, **Stevens-Lohse2013**] (see also part 2 of [**Ahlers2009**]). This theory gives predictions for regimes and the scalings of Nu and Re with Ra and Pr and is

completed by fits of the empirical prefactors using available data. It is a mix between two exact relations, derived from global energy budgets from the basic equations, and empirical dimensional arguments. The equations that describe Rayleigh-Benard convection however have a very rich mathematical structure, and there may be more to infer from them than just two global constraints.

Ultimate regime and dissipative anomaly

In a recent work, for example, Eyink and Drivas showed that the 'ultimate' scaling regime $Nu \sim Re^{1/2}$ can only hold if there is a dissipative anomaly both for the thermal ε_T and the kinetic ε_u energy, in the sense that $\lim_{V, \kappa \rightarrow 0} \varepsilon_u$ and $\lim_{V, \kappa \rightarrow 0} \varepsilon_T$ at fixed Pr are finite and positive. A similar phenomenon occurring for 3D classical turbulence (also known as the zeroth law of turbulence [frisch]) is thought to be connected to possible weak solutions of the Navier-Stokes equations [DuchonRobert]. Since Onsager [Onsager, EyinkSreenivasan], we know that corresponding solutions, if they exist, must have a Hölder exponent smaller or equal to $1/3$, meaning that the velocity field obeys *all* x s.t. $|u(x + \ell) - u(x)| \leq A\ell^h$, $h \leq 1/3$ in the limit $\ell \rightarrow 0$. As discussed in [Dubrulle19], this property has a lot of interesting consequences on the scaling properties of the velocity field, and enables to connect intermittency of the velocity and dissipation structure functions with location of high local energy transfer, using the multifractal phenomenology. The heart of the connection lies in a weak Karman-Howarth equation, that can be derived using properties of weak solutions of Navier-Stokes equations.



Bibliography

Articles

- [1] D. S. Agafontsev, E. A. Kuznetsov, and A. A. Mailybaev. “Development of high vorticity in incompressible 3D Euler equations: Influence of initial conditions”. In: *JETP Letters* 104.10 (Nov. 2016), pages 685–689. ISSN: 1090-6487. DOI: 10.1134/S002136401622001X. URL: <https://doi.org/10.1134/S002136401622001X> (cited on page 59).
- [2] D. S. Agafontsev, E. A. Kuznetsov, and A. A. Mailybaev. “Asymptotic solution for high-vorticity regions in incompressible three-dimensional Euler equations”. In: *Journal of Fluid Mechanics* 813 (2017), R1. DOI: 10.1017/jfm.2017.1 (cited on page 59).
- [3] Arneodo, A. et al. “Structure functions in turbulence, in various flow configurations, at Reynolds number between 30 and 5000, using extended self-similarity”. In: *Europhys. Lett.* 34.6 (1996), pages 411–416. DOI: 10.1209/epl/i1996-00472-2. URL: <https://doi.org/10.1209/epl/i1996-00472-2> (cited on page 61).
- [4] A. Babiano et al. “Chaotic advection in point vortex models and two-dimensional turbulence”. In: *Physics of Fluids* 6.7 (1994), pages 2465–2474. DOI: 10.1063/1.868194. eprint: <https://doi.org/10.1063/1.868194>. URL: <https://doi.org/10.1063/1.868194> (cited on page 113).
- [5] R. Benzi et al. “Extended self-similarity in turbulent flows”. In: *Phys. Rev. E* 48 (1 July 1993), R29–R32. DOI: 10.1103/PhysRevE.48.R29. URL: <https://link.aps.org/doi/10.1103/PhysRevE.48.R29> (cited on page 61).
- [6] Jean-Philippe Bouchaud and Antoine Georges. “Anomalous diffusion in disordered media: Statistical mechanisms, models and physical applications”. In: *Physics Reports* 195.4 (1990), pages 127–293. ISSN: 0370-1573. DOI: [https://doi.org/10.1016/0370-1573\(90\)90099-N](https://doi.org/10.1016/0370-1573(90)90099-N). URL: <https://www.sciencedirect.com/science/article/pii/037015739090099N> (cited on page 115).

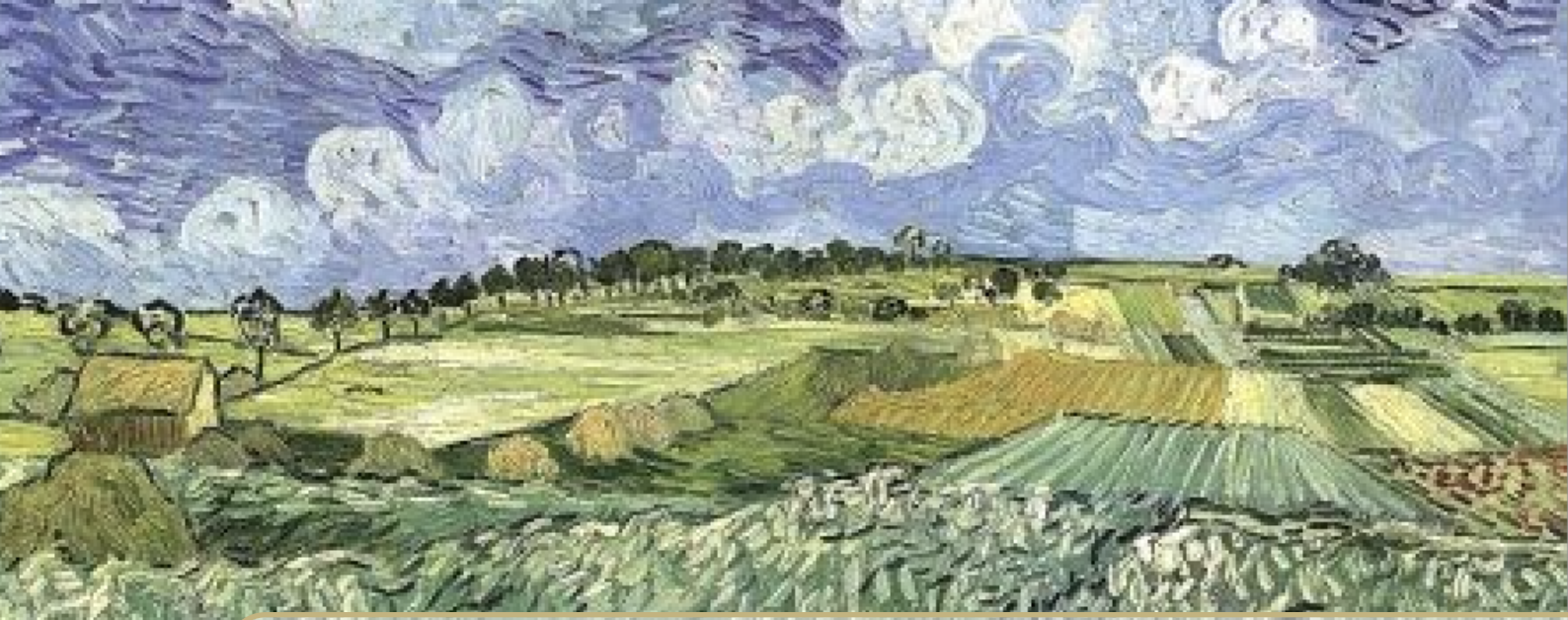
- [8] T. Buckmaster et al. “Onsager’s Conjecture for Admissible Weak Solutions”. In: *Communications on Pure and Applied Mathematics* (2018). DOI: 10.1002/cpa.21781. eprint: <https://onlinelibrary.wiley.com/doi/pdf/10.1002/cpa.21781>. URL: <https://onlinelibrary.wiley.com/doi/abs/10.1002/cpa.21781> (cited on page 42).
- [9] L. Caffarelli, R. Kohn, and L. Nirenberg. “Partial regularity of suitable weak solutions of the Navier-Stokes equations”. In: *Communications on Pure and Applied Mathematics* 35.6 (1982), pages 771–831. ISSN: 1097-0312. DOI: 10.1002/cpa.3160350604. URL: <http://dx.doi.org/10.1002/cpa.3160350604> (cited on page 88).
- [10] C. S. Campolina and A. A. Mailybaev. “Chaotic Blowup in the 3D Incompressible Euler Equations on a Logarithmic Lattice”. In: *Phys. Rev. Lett.* 121 (6 Aug. 2018), page 064501. DOI: 10.1103/PhysRevLett.121.064501. URL: <https://link.aps.org/doi/10.1103/PhysRevLett.121.064501> (cited on page 37).
- [11] D. Chae. “Nonexistence of Self-Similar Singularities for the 3D Incompressible Euler Equations”. In: *Commun. Math. Phys.* 1.273 (2007), pages 203–215 (cited on pages 37, 102).
- [12] M. Clusel and E. Bertin. “Global fluctuations in physical systems: a subtle interplay between sum and extreme value statistics”. In: *International Journal of Modern Physics B* 22.20 (2008), pages 3311–3368. DOI: 10.1142/S021797920804853X. eprint: <https://doi.org/10.1142/S021797920804853X>. URL: <https://doi.org/10.1142/S021797920804853X> (cited on page 70).
- [13] Andrea Crisanti et al. “Dynamics of passively advected impurities in simple two-dimensional flow models”. In: *Physics of Fluids A: Fluid Dynamics* 4.8 (1992), pages 1805–1820. DOI: 10.1063/1.858402. eprint: <https://doi.org/10.1063/1.858402>. URL: <https://doi.org/10.1063/1.858402> (cited on page 118).
- [15] P. Debue et al. “Dissipation, intermittency, and singularities in incompressible turbulent flows”. In: *Phys. Rev. E* 97 (5 May 2018), page 053101. DOI: 10.1103/PhysRevE.97.053101. URL: <https://link.aps.org/doi/10.1103/PhysRevE.97.053101> (cited on pages 18, 49, 62, 63, 79, 82, 84).
- [16] Th. Dombre and J-L. Gilson. “Intermittency, chaos and singular fluctuations in the mixed Obukhov-Novikov shell model of turbulence”. In: *Physica D: Nonlinear Phenomena* 111.1 (1998), pages 265–287. ISSN: 0167-2789. DOI: [https://doi.org/10.1016/S0167-2789\(97\)80015-2](https://doi.org/10.1016/S0167-2789(97)80015-2). URL: <http://www.sciencedirect.com/science/article/pii/S0167278997800152> (cited on page 24).
- [17] T. D. Drivas and G. L. Eyink. “An Onsager Singularity Theorem for Leray Solutions of Incompressible Navier-Stokes”. In: *arXiv:1710.05205* (2017) (cited on page 84).
- [19] B. Dubrulle. “A turbulent closure model for thin accretion disks”. In: 266.1 (Dec. 1992), pages 592–604 (cited on page 111).
- [20] B. Dubrulle, G. Morfill, and M. Sterzik. “The dust subdisk in the protoplanetary nebula.” In: 114.2 (Apr. 1995), pages 237–246. DOI: 10.1006/icar.1995.1058 (cited on page 127).
- [21] B. Dubrulle and L. Valdettaro. “Consequences of rotation in energetics of accretion disks.” In: 263 (Sept. 1992), pages 387–400 (cited on pages 110, 111).
- [22] Berengere Dubrulle. “Differential Rotation as a Source of Angular Momentum Transfer in the Solar Nebula”. In: 106.1 (Nov. 1993), pages 59–76. DOI: 10.1006/icar.1993.1158 (cited on page 127).

- [23] Bérengère Dubrulle and Uriel Frisch. “Eddy viscosity of parity-invariant flow”. In: *Phys. Rev. A* 43 (10 May 1991), pages 5355–5364. DOI: 10.1103/PhysRevA.43.5355. URL: <https://link.aps.org/doi/10.1103/PhysRevA.43.5355> (cited on pages 110, 132, 136, 137).
- [24] J. Duchon and R. Robert. “Inertial energy dissipation for weak solutions of incompressible Euler and Navier-Stokes equations”. In: *Nonlinearity* 13.1 (2000), page 249 (cited on pages 73, 75).
- [25] J. Eggers and M.A. Fontelos. “The role of self-similarity in singularities of partial differential equations”. In: *Nonlinearity* 22 (2009), R1–R44 (cited on page 24).
- [27] G. L. Eyink and K. R. Sreenivasan. “Onsager and the theory of hydrodynamic turbulence”. In: *Rev. Mod. Phys.* 78 (1 Jan. 2006), pages 87–135. DOI: 10.1103/RevModPhys.78.87. URL: <https://link.aps.org/doi/10.1103/RevModPhys.78.87> (cited on page 77).
- [28] G. Falkovich, K. Gawdzki, and M. Vergassola. “Particles and fields in fluid turbulence”. In: *Rev. Mod. Phys.* 73 (4 Nov. 2001), pages 913–975. DOI: 10.1103/RevModPhys.73.913. URL: <https://link.aps.org/doi/10.1103/RevModPhys.73.913> (cited on page 64).
- [31] U. Frisch, Z.S. She, and P.L. Sulem. “Large-scale flow driven by the anisotropic kinetic alpha effect”. In: *Physica D: Nonlinear Phenomena* 28.3 (1987), pages 382–392. ISSN: 0167-2789. DOI: [https://doi.org/10.1016/0167-2789\(87\)90026-1](https://doi.org/10.1016/0167-2789(87)90026-1). URL: <https://www.sciencedirect.com/science/article/pii/0167278987900261> (cited on pages 110, 124).
- [32] S. Gama, U. Frisch, and H. Scholl. “The two-dimensional Navier-Stokes equations with a large-scale instability of the Kuramoto-Sivashinsky type: Numerical exploration on the Connection Machine”. In: *Journal of Scientific Computing* 6.4 (1991), pages 425–452. DOI: <https://doi.org/10.1007/BF01060033> (cited on pages 126, 127).
- [33] S. Gama, M. Vergassola, and U. Frisch. “Negative eddy viscosity in isotropically forced two-dimensional flow: linear and nonlinear dynamics”. In: *Journal of Fluid Mechanics* 260 (1994), pages 95–126. DOI: 10.1017/S0022112094003459 (cited on pages 110, 125).
- [34] Y. Kimura and H. K. Moffatt. “A tent model of vortex reconnection under Biot-Savart evolution”. In: *Journal of Fluid Mechanics* 834 (2018), R1. DOI: 10.1017/jfm.2017.769 (cited on page 37).
- [35] L. L. Kitchatinov, G. Ruediger, and G. Khomenko. “Large-scale vortices in rotating stratified disks.” In: 287 (July 1994), pages 320–324 (cited on pages 110, 124).
- [37] A. N. Kolmogorov. “The local structure of turbulence in incompressible viscous fluids for very large Reynolds number”. In: *Dokl. Akad. Nauk SSSR [Sov. Phys.-Dokl.]* 30 (1941), page 913 (cited on page 49).
- [38] A. N. Kolmogorov. “A refinement of previous hypotheses concerning the local structure of turbulence in a viscous incompressible fluid at high Reynolds number”. In: *J. Fluid Mech.* 13 (1962), page 82 (cited on page 64).
- [39] R. H. Kraichnan. “On Kolmogorov’s inertial-range theories”. In: *J. Fluid Mech.* 62.2 (1974), pages 305–330 (cited on page 70).
- [40] R. H. Kraichnan. “Remarks on turbulence theory”. In: *Adv. Math.* 16 (1975), page 305 (cited on page 99).
- [41] D. Kuzzay et al. “New method for detecting singularities in experimental incompressible flows”. In: *Nonlinearity* 30.6 (2017), page 2381. URL: <http://stacks.iop.org/0951-7715/30/i=6/a=2381> (cited on page 78).

- [42] M. Leberre and Y. Pomeau. “Recording of Leray-type singular events in a high speed wind tunnel”. In: <https://arxiv.org/abs/1801.01762> (2018) (cited on page 37).
- [43] J. Leray. “Sur le mouvement d’un liquide visqueux emplissant l’espace”. In: *Acta Math.* 63 (1934), page 193248 (cited on pages 37, 43, 64).
- [44] Y. Li et al. “A public turbulence database cluster and applications to study Lagrangian evolution of velocity increments in turbulence”. In: *J. Turbulence* 9 (2008), page 31 (cited on page 49).
- [46] A. A. Mailybaev. “Renormalization and universality of blowup in hydrodynamic flows”. In: *Phys. Rev. E* 85 (6 June 2012), page 066317. DOI: 10.1103/PhysRevE.85.066317. URL: <https://link.aps.org/doi/10.1103/PhysRevE.85.066317> (cited on page 24).
- [47] A. A. Mailybaev. “Blowup as a driving mechanism of turbulence in shell models”. In: *Phys. Rev. E* 87 (2013), page 053011 (cited on page 24).
- [49] Ch. Meneveau and K. R. Sreenivasan. “The multifractal nature of turbulent energy dissipation”. In: *Journal of Fluid Mechanics* 224 (1991), pages 429–484. DOI: 10.1017/S0022112091001830 (cited on page 141).
- [50] H. K. Moffatt. “The mean electromotive force generated by turbulence in the limit of perfect conductivity”. In: *Journal of Fluid Mechanics* 65.1 (1974), pages 1–10. DOI: 10.1017/S0022112074001200 (cited on page 110).
- [51] J. F. Muzy, E. Bacry, and A. Arneodo. “Wavelets and multifractal formalism for singular signals: Application to turbulence data”. In: *Phys. Rev. Lett.* 67.25 (1991), page 3515 (cited on pages 41, 60, 87, 100).
- [52] S V Nazarenko and V N Grebenev. “Self-similar formation of the Kolmogorov spectrum in the Leith model of turbulence”. In: *Journal of Physics A: Mathematical and Theoretical* 50.3 (2017), page 035501. URL: <http://stacks.iop.org/1751-8121/50/i=3/a=035501> (cited on page 37).
- [53] J. Nečas, M. Ružicka, and V. Sverák. “On Leray’s self-similar solutions of the Navier-Stokes equations”. In: *Acta Math.* 176.2 (1996), pages 283–294. DOI: 10.1007/BF02551584. URL: <https://doi.org/10.1007/BF02551584> (cited on page 37).
- [54] C. Nore et al. “Numerical simulation of the von Karman sodium dynamo experiment”. In: *Journal of Fluid Mechanics* 854 (2018), pages 164–195. DOI: 10.1017/jfm.2018.582 (cited on page 141).
- [55] L. Onsager. “Statistical hydrodynamics”. In: *Il Nuovo Cimento (1943-1954)* 6.2 (1949), pages 279–287 (cited on page 77).
- [56] G. Paladin and A. Vulpiani. “Anomalous scaling laws in multifractal objects”. In: *Phys. Reports* 156.4 (1987), pages 147–225 (cited on page 87).
- [57] R. M. Pereira, Ch. Garban, and L. Chevillard. “A dissipative random velocity field for fully developed fluid turbulence”. In: *Journal of Fluid Mechanics* 794 (2016), pages 369–408. DOI: 10.1017/jfm.2016.166 (cited on page 141).
- [58] A. Pumir and E. D. Siggia. “Finite-time singularities in the axisymmetric three-dimension Euler equations”. In: *Phys. Rev. Lett.* 68 (10 Mar. 1992), pages 1511–1514. DOI: 10.1103/PhysRevLett.68.1511. URL: <https://link.aps.org/doi/10.1103/PhysRevLett.68.1511> (cited on page 59).
- [59] F. Ravelet, A. Chiffaudel, and F. Daviaud. “Supercritical transition to turbulence in an inertially driven von Kármán closed flow”. In: *J. Fluid Mech.* 601 (2008), pages 339–364 (cited on page 18).

- [60] B. Saint-Michel et al. “Probing quantum and classical turbulence analogy in von Karman liquid helium, nitrogen, and water experiments”. In: *Physics of Fluids* 26.12 (2014), page 125109. DOI: 10.1063/1.4904378. eprint: <https://doi.org/10.1063/1.4904378>. URL: <https://doi.org/10.1063/1.4904378> (cited on pages 18, 61, 64).
- [61] E. W. Saw et al. “Experimental characterization of extreme events of inertial dissipation in a turbulent swirling flow”. In: *Nature Comm.* 7 (2016), page 12466 (cited on pages 78, 79, 81, 88).
- [62] C. B. da Silva and J. C. F. Pereira. “Invariants of the velocity-gradient, rate-of-strain, and rate-of-rotation tensors across the turbulent/nonturbulent interface in jets”. In: *Physics of Fluids* 20.5 (2008), page 055101. DOI: 10.1063/1.2912513. eprint: <https://doi.org/10.1063/1.2912513>. URL: <https://doi.org/10.1063/1.2912513> (cited on page 59).
- [63] M. Steenbeck, F. Krause, and K.-H. Rädler. “Berechnung der mittleren Lorentz-Feldstärke für ein elektrisch leitendes Medium in turbulenter, durch Coriolis-Kräfte beeinflußter Bewegung”. In: *Zeitschrift für Naturforschung A* 21.4 (1966), pages 369–376. DOI: doi:10.1515/zna-1966-0401. URL: <https://doi.org/10.1515/zna-1966-0401> (cited on page 110).
- [64] P. L. Sulem et al. “Generation of large-scale structures in three-dimensional flow lacking parity-invariance”. In: *Journal of Fluid Mechanics* 205 (1989), pages 341–358. DOI: 10.1017/S0022112089002065 (cited on page 110).
- [65] P. Tanga et al. “Forming Planetesimals in Vortices”. In: 121.1 (May 1996), pages 158–170. DOI: 10.1006/icar.1996.0076 (cited on pages 118, 125, 127).
- [66] G.I. Taylor. “Production and dissipation of vorticity in a turbulent fluid”. In: *Proceedings of the Royal Society* 164.916 (1938), page 15 (cited on page 59).
- [67] H. Touchette. “The large deviation approach to statistical mechanics”. In: *Physics Reports* 478.1 (2009), pages 1–69. ISSN: 0370-1573. DOI: <https://doi.org/10.1016/j.physrep.2009.05.002>. URL: <http://www.sciencedirect.com/science/article/pii/S0370157309001410> (cited on pages 42, 70).
- [69] A. Wirth, S. Gama, and U. Frisch. “Eddy viscosity of three-dimensional flow”. In: *Journal of Fluid Mechanics* 288 (1995), pages 249–264. DOI: 10.1017/S0022112095001133 (cited on page 110).
- [70] P. K. Yeung, X. M. Zhai, and K. R. Sreenivasan. “Extreme events in computational turbulence”. In: *Proceedings of the National Academy of Sciences* 112.41 (2015), pages 12633–12638. ISSN: 0027-8424. DOI: 10.1073/pnas.1517368112. eprint: <http://www.pnas.org/content/112/41/12633.full.pdf>. URL: <http://www.pnas.org/content/112/41/12633> (cited on page 89).

Books



Index

A

Additional properties of Multifractals 99
AKA effect 124

B

Blow-ups 23, 27, 37
Burgers 42, 88

C

Cascades 53
Closure 129
Convection scaling laws 151

E

Eddy viscosity 132
Equations (of Fluid Dynamics) 15
Extreme events 88

F

Filters 130

H

HC 41

I

Intermittency 60

K

K41 47
K62 67
KHM 52

L

LES 131
Log-lattice 143
Log-normal model 96

M

Multifractal refined similarity 99
Multifractal spectrum 93
Multifractals 42, 87
Multiscale method 120

N

Negative eddy-viscosity 125

O

Onsager's conjecture 77

P

Particles 113

R

- RANS 130
Rayleigh-Benard 147
RDT 137
Richardson law 111

S

- Scale separation 108
Self-similar blow up 87, 100
Shell Model 142
Shock 77
Symmetries 57

T

- Turbulence 13
Turbulent diffusivity 121
Turbulent transport 107

W

- WKHM 73

Z

- Zeroth law of turbulence 61